Applications of computer algebra to the theory of electron energy loss

Thesis

APPLICATIONS OF COMPUTER ALGEBRA

TO

THE THEORY OF ELECTRON ENERGY LOSS

Mingliang Chen, B.Sc., M.Sc.

Thesis submitted to be examined for the
degree of Doctor of Philosophy, in Physics.

The Open University
December, 1993

Paginated

blank pages are scanned as found in original thesis

No information is missing

To my wife, Hong Lu

You can choose any degrees of freedom you like to describe a problem–but if you choose the wrong ones, you'll be sorry.

——S. Weinberg

EX12

HIGHER DEGREES OFFICE

LIBRARY AUTHORISATION FORM

Please return this form to the Higher Degrees Office with the bound library copies of your thesis. All students should complete Part 1. Part 2 applies only to PhD students.

Student: MINGLIANG CHEN PI: M7063156

Degree: PhD

Thesis title: Applications of Computer Algebra to The Theory of Electron Energy Loss

Part 1 Open University Library Authorisation (to be completed by all students)

I confirm that I am willing for my thesis to be made available to readers by the Open University Library, and that it may be photocopied, subject to the discretion of the Librarian.

Signed: [signature] Date: 14/4/94

Part 2 British Library Authorisation (to be completed by PhD students only)

If you want a copy of your PhD thesis to be held by the British Library, you must sign a British Doctoral Thesis Agreement Form. You should return it to the Higher Degrees Office with this form and your bound thesis. *You are also required to supply a third, unbound copy of your thesis.* The British Library will use this to make their microfilm copy; it will not be returned. Information on the presentation of the thesis is given in the Agreement Form.

If your thesis is part of a collaborative group project, you will need to obtain the signatures of others involved for the Agreement Form.

The University has agreed that the lodging of your thesis with the British Library should be voluntary. Please tick either (a) or (b) below to indicate your intentions.

(a) ☑ I am willing for the Open University to supply the British Library with a copy of my thesis. A signed Agreement Form and 3 copies of my thesis are attached (two bound as specified in Section 9.4 of the Research Degree Handbook and the third unbound).

(b) ☐ I do not wish the Open University to supply a copy of my thesis to the British Library.

Signed: [signature] Date: 14/4/94

EX12/January 1993/dg/akb

Abstract

This thesis develops dielectric theory in multilayers and following cases have been considered:

- Normal incidence on a multilayered slab with n isotropic layers.
- Parallel incidence on a multilayered slab with n isotropic layers.
- Normal and parallel incidence on a multilayered with n anisotropic layers, analysed in the non-retarded limit.

In each case we have developed the appropriate transfer matrix recurrence relation and solved it exactly, using computer algebra (REDUCE and MATHEMATICA) as an essential guide. For all the problems listed above, we have obtained *closed-form* solutions for the dispersion relations of surface and interface plasmons and for the angle-resolved energy-loss function. The energy-loss spectrum is then obtained by integrating over wavevectors. The formulas we have derived are applied to real materials such as Al/Mg, Al/Al_2O_3, $Al/SiO_2/Si$, diamond and graphite.

PREFACE

This thesis is an account of the work carried out at the Department of Physics, The Open University, under the supervision of Dr. John Bolton between October 1989 and December 1993. I declare that this thesis has not been submitted for any other qualification to this or any other university. The material is original, except where due reference is made to other sources.

Accounts of parts of this work have been published in the following papers:

1. M. Chen, J. P. R. Bolton and A. J. McGibbon, "Damped Surface Plasmons in Thin Slabs and Wedges of Diamond", *EMAG-MICRO 91: Inst. Phys. Conf. Ser. No 119*, 125 (1991).

2. M. Chen, J. P. R. Bolton and L. M. Brown, "Imaging Surface States in the Electron Microscope: Dielectric Theory and The Born Approximation", *EMAG-MICRO 91: Inst. Phys. Conf. Ser. No 119*, 499 (1991).

3. M. Chen and J. P. R. Bolton, "Retarded Dielectric Theory of Electron Energy Loss in Multilayers and Superlattices", *Superlattices and Microstructures, Vol. 12, No 4*, 531(1992).

4. J. P. R. Bolton and M. Chen, "Electron Energy Loss in Multilayered Slabs: Normal Incidence", Submitted to *Ultramicroscopy*.

5. J. P. R. Bolton and M. Chen, "Electron Energy Loss in Multilayered

Slabs: Parallel Incidence", Submitted to *Ultramicroscopy.*

6. J. P. R. Bolton and M. Chen, "Electron Energy Loss in Anisotropic Salbs and Multilayers", Submitted to *Ultramicroscopy.*

I am glad to have this opportunity to express my deepest gratitude to my supervisor, Dr. John Bolton, without whom this work would not have been possible. Throughout the past four years there has rarely been a day that he was not available to help or advise me. He guided my steps in subject with clarity, patience and continuous encouragement. His friendship makes my stay in England easy.

I have benefitted greatly from visiting to Cambridge University. In particular I am greatly indebted to Prof. L.M. Brown, F.R.S. for hospitality and supervision of my experimental work and continued encouragement and suggestion of topics. Thanks are also given to the following members of the Cavendish Laboratory of Cambridge University: Drs. A.J. McGibon and P. Fallon for help in experimental work, Dr. J. Yuan for fruitful discussions about the anisotropic problem, and Dr. C.A. Walsh for offering theoretical details about the single interface and sandwich problems.

I thank Drs. Steve Swithenby, Tom Smith, Professors Russell Stannard and S.J. Bell Burnell together with the staffs, students and secretaries of the Physics Department of the Open University, for making my stay there so pleasant. I gratefully acknowledge an Open University award of research studentship which enabled me to come to England. I would also like to give my thanks to the academic computing service of Open University for providing reliable computing facilities.

Finally I thank my wife for her support, confidence and love through all those long tiring times and our parents for their constant encouragement, without

which I would not have been able to embark on my graduate studies.

Contents

Part I

Background Material

Chapter 1.

An Introduction to EELS

The purpose of this thesis is to extend the dielectric theory of electron energy loss to situations in which the algebra becomes very complex – including multilayered slabs and anisotropic media. Computer algebra is used as a powerful tool to help obtaining closed form solutions for dispersion relations and energy-loss spectra. In this introductory chapter, the subject of EELS is briefly introduced and the theory used in this thesis is outlined.

In a transmission electron microscope, electrons are accelerated to high energies and transmitted through a thin specimen so as to understand the structure and behaviour of materials. An electron passing through a sample may be scattered. The scattering is divided into *elastic scattering* and *inelastic scattering* according to whether or not the energy of the electron is significantly changed. Elastic scattering may be regarded as being due to the Coulomb interaction of the incoming electron with an *atomic nucleus* or to diffraction by crystal planes. It gives rise to the usual contrast mechanism for imaging the specimen and its diffraction pattern. Inelastic scattering arises from the Coulomb interactions of the incident electron with the *electrons* of the specimen. Either single-electron or collective plasmon modes are produced and the incident electron loses energy. Electron energy loss spectroscopy (EELS) measures the energy (and sometimes the angular distribution) of a mono-energetic electron beam that has interacted with a sample. In this chapter, I begin with fundamental features of the electron

energy loss spectrum and then introduce the basic theory that will be used in this thesis.

1.1. The electron energy-loss spectrum

Electrons passing through a material may lose energy by a variety of mechanisms. Briefly, a typical EELS spectrum recorded in the electron microscope consists of three main regions as shown in Figure 1.1.

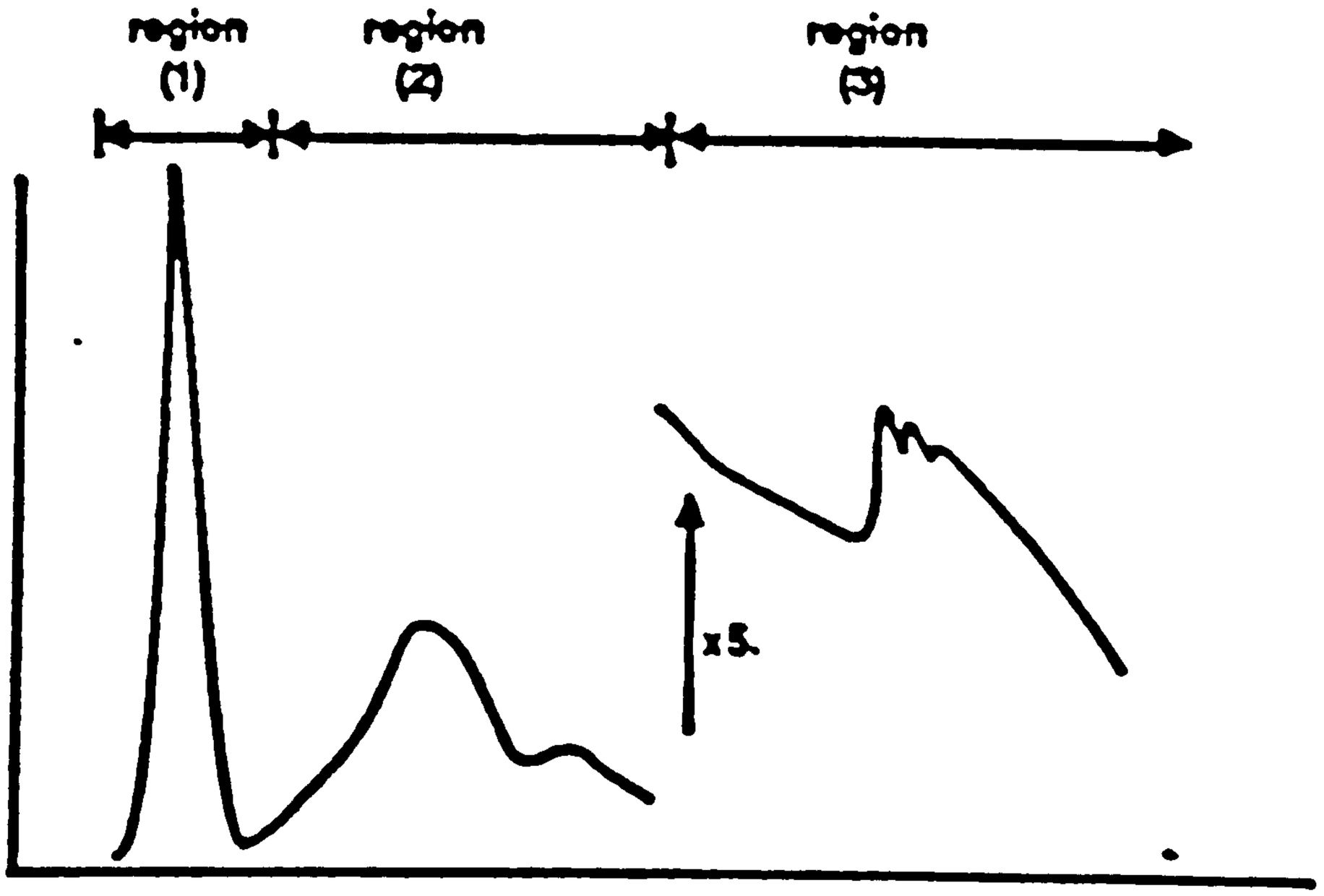

Figure 1.1 Schematic diagram of the energy-loss spectrum observed in an electron microscope [1].

The smallest energy losses, which are typically of the order of 10-100 meV, arise from the excitation of phonons, or vibrations of atoms. As the resolution of EELS in the electron microscope is about 1 eV, this energy cannot be resolved and is therefore included in the *zero-loss* peak in which the electrons

appear to be scattered elastically.

At higher energies, typically a few hundred eV, "edges" can be seen in the spectrum—indicating the onset of excitations from the various inner atomic shells to the conduction band. The edges are characteristic of the element whose electrons are excited and their energy and height can be used for elemental analysis.

The part of the spectrum below the onset of the inner shell edges, typically 1 to 50 eV, consists primarily of a complicated mixture of single electron excitations to vacant states and collective excitations. The positions of the single electron excitation peaks are related to the joint density of states between the conduction and valence bands, whereas the energy required for collective excitations depends mainly on the electron density in the solid. In materials which support such excitations there is a peak in the loss spectrum around energy-loss $\hbar\omega_p$ where ω_p is the plasmon frequency. Within the free-electron model of solids, an expression for the frequency of the plasmon excitations is readily derived [2]

$$\omega_p = (ne^2/\varepsilon_0 m)^{\frac{1}{2}}$$

where n is the number density of the electron gas, $-e$ is the charge of an electron, ε_0 is the permittivity of free space and m is the electron mass.

In finite media plasmons can be excited at the surfaces or at the interface between two media. In addition there may be structure arising from Cerenkov radiation at frequencies for which the speed of light in the medium is less than that of the incident electron. Transition radiation can also be produced when the electron passes from one medium to another. An extensive review of these contributions has been given by Raether [3]. The low loss outer shell excitations are the main theme of this thesis.

1.2. Macroscopic electrodynamics of EELS

There are two main theoretical treatments of inelastic electron scattering– *Bethe theory* and *dielectric theory*. The Bethe theory is a microscopic theory, which is based on the Born approximation of quantum mechanics [4] and is mainly used for inner shell excitations. The dielectric theory is a macroscopic effective medium theory and is used for outer shell excitations. Since this thesis concentrates on outer shell excitations, it will be based on the dielectric theory. Within the dielectric theory model, the characteristics of the medium are provided by the components of the complex dielectric tensor $\epsilon^{(ij)}$. By definition, this links the vectors $\mathbf{E}$ and $\mathbf{D}$ in an infinite linear homogeneous medium[1] as follows:

$$D_i(\mathbf{r},t) = \epsilon_0 \int \mathrm{d}\mathbf{r}'\mathrm{d}t'\epsilon^{(ij)}(\mathbf{r}-\mathbf{r}',t-t')E_j(\mathbf{r}',t') \tag{1.1}$$

Taking the Fourier transformation of Equation 1.1 with respect to space and time, one obtains

$$D_i(\mathbf{k},\omega) = \varepsilon_0\epsilon^{(ij)}(\mathbf{k},\omega)E_j(\mathbf{k},\omega) \tag{1.2}$$

Here, and throughout this thesis we define the Fourier transforms and their inverses by

$$E_i(\mathbf{r},t) = \frac{1}{(2\pi)^4}\int_{-\infty}^{\infty} E_i(\mathbf{k},\omega)\mathrm{e}^{\mathbf{i}(\mathbf{k}\cdot\mathbf{r}-\omega t)}\mathrm{d}\omega\mathrm{d}\mathbf{k}$$

$$E_i(\mathbf{k},\omega) = \int_{-\infty}^{\infty} E_i(\mathbf{r},t)\mathrm{e}^{-\mathbf{i}(\mathbf{k}\cdot\mathbf{r}-\omega t)}\mathrm{d}t\mathrm{d}\mathbf{r}$$

with analogous equations for $\mathbf{D}$.

[1] Here and throughout this introduction summation is to be carried out over all tensorial subscripts which occur twice.

Equation 1.2 takes spatial dispersion as well as frequency dispersion into account[2]. The physical nature of spatial and frequency dispersion is very easily understood. As indicated in Equation 1.1, the displacement field $\mathbf{D}(\mathbf{r}, t)$ at a given position and instant is determined not only by the electric field value $\mathbf{E}(\mathbf{r}, t)$ at that instant but also by electric field values at neighbouring points and previous times. This translates into a wavevector- and frequency-dependence of the spatially and temporally Fourier-transformed dielectric function. In the context of electron energy loss studies, the spatial dispersion can be regarded as being weak.[3] Unless the energy-loss spectrum is recorded using a sufficiently small collection aperture, contributions from different values of $\mathbf{k}$ cause only a slight broadening and upward shift of the plasmon peak [4]. This study will neglect spatial dispersion, corresponding to a local dielectric function. Most of the applications of dielectric theory to electron energy loss spectroscopy to date have also used local dielectric functions.

In the local approximation,

$$\epsilon^{(ij)}(\mathbf{r} - \mathbf{r}', t - t') = \epsilon^{(ij)}(t - t')\delta(\mathbf{r} - \mathbf{r}')$$

so Equation 1.2 becomes

$$D_i(\omega) = \varepsilon_0 \epsilon^{(ij)}(\omega) E_j(\omega) \tag{1.3}$$

[2]The term "spatial dispersion" indicates the existence of a $\mathbf{k}$ dependence of $\epsilon^{(ij)}$ and frequency dispersion means a ω dependence of $\epsilon^{(ij)}$. In generally, a local dielectric function in real space is non-dispersive in $\mathbf{k}$ space. Whereas a non-local dielectric function in real space is dispersive in $\mathbf{k}$ space.

[3]In the electron microscope, most of scattering has $k \leq 0.1k_c$ (especially from surface and interface–the subject of this thesis), where $k_c = 15nm^{-1}$ is cut-off wavevector corresponding to scattering through a maximum angle of 9 mrad. So the conditions $kv_F/\omega << 1$ and $\hbar k^2/2m\omega << 1$ are generally met. Under these circumstance, we have [5]

$$\epsilon^{\mathrm{RPA}}(k, \omega) \approx \epsilon^{\mathrm{RPA}}(0, \omega).$$

The dielectric function can be used to predict the low-energy region of the electron energy loss spectrum, which is generally dominated by bulk plasmon excitations and interband transitions and may also include surface and interface excitations. These spectra can be calculated theoretically in terms of the dielectric function by evaluating the work done on an electron by the electric field $\mathbf{E}$ induced in the medium through or near which the electron is travelling. If an electron with velocity enters the crystal, the work done moving against the field is expressed by

$$\begin{aligned} W &= \int \mathbf{j}_{\mathrm{ext}}(x,y,z,t)\cdot\mathbf{E}(x,y,z,t)\mathrm{d}\mathbf{r}\mathrm{d}t \\ &= \frac{1}{(2\pi)^3}\int \mathbf{j}^*_{\mathrm{ext}}(k_x,k_y,z,\omega)\cdot\mathbf{E}(k_x,k_y,z,\omega)\mathrm{d}k_x\mathrm{d}k_y\mathrm{d}z\mathrm{d}\omega \end{aligned} \tag{1.4}$$

where $\mathbf{j}_{\mathrm{ext}}(x,y,z,t)$ is the current density. By calculating the work done on the incident electron, and interpreting the result in terms of the transfer of quanta of energy $\hbar\omega$, we can write [6]

$$W = \int_0^\infty \hbar\omega \mathrm{d}(\hbar\omega) \int_{-\infty}^{\infty} \mathrm{d}^2k \frac{\mathrm{d}^2P}{\mathrm{d}(\hbar\omega)\mathrm{d}k} \tag{1.5}$$

where the semiclassical energy-loss function $\mathrm{d}^2P/\mathrm{d}(\hbar\omega)\mathrm{d}k$ is interpreted as the probability density for creating an excitation of energy $\hbar\omega$ and $k = \sqrt{k_x^2 + k_y^2}$ is magnitude of transverse wavevector. The loss function can also be integrated over wavevectors to obtain the scattering probability per energy range, $I(\hbar\omega)$. If all the scattered electrons were collected, one would expect that

$$I(\hbar\omega) = \int_{-\infty}^{\infty} \frac{\mathrm{d}^2P}{\mathrm{d}(\hbar\omega)\mathrm{d}k}\mathrm{d}^2k \tag{1.6}$$

Therefore, the fundamental problem of the dielectric theory of electron energy loss consists of finding the work done on the incident electron by the induced electric field. The first step is to find the electric field by solving Maxwell's equations with the appropriate source terms and boundary condi-

tions. Maxwell's equations are

$$\nabla \cdot \mathbf{D} = \rho_{\text{ext}}$$

$$\nabla \times \mathbf{E} = -\frac{\partial \mathbf{B}}{\partial t}$$

$$\nabla \cdot \mathbf{B} = 0$$

$$\nabla \times \mathbf{H} = \frac{\partial \mathbf{D}}{\partial t} + \mathbf{j}_{\text{ext}}$$

where $\mathbf{E}$ is the electric field strength, $\mathbf{D}$ and $\mathbf{B}$ are the electric displacement field and magnetic field induction, and $\mathbf{j}_{\text{ext}}$ and ρ_{ext} are the current and charge densities of the external sources [4]. For non-magnetic media, all the properties of the medium are expressed in the relations linking $\mathbf{D}$ with the vectors $\mathbf{E}$ and $\mathbf{B}$.

If an abrupt interface exists between two media it is necessary to use boundary conditions which can themselves be obtained from Maxwell's equations. These conditions have the form

$$E_{1t} = E_{2t}, \qquad D_{1n} = D_{2n}$$

$$H_{1t} = H_{2t}, \qquad B_{1n} = B_{2n}$$

where the subscripts n and t refer to the normal and tangential components.

For isotropic non-magnetic medium (assuming $\mu = 1$), the electromagnetic fields can be conveniently expressed in terms of the Hertz vector $\mathbf{\Pi}$ [7]:

$$\mathbf{E}(\mathbf{r},\omega) = \nabla(\nabla \cdot \mathbf{\Pi}(\mathbf{r},\omega)) + (\epsilon\, \omega^2/c^2)\mathbf{\Pi}(\mathbf{r},\omega)$$

[4] indicating that the quantities $\mathbf{j}_{\text{ext}}$ and ρ_{ext} are assumed to be given independently of $\mathbf{E}, \mathbf{D}$ and $\mathbf{B}$.

$$\mathbf{H}(\mathbf{r},\omega) = -(\mathrm{i}\omega\epsilon/c)\nabla \times \mathbf{\Pi}(\mathbf{r},\omega)$$

where the spectral analysis used is

$$\mathbf{\Pi}(\mathbf{r},t) = \frac{1}{2\pi}\int_{-\infty}^{\infty} \mathbf{\Pi}(\mathbf{r},\omega)\mathrm{e}^{-\mathrm{i}\omega t}\mathrm{d}\omega$$

and similarly for other quantities. Maxwell's equations then reduce to a wave equation for the Hertz vector [7]:

$$\left(\nabla^2 + \epsilon\,\omega^2/c^2\right)\mathbf{\Pi}(\mathbf{r},\omega) = (1/\mathrm{i}\omega\epsilon_0\epsilon)\mathbf{j}_{\mathbf{ext}}(\mathbf{r},\omega) \tag{1.7}$$

In the case of two adjacent materials, characterised by the dielectric functions $\epsilon_1(\omega)$ and $\epsilon_2(\omega)$, with interface in the $x-y$ plane, the boundary conditions for the Hertz vector take the form

$$\epsilon_1\Pi_1^x = \epsilon_2\Pi_2^x$$

$$\mathrm{i}k_x\Pi_1^x + \frac{\partial\Pi_1^z}{\partial z} = \mathrm{i}k_x\Pi_2^x + \frac{\partial\Pi_2^z}{\partial z}$$

$$\epsilon_1\Pi_1^z = \epsilon_2\Pi_2^z$$

and

$$\epsilon_1\frac{\partial\Pi_1^x}{\partial z} = \epsilon_2\frac{\partial\Pi_2^x}{\partial z}$$

where we have assumed that $\mathbf{\Pi}$ has components only in the $\hat{x}$ (tangential component) and $\hat{z}$ (normal component) directions.

In the non-retarded limit, the dielectric theory involves solving Poisson's equation:

$$\nabla^2\phi(\mathbf{r},\omega) = -\rho_{\mathbf{ext}}(\mathbf{r},\omega)/\varepsilon_0\epsilon \tag{1.8}$$

where $\phi(\mathbf{r},\omega)$ is electric potential which is related to the electric field by

$$\mathbf{E} = -\nabla\phi \tag{1.9}$$

and satisfies the boundary conditions

$$\phi_1 = \phi_2 \qquad \text{and} \qquad \epsilon_1 \frac{\partial \phi_1}{\partial z} = \epsilon_2 \frac{\partial \phi_2}{\partial z}$$

For an anisotropic medium, the problem becomes more complicated. We will discuss this in Part III of this thesis. Equation 1.7 is the basic equation used in Part II of this thesis, which uses computer algebra to solve this equation in different situations.

In summary, this chapter introduced electron energy loss spectroscopy and dielectric theory. The basic formulae will be applied to various complex systems to predict electron energy-loss spectra. In the next chapter, we first review theoretical developments of dielectric theory and identify some important solved problems. Subsequently, Part II (Chapters 3–6) studies multilayered isotropic media and Part III (Chapter 7 and 8) studies multilayered anisotropic media.

CHAPTER 2.

THEORETICAL DEVELOPMENTS

Dielectric theory of electron energy-loss spectroscopy has been widely developed. This chapter will review some literature related to this thesis. The main aims of the thesis are also presented.

2.1. Introduction

Electron energy loss spectroscopy was started in the early thirties by the work of Rudberg [8, 9]. In this early work, primary electrons of a few hundreds eV were reflected from the surfaces of evaporated metal films. The reflected beam was dispersed in energy, spatially separated by a magnetic prism and its intensity measured as a function of position, and hence of energy, by a quadrant electrometer. Rudberg was able to show that the spectrum obtained was characteristic of the material being studied.

Bohm and Pines [10] explained the observations of Rudberg using a wave-mechanical treatment in which a fast electron can give up energy $\hbar\omega$ to the electron gas in a solid, by creating a *plasmon*. More generally, Hubbard [11] showed that fast charged particles lose energy in a bulk dielectric medium in a way that depends on $\mathrm{Im}(-1/\epsilon(\omega))$. Ritchie [6] first predicted that different plasmon oscillations should be possible at the surface of a Drude metal.

Ruthemann [12] first measured the loss spectrum of electrons which had been transmitted through a thin film. After the invention of the electron microscope electron energy loss was incorporated first into the TEM(transmission electron microscope) and later into the STEM(scanning transmission electron microscope). A typical STEM provides a focused 100 kV electron beam within a probe of diameter less than 0.8 nm. This gives an energy–loss spectrum from a precisely defined region. Some capabilities of the modern analytical STEM have been discussed by Pennycook [13].

2.2. Planar geometries

2.2.1. Normal incidence

Dielectric theory gives a standard procedure for finding the energy loss spectrum of electrons passing through dielectric media. The electron energy loss spectra due to plasmon excitations and interband transitions can be calculated theoretically in terms of the dielectric function by evaluating the work done on an electron by the electric field **E** induced in the medium through or near which the electron is travelling. This theory has been widely used to study the interaction of fast electrons with plasmons in thin films and to analyse energy loss spectra obtained in a STEM.

The interaction of charged particles with thin films was first treated by Ritchie [6] who used classical (i.e. non-retarded) dielectric theory. By solving Poisson's equation to obtain the electric potential everywhere in space, he derived the total transition probability[1]

$$\left(\frac{\mathrm{d}^2P}{\mathrm{d}(\hbar\omega)\mathrm{d}k}\right)_{\text{classical}} = \frac{e^2}{4\pi^3\varepsilon_0\hbar^2v^2}\mathrm{Im}(\chi_{\text{bulk}} + \chi_{\text{surface}})$$

where

[1]It is necessary to correct a misprint in Ritchie's expression for the surface contribution. I have checked Equation 2.1 with a REDUCE program.

$$\chi_{\text{bulk}} = -\frac{1}{\epsilon}\left(\frac{a}{k^2+\omega^2/v^2}\right)$$

and

$$\chi_{\text{surface}} = -\frac{2k}{(k^2+\omega^2/v^2)^2}\left(1-\frac{1}{\epsilon}\right) \times \frac{2(\epsilon-1)\cos(\omega a/v)+(\epsilon-1)^2\exp(-ka)+(1-\epsilon^2)\exp(ka)}{(\epsilon-1)^2\exp(-ka)-(\epsilon+1)^2\exp(ka)} \quad (2.1)$$

where $k = \sqrt{k_x^2+k_y^2}$ is the magnitude of the transverse wavevector, $\epsilon(\omega)$ is the dielectric function of the thin film and a is its thickness. Ritchie's studies were a turning point in the treatment of electron interaction after the earlier works of Pines and Bohm [10, 14, 15, 16, 17, 18], Hubbard [11] and Ferrell [19]. He predicted that a surface plasmon exists at the surfaces of the film. For a simple dielectric function (based on the Drude model of a metal) the surface plasmon frequency was predicted to be $\omega_s = \omega_p/\sqrt{2}$, a result which was confirmed by Powell and Swan [20] experimentally.

Kröger [21, 22] calculated the losses suffered by an electron passing through a thin film including the effects of retardation. Starting from Maxwell's equations, Kröger showed that[2]

$$\left(\frac{\mathrm{d}^2P}{\mathrm{d}(\hbar\omega)\mathrm{d}k}\right)_{\text{retarded}} = \frac{e^2}{4\pi^3\varepsilon_0\hbar^2v^2}\mathrm{Im}(\chi_{\text{bulk}}+\chi_{\text{surface}})$$

where

$$\chi_{\text{bulk}} = -\frac{1-\epsilon\beta^2}{\epsilon p^2}a$$

[2]Kröger's original expression for p_{01} was misprinted. The result presented here has been corrected and was checked by REDUCE and MATHEMATICA programs. It is worth noting that Kröger's misprint has propagated, along with other errors, in many papers [23, 1, 24]. This is not surprising in views of complexity of the result, but it does illustrate the advantage of planing such calculations on a reliable footing by carrying them out via computer algebra.

$$\chi_{\text{surface}} = \frac{2k^2(\epsilon-1)^2}{p_0^4 p^4}\left[\frac{p_{01}^4}{\epsilon}\left(\frac{\sin^2(\omega a/2v)}{L^+}+\frac{\cos^2(\omega a/2v)}{L^-}\right)\right.$$
$$+\beta^2 q_0\frac{\omega}{v}p_{01}^2\left(\frac{1}{L^+}-\frac{1}{L^-}\right)\sin(\omega a/v) \qquad (2.2)$$
$$\left.-\beta^2\frac{\omega^2}{v^2}q_0 q\left(\frac{\cos^2(\omega a/2v)\tanh(qa/2)}{L^+}+\frac{\sin^2(\omega a/2v)\coth(qa/2)}{L^-}\right)\right]$$

where

$$\beta = v/c, \qquad q=\sqrt{k^2-\epsilon\frac{\omega^2}{c^2}}, \qquad q_0=\sqrt{k^2-\frac{\omega^2}{c^2}}$$
$$L^+ = q_0\epsilon + q\tanh(qa/2), \qquad L^- = q_0\epsilon + q\coth(qa/2)$$
$$p^2 = q^2+\frac{\omega^2}{v^2}, \qquad p_0^2 = q_0^2+\frac{\omega^2}{v^2}, \qquad p_{01}^2 = k^2+\frac{\omega^2}{v^2}-(\epsilon+1)\frac{\omega^2}{c^2}$$

These expressions give a complete macroscopic description of the energy losses for normal incidence on a thin film, including plasmons, interband transitions, Cerenkov radiation and transition radiation. Kröger also extended his studies to oblique incidence [22] and separated out the contributions due to Cherenkov losses and transition radiation.

For multilayered slabs, Ritchter and Geiger [25] have used dielectric theory to analyse the energy loss of electrons for the case of normal incidence on a multilayered structure. In their studies, retardation effects were neglected. Both the dispersion relation and the scattering probability were fully solved for three layered systems. Numerical examples for two-metallic-layer system (Al/Mg) and tarnished metals (eg. Al/Al_2O_3, Be/BeO, Ag/Ag_2S) were also discussed.

A retarded theory of electron energy loss for normal incidence on m adjacent films was developed by Chase and Kliewer in 1970 [26]. They developed a transfer matrix algorithm, which was solved numerically to find the energy

loss. However, this approach provides no insight into the analytic form of the solution or its relationship to the well-known results established for a single slab [6, 21]. Moreover, their final equations were only applied to the special two-layer case, LiF on a conducting substrate in the energy region of the surface modes of vibration.

2.2.2. Parallel incidence

Interface effects on the inelastic electron scattering probability are more significant when electron travels parallel to the interfaces of the specimen. An example of work on parallel incidence is a paper by Echenique and Pendry [27], which evaluated the imaginary part of the self energy for an electron travelling in a vacuum parallel to the surface of a semi-infinite solid. Echenique adapted this formalism to the case of an electron in a STEM, and presented expressions for the probability of an electron losing an energy E per unit path length [28] in the classical approximation, but including the effects of spatial dispersion. In order to compare local and non-local effects, Echenique used following simple expression for non-local dielectric function

$$\epsilon(k,\omega) = 1 + \frac{\omega_p^2}{\beta^2 k^2 + O(k^4) - \omega(\omega + i\gamma)}$$

where $\beta^2 = (3/5)v_f^2$ is a constant related to the Fermi velocity v_f in an electron gas of plasmon frequency ω_p and γ is a small damping constant. He found out that effects of non-locality are important only at short distances from the surface, being of the order of 1% for distances greater than 1 nm. This model was also used to derive the probability of MgO surface excitations, with relativistic effects included [29].

Howie and Milne [30] used a similar approach and calculated non-retarded energy loss spectra for an electron beam reflected at a small glancing angle from the surface of copper and MgO crystals. In their second paper an analysis of the silicon/silicon oxide system was presented [31]. They found

an 8 eV peak in the vicinity of the interface but this was only visible when the beam was within 2 nm of the interface. They also noticed a shift of the main plasmon peaks towards each other at the interface. The GaAs/vacuum interface was briefly treated in reference [31] as well.

Batson [32, 33] studied surface plasmon scattering on flat surfaces by high-energy electrons. In reference [32], he discussed the spatial localization of bulk plasmons in case of aluminum. Predictions for a planar aluminum/aluminum oxide/vacuum system with the electron beam moving through the vacuum parallel to the solid/vacuum boundary were compared with experiment. The model predicted an 8.8 eV surface plasmon energy which compared reasonably well to the 7.8 eV experimental value at a 1 nm impact parameter. With the electron moving in the aluminium region, the surface plasmon was observed at a much lower intensity and the energy shifted to lower position by 0.6 eV. The agreement was satisfactory for the fitted oxide thickness of 5 nm, providing that such model describes the inelastic scattering probability at least for the distances greater than 1 nm. This result also confirmed the theoretical estimates of Echenique for this system [28].

The interaction of a relativistic electron beam, travelling parallel to the surface of semi-infinite medium (with dielectric function $\epsilon(\omega)$), including the effects of retardation, was analysed by Garcia-Molina, Gras-Marti, Howie and Ritchie [34]. With Maxwell's equations expressed in term of term of the Hertz vector, they derived the excitation probability for an electron travelling both inside and outside the medium. A detailed numerical analysis was carried out for MgO single surface. They found that the effects of retardation can be significant, particularly for beam energy losses in energy regions where the real part of the dielectric constant is large. The retarded excitation probability is typically about 10-30% larger than the non-retarded result, for electron energies greater than 100 keV.

Parker [35] and Walsh [36] have considered a three layered structure, ie. a slab with thickness a and dielectric function ϵ_1 (medium 1) sandwiched by two semi-infinite media with dielectric function ϵ_0 (medium 0) and ϵ_2 (medium 2) respectively. The excitation probability per unit path and per unit energy range for an electron travelling in medium 2 at the distance z_b from the interface of ϵ_0/ϵ_1 is given by[3]

$$\frac{\mathrm{d}^2P}{\mathrm{d}(\hbar\omega)\mathrm{d}x} = \frac{Q^2}{2\pi^2\hbar^2v^2}\int_0^\infty dk_y \mathrm{Im}\left\{\chi_{\mathrm{bulk}} + \chi_{\mathrm{surface}}\right\}$$

where for external beam (electron travels in medium 2)

$$\chi_{\mathrm{bulk}} = -\frac{\mu_2^2}{\epsilon_2 q_2}$$

$$\begin{aligned}\chi_{\mathrm{surface}} = &-\frac{\mu_2^2}{\epsilon_2 q_2 L_1}\left(\frac{q_1+q_0}{q_1-q_0}\mathrm{e}^{2q_1a} + \frac{q_2+q_1}{q_2-q_1}\right)\mathrm{e}^{-2q_2z_b} \\ &+ \frac{2q_2}{\epsilon_2 L_1 L_2}(\epsilon_0 q_1 - \epsilon_1 q_0)\left\{4(\epsilon_0-\epsilon_1)(q_1-q_0)\epsilon_2 q_1^2\mathrm{e}^{2q_1a}\right. \\ &\left.+ (\epsilon_1-\epsilon_2)\left(\frac{q_1+q_0}{q_1-q_0}\mathrm{e}^{2q_1a}+1\right)\right)\left(\frac{\epsilon_0 q_1+\epsilon_1 q_0}{\epsilon_0 q_1-\epsilon_1 q_0}\mathrm{e}^{2q_1a}+1\right)\mathrm{e}^{-2q_2z_b}\Bigg\}\end{aligned} \tag{2.3}$$

where

$$k^2 = k_y^2 + \frac{\omega^2}{v^2}, \qquad q_i^2 = k^2 - \epsilon_i\frac{\omega^2}{c^2}, \qquad \mu_i = 1 - \epsilon_i\frac{v^2}{c^2}$$

$$L_1 = \frac{q_2+q_1}{q_2-q_1}\frac{q_1+q_0}{q_1-q_0}\mathrm{e}^{2q_2a} + 1$$

and

$$L_2 = \frac{\epsilon_1 q_2+\epsilon_2 q_1}{\epsilon_1 q_2-\epsilon_2 q_1}\frac{\epsilon_0 q_1+\epsilon_1 q_0}{\epsilon_0 q_1-\epsilon_1 q_0}\mathrm{e}^{2q_2a} + 1$$

For an internal beam, ie. with the electron travelling in medium 1,

[3]Equations 2.3 and 2.4 and related quantities have been rearranged here so that they can be written in the simplest possible form.

$$\chi_{\text{bulk}}(k,\omega) = -\frac{\mu_1}{\epsilon_1 q_1}$$

and

$$\chi_{\text{surface}} = \frac{\mu_1}{\epsilon_1 q_1 L_1}\lambda_1 + \frac{2q_1}{\epsilon_1 L_1 L_2}\{\lambda_2(\epsilon_2-\epsilon_1)+\lambda_3(\epsilon_0-\epsilon_1)\} \tag{2.4}$$

where

$$\lambda_1 = \frac{q_2+q_1}{q_2-q_1}e^{2q_1(a-z_b)} + \frac{q_1+q_0}{q_1-q_0}e^{2q_1 z_b} - 2$$

$$\lambda_2 = \left(\frac{q_1+q_0}{q_1-q_0}e^{2q_1 z_b}+1\right)\left(\frac{\epsilon_0 q_1+\epsilon_1 q_0}{\epsilon_0 q_1-\epsilon_1 q_0}e^{2q_1 z_b}+1\right)e^{2q_1(a-z_b)}$$

and

$$\lambda_3 = \left(\frac{q_2+q_1}{q_2-q_1}e^{2q_1(a-z_b)}+1\right)\left(\frac{\epsilon_1 q_2+\epsilon_2 q_1}{\epsilon_1 q_2-\epsilon_2 q_1}e^{2q_1(a-z_b)}+1\right)e^{2q_1 z_b}$$

It is worth noting that Ritchie has considered the quantum corrections to the classically computed spatial distributions of energy loss suffered by fast electrons in electron microscopy [37]. He found out that at higher incident energies (10-100 keV) an electron behaves classically at all impact parameters for valence-electron excitations. Numerical examples were given for excitations of a hydrogenic atom, a surface plasmon on a sphere and a surface plasmon at a plane metallic boundary. The follow-up paper with Howie extended this theory to the excitation of electronic transitions in a STEM geometry.

2.3. Non-planar geometries

Recent developments and applications of STEM have stimulated renewed interest in the interaction of high-energy electron beams with small particles (see, for example, [38, 39, 40, 41, 42]). The problem of extending the dielectric model to deal with the case of small isolated spheres has attracted

considerable attention. The free-electron model, originally used by Fujimoto and Komaki [43] in a broad-beam geometry, has been applied to the case of a localised beam by Schmeits [44] and Kohl [45] for the case of dipole $l = 1$ or quadrupole $l = 2$ excitations. The contribution of higher l modes has been identified by Acheche et al [46, 47, 48]. Batson [49, 38, 39, 50] has used dielectric theory to determined the resonance frequencies of small spheres. Ferrell and Echenique [51] have established a dielectric model, valid for electron trajectories outside a spherical particle, to obtain the energy loss probability for an electron moving in a vacuum outside a dielectric sphere. Further generalization to include the possible presence of a surface coating was studied by Echenique et al [52]. Computations to high l values were compared with experimental data obtained from Ag catalyst particles.

As summarized above, the study of small particles with EELS has been mainly carried out on the basis of isolated metal particles. But, in most cases, the spheres are supported by a substrate (for example, most catalytic particles are supported by some kind of support). Using classical dielectric theory, Wang and Cowley [53] studied the effects of an underlying planar surface on the surface plasmon of small metal spheres. Fast-electron scattering by bispherical surface-plasmon modes were studied by Schmeits and Dambly [54]. More recently, surface and interface plasmon modes on small semiconductor spheres were studied by Ugarte, Colliex and Trebbia [55]. They discussed collective excitation modes in the bulk and at the interfaces and surfaces of small spherical silicon particles covered with a thin oxide coating.

Several authors have reported the possibility of drilling holes of nanometer-size diameter in beam sensitive materials [56, 57]: this has restimulated the interest in energy-loss studies in a cylindrical geometry [58, 59, 60, 61, 62]. For example, Chu et al [63] have obtained an expression for the work done on charged particles passing through a cylindrical hole in a conducting medium

by solving Poisson's equation. A relativistically correct expression for an electron travelling down the center of a cylindrical hole has also given by De Zutter and De Vleeschauwer [64]. Walsh extended this theory to study the energy loss of fast electrons travelling parallel to the axis of a cylindrical interface at arbitrary distance from the centre [60]. Her expression was evaluated for the case of an electron travelling through a hole in aluminium and through a hole in amorphous aluminium fluoride and a comparison made with the corresponding non-relativistic expression obtained from Poisson's equation [59].

Excitation of edge modes in the interaction of electron beams with dielectric wedges has also received some attention. The calculation of the dispersion relations for electrostatic modes of sharp-edged wedge, neglecting spatial dispersion, was due to Dobrzynsky and Maradudin [65][4]. Davis [66] has considered the electrostatic modes of a hyperbolic cylinder. A non-retarded calculation of the excitation probability for an electron passing parallel to a dielectric parabolic wedge surface was carried by Garcia-Molina et al [67]. They used this theory to explained some of the main features of available experimental data for MgO crystallites [68].

2.4. Anisotropic media

The interaction of an electron beam with anisotropic solids has a long history [69]. For isotropic materials the specimen orientation has no effect on the energy loss spectrum. For anisotropic materials, however, the situation is different because electronic transitions depend on the direction of the electric field in the crystal. Energy loss studies on graphite [70, 71, 72] and on the CuO–based high–temperature superconductors [73, 74] have shown that the fine structure of the loss spectrum depends on the specimen orientation.

[4] I have derived an equivalent expression before I saw Dobrazynsky and Maradudin's paper.

The dielectric treatment of electron energy loss in anisotropic crystals involves the dielectric tensor as defined in Equation 1.3. Starting from Poisson's equation, Hubbard [69] showed that the bulk energy loss probability is proportional to

$$-\mathrm{Im}\left(\frac{1}{\sum_{ij} k_i \epsilon^{(ij)} k_j}\right) \tag{2.5}$$

The loss spectra therefore depend on the direction of the momentum transfer **k**. Raether and co-workers [23, 70] in Germany have used Equation 2.5 and a Kramers-Kronig analysis to derive optical constants for graphite and MOS_2 etc. L.M. Brown's group in Cambridge recently established a method based on Equation 2.5 to determine the anisotropic dielectric function by electronic energy loss spectroscopy in STEM [75, 76]. All these studies deal only with non-retarded bulk effects.

2.5. Motivation and plan of this work

2.5.1. Motivation

Sections 2.2., 2.3 and 2.4 reviewed theoretical developments in the dielectric theory of electron energy loss. The basic theme of this thesis is to develop dielectric theory for multilayered slabs composed of either isotropic or anisotropic media. In dielectric theory, the electric fields can be calculated by solving Maxwell's equations with appropriate source terms subject to the usual boundary conditions at surfaces and interfaces. In principle, this procedure is straightforward but, in practice, it is difficult to find exact solutions to Maxwell's equations in complicated geometries because the algebra becomes very lengthy.

This difficulty is addressed in this thesis by using computer algebra (RE-

and MATHEMATICA) [77]. The one of aims in this work is to develop computer algebra programs in REDUCE and MATHEMATICA which automatically find the appropriate solutions of Maxwell's equations and use them to construct closed-form, but compact expressions for the energy loss spectrum. The algebra involved in such calculations is very cumbersome and time–consuming if done by hand. By contrast, the computer algebra programs are convenient, safe and sure. Moreover, the analytic solutions can be written directly into a FORTRAN program which is used to find numerical results. Computer algebra is routinely used in particle physics but has not been very widely in solid state physics. I believe that this situation will change dramatically in the immediate future.

The initial plan of this work was to rely on computer algebra to provide answers in a few special cases (double or triple layered slabs, for example) but it has emerged that a *combination* of computer algebra and hand calculation produces more general and more compact results.

2.5.2. Plan of this work

The work in this thesis is divided into two parts. Part II studies the multilayered slabs of isotropic media and Part III studies the multilayered slabs of anisotropic media.

In Part II, we first develop dielectric theory for an electron travelling normal to the interface of a multilayered slab. In Chapter 3, with the aid of computer algebra, we obtain closed-form expressions for the dispersion relation and the energy-loss probability. In Chapter 4, we develop an analytic expression for the energy loss probability when an electron travels parallel to the interfaces of the multilayered slab. Chapter 5 specialises to the plasmon losses of a fast electron passing through a single film. Detailed calculations on

damped surface plasmons and electron energy loss in thin slabs of insulators and semiconductors are presented as an independent work and also in order to introduce Chapter 6. In Chapter 6, the theory developed in Chapters 3 and 4 is applied to several multilayer systems, including Al/Mg, Al/Al_2O_3 and Al/SiO_2/Si.

Part III studies the electron energy loss spectrum in multilayered anisotropic media. In Chapter 7, we develop classical dielectric theory to study electron energy loss in layered anisotropic media, taking the beam to be both normal and parallel to the interface. This theory is applied to graphite in Chapter 8.

Finally, some conclusions are drawn in Chapter 9. The possible prospects for future applications, including studies of surface and interface polaritons will be discussed.

Part II

Multilayered Isotropic Media

Chapter 3.

Theory (i): Normal Incidence

This chapter develops the retarded dielectric theory of energy loss for electrons travelling normal to a slab composed of any given number of layers. An ansatz for the solution to Maxwell's equations is expressed in a recursive form. This allows analytic expressions to be constructed for the plasmon dispersion relation and energy loss probability, including the effects of retardation.

3.1. Introduction

This chapter develops the dielectric theory of energy loss in multilayers to include retardation effects for electrons travelling normal to the interfaces of a slab composed of any given number of thin layers. In the retarded version of dielectric theory, electric fields can be calculated by solving Maxwell's equations with appropriate source terms, and considering the boundary conditions at surfaces and interfaces. In principle, this procedure is straightforward but, in practice, it is difficult to find exact solutions to Maxwell's equations in complicated geometries. As mentioned in Chapter 1, this kind of calculation involves algebra of tedious length and can be done by using computer algebra [77]. It is best approached using a *combination* of computer algebra and hand calculation, so as to obtain general results, valid for any number of layers.

Section 3.2 defines the problem and casts the boundary conditions in the form of a transfer matrix recurrence relation for the Hertz vector. Section 3.3 derives the dispersion relation for surface and interface plasmons. Section 3.4 derives the solution for the Hertz vector. Section 3.5 obtains an analytic expression for the electron energy loss probability. And finally in Section 3.6, symmetry relations for the main theoretical results are presented.

3.2. Implementation of Maxwell's equations

3.2.1. Scattering geometry

Let us consider the case of a relativistic electron passing through a multilayered slab of given number of layers (Figure 3.1). We choose the coordinate system so that the stratification is perpendicular to the z-axis, and the plane of incidence is along the z-axis. The complete slab is assumed to lie in the region $0 \leq z \leq a$ and extend to infinity in both the x and y directions. The plane $z = 0$ forms the interface between an external region and an outer layer of the slab. The plane $z = z_j$ separates the j^{th} and $(j+1)^{\text{th}}$ medium. Hence, the thickness of the j^{th} film is $a_j = z_j - z_{j-1}$. The layers are labelled 1 to n and the external media labelled 0 and $n+1$.

3.2.2. Maxwell's equations and the Hertz vector

We assume that the electron travels along the z direction at constant speed, so that it produces the current density

$$\mathbf{j}_{\text{ext}}(\mathbf{r}, t) = Q\, v\, \hat{\mathbf{z}}\, \delta(z - vt)\delta(x)\delta(y) \tag{3.1}$$

where Q is the charge of the electron and v its speed. In $\mathbf{k}$-ω space, the current density becomes

$$\mathbf{J}_{\text{ext}}(\mathbf{k}, \omega) = Q\mathrm{e}^{\mathrm{i}\omega z/v}\hat{\mathbf{z}} \tag{3.2}$$

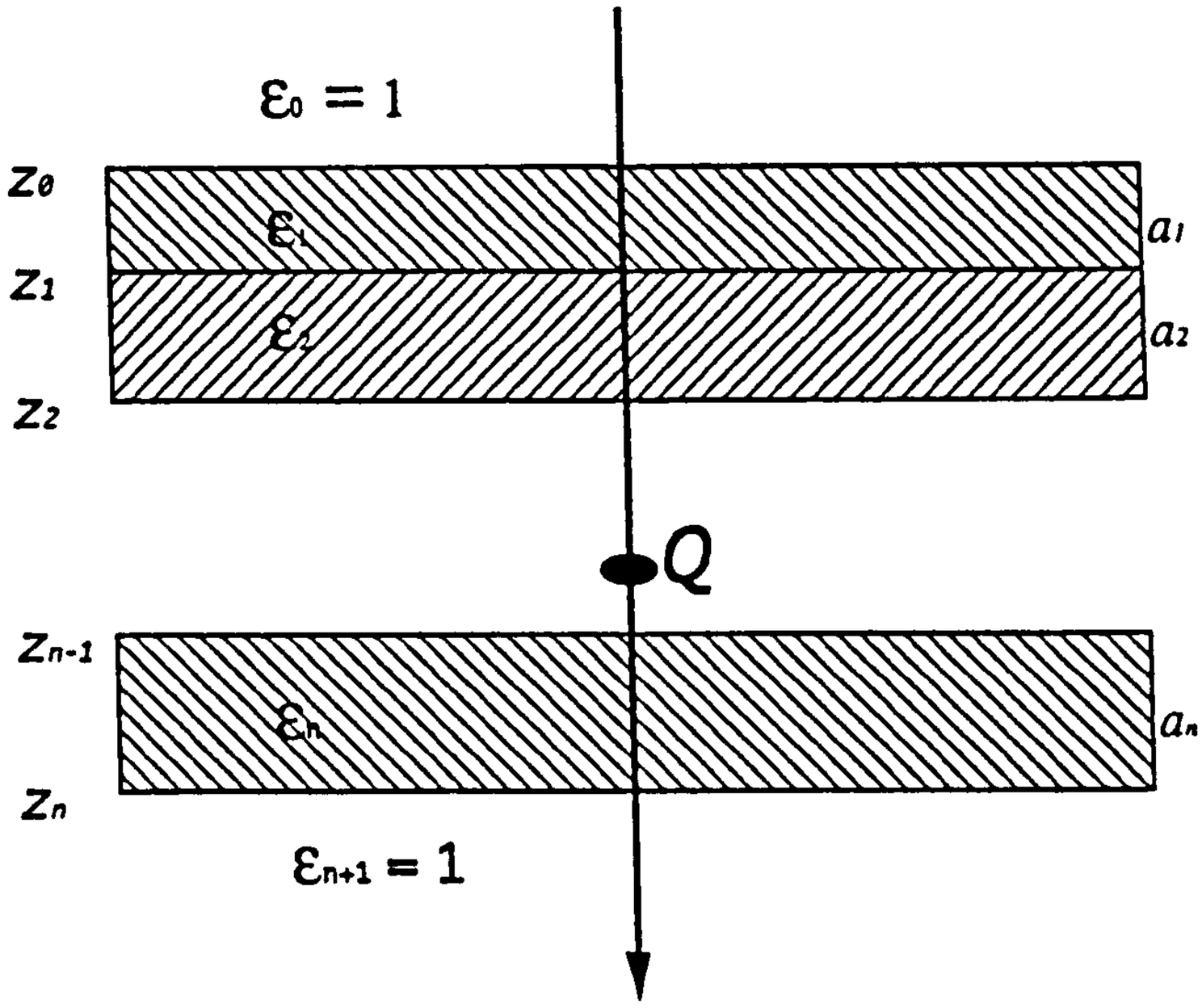

Figure 3.1 Cross section through the n-layered system considered in the text and the wave vector transfer of the beam electron during the collision.

Taking the Fourier transform of the wave equation for the Hertz vector (Equation 1.7) with respect to x and y one obtains

$$\frac{\mathrm{d}^2}{\mathrm{d}z^2}\Pi^x(k,\omega,z) - q^2\Pi^x(k,\omega,z) = 0 \tag{3.3}$$

$$\frac{\mathrm{d}^2}{\mathrm{d}z^2}\Pi^y(k,\omega,z) - q^2\Pi^y(k,\omega,z) = 0 \tag{3.4}$$

$$\frac{\mathrm{d}^2}{\mathrm{d}z^2}\Pi^z(k,\omega,z) - q^2\Pi^z(k,\omega,z) = \frac{Q}{\mathrm{i}\omega\varepsilon_0\epsilon}\mathrm{e}^{\mathrm{i}\omega z/v} \tag{3.5}$$

where $q = \sqrt{k^2 - \epsilon\,\omega^2/c^2}$, $k = \sqrt{k_x^2 + k_y^2}$ is the magnitude of the transverse wavevector[1] and ϵ is the complex local dielectric function $\epsilon(\omega)$. Equations 3.3–3.5 are general wave equations. For different media, one has only to set $\epsilon = \epsilon_1, \epsilon_2, \cdots$ etc.

[1]For the sake of definiteness, the square root taken in such a way that q has a positive real part.

Since the electron beam passes along the z-axis we can argue, by axial symmetry, that the transverse components of the Hertz vector vanish. The Hertz vector in the j^{th} region then takes the form

$$\begin{aligned} \Pi_j^x &= 0 \\ \Pi_j^y &= 0 \\ \Pi_j^z &= \Big(\sum_{\sigma=\pm} A_j^\sigma \exp(\sigma q_j z)\Big) - \frac{Q}{\mathrm{i}\omega\epsilon_0\epsilon_j p_j^2}\mathrm{e}^{\mathrm{i}\omega z/v} \end{aligned} \tag{3.6}$$

where

$$p_j^2 = k^2 - \epsilon_j\omega^2/c^2 + \omega^2/v^2 \tag{3.7}$$

Here, and throughout this thesis, the symbol σ is used to denote $\pm$, with $\sigma^2 = +$.

Because of axial symmetry, the undetermined coefficients A_j^σ depend only k and ω. In principle, these coefficients can be found from boundary conditions at the $n+1$ surfaces and interfaces. As one has to solve $2n+2$ linear equations, the algebra soon becomes very complicated and cannot reasonably done by hand when n is large. At a very early stage, I wrote a computer algebra program (in REDUCE) to solve these equations directly. But the implementation of REDUCE on a VAX 8800 can perform the calculation for only 8 linear equations, which means that, at the best, one can only solve the problem for three layer systems. It is better to incorporate the boundary conditions by progressing one interface at a time, using a transfer matrix recurrence relation. The similarity in form of the Hertz vector in each medium (Equation 3.6) then allows us to solve the equations recursively. In the following subsections I will carry out this procedure.

3.2.3. The transfer matrix recurrence relation

At the boundary $z = z_{j+1}$, the boundary conditions for electromagnetic fields yield following relationship:

$$h^{+}_{j+1,j+1}\begin{pmatrix} A^{+}_{j+1} \\ A^{-}_{j+1} \end{pmatrix} = \begin{pmatrix} h^{+}_{j+1,j}\mathrm{e}^{(q_j-q_{j+1})z_j} & h^{-}_{j+1,j}\mathrm{e}^{-(q_j+q_{j+1})z_j} \\ h^{-}_{j+1,j}\mathrm{e}^{(q_j+q_{j+1})z_j} & h^{+}_{j+1,j}\mathrm{e}^{-(q_j-q_{j+1})z_j} \end{pmatrix}\begin{pmatrix} A^{+}_{j} \\ A^{-}_{j} \end{pmatrix} + \frac{Q}{\epsilon_0 v}\begin{pmatrix} S^{+}_{j,j+1}\mathrm{e}^{-(q_j-\mathrm{i}\omega/v)z_j} \\ -S^{-}_{j,j+1}\mathrm{e}^{(q_j+\mathrm{i}\omega/v)z_j} \end{pmatrix} \tag{3.8}$$

where

$$\begin{aligned} S^{\sigma}_{ij} &= \frac{d_{ij}s^{\sigma}_{ij}}{\epsilon_i\, p_i^2 p_j^2} \\ s^{\sigma}_{ij} &= p^2_{ij} + \sigma \mathrm{i}\epsilon_i q_j v\omega/c^2 \\ d_{ij} &= \epsilon_i - \epsilon_j \\ p^2_{ij} &= k^2 - (\epsilon_i+\epsilon_j)\omega^2/c^2 + \omega^2/v^2 \\ h^{\sigma}_{ij} &= q_i\epsilon_j + \sigma q_j\epsilon_i \end{aligned} \tag{3.9}$$

This result has been explicitly checked with a computer algebra program.

In order to write the recurrence relation in the simplest possible form we scale the Hertz vector coefficients as follows

$$\alpha^{\sigma}_j = \frac{\varepsilon_0 v}{Q}A^{\sigma}_j \mathrm{e}^{(\sigma q_j - \mathrm{i}\omega/v)z_{j-1}} \qquad \text{for} \quad j \geq 1 \qquad \text{and} \quad \alpha^{\sigma}_0 = \frac{\varepsilon_0 v}{Q}A^{\sigma}_0 \tag{3.10}$$

and define the *coefficient vector* for the j^{th} layer as

$$\boldsymbol{\alpha}_j = \begin{pmatrix} \alpha^{+}_j \\ \alpha^{-}_j \end{pmatrix}. \tag{3.11}$$

The *source vector* for the j^{th} layer is redefined as

$$\mathbf{S}_j = \begin{pmatrix} S^+_{j,j+1} \\ -S^-_{j,j+1} \end{pmatrix}. \tag{3.12}$$

Finally, we introduce the variables

$$f_j = \mathrm{e}^{q_j a_j} \qquad \text{with} \quad f_0 = f_{n+1} = 1$$

and

$$b^\sigma_j = \mathrm{e}^{\sigma \mathrm{i}\omega a_j / v} \qquad \text{with} \quad b^\sigma_0 = b^\sigma_{n+1} = 1$$

and define the *transfer matrix* between the j^{th} and $(j+1)^{\text{th}}$ layers as

$$\tau^{(j+1,j)} = \begin{pmatrix} h^+_{j+1,j} f_j^2 & h^-_{j+1,j} \\ h^-_{j+1,j} f_j^2 & h^+_{j+1,j} \end{pmatrix}. \tag{3.13}$$

The recurrence relation for the Hertz vector coefficients can then be written compactly as

Box 1. Recurrence relation for normal incidence

$$h^+_{j+1,j+1}\boldsymbol{\alpha}_{j+1} = \frac{1}{f_j b^+_j}\tau^{(j+1,j)}\boldsymbol{\alpha}_j + \mathbf{S}_j. \tag{3.14}$$

Starting Equation 3.14 and applying the boundary conditions at infinity one obtains the coefficient vector in the first external region

$$\alpha^-_0 = 0; \quad \alpha^+_0 = \frac{-1}{\tau^{(n+1,0)}_{11}} \sum_{k=0}^{n} \psi^+_{1k} \left(\tau^{(n+1,k+1)}_{11} S^+_{k,k+1} - \tau^{(n+1,k+1)}_{12} S^-_{k,k+1} \right) \tag{3.15}$$

where

$$\psi_{ij}^{\sigma} = \prod_{k=i}^{j} h_{kk}^{+} f_k b_k^{\sigma} \qquad \text{with initial value} \quad \psi_{i,i-1}^{\sigma} = 1. \tag{3.16}$$

Equation 3.14 can then be used recursively to find the coefficient vectors in successive layers and these allow us to find the energy lost by the beam. In principle, this procedure can be carried through algebraically. In practice, the coefficients become progressively more complicated as j increases and the resulting expression for the energy loss function is very complicated indeed, even for double or triple slabs. It is always possible to proceed numerically [25, 26, 77], but this approach provides no insight into the analytic form of the solution or its relationship to the well-known results established for a single slab [21, 22].

My main aim here is to provide closed formulae for the dispersion relation and the energy loss probability, expressed in the simplest possible terms and valid for any number of slabs. A preliminary step is to simplify the solution for a double slab by using computer algebra (mainly MATHEMATICA, supplemented by packages of our own which facilitate the simplification of large multinomials). As expected, considerable simplifications were revealed; building on this experience general solutions were constructed, which are described below.

3.3. The dispersion relation and dispersion bracket

Equation 3.14 is a convenient starting point for the analysis. Setting the source terms equal to zero for the moment and requiring α_{n+1}^{+} to vanish while α_0^{+} is non-zero, it gives the dispersion relation:

$$\tau_{11}^{(n+1,0)} = 0 \tag{3.17}$$

where $\tau^{(ji)}$ is the product of transfer matrices, defined by

$$\tau^{(ji)} = \prod_{k=i}^{j-1} \tau^{(k+1,k)} \tag{3.18}$$

with the product ordered from right to left.

We[2] now introduce a new algebraic operation which can be applied to any product of terms bearing ± superscripts interspersed by f^2 factors, such as $h_{32}^- f_2^2 h_{21}^+ f_1^2 h_{10}^-$. The product is assumed to be ordered so that the subscripts increase monotonically from one end to the other. We then define a **contraction** of the ordered product by choosing two terms with ± superscripts, reversing the signs of these superscripts and removing all the f^2 factors between them. The contraction is represented by a square overbrace so, for example,

$$h_{32}^- f_2^2 \overbrace{h_{21}^+ f_1^2 h_{10}^-} = h_{32}^- f_2^2 h_{21}^- h_{10}^+$$

Boundary conditions at successive interfaces lead us to consider the *sum* of all *nonoverlapping* contractions of the ordered product (including the term with no contractions). Such a sum will be referred to as a **dispersion bracket.** Throughout this work, dispersion brackets will be denoted by *square* brackets. This notation finds an immediate application in interpreting the dispersion relation for an n-layer slab because it is quite easy to show that Equation 3.17 takes the form(see Appendix A)

Box 2. Dispersion relation for TM mode

$$[C_{n0}] = 0 \tag{3.19}$$

where we define

[2]Thanks are given to Dr John Bolton for suggesting the use of dispersion bracket described in this paragraph.

$$C_{ji} = \prod_{k=i}^{j} h^{+}_{k+1,k} f^2_k = h^{+}_{j+1,j} f^2_j h^{+}_{jj-1} f^2_{j-1} \cdots h^{+}_{i+1i} f^2_i \tag{3.20}$$

and, for future use, specify the initial values

$$C_{i-1,i} = 1 \qquad \text{and} \quad C_{i-2,i} = 0$$

To illustrate this notation, the dispersion relation for a single slab is

$$\begin{aligned}
[C_{10}] &= \left[h^{+}_{21} f^2_1 h^{+}_{10}\right] \\
&= h^{+}_{21} f^2_1 h^{+}_{10} + \overline{\left\lceil h^{+}_{21} f^2_1 h^{+}_{10} \right\rceil} \\
&= h^{+}_{21} f^2_1 h^{+}_{10} + h^{-}_{21} h^{-}_{10} \\
&= 0
\end{aligned} \tag{3.21}$$

which agrees with the conclusions of reference [78] for a single slab.

One can further check Equation 3.19 against known results for low n. Evaluating Equation 3.19 for $n = 2$ gives the dispersion relation for double slabs:

$$\begin{aligned}
[C_{20}] &= \left[h^{+}_{32} f^2_2 h^{+}_{21} f^2_1 h^{+}_{10}\right] \\
&= h^{+}_{32} f^2_2 h^{+}_{21} f^2_1 h^{+}_{10} + \overline{\left\lceil h^{+}_{32} f^2_2 h^{+}_{21} \right\rceil} f^2_1 h^{+}_{10} + \overline{\left\lceil h^{+}_{32} f^2_2 h^{+}_{21} f^2_1 h^{+}_{10} \right\rceil} + h^{+}_{32} f^2_2 \overline{\left\lceil h^{+}_{21} f^2_1 h^{+}_{10} \right\rceil} \\
&= h^{+}_{32} f^2_2 h^{+}_{21} f^2_1 h^{+}_{10} + h^{-}_{32} h^{-}_{21} f^2_1 h^{+}_{10} + h^{-}_{32} h^{+}_{21} h^{-}_{10} + h^{+}_{32} f^2_2 h^{-}_{21} h^{-}_{10} \\
&= 0
\end{aligned} \tag{3.22}$$

Taking the electrostatic limit, one recovers the results of reference [25] for double slabs[3]. Setting $n = 3$ in Equation 3.19, the dispersion relation for

[3]It is necessary to correct an obvious misprint in Richter and Geiger's expression for a double slab.

triple slabs can also be obtained.

However, the dispersion bracket notation has its main application in manipulating expressions for the Hertz vector and the energy loss spectrum. Section 3.4 and 3.5 will discuss these applications.

3.4. Solution for the Hertz vector

As mentioned in Section 3.2, the algebra for finding the solution of Hertz vector becomes very complicated as n increases and cannot reasonably be done by hand. This problem has been tackled by writing computer algebra programs in REDUCE and MATHEMATICA as outlined in Figure 3.2. Firstly, with the transfer matrix method suggested in above section, REDUCE programs produce the Hertz coefficients for $n = 1, 2, \cdots, 11$. These coefficients were checked against independent solutions obtained from direct REDUCE programs that do not rely on the transfer matrix recurrence relation. MATHEMATICA can then be used to simplify the REDUCE results for $n = 1, 2$ and 3 and from these simplified solutions, general formulae were guessed. These formulae were checked against the original REDUCE results for $n = 1 \cdots 7$. The algebraic manipulations performed in this stage are very lengthy. A NEXT computer needs 24 hours CPU time to finish for $n = 7$. Therefore we only carried out these calculations for $n \leq 7$. Finally, the guessed analytical expressions were proved using mathematical induction and the transfer matrix recurrence relation (Equation 3.14) .

In more detail, the computer algebra programs *suggest* (but do not prove) the following general formula for the coefficient vector in the j^{th} region of an n layer slab:

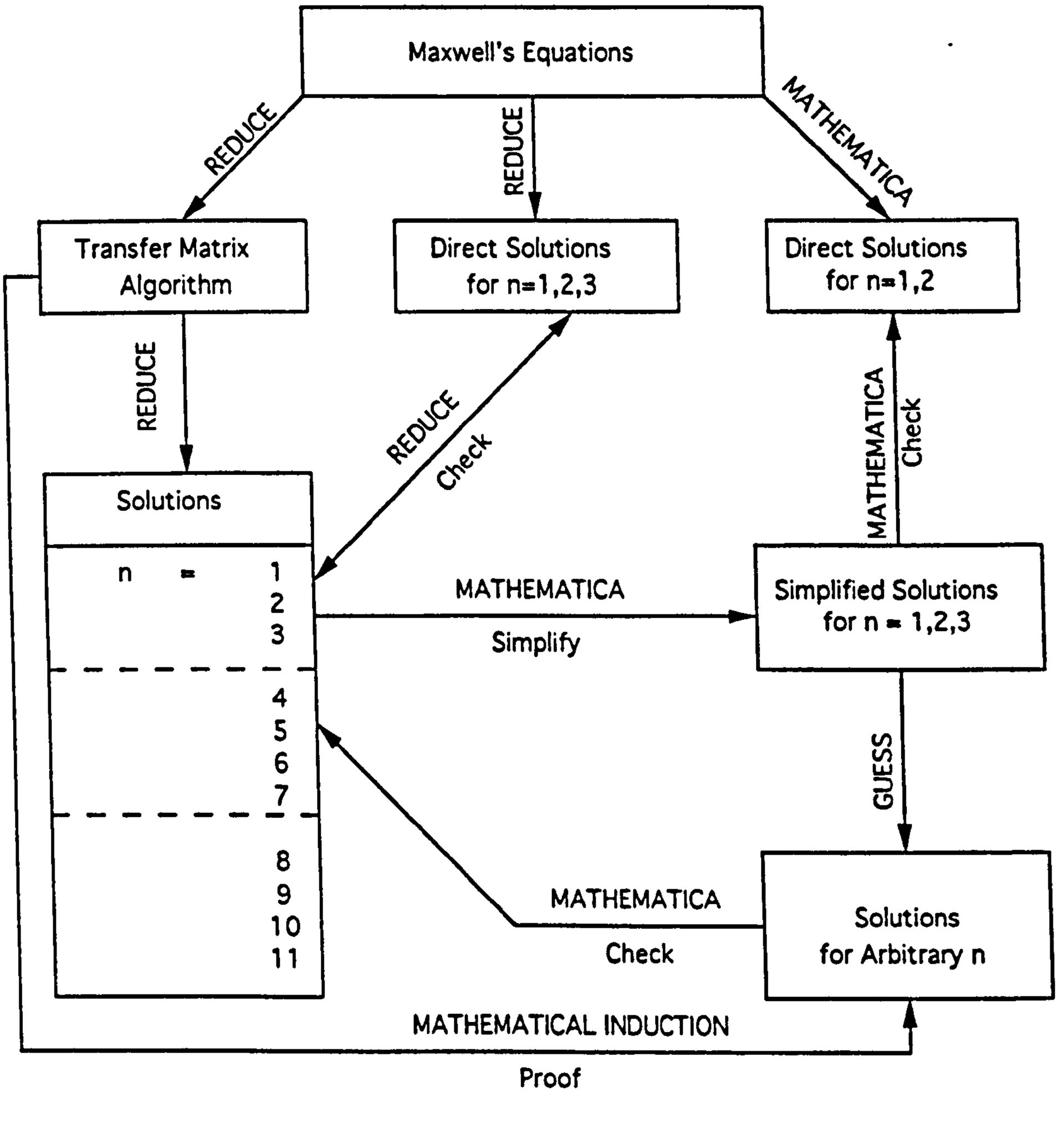

Figure 3.2 Flow chart for finding solutions of Maxwell's equations.

Box 3. Solution for Hertz vector

$$\boldsymbol{\alpha}_j = \frac{1}{[C_{n0}]} \left\{ \mathbf{M}_{nj} \sum_{k=0}^{j-1} \psi^-_{k+1,j-1} \left[X^-_{k0} \right] - \mathbf{N}_{j-1,0} f_j b^+_j \sum_{k=j}^{n} \psi^+_{j+1,k} \left[Y^+_{kn} \right] \right\} \quad (3.23)$$

where

$$\mathbf{M}_{ji} = \begin{pmatrix} -[D_{ji}] \\ [C_{ji}] \end{pmatrix}$$

$$\mathbf{N}_{ji} = \begin{pmatrix} [C_{ji}] \\ [E_{ji}] \end{pmatrix}$$

$$X^\sigma_{ji} = S^\sigma_{j+1,j} f_j^2 C_{j-1,i}$$

$$Y^\sigma_{ij} = S^\sigma_{i,i+1} C_{j,i+1}$$

$$D_{ji} = C_{j,i+1} h^-_{i+1,i}$$

and

$$E_{ji} = h^-_{j+1,j} f_j^2 C_{j-1,i}$$

These definitions imply that

$$X^\sigma_{ji} = S^\sigma_{j+1,j} f_j^2 h^+_{j,j-1} f^2_{j-1} \cdots h^+_{i+1,i} f_i^2$$

$$Y^\sigma_{ij} = S^\sigma_{i,i+1} f^2_{i+1} h^+_{i+1,i+1} \cdots f^2_{j-1} h^+_{j,j-1} f_j^2 h^+_{j+1,j}$$

$$D_{ji} = h^+_{j+1,j} f_j^2 \cdots h^-_{i+1,i}$$

and

$$E_{ji} = h^{-}_{j+1,j} f_j^2 \cdots h^{+}_{i+1,i} f_i^2$$

where the initial values have to be specified

$$X^{\sigma}_{ii} = S^{\sigma}_{i+1,i} f_i^2$$

$$Y^{\sigma}_{ii} = S^{\sigma}_{i,i+1}$$

and

$$X^{\sigma}_{i-1,i} = Y^{\sigma}_{i,i-1} = D_{i-1,i} = E_{i-1,i} = 0$$

The mathematical proof of Equation 3.23 is given in Appendix B. The proof is based on mathematical induction, so it is shown that

1. The previous expressions for α_0^+ and α_0^- (Equations 3.15) are recovered on substituting $j = 0$ in Equation 3.23.

2. The transfer matrix recurrence relation (Equation 3.14) guarantees that, if Equation 3.23 is valid for $j = k$, then it is also valid for $j = k+1$.

The proof is lengthy, but it rests on some simple properties of dispersion brackets and on the identity

$$h^{+}_{jj} S^{\sigma}_{ji} + h^{+}_{ji} S^{\sigma}_{ij} + h^{-}_{ji} S^{-\sigma}_{ij} = 0. \tag{3.24}$$

Of course, a key element in obtaining the proof of is the initial guess that Equation 3.23 is correct. It is here that computer algebra investigations, for n=1,2 and 3, followed by computer algebra checks for n=4,5,6 and 7 were invaluable. A further advantage of using computer algebra is that we can be fairly confident that Equation 3.23 has been expressed in the simplest possible form. This is important because it is all too easy to produce results that are correct but are of quite unmanageable length.

3.5. Solution for the energy loss spectrum

When an electron passes through a medium, the electric field of the electron polarizes the medium which, in turn, acts on the the electron, causing it to slow down. As we addressed previously, with dielectric theory, the scattering probability can be determined by calculating the work done on the electron as it moves against the induced electric field. From Equations 1.4 and 3.2, this work is given by

$$W = \frac{Q}{(2\pi)^2}\int_{-\infty}^{\infty}\mathrm{d}\omega\int_{0}^{\infty}\mathrm{d}k k\int_{-\infty}^{\infty}E_z(z,k,\omega)\mathrm{e}^{-\mathrm{i}\omega z/v}\mathrm{d}z$$

where E_z represents the electric field in the medium. By calculating the work done on the incoming particle by the electric field induced in the slab, and interpreting the result in terms of a transfer of quanta of energy $\hbar\omega$, one can find the semiclassical energy loss function $\mathrm{d}^2P/\mathrm{d}\omega\mathrm{d}k$. This is normalised in such a way that the work done by a particle traversing the multilayered slab is given by

$$W = 2\pi\int_0^\infty \mathrm{d}(\hbar\omega)\,\hbar\omega\int_0^\infty \mathrm{d}k\,k\frac{\mathrm{d}^2P}{\mathrm{d}(\hbar\omega)\mathrm{d}k}.$$

Using Equation 3.6, one can expressed the work done in terms of the Hertz vector coefficients

$$W = -\frac{Q}{4\pi^2}\sum_{i=0}^{n+1}\int_{-\infty}^{\infty}\mathrm{d}\omega\int_0^\infty \mathrm{d}k\,k\int_{z_{i-1}}^{z_i}\mathrm{d}z \tag{3.25}$$
$$\left\{\frac{Q}{\mathrm{i}\epsilon_0\epsilon_i\omega p_i^2}\left(\frac{\omega^2}{v^2}-\epsilon_i\frac{\omega^2}{c^2}\right)+k^2\left(A_i^+\mathrm{e}^{(q_i-\mathrm{i}\omega/v)z}+A_i^-\mathrm{e}^{-(q_i+\mathrm{i}\omega/v)z}\right)\right\}$$

For the integration over ω of a function $g(\omega)$ which is the Fourier transform of a real function $g(t)$, we have

$$g(-\omega) = g^*(\omega)$$

So

$$\begin{aligned}\int_{-\infty}^{\infty} \mathrm{d}\omega g(\omega) &= \int_{-\infty}^{\infty} \mathrm{d}\omega g(\omega) + \int_{-\infty}^{0} \mathrm{d}\omega g(\omega) \\ &= \int_{0}^{\infty} \mathrm{d}\omega \left(g(\omega) + g(-\omega)\right) \\ &= \int_{0}^{\infty} \mathrm{d}\omega \left(g(\omega) + g^{*}(\omega)\right) \\ &= 2\int_{0}^{\infty} \mathrm{d}\omega \mathrm{Re} g(\omega)\end{aligned}$$

Writing $g(\omega) = h(\omega)/\mathtt{i}$, this can also be expressed as

$$\int_{-\infty}^{\infty} \mathrm{d}\omega \frac{h(\omega)}{\mathtt{i}} = 2\int_{0}^{\infty} \mathrm{d}\omega \mathrm{Im} h(\omega)$$

So the energy loss function can be expressed as

Box 4. Energy loss function for normal incidence

$$\frac{\mathrm{d}^2 P}{\mathrm{d}(\hbar\omega)\mathrm{d}k} = \frac{Q^2}{4\pi^3 \epsilon_0 \hbar^2 v^2} \mathrm{Im}\left(\chi_{\mathrm{bulk}} + \chi_{\mathrm{bdy}}\right) \tag{3.26}$$

where χ_{bulk} represents the bulk contribution and χ_{bdy} represents the boundary contributions (due to surfaces and interfaces). The calculation shows that the bulk contribution is a sum over layers, with the i^{th} layer contributing an amount proportional to its thickness, a_i, and to the energy loss per unit length in an infinite bulk medium with dielectric function ϵ_i [79]:

Box 5. Bulk contribution to energy loss function

$$\chi_{\mathrm{bulk}} = \sum_{i=1}^{n} \frac{a_i}{p_i^2}\left(\frac{v^2}{c^2} - \frac{1}{\epsilon_i}\right) \tag{3.27}$$

The boundary contributions are more complicated. In terms of the rescaled

Hertz vector coefficients, they are given by

$$\chi_{\text{bdy}} = -\sum_{i=0}^{n+1} \frac{k^2}{p_i^2} \sum_{\sigma=\pm} (1 - \sigma i q_i v/\omega)\, \alpha_i^\sigma \beta_i^\sigma \tag{3.28}$$

where

$$\beta_i^\sigma = \begin{cases} 1 & \text{if} \quad i = 0 \\ f_1^\sigma b_i^- - 1 & \text{if} \quad 1 \le i \le n \\ -1 & \text{if} \quad i = n+1. \end{cases} \tag{3.29}$$

These expressions, combined with Equation 3.23, yield an very lengthy expression for the energy loss spectrum. Since our aim is to produce a compact expression for the energy-loss probability, it is not satisfactory to leave the answer in this form. The main algebraic task in this calculation is therefore to reduce Equations 3.23, 3.28, 3.29 to a manageable form. Substituting the Hertz coefficients obtained in Section 3.3 and making full use of the properties of dispersion brackets , we eventually obtain

$$\chi_{\text{bdy}} = \frac{k^2}{[C_{n0}]} \sum_{i=0}^{n} \sum_{j=i}^{n} \frac{(\epsilon_i - \epsilon_{i+1})(\epsilon_j - \epsilon_{j+1}) T_{ij}^{(n)}}{\epsilon_{i+1}\, \epsilon_j\, p_i^2\, p_{i+1}^2\, p_j^2\, p_{j+1}^2} \tag{3.30}$$

where

$$T_{ij}^{(n)} = \sum_{\sigma=\pm} z_{ij} \psi_{i+1,j}^\sigma \left[x_{i0}^\sigma\right] \left[y_{jn}^\sigma\right], \tag{3.31}$$

$$x_{ji}^\sigma = s_{j+1,j}^\sigma f_j^2 C_{j-1,i} = s_{j+1,j}^\sigma f_j^2 \ldots h_{i+1,i}^+ f_i^2 \tag{3.32}$$

$$y_{ij}^\sigma = s_{i,i+1}^\sigma C_{j,i+1} = s_{i,i+1}^\sigma f_{i+1}^2 \ldots h_{j,j+1}^+. \tag{3.33}$$

and

$$z_{ij} = 1 - \tfrac{1}{2}\delta_{ij} = \begin{cases} \frac{1}{2} & \text{if} \quad i = j \\ 1 & \text{otherwise.} \end{cases} \tag{3.34}$$

The final result can also be expressed as

Box 6. Boundary contribution to energy loss function

$$\chi_{\text{bdy}} = -\frac{k^2}{[C_{n0}]} \sum_{i=0}^{n} \sum_{j=i}^{n} \sum_{\sigma=\pm} z_{ij} \psi^{\sigma}_{i+1,j} \left[X^{\sigma}_{i0}\right] \left[Y^{\sigma}_{jn}\right] \tag{3.35}$$

Appendix B gives a full proof of Equations 3.30 and 3.35.

Equations 3.27 and 3.30 or 3.35 are the main theoretical results of this chapter. Together with the subsidiary definitions of Equations 3.26, 3.34 and 3.31—3.33, they provide remarkably simple expressions for the semiclassical energy loss function valid for normal incidence on an arbitrary multilayered slab.

3.5.1. Particular cases of the energy-loss spectrum

One way of checking our expressions for the energy loss probability is to compare it with known results. Evaluating χ_{bdy} for $n = 1$ gives

$$\chi_{\text{bulk}} = \frac{a_1}{p_1^2} \left(\frac{v^2}{c^2} - \frac{1}{\epsilon_1} \right) \tag{3.36}$$

and

$$\chi_{\text{bdy}} = \frac{(\epsilon_0 - \epsilon_1)^2 k^2}{\epsilon_1 p_0^4 p_1^4 [C_{10}]} \sum_{\sigma=\pm} s^{\sigma}_{10} \left([y^{\sigma}_{01}] + \psi^{\sigma}_{11} s^{\sigma}_{10} \right) \tag{3.37}$$

Both these equations agree with Kröger's expression for a single slab [21], although they have the advantage of expressing this result in an especially simple way. This type of checking cannot be pressed further because there are no published formulae for $n > 1$, however we have checked that Equation 3.35 is consistent with the solution for $n = 2$ which was obtained using the direct approach mentioned just below Equation 3.6 in Section 3.2.

3.6. Symmetries and symmetrical slabs

So far, closed-form solutions for the dispersion relation, the Hertz vector and the energy loss function have been constructed. This section will investigate their symmetry properties and examine simplifications that arise for symmetrical slabs. Four symmetry operators can be defined:

1. $\hat{\mathcal{P}}_k$ reverses the sign of q_k but leaves q_j unchanged for $j \neq k$.

2. $\hat{\mathcal{S}}$ reverses the labelling of the regions so that $k \rightarrow n + 1 - k$.

3. $\hat{\mathcal{T}}_\omega$ reverses the sign of ω.

4. $\hat{\mathcal{T}}_v$ reverses the sign of v.

We also consider the operator $\hat{\mathcal{J}}_{k,k+1}$ that causes two neighbouring regions k and $k+1$ to coalesce. (This is accomplished by setting $\epsilon_{k+1} \rightarrow \epsilon_k$, $q_{k+1} \rightarrow q_k$ etc., $2a_k \rightarrow a_k$ and then renumbering regions $j \rightarrow j - 1$ for $j \geq k$.)

3.6.1. Symmetries of the dispersion relation

It is easy to see that

$$\hat{\mathcal{S}}\,[C_{n0}] = [C_{n0}]$$

$$\hat{\mathcal{T}}_\omega\,[C_{n0}] = [C_{n0}]^*$$

and

$$\hat{\mathcal{T}}_v\,[C_{n0}] = [C_{n0}]$$

In Appendix B, we will prove that

$$\hat{\mathcal{P}}_k\,[C_{n0}] = -\,[C_{n0}]\,/f_k^2 \qquad \text{for} \quad k = 1 \ldots n \tag{3.38}$$

It follows that the dispersion relation (Equation 3.19) is invariant under all four symmetry operations, as it must be.

Moreover,

$$\hat{\mathcal{J}}_{k,k+1}\,[C_{n0}] = h_{kk}^{+}\,[C_{n-1,0}]$$

so the dispersion relation correctly becomes that for an $n-1$ layered slab when two neighbouring regions coalesce.

The symmetry properties discussed above lead to simplifications when the slab is symmetrical about its middle layer. We consider a slab containing $n = 2m+1$ layers, whose geometric and dielectric properties are symmetrical about the $(m+1)^{\text{th}}$ layer: $\epsilon_k = \epsilon_{2m+2-k}$ and $a_k = a_{2m+2-k}$. We have shown that the dispersion relation for such a slab can always be factorised as follows

$$[C_{2m+1,0}] = L_{m0}^{+} L_{m0}^{-} = 0$$

where

$$L_{m0}^{\sigma} = [C_{m0}]\,f_{m+1} + \sigma\,[E_{m0}]$$

This result agrees with the special cases $m = 0$, $m = 1$, $m = 2$ and $m = 3$ discussed in references [78] and [80]. In general, the factorisation of the

dispersion relation is a considerable simplification. Its physical significance can be understood by noting that the solutions of $L^{\sigma}_{m0} = 0$ obey

$$\frac{A^{+}_{n+1-j} e^{q_j a/2}}{A^{-}_{j} e^{-q_j a/2}} = -\sigma$$

This shows that the solutions corresponding to $L^{+}_{m0} = 0$ are antisymmetric in their Hertz vectors (and electric fields) and therefore symmetric in their charge distributions: these modes will be described as being *symmetric*. By a similar argument, the solutions corresponding to $L^{-}_{m0} = 0$ are antisymmetric in their charge distributions.

3.6.2. Symmetries of the Hertz vector

With the basic operations shown in Appendix B, the Hertz vector coefficients, calculated from Equation 3.23, obey the identities

$$\hat{\mathcal{P}}_k \alpha^{\sigma}_j = \begin{cases} \alpha^{-\sigma}_j & \text{if} \quad k = j \\ \\ \alpha^{\sigma}_j & \text{if} \quad k \neq j \end{cases}$$

$$\hat{\mathcal{S}}\hat{\mathcal{T}}_v(\alpha^{\sigma}_j) = -e^{-(\sigma q_{n+1-j} + i\omega/v) a_{n+1-j}} \alpha^{-\sigma}_{n+1-j}.$$

where a is the total thickness of the slab. These identities mean that the Hertz vector can be reconstructed from a partial knowledge of its coefficients. For example[4], if the A^{+}_{i} are known algebraic functions from $i = 0$ to $i = \lceil \frac{n}{2} \rceil$, the remaining coefficients and hence the full Hertz vector can be found by applying the operators $\hat{\mathcal{P}}_i$ and $\hat{\mathcal{S}}\hat{\mathcal{T}}_v$.

Solution 3.23 can also be checked by considering two neighbouring regions coalesce. Using n and $n-1$ to denote the number of layers in the slab, Equation 3.23 gives

[4] In this thesis, the notations $\lceil x \rceil$ and $\lfloor x \rfloor$ are used for the ceiling and floor of x – the integers obtained by rounding any fractions in x up and down, respectively.

$$\hat{\mathcal{J}}_{k,k+1}A_j^\sigma(n) = A_j^\sigma(n-1) \qquad \text{for} \quad 1 \le j \le k-1$$

$$\hat{\mathcal{J}}_{k,k+1}A_j^\sigma(n) = A_{j-1}^\sigma(n-1) \qquad \text{for} \quad k+1 \le j \le n.$$

as expected.

3.6.3. Symmetries of the energy loss function

Finally, it can be shown that Equation 3.35 provides an energy loss function χ_{bdy} that is invariant under $\mathcal{P}_k$, $\mathcal{T}_v$ and $\mathcal{S}$ and which is complex conjugated under $\mathcal{T}_\omega$:

$$\mathcal{P}_k(\chi_{\text{bdy}}) = \chi_{\text{bdy}}$$

$$\mathcal{T}_v(\chi_{\text{bdy}}) = \chi_{\text{bdy}}$$

$$\mathcal{S}(\chi_{\text{bdy}}) = \chi_{\text{bdy}}$$

and

$$\mathcal{T}_\omega(\chi_{\text{bdy}}) = \chi_{\text{bdy}}^*$$

Appendix B.3 will give detailed proofs of these results.

The energy loss caused by a (possibly asymmetric) sample is predicted to be independent of the sense of travel of the beam. Moreover, Equation 3.35 produces a result appropriate to $n-1$ layers when two neighbouring regions coalesce. One further notes that

$$\hat{S}T_{ij}^{(n)} = T_{n-j,n-i}^{(n)}.$$

This identity can be used to simplify calculations based on Equation 3.30: instead of evaluating $\frac{1}{2}(n+1)(n+2)$ different $T_{ij}^{(n)}$ terms, one can concentrate

on just $(\lfloor \frac{n}{2} \rfloor + 1)(\lceil \frac{n}{2} \rceil + 1)$ terms, obtaining the remainder by means of the transformation $k \rightarrow n + 1 - k$.

In the case of a symmetrical slab the formula for the energy loss spectrum due to boundaries can be simplified to

Box 7. Boundary contribution for a symmetrical slab

$$\chi_{\text{bdy}} = \frac{2k^2}{L^+_{m0} L^-_{m0}} \sum_{i=0}^{m} \sum_{j=i}^{n-i} \frac{(\epsilon_i - \epsilon_{i+1})(\epsilon_j - \epsilon_{j+1}) t^{(n)}_{ij}}{\epsilon_{i+1}\, \epsilon_j\, p_i^2\, p_{i+1}^2\, p_j^2\, p_{j+1}^2}$$

where

$$t^{(n)}_{ij} = \sum_{\sigma=\pm} z_{ij} z_{i,n-j} \psi^{\sigma}_{i+1,j} \left[x^{\sigma}_{i0} \right] \left[y^{\sigma}_{jn} \right],$$

This result involves only $(m+2)/(2m+3)$ as many terms as Equation 3.30 for a general $2m+1$ layer slab.

3.7. Summary

Equations 3.19 and 3.35 derived in this chapter provide a straightforward way of calculating the dispersion relation and energy loss spectrum for normal incidence on any multilayered slab. These equations have been expressed in as simple a form as possible, and checked them against known results. Consideration has been given to the action of symmetry operators on our results; in the case of symmetrical slabs this leads to further simplifications. In Chapter 4 these methods will be extended to study parallel incidence. In Chapter 7 they will be extended to multilayered anisotropic slabs.

Chapter 4.

Theory (ii): Parallel Incidence

This chapter develops the dielectric theory of energy loss, including retardation effects, for electrons travelling parallel to the interfaces of a stratified slab. A 4×4 transfer matrix recurrence relation is introduced to implement the boundary conditions at surfaces and interfaces. This recurrence relation is solved exactly to provide closed formulae for the dispersion relation, the Hertz vector and the energy loss probability, valid for any position of the beam and any number of layers.

4.1. Introduction

Chapter 3 developed the dielectric theory of electron energy loss for normal incidence on a multilayered slab, obtaining compact formulae for the Hertz vector, the dispersion relation and the energy loss spectrum. In this chapter, we carry out similar calculations for parallel incidence. In some respects, this is a more complicated task than for normal incidence because one now has to deal with a 4×4 transfer matrix and allow for the beam to be in any layer of the slab or in either of the external regions. In compensation, however, the source terms do not vary from layer to layer and the work done by the beam can be calculated without summing over layers. So far as possible, I will adopt the notation of Chapter 3. In particular, the variables σ, f_j, h^{σ}_{ji}, q_j, C_{ji}, D_{ji}, E_{ji}, $\mathbf{M}_{ji}$ and $\mathbf{N}_{ji}$ will be reused and extensive use made of the

dispersion bracket notation.

This chapter is organised as follows. In Section 4.2, we state the problem and develop a transfer matrix recurrence relation for the Hertz vector which incorporates the relevant boundary conditions. In Section 4.3, this recurrence relation is solved and a closed formulae for the dispersion relation is obtained. Sections 4.4 to 4.6 derive expressions for the Hertz vector and the semiclassical energy loss spectrum. The symmetries of these results are examined and special cases compared with previously established results.

4.2. Implemention of Maxwell's equations

4.2.1. Scattering geometry

We consider a stratified slab, similar to that described for normal incidence. The slab comprises n layers, labelled 1...n. The j^{th} layer lies between z_{j-1} and z_j, has thickness $a_j = z_j - z_{j-1}$ and local dielectric function $\epsilon_j(\omega)$. The external regions, which need not be vacua, are labelled 0 and $n+1$ and extend from $z_{-1} = -\infty$ to $z_0 = 0$ and from $z_n = a$ to $z_{n+1} = +\infty$. The incident beam is assumed to travel at constant speed v parallel to the x-axis and to occupy region m, where $0 \leq m \leq n+1$. We investigate the effects of a particle in the beam of charge Q, with coordinates $x = vt, y = 0$ and $z = z_b$. Primes are used to distinguish between the subregions on either side of the beam: m' lies between z_{m-1} and z_b, while m'' lies between z_b and z_m. Figure 4.1 shows this scattering geometry.

4.2.2. The Hertz vector

We still start from Maxwell's equations expressed in terms of the Hertz vector [7]. From symmetry, one may assume that Π has components only in the $\hat{x}$ and $\hat{z}$ directions, $\mathbf{\Pi} = (\Pi^x(z), 0, \Pi^z(z))$ and has wave equations for the

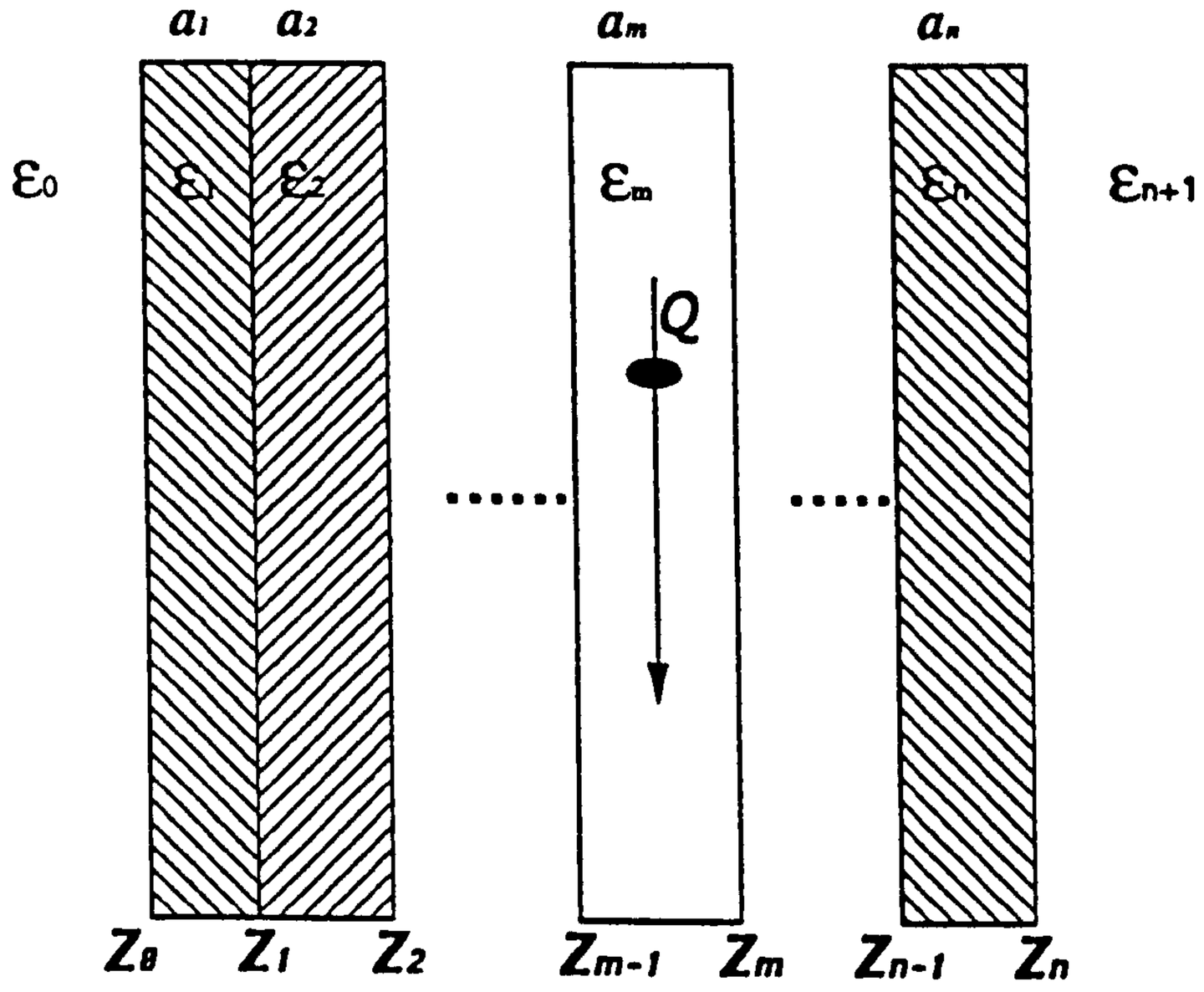

Figure 4.1 Cross section through the $n-$layer system considered in the text and the wave vector transfer of the beam electron during the collision.

x-component and the z-component:

$$\frac{\mathrm{d}^2}{\mathrm{d}z^2}\Pi_x(k_x,k_y,\omega,z) - q^2\Pi_x(k_x,k_y,\omega,z) = (1/\mathrm{i}\omega\epsilon_0\epsilon)j_x(k_x,k_y,\omega,z) \qquad (4.1)$$

$$\frac{\mathrm{d}^2}{\mathrm{d}z^2}\Pi_z(k_x,k_y,\omega,z) - q^2\Pi_z(k_x,k_y,\omega,z) = 0 \qquad (4.2)$$

where $q = (k^2 - \epsilon\,\omega^2/c^2)^{\frac{1}{2}}$. For different media, one has only to set $\epsilon = \epsilon_0, \epsilon_1, \cdots$ etc.

The charged beam which moves along the x axis with (constant) velocity v and at a fixed z-coordinate z_b from the $z-$axis, produced the current density

$$\mathbf{j}(\mathbf{r},t) = Q\,v\,\delta(x-vt)\delta(y)\delta(z-z_b)\hat{\mathbf{x}} \qquad (4.3)$$

Taking the Fourier transform with respect to x, y and t then gives

$$\mathbf{j}(k_x, k_y, \omega, z) = 2\pi Q v \delta(z - z_b)\delta(k_x v - \omega)\hat{\mathbf{x}}$$

Away from the beam level $z = z_b$, the particular solution of Equations 4.1 and 4.2 in a region j can be written as

$$\mathbf{\Pi}^{(j)}(k_x, k_y, z, \omega) = \hat{\mathbf{\Pi}}^{(j)}\delta(k_x v - \omega)$$

where the reduced Hertz vector $\hat{\mathbf{\Pi}}^{(j)}$ contains no delta function factors and takes the form

$$\hat{\mathbf{\Pi}}^{(j)} = \begin{pmatrix} A_j^+ e^{q_j z} + A_j^- e^{-q_j z} \\ 0 \\ B_j^+ e^{q_j z} + B_j^- e^{-q_j z} \end{pmatrix} \tag{4.4}$$

where the A_j^σ and B_j^σ are undetermined coefficients.

At the beam level, the reduced Hertz vector is continuous:

$$\hat{\Pi}_z^{(m'')}\Big|_{z_b^+} - \hat{\Pi}_z^{(m')}\Big|_{z_b^-} = 0 \tag{4.5}$$

but is discontinuous in slope:

$$\frac{d\hat{\Pi}_x^{(m'')}}{dz}\Big|_{z_b^+} - \frac{d\hat{\Pi}_x^{(m')}}{dz}\Big|_{z_b^-} = 2q_m\lambda_m \tag{4.6}$$

where

$$z_b^\sigma = z_b + \sigma\epsilon, \epsilon \to 0^+.$$

and

$$\lambda_m = \frac{\pi Q v}{i\omega\epsilon_0 q_m \epsilon_m} \tag{4.7}$$

In Equation 4.4 the coefficients A_j^σ and B_j^σ depend on ω, $k_x = \omega/v$ and k_y and, of course, on the region j and the beam region m. The discontinuity

in slope at $z = z_b$ is dealt with by allowing the coefficients $A^{\sigma}_{m'}$ in subregion m' to differ from the coefficients $A^{\sigma}_{m''}$ in subregion m''. Since the boundary conditions at infinity require four of the coefficients to vanish, there remain $4n+6$ undetermined coefficients. These coefficients can be found by supplementing the $4n+4$ linear equations that describe the continuity of E_x, E_y, H_x and H_y at the $n+1$ interfaces with the 2 equations that describe the continuity of $\hat{\Pi}_x$ and the discontinuity of $\mathrm{d}\hat{\Pi}_x/\mathrm{d}z$ at $z = z_b$.

In principle, it is possible to solve this system of $4n+6$ equations directly using computer algebra. My early work followed this direct approach and gave results for a single slab consistent with reference [35]. In practice, however, such calculations soon become unwieldy and it is far better to describe the boundary conditions in terms of a transfer matrix recurrence relation.

4.2.3. The transfer matrix recurrence relation

In order to express recurrence relation in the simplest possible form the Hertz vector coefficients are rescaled as follows:

$$\alpha^{\sigma}_j = A^{\sigma}_j \mathrm{e}^{\sigma q_j z_{j-1}}/\lambda_m \qquad \text{with} \quad \alpha^{\sigma}_0 = A^{\sigma}_0/\lambda_m$$

$$\beta^{\sigma}_j = B^{\sigma}_j \mathrm{e}^{\sigma q_j z_{j-1}}/(\mathrm{i}k_x\lambda_m) \qquad \text{with} \quad \beta^{\sigma}_0 = B^{\sigma}_0/(\mathrm{i}k_x\lambda_m)$$

A REDUCE computer algebra program has been used to express the continuity of the electromagnetic fields at the j^{th} interface in terms of a transfer matrix recurrence relation. This shows that

$$\mathbf{C}_{j+1} = T^{(j+1,j)}\mathbf{C}_j \qquad \text{for} \quad j \neq m' \tag{4.8}$$

where

$$\mathbf{C}_j = \left(\alpha^{+}_j,\ \alpha^{-}_j,\ \beta^{+}_j,\ \beta^{-}_j \right)^{\mathrm{T}}.$$

is the *coefficient vector* and

$$T^{(j+1,j)} = \frac{1}{h^+_{j+1,j+1} f_j} \begin{pmatrix} \epsilon_j \begin{pmatrix} \tilde{h}^+_{j+1,j} f_j^2 & \tilde{h}^-_{j+1,j} \\ \tilde{h}^-_{j+1,j} f_j^2 & \tilde{h}^+_{j+1,j} \end{pmatrix} & \begin{pmatrix} 0 & 0 \\ 0 & 0 \end{pmatrix} \\ d_{j+1,j} \begin{pmatrix} f_j^2 & 1 \\ -f_j^2 & -1 \end{pmatrix} \begin{pmatrix} h^+_{j+1,j} f_j^2 & h^-_{j+1,j} \\ h^-_{j+1,j} f_j^2 & h^+_{j+1,j} \end{pmatrix} & \end{pmatrix} \tag{4.9}$$

is the *transfer matrix.* In above expression, I have introduced the variable

$$\tilde{h}^\sigma_{ij} = q_i + \sigma q_j. \tag{4.10}$$

and have also used the variables $f_j = \mathrm{e}^{q_j a_j}$ (with $f_0 = f_{n+1} = 1$), $d_{ij} = \epsilon_i - \epsilon_j$ and $h^\sigma_{ij} = q_i \epsilon_j + \sigma q_j \epsilon_i$, exactly as in the normal calculation.

For future use it also worth defining

$$\boldsymbol{\alpha}_j = \begin{pmatrix} \alpha^+_j, & \alpha^-_j \end{pmatrix}^{\mathrm{T}}$$

$$\boldsymbol{\beta}_j = \begin{pmatrix} \beta^+_j, & \beta^-_j \end{pmatrix}^{\mathrm{T}}$$

In the beam layer, the boundary conditions 4.6 and 4.5 ensure that the Hertz coefficients on either side of the beam are related by

$$\mathbf{C}_{m''} = \mathbf{C}_{m'} + \mathbf{G}_m \tag{4.11}$$

where

$$\mathbf{G}_m = \begin{pmatrix} g^-_m, & -g^+_m, & 0, & 0 \end{pmatrix}^{\mathrm{T}}$$

is the *source vector* and

$$g_j^\sigma = \mathrm{e}^{\sigma q_j (z_b - z_{j-1})} \qquad \text{and} \qquad g_0^\sigma = \mathrm{e}^{\sigma q_0 z_b}.$$

So, combining Equations 4.8 and 4.11 leads to the recurrence relation

Box 8. Recurrence relation for parallel incidence

$$\mathbf{C}_{j+1} = T^{(j+1,j)}(\mathbf{C}_j + \delta_{jm'}\mathbf{G}_m)$$

with

$$T^{(m'',m')} = I \tag{4.12}$$

In principle, this recurrence relation can be iterated to express the coefficients in region 0 in terms of those in region $n+1$. The boundary conditions at infinity then allow us to determine the coefficients in region 0 and use Equation 4.12 to generate all the other coefficients. Such a procedure can be carried through numerically without difficulty but this approach offers little insight into the nature of the solutions or their relationship to previously derived results for bulk, single interfaces and single slabs. As in the case of normal incidence we will therefore prefer to proceed analytically, with the aim of obtaining closed formulae for the quantities of interest.

4.3. The dispersion relation

It is easy to write down a formal solution to the recurrence relation:

$$\mathbf{C}_j = T^{(j0)}\mathbf{C}_0 + T^{(jm)}\mathbf{G}_m \tag{4.13}$$

where the *generalised transfer matrix* $T^{(ji)}$ is defined by the product

$$T^{(ji)} = \prod_{k=i}^{j-1} T^{(k+1,k)}, \tag{4.14}$$

with successive matrices ordered from right to left. Starting from Equation 4.13, with the source terms set equal to zero, and using the boundary conditions at infinity, we can obtain a formal expression for the dispersion relation:

$$T_{11}^{(n+1,0)} T_{33}^{(n+1,0)} = 0.$$

In order to interpret this equation we shall now use the dispersion brackets ($[C_{ji}]$, $[D_{ji}]$ etc.) of Chapter 3. Also here, and throughout this chapter, we shall use a convenient shorthand: for any quantity X, we extend the tilde notation of Equation 4.10 so that $\tilde{X}$ is defined by replacing each h_{ji}^{σ} variable in X by the corresponding $\tilde{h}_{ji}^{\sigma}$. For example,

$$\begin{aligned}\left[\tilde{C}_{21}\right] &= \tilde{h}_{32}^{+} f_2^2 \tilde{h}_{21}^{+} f_1^2 + \tilde{h}_{32}^{-} \tilde{h}_{21}^{-} f_1^2 \\ &= (q_3 + q_2) f_2^2 (q_2 + q_1) f_1^2 + (q_3 - q_2)(q_2 - q_1) f_1^2.\end{aligned}$$

Using this notation and carrying out a calculation analogous to that for normal incidence, the dispersion relation takes the form

Box 9. Dispersion relation for TM and TE modes

$$\left[C_{n0}\right]\left[\tilde{C}_{n0}\right] = 0. \tag{4.15}$$

In general, solutions of the dispersion relation are obtained with ω in the lower-half complex plane so, for real frequencies, the dispersion relation is only approximately satisfied. However, it will become clear from final expression for the energy loss probability (Equation 4.27), that the real frequencies for which the dispersion relation is close to being satisfied are often those for

which there is a high probability of energy loss. The solutions of Equation 4.15 are of two types (cf. reference [3]). Those with $[C_{n0}] = 0$ have already been identified in Chapter 2. The solutions with $[\tilde{C}_{n0}] = 0$ are not excited by normal incidence but, at this stage of the argument, cannot be ruled out for parallel incidence. (The example of Al/Al_2O_3 multilayers in Chapter 6 will shed further light on this point.)

For symmetrical slabs with $2j+1$ layers, the dispersion relation can be further factorised (cf. Chapter 3) to give

$$(L^+_{j0}L^-_{j0})(\tilde{L}^+_{j0}\tilde{L}^-_{j0}) = 0. \tag{4.16}$$

where $L^\sigma_{j0} = [C_{j0}]\, f_{j+1} + \sigma\,[E_{j0}]$ and (of course) $\tilde{L}^\sigma_{j0} = \left[\tilde{C}_{j0}\right] f_{j+1} + \sigma\left[\tilde{E}_{j0}\right]$. The equation $L^\sigma_{j0} = 0$ gives TM modes while $\tilde{L}^\sigma_{j0} = 0$ gives TE modes. In each case, the + and − superscripts correspond respectively to symmetric and antisymmetric solutions.

Special cases of our dispersion relation agree with established results for low values of n. For example in the case of a single slab surrounded by a homogeneous medium, $n = 1$ and $j = 0$ so Equation 4.16 becomes

$$\left\{(q_0\epsilon_1 + q_1\epsilon_0)^2 f_1^2 - (q_0\epsilon_1 - q_1\epsilon_0)^2\right\}\left\{(q_0 + q_1)^2 f_1^2 - (q_0 - q_1)^2\right\} = 0.$$

In this case, the solutions split into the TM modes

$$\frac{q_0\epsilon_1 + q_1\epsilon_0}{q_0\epsilon_1 - q_1\epsilon_0} = \pm e^{-q_1 a_1}$$

and the TE modes

$$\frac{q_0 + q_1}{q_0 - q_1} = \pm e^{-q_1 a_1}$$

previously given in references [78] and [81]. Also, since the number of interfaces is $n + 1$, the case of a single interface corresponds to taking $n = 0$,

Substituting this value in Equation 4.15 gives

$$(q_0\epsilon_1 + q_1\epsilon_0)(q_0 + q_1) = 0$$

which is again of the expected form, having the trivial solution $\epsilon_1 + \epsilon_0 = 0$ in the electrostatic limit.

4.4. Solution for the Hertz vector

4.4.1. The generalised transfer matrix

In order to solve the inhomogeneous transfer matrix recurrence relation (Equation 4.13) it is necessary to obtain an explicit formula for the generalised transfer matrix (Equation 4.14). Our solution can be described by introducing several new quantities:

$$\eta_{ij} = \prod_{k=i}^{j} \epsilon_k$$

$$\kappa_{ij} = \prod_{k=i}^{j} h^{+}_{k+1,k+1} f_k$$

$$\Theta^{\sigma}_{ji} = [C_{j,i+1}] + \sigma\,[D_{j,i+1}]$$

$$\Phi^{\sigma}_{ji} = [E_{j,i+1}] + \sigma\,[F_{j,i+1}]$$

$$\Omega^{\sigma}_{ji} = [D_{j-1,i}]\,f_j^2 + \sigma\,[F_{j-1,i}]\,.$$

and

$$\Lambda^{\sigma}_{ji} = [C_{j-1,i}]\,f_j^2 + \sigma\,[E_{j-1,i}]$$

Substituting the transfer matrix 4.9 into Equation 4.14 one finds that the generalised transfer matrix has a block triangular form:

$$T^{(ji)} = \frac{1}{\kappa_{i,j-1}} \begin{pmatrix} \eta_{i,j-1}\tilde{\tau}^{(ji)} & 0 \\ \chi^{(ji)} & \tau^{(ji)} \end{pmatrix} \tag{4.17}$$

where $\tau^{(ji)}$ is defined

$$\tau^{(ji)} = \begin{pmatrix} [C_{j-1,i}] & [D_{j-1,i}] \\ [E_{j-1,i}] & [F_{j-1,i}] \end{pmatrix}$$

with $[C_{ji}], [D_{ji}]$ and $[E_{ji}]$ defined as before (Chapter 3). The dispersion bracket $[F_{ji}]$ does not appear in the final results, but it is needed for intermediate calculations. It is defined by

$$F_{ji} = h^-_{j+1,j} f_j^2 C_{j+1,i-1} h^-_{i+1,i} = h^-_{j+1,j} f_j^2 \cdots h^-_{i+1,i}$$

with the initial values

$$[F_{i-1,i}] = 1 \qquad \text{and} \qquad [F_{ii}] = h^+_{i+1,i}$$

The definition of $\tilde{\tau}^{(ji)}$ is similar, but involves the $\tilde{h}^{\sigma}_{j-i,i}$ (as explained in Section 4.3):

$$\tilde{\tau}^{(ji)} = \begin{pmatrix} [\tilde{C}_{j-1,i}] & [\tilde{D}_{j-1,i}] \\ [\tilde{E}_{j-1,i}] & [\tilde{F}_{j-1,i}] \end{pmatrix}$$

Finally,

$$\chi^{(ji)} = \sum_{k=i}^{j-1} d_{k+1,k}\eta_{i,k-1} \begin{pmatrix} \Theta^-_{j-1,k}\tilde{\Lambda}^+_{ki} & \Theta^-_{j-1,k}\tilde{\Omega}^+_{ki} \\ \Phi^-_{j-1,k}\tilde{\Lambda}^+_{ki} & \Phi^-_{j-1,k}\tilde{\Omega}^+_{ki} \end{pmatrix}$$

The matrices $\tau^{(ji)}, \tilde{\tau}^{(ji)}$ and $\mathbf{0}$ are easily obtained from the product of transfer matrices, but the form of $\chi^{(ji)}$ is not so obvious. In Appendix A, a detailed

derivation of $\chi^{(ji)}$ will be given.

4.4.2. Solutions for the Hertz vector coefficients

Once the generalised transfer matrix has been specified, it is possible to find the Hertz vector coefficients in every region. In the context of energy-loss calculations we only need the Hertz vector coefficients $\alpha_{m'}$, $\alpha_{m''}$, $\beta_{m'}$ and $\beta_{m''}$ in the beam layer. These are given by Equations 4.22–4.24 below. However, in order to show the methods used to obtain the beam layer coefficients, I have give a sketch of the definition of α and β for all values of j. Fortunately, considerable simplifications occur on setting j equal to m' or m''.

Before we can state our solution for the Hertz vector, it is desirable to introduce some new variables. Using the notation of dispersion brackets introduced in the context of normal incidence, we define

$$\rho_{ij} = \prod_{k=i}^{j} (2q_k f_k) \,.$$

$$\gamma^{\sigma}_{ji} = [C_{ji}]\, g^{-}_{i} + \sigma\, [D_{ji}]\, g^{+}_{i}$$

$$\zeta^{\sigma}_{ji} = [C_{ji}]\, g^{+}_{j+1} + \sigma\, [E_{ji}]\, g^{-}_{j+1}$$

$$W_{ij} = \sum_{k=i}^{j} \left(\frac{\epsilon_{k+1} - \epsilon_k}{\epsilon_{k+1}} \right) \nu_{k+1,j} \tilde{\Lambda}^{+}_{ki} \Lambda^{+}_{ki}$$

$$X_{ij} = \sum_{k=i}^{j} (\epsilon_{k+1} - \epsilon_k) \eta_{i,k-1} \Theta^{-}_{nk} \tilde{\Lambda}^{+}_{k0}$$

$$Y_{ij} = \sum_{k=i}^{j} (\epsilon_{k+1} - \epsilon_k) \eta_{k+2,j+1} \tilde{\Theta}^{-}_{nk} \Lambda^{+}_{k0} .$$

$$Z_{ij} = \sum_{k=i}^{j} \left(\frac{\epsilon_{k+1} - \epsilon_k}{\epsilon_k} \right) \nu_{i+1,k} \tilde{\Theta}^{-}_{jk} \Theta^{-}_{jk}$$

and

$$\nu_{ij} = \prod_{k=i}^{j} h_{kk}^{+} \tilde{h}_{kk}^{+} f_k^2 = \prod_{k=i}^{j} 4 q_k^2 f_k^2 \epsilon_k \qquad \text{with} \quad \nu_{i+1,i} = 1.$$

In terms of this notations, and using the definitions

$$\mathbf{M}_{ji} = \begin{pmatrix} -[D_{ji}] \\ [C_{ji}] \end{pmatrix} \qquad \text{and} \quad \mathbf{N}_{ji} = \begin{pmatrix} [C_{ji}] \\ [E_{ji}] \end{pmatrix},$$

previously given in Chapter 3, the coefficient vectors for $j \leq m'$ take the forms

Box 10. Coefficients of the Hertz vector for $j \leq m'$

$$\boldsymbol{\alpha}_j = -\frac{q_m \epsilon_m}{q_j \epsilon_j} \rho_{j,m-1} \frac{\bar{\tilde{\gamma}}_{nm}}{[\tilde{C}_{n0}]} \widetilde{\mathbf{N}}_{j-1,0} \tag{4.18}$$

and

$$\boldsymbol{\beta}_j = \frac{q_m \epsilon_m}{q_j \epsilon_j} \frac{\rho_{j,m-1}}{[\tilde{C}_{n0}]\,[C_{n0}]} \Big\{ 2 q_j \epsilon_j \bar{\tilde{\gamma}}_{nm} W_{0,j-1} \mathbf{M}_{nj} + (\bar{\tilde{\gamma}}_{nm} X_{j,m-1} + 2 q_m f_m^2 \tilde{\zeta}_{m-1,0}^{+} \eta_{jm} Z_{mn}) \mathbf{N}_{j-1,0} \Big\} \tag{4.19}$$

For $j \geq m''$, the coefficients take the following forms:

Box 11. Coefficients of the Hertz vector for $j \geq m''$

$$\boldsymbol{\alpha}_j = -\frac{\epsilon_m}{\epsilon_j}\rho_{m,j-1}\frac{\tilde{\zeta}^+_{m-1,0}}{\left[\tilde{C}_{n0}\right]}\widetilde{\mathbf{M}}_{nj} \tag{4.20}$$

$$\begin{aligned}\boldsymbol{\beta}_j = \frac{\epsilon_m}{\epsilon_j}\frac{\rho_{m,j-1}}{\left[\tilde{C}_{n0}\right]\left[C_{n0}\right]}\Big\{&(2q_m\tilde{\gamma}^-_{nm}\eta_{mj}W_{0,m-1} + \tilde{\zeta}^+_{m-1,0}Y_{m,j-1})\mathbf{M}_{nj} \\ &+ 2q_j\epsilon_j f_j^2\tilde{\zeta}^+_{m-1,0}Z_{jn}\mathbf{N}_{j-1,0}\Big\}\end{aligned} \tag{4.21}$$

In Appendix C, a detailed derivation of all these coefficients will be given.

These expressions are rather daunting. However, as promised considerable simplifications occur in the subregions on either side of the beam. Substituting $j = m'$ and m'' in Equations 4.18–4.21 finally yields

Box 12. Coefficients of the Hertz vector in the beam layer

$$\boldsymbol{\alpha}_{m'} = -\frac{\tilde{\gamma}^-_{nm}}{\left[\tilde{C}_{n0}\right]}\widetilde{\mathbf{N}}_{m-1,0} \tag{4.22}$$

$$\boldsymbol{\alpha}_{m''} = -\frac{\tilde{\zeta}^+_{m-1,0}}{\left[\tilde{C}_{n0}\right]}\widetilde{\mathbf{M}}_{nm} \tag{4.23}$$

and

$$\boldsymbol{\beta}_{m'} = \boldsymbol{\beta}_{m''} = \frac{2q_m\epsilon_m}{\left[\tilde{C}_{n0}\right]\left[C_{n0}\right]}\left(\tilde{\gamma}^-_{nm}W_{0,m-1}\mathbf{M}_{nm} + f_m^2\tilde{\zeta}^+_{m-1,0}Z_{mn}\mathbf{N}_{m-1,0}\right). \tag{4.24}$$

Even in the context of energy loss calculations, these solutions for the Hertz vector are not of primary interest. Our main purpose is to use these results to obtain a closed-form semiclassical expression for the energy-loss spectrum.

This will be done in the next section.

4.5. The energy-loss spectrum

The electron travels in m^{th} medium against the electric field in m^{th} medium. The work done per unit path length moving against this field is

$$\begin{aligned} -\frac{\mathrm{d}W}{\mathrm{d}x} &= QE_m^x(x=vt, y=0, z=z_b, t) \\ &= \frac{Q}{(2\pi)^3}\int\int\int_{-\infty}^{\infty}\mathrm{d}k_x\mathrm{d}k_y\mathrm{d}\omega\mathrm{e}^{\mathrm{i}(k_x v-\omega)t}E_m^x(k_x,k_y,z_b,\omega) \\ &= \frac{Q}{(2\pi)^3}\int\int_{-\infty}^{\infty}\tilde{E}_m^x(k_x,k_y,z_b,\omega)\Big|_{k_x=\omega/v}\mathrm{d}k_y\mathrm{d}\omega \end{aligned}$$

where we have defined

$$E_m^x(k_x,k_y,z_b,\omega) = \tilde{E}_m^x(k_x,k_y,z_b,\omega)\delta(k_x v-\omega)$$

A straightforward calculation shows that

$$E_m^x(k_x,k_y,z_b,\omega) = \sum_{\sigma=\pm}\left\{(\epsilon_m\omega^2/c^2-k_x^2)A_{m'}^{\sigma}\mathrm{e}^{\sigma q_m z_b}+\mathrm{i}q_m k_x\sigma B_{m'}^{+}\mathrm{e}^{\sigma q_m z_b}\right\}$$

In order to calculate the semiclassical energy loss spectrum we write

$$\frac{\mathrm{d}W}{\mathrm{d}x} = \int_0^{\infty}\mathrm{d}(\hbar\omega)\,\hbar\omega\int_0^{k_c}\mathrm{d}k_y\,\frac{\mathrm{d}^3P}{\mathrm{d}(\hbar\omega)\mathrm{d}k_y\mathrm{d}x}$$

where k_c is an appropriate wavevector cut-off and $\mathrm{d}^2P/\mathrm{d}(\hbar\omega)\mathrm{d}k_x\mathrm{d}x$ is interpreted as the probability per unit path length of exciting an individual quantum of of energy $\hbar\omega$ and wavevector component k_y. Equivalently, if one defines the scattering probability per unit path length per unit energy range as

$$\frac{\mathrm{d}I(\hbar\omega)}{\mathrm{d}x} = \int_0^{k_c}\mathrm{d}k_y\,\frac{\mathrm{d}^3P}{\mathrm{d}(\hbar\omega)\mathrm{d}k_y\mathrm{d}x}$$

we have

$$\frac{\mathrm{d}W}{\mathrm{d}x} = \int_0^\infty \mathrm{d}(\hbar\omega)\, \hbar\omega \frac{\mathrm{d}I(\hbar\omega)}{\mathrm{d}x}$$

A straightforward calculation shows that the energy loss probability is described by the function

Box 13. Energy loss function

$$\frac{\mathrm{d}^3P}{\mathrm{d}(\hbar\omega)\mathrm{d}k_y\mathrm{d}x} = \frac{Q^2}{2\pi^2\epsilon_0\hbar^2v^2}\mathrm{Im}\left\{\chi_m^{(n)}\right\}_{k_z\to\omega/v} \tag{4.25}$$

where

$$\chi_m^{(n)} = \frac{1}{q_m\epsilon_m}\sum_{\sigma=\pm}\left\{(1-\epsilon_m v^2/c^2)\alpha_m^\sigma g_m^\sigma + q_m\sigma\beta_m^\sigma g_m^\sigma\right\} \tag{4.26}$$

It makes no difference, in Equation 4.26, whether one chooses to use $\alpha_{m'}^\sigma$ or $\alpha_{m''}^\sigma$. Whichever choice is made, our solution for the Hertz vector (Equations 4.22—4.24) leads to the following explicit expression for the energy loss function for the beam in the m^{th} region in or outside an n layer slab:

Box 14. The energy loss function for parallel incidence

$$\begin{aligned}\chi_m^{(n)} = &\left(\frac{v^2}{c^2} - \frac{1}{\epsilon_m}\right)\frac{\tilde{\gamma}_{nm}^-\tilde{\zeta}_{m-1,0}^+}{q_m\left[\tilde{C}_{n0}\right]} \\ &+ \frac{2q_m}{\left[\tilde{C}_{n0}\right]\left[C_{n0}\right]}\left(f_m^2\tilde{\zeta}_{m-1,0}^+\zeta_{m-1,0}^- Z_{mn} - \tilde{\gamma}_{nm}^-\gamma_{nm}^+ W_{0,m-1}\right)\end{aligned} \tag{4.27}$$

This equation is the main result of our analysis. It provides a compact, closed formula for the semiclassical energy loss spectrum, which is valid for all choices of the beam region m, the beam position z_b (which enters via the

γ and ζ variables), the number of layers n and the thickness and composition of the layers (specified by a_j and $\epsilon_j(\omega)$).

4.5.1. Comparison with known results

Equation 4.27 can be compared with known results. First, consider the case of a single slab. On substituting $n = 1$ and $m = 0$ in Equation 4.27, we obtain (a compact form of) Parker's formula for an *external* beam(Equation 2.3):

$$\chi_0^{(1)} = \left(\frac{v^2}{c^2} - \frac{1}{\epsilon_0}\right) \frac{\tilde{\gamma}_{10}^{-}\, g_0^{+}}{q_0 \left[\tilde{C}_{10}\right]} + \frac{(2q_0/\epsilon_0)(g_0^{+})^2}{\left[\tilde{C}_{10}\right]\left[C_{10}\right]} \left(4(\epsilon_2 - \epsilon_1)\epsilon_0 q_1^2 f_1^2 + (\epsilon_1 - \epsilon_0)\tilde{\Theta}_{10}^{-}\Theta_{10}^{-}\right). \qquad (4.28)$$

Substituting $n = 1$ and $m = 2$ gives the same answer, but with the replacements $\epsilon_0 \leftrightarrow \epsilon_2$, $q_0 \leftrightarrow q_2$ and $g_0^{\sigma} \leftrightarrow g_2^{-\sigma}$, as expected from symmetry. On the other hand, substituting $n = 1$ and $m = 1$ into Equation 4.27 gives Parker's formula for an *internal* beam(Equation 2.4):

$$\chi_1^{(1)} = \left(\frac{v^2}{c^2} - \frac{1}{\epsilon_1}\right) \frac{\tilde{\gamma}_{11}^{-}\, \tilde{\zeta}_{00}^{+}}{q_1 \left[\tilde{C}_{10}\right]} + \frac{2q_1/\epsilon_1}{\left[\tilde{C}_{10}\right]\left[C_{10}\right]} \left((\epsilon_2 - \epsilon_1) f_1^2 \tilde{\zeta}_{00}^{+}\, \zeta_{00}^{-} + (\epsilon_0 - \epsilon_1)\tilde{\gamma}_{11}^{-}\gamma_{11}^{+}\right). \qquad (4.29)$$

Equation 4.27 can even be used where no slab is present. Since the number of interfaces is $n+1$, the case of a single interface can be analysed by taking $n = 0$. If we also set $m = 0$, Equation 4.27 gives

$$\chi_0^{(0)} = \left(\frac{v^2}{c^2} - \frac{1}{\epsilon_0}\right) \frac{(q_1 + q_0) - (q_1 - q_0)(g_0^{+})^2}{q_0(q_1 + q_0)}$$

$$+\frac{2q_0(\epsilon_1-\epsilon_0)(g_0^+)^2}{\epsilon_0(q_1+q_0)(q_1\epsilon_0+q_0\epsilon_1)} \tag{4.30}$$

which agrees with the standard formula for a relativistic interface [34, 36]. Substituting $n=0$ and $m=1$ in Equation 4.27 gives the same answer, but with the replacements $\epsilon_0 \leftrightarrow \epsilon_1$, $q_0 \leftrightarrow q_1$ and $g_0^\sigma \leftrightarrow g_1^{-\sigma}$, as expected from the symmetry.

Finally, one can consider the case of a bulk medium with no interfaces, which corresponds to $n=-1$. Substituting $n=-1$ and $m=0$ into Equation 4.27 gives

$$\chi_0^{(-1)} = \frac{1}{q_0}\left(\frac{v^2}{c^2}-\frac{1}{\epsilon_0}\right) \tag{4.31}$$

which, after integrating over the azimuthal angle, gives a result equivalent to that of Landau and Lifshitz [79].

4.6. Symmetries and symmetrical slabs

Chapter 3 introduced four symmetry operators:

1. $\hat{\mathcal{P}}_k$ reverses the sign of q_k but leaves all the other q_j unchanged;
2. $\hat{\mathcal{T}}_v$ reverses the sign of v;
3. $\hat{\mathcal{S}}$ reverses the labelling of layers so that $q_j \rightarrow q_{n+1-j}$ etc;
4. $\mathcal{T}_\omega$ reverses the sign of ω.

In this section the symmetrical properties of energy loss function and Hertz vector coefficients in parallel incidence will be examined.

Inspection of Equation 4.27 immediately shows that

$$\hat{\mathcal{T}}_v(\chi_m^{(n)}) = \left(\chi_m^{(n)}\right)$$

and

$$\hat{\mathcal{T}}_\omega(\chi_m^{(n)}) = \left(\chi_m^{(n)}\right)^*$$

The transformation $\mathcal{P}_k$ has a less trivial effect. For example,

$$\hat{\mathcal{P}}_k(\zeta_{m-1,0}^\sigma) = \begin{cases} -\zeta_{m-1,0}^\sigma / f_k^2 & \text{if} \quad 0 < k \leq m-1 \\ -\sigma\zeta_{m-1,0}^\sigma & \text{if} \quad k = m \\ \zeta_{m-1,0}^\sigma & \text{if} \quad k \geq m+1 \end{cases}$$

However, by applying $\hat{\mathcal{P}}_k$ to all the terms in Equation 4.27, and considering all possible cases, it is easy to show that

$$\mathcal{P}_k(\chi_m^{(n)}) = \chi_m^{(n)} \qquad \text{for all } k.$$

Finally, consider the transformation $\hat{\mathcal{S}}$. This produces

$$\hat{\mathcal{S}}(\gamma_{nm}^\sigma) = \zeta_{n-m,0}^{-\sigma} f_{n+1-m}$$

$$\hat{\mathcal{S}}(\zeta_{m-1,0}^\sigma) = \gamma_{n,n+1-m}^{-\sigma} / f_{n+1-m}$$

$$\hat{\mathcal{S}}(W_{0,m-1}) = -Z_{n+1-m,n}$$

$$\hat{\mathcal{S}}(Z_{mn}) = -W_{0,n-m}$$

and when these results are substituted in Equation 4.27 one finds that

$$\hat{\mathcal{S}}(\chi_m^{(n)}) = \chi_{n+1-m}^{(n)},$$

as expected.

Another way of checking our result is to consider the effect of allowing two neighbouring regions to coalesce. This corresponds to making the replacements $\epsilon_{k+1} \rightarrow \epsilon_k$, $q_{k+1} \rightarrow q_k$ etc., $2a_k \rightarrow a_k$ and then renumbering the layers $j \rightarrow j-1$ for $j \geq k$. When this transformation is applied to Equation 4.27, the expression for $\chi_m^{(n)}$ becomes $\chi_{m-1}^{(n-1)}$ if $k < m$ or $\chi_m^{(n-1)}$ if $k > m$.

As in normal incidence, it is possible to show that the Hertz vector coefficients satisfy simple symmetry properties. For example,

$$\hat{\mathcal{P}}_k \alpha_j^\sigma = \begin{cases} \alpha_j^\sigma & \text{if} \quad k \neq j, \quad k \neq m \\ -\alpha_j^\sigma & \text{if} \quad k = m \neq j \\ \alpha_j^{-\sigma} & \text{if} \quad k = j \neq m \\ -\alpha_j^{-\sigma} & \text{if} \quad k = j = m \end{cases}$$

with precisely similar results for β_j^σ. Also, if one uses brackets to show the dependence of the Hertz vector coefficients on the beam layer, one has

$$\hat{\mathcal{S}} \alpha_j^\sigma = f_{n+1-j}^{-\sigma} \alpha_{n+1-j}^{-\sigma}(n+1-m)$$

and

$$\hat{\mathcal{S}} \beta_j^\sigma(m) = -f_{n+1-j}^{-\sigma} \beta_{n+1-j}^{-\sigma}(n+1-m)$$

All these results are consistent with Equation 4.26.

4.7. The energy-loss spectrum in the non-retarded case

The electron energy-loss spectrum in non-relativistic limit can be obtained by solving Poisson's equation. In Appendix D, a detailed derivation of analytical expression for energy-loss spectrum will be given. Here, we list main

results.

According Appendix D, the energy loss function is

$$\frac{\mathrm{d}^2 P}{\mathrm{d}(\hbar\omega)\mathrm{d}x} = \frac{Q^2}{2\pi^2\varepsilon_0\hbar^2 v^2}\int_0^\infty \mathrm{Im}\left(\chi_n^{(m)}\right)$$

where

Box 15. The classical limit of energy loss function for parallel incidence

$$\chi_n^{(m)} = \frac{\check{\gamma}_{nm}^{-}\check{\zeta}_{m-1,0}^{+}}{k\epsilon_m\left[\check{C}_{n0}\right]} \tag{4.32}$$

with

$$\check{\gamma}_{nm}^{-} = \left[\check{C}_{nm}\right] g_m^{-} - \left[\check{D}_{nm}\right] g_m^{+}$$

$$\check{\zeta}_{m-1,0}^{+} = \left[\check{C}_{m-10}\right] g_m^{+} + \left[\check{E}_{m-10}\right] g_m^{-}$$

and

$$g_m^{\sigma} = \mathrm{e}^{\sigma k(z_b - z_{m-1})}$$

where we have used a convenient shorthand: the dispersion brackets $\left[\check{C}_{ji}\right]$, $\left[\check{D}_{ji}\right]$ and $\left[\check{E}_{ji}\right]$ are defined similarly to $[C_{ji}]$, $[D_{ji}]$ and $[E_{ji}]$, but replacing each h_{ji}^{σ} variable by $\check{h}_{ji}^{\sigma}$:

$$\check{h}_{ji}^{\sigma} = \epsilon_j + \sigma\epsilon_i$$

and with each f_j variable by $\check{f}_j$:

$$\check{f}_j = \mathrm{e}^{ka_j}$$

In Appendix D we will prove that Equation 4.32 is equal to Equation 4.27 by taking $c \to \infty$.

4.8. Summary

In this chapter the programme of Chapter 3 was extended to deal with parallel incidence on a multilayered slab, obtaining closed formulae for the dispersion relation and the energy loss spectrum. The dispersion bracket algebra, introduced in the context of normal incidence, has turned out to be valuable in the case of parallel incidence as well. The type of calculations outlined here can be extended to other cases. In Part III of this thesis, we use computer algebra and dispersion brackets to analyse energy loss in anisotropic slabs, but first we will apply our theoretical results for isotropic multilayers to real and model systems.

CHAPTER 5.

APPLICATIONS (I): THIN FILMS

This chapter applies formulae developed for multilayered slabs to the simplest possible case of a single slab. A method is developed for calculating dispersion relation in real materials and applied to thin slabs of diamond. The surface plasmons in thin slabs of diamond are investigated by evaluating the dispersion curves and the energy-loss spectra for electrons travelling normal or parallel to the surface of slabs. Theoretical results are compared with experimental electron energy loss spectra which I obtained in the electron microscope.

5.1. Introduction

As indicated in Chapter 2, the collective excitations of electrons in thin films have been studied extensively by means of dielectric theory. In the electrostatic approximation, Ritchie first derived the loss probability for normal incidence on a single slab [6]. Kröger extended this study to include the effects of retardation [21]. These theories have been used by many researchers to explain energy loss experiments and surface plasmon excitations in single slabs. But many of these studies have concentrated on simple models (e.g. the Drude model has often been used to analyse the dispersion relation.). In many experimental investigations, however, semiconductors and insulators have interested experimentalist as well as metals. The purposes of this chapter are

- To develop a general method to calculate the dispersion relations of surface plasmons in real materials;
- To investigate the relationship between dispersion relations and energy-loss spectrum;
- To compare calculated results with energy-loss experiments.

This chapter will calculate surface plasmon and energy loss in thin slabs of diamond as an example.

5.2. Surface plasmons in thin slabs of diamond

5.2.1. The dispersion relation for single slabs

In Section 3.3, we derived the dispersion relation for single slabs. By assuming $\epsilon_1 = \epsilon$ and $\epsilon_2 = \epsilon_0 = 1$, Equation 3.21 can be simplified as

$$\epsilon q_0 + q = \sigma(\epsilon q_0 - q)\mathrm{e}^{-q\tau} \tag{5.1}$$

where $q_0 = \sqrt{k^2 - \omega^2/c^2}$, $q = \sqrt{k^2 - \epsilon\omega^2/c^2}$, k is the magnitude of the transverse wavevector, $\epsilon(\omega)$ is the complex dielectric function, τ is the thickness of the slab and sign $\sigma = \pm$ corresponds to modes that have symmetric/antisymmetric electric field distributions across the slab. Table 5.1 shows symmetric/asymmetric relationships of electric charge (Q), electric potential (ϕ), electric field (E) and Hertz vector ($\mathbf{\Pi}$) with σ.

In the electrostatic limit [82], Equation 5.1 becomes

$$\epsilon + 1 = \sigma(\epsilon - 1)\mathrm{e}^{-k\tau} \tag{5.2}$$

It is also possible for electromagnetic TE modes to exist with dispersion relation

σ	Q	ϕ	E	Π
+	S	S	A	A
−	A	A	S	S

Table 5.1 Symmetric/asymmetric relations where S represents symmetric and A represents asymmetric.

$$q_0 + q = \sigma(q_0 + q)\mathrm{e}^{-q\tau} \tag{5.3}$$

As part of a general study of dispersion relations in specimens with more complicated geometries, we have written a computer algebra program which automatically yields Equations 5.1—5.3. This program shows that no other normal mode solutions are consistent with the necessary boundary conditions. Physically the charge would oscillate in the y direction due to TE mode. Since these modes produce no excess charge on the top and bottom surfaces, they are not self-sustaining in an infinitely wide slab [3]. The TE modes will not be discussed further.

Equation 5.2 was also derived by Ferrell [82] who used the electrostatic approximation, $\mathbf{E} = -\nabla\varphi$, and the local approximation, $\epsilon(k,\omega) = \epsilon(0,\omega) = \epsilon(\omega)$, to solve Laplace equation $\nabla^2\varphi = 0$ in slabs. With Equation 5.2 Ferrell predicted the radiation of plasma oscillations in metal films, using the Drude dielectric function to model a metallic medium. Two interesting limiting cases were obtained: (a). For short wavelengths or thick slabs, $k\tau \gg 1$, the surface waves become decoupled and do not interfere with one another. Each surface sustains independent oscillations at the reduced frequency of $\omega_p/\sqrt{2}$, that is the characteristics of single plane boundary between a Drude metal and a vacuum. (b). In the limit of very long wavelengths or very thin slabs, the asymmetric oscillation, ie the higher frequency mode($\omega^{\text{asymmetric}}$)(–sign in Equation 5.2), approaches the value ω_p for $k\tau \rightarrow 0$, whereas the frequency of the symmetric mode($\omega^{\text{symmetric}}$) decreases to zero with $k\tau \rightarrow 0$.

In retarded case, for $k\tau \gg 1$, the surface plasmons excited on each surface of a film are essentially similar to that of non-retarded case. However, in the limit of very long wavelengths or very thin slabs, the frequency of the asymmetric mode approaches to zero as $k\tau \rightarrow 0$.

5.2.2. Surface plasmons in the real materials

So long as we are dealing with simple real dielectric functions (such as $\epsilon(\omega) = 1 - \omega_p^2/\omega^2$) it is possible to solve the dispersion relation explicitly. In practice, dielectric functions are complex and complicated and it is not so clear how to solve the dispersion relation. The main purpose of this chapter is to develop a numerical method that is suitable for predicting the plasmon dispersion relation in a thin slab of a real material. In many cases, no simple model can be found that adequately represents the experimentally determined dielectric data. Since experimental data is defined only for real ω, while the appropriate solutions of Equations 5.1 and 5.2 occur in the lower-half complex ω plane, it is necessary to establish a reliable method of extending $\epsilon(\omega)$ into the lower-half plane. The main question to decide is which quantity should be expanded. Care is needed because the functions $\epsilon(\omega)$ and $1/\epsilon(\omega)$ both have poles in the region of interest. Direct expansion of either of these functions is therefore likely to be unreliable. However, consider the function

$$f(\omega) = \frac{\epsilon(\omega) + 1}{\epsilon(\omega) - 1} \tag{5.4}$$

with $f(\omega) = f'(\omega) + if''(\omega)$. This function remains finite at the poles $\epsilon(\omega)$ and $1/\epsilon(\omega)$. Its only poles occur when $\epsilon(\omega) = 1$, corresponding to complete transparency; although $\epsilon(\omega)$ approaches 1 as $\omega \rightarrow \infty$, it is expected that this function will have no poles in the energy-loss region. Therefore, in the following, we will expand Equation 5.4 rather than any other function.

(1). Solution of non-retarded dispersion relation

As the dielectric function is complex, it is obvious that $\mathrm{Im}f(\omega) \neq 0$. This means that there are no solutions of Equation 5.1 for real ω because the left hand side of this equation is complex while the right hand side is real. The wave number k cannot be complex because this would not permit bounded solutions in slabs of infinite area. So one has to assume complex ω and take $\omega = \nu - i\Delta$ so that the non-retarded dispersion relation is written as

$$\begin{cases} \mathrm{Im}f(\nu - i\Delta) = 0 \\ \mathrm{Re}f(\nu - i\Delta) = \pm \mathrm{e}^{-k\tau} \end{cases} \tag{5.5}$$

where ν is real and Δ must be positive in order to get the bounded solutions.

The function f is assumed to be analytic in a strip around the real axis. We then expand to second order and ignore the higher order terms to obtain

$$f(\nu - i\Delta) \simeq f(\nu) - i(\mathrm{d}f(\nu)/\mathrm{d}\nu)\Delta - \tfrac{1}{2}(\mathrm{d}^2 f(\nu)/\mathrm{d}\nu^2)\Delta^2 \tag{5.6}$$

This approximation can then be used to obtain numerical solution of Equations 5.5 by Newton Raphson or secant iteration.

As experimental measurements incorporate random errors to one has to smooth the experimental data. Again, because the function $f(\omega)$ is smoother than the dielectric function and does not have poles in region of interest, it is the appropriate function to smooth. In this study, cubic splines are used to fit $f(\omega)$.

(2). Solution of retarded dispersion relation

In the calculation of the retardation dispersion relation of plasmons in thin slabs, the Equation 5.1 is replaced by Equation 5.2, which can be written in the form

$$h(\omega) = \frac{\epsilon q_0 + q}{\epsilon q_0 - q} - (\pm)\mathrm{e}^{-q\tau} = 0 \tag{5.7}$$

However, direct expansion of the function $h(\omega)$ is unsafe because q_0 has a branch cut along the real axis. Extensive tests have confirmed this. We have found that the most reliable procedure is sticks to an expansion of the function $f(\omega)$, just as in non-retarded case. The dielectric function $\epsilon(\nu)$ is used to construct $f(\nu)$, which is then smoothed and fitted with a cubic spline. The values $f(\nu), \mathrm{d}f(\nu)/\mathrm{d}\nu$ and $\mathrm{d}^2 f(\nu)/\mathrm{d}\nu^2$ are then used to find a second-order approximation to $f(\omega)$ at a point $\omega = \nu - i\Delta$ in the lower-half frequency plane($\Delta > 0$). One then inverts to find $\epsilon(\omega)$ and solve Equation 5.1 by secant iteration, with protection against overshoot and cycling. Extensive tests with model dielectric functions(Lorentzian, double Lorentzian, and Gaussian) have confirmed that this method is reliable, and can be trusted provided $\Delta << \nu$. Our tests include the addition of random noise (to simulate experimental inaccuracies). Small amounts of noise ($\leq 10\%$) can be overcome by using a smoothing spline on $f(\nu)$, prior to expansion; note again that $f(\nu)$ is the appropriate quantity to smooth because it varies much less rapidly than $\epsilon(\nu)$.

It is also worthwhile noting that in Equation 5.7, $q = 0$ must be one of the symmetric solutions as well. This solution does not depend on the thickness τ of the slab and can be interpreted as a transverse bulk plasmon; this solution will be presented with other solutions obtained from Equation 5.7.

5.2.3. Surface plasmon in thin slabs of diamond

Diamond, with an indirect band gap of approximately 5.5 eV, is an ideal material for low-energy studies in the STEM, which has an energy resolution of $\sim$ 0.5 eV. In this section, we study surface plasmons and EELS in thin slabs of diamond. The dielectric function is shown in Figure 5.1. In Figure 5.1, the dielectric function of diamond between 6.0 eV and 30.0 eV is taken from the *Handbook of Optical Constants* [83], based on reflectance data of Phillipp and Taft [84]. The dielectric function between 30.0 eV and 40.0 eV is derived by Fallon from the electron energy loss spectrum obtained from the bulk materials [85]. Since smoothing of the dielectric data from these two different sources could be misleading, this calculation will be confined to the energy region between 6 eV and 30 eV.

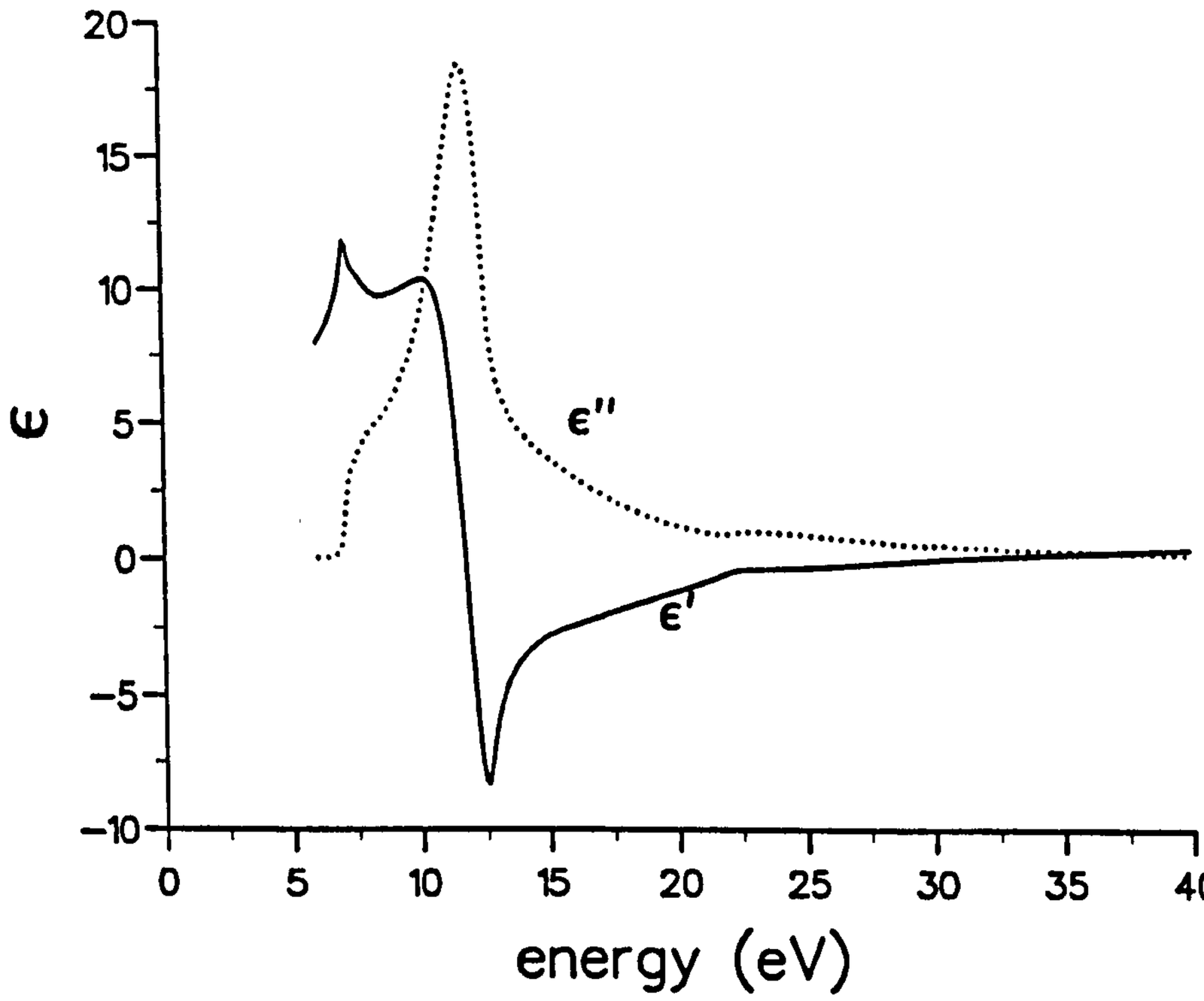

Figure 5.1 Dielectric function of diamond. The data was taken from reference [83] for 6.0 to 30 eV and reference [85] for 30 to 40 eV.

Figures 5.2 and 5.3 show the results obtained for a thin slab of thickness $\tau = 80$ Å in retarded case. For display purposes, the solutions have been split into 'surface plasmon modes' (Figures 5.2a) and 'other modes' (Figures 5.3a). The former are distinguished by the fact that the solutions decay exponentially away from the surfaces for $k > \nu/c$. Figures 5.2b and 5.3b show that the damping of all modes is light enough to justify our second-order expansion.

Figure 5.2a shows that the surface plasmon modes occur in two pairs of antisymmetric and symmetric modes, which approach *two* characteristic energies (21.2 eV and 26.6 eV) at which the density of states of surface plasmons is high. Calculations based Equation (5.2) shown that this fact remains valid for slabs of any thickness in the electrostatic limit. Furthermore, the existence in the upper two branches of surface plasmons inside the light cone ($\omega = ck$) means that it is possible to excite modes that emit electromagnetic radiation, which is different to the behaviour found in metal slabs [3].

In Figure 5.3, other solutions to Equation 5.1 are shown. The dashed lines indicate solutions with $q = 0$; these solutions correspond to transverse bulk modes [86] and do not depend on the thickness of the slab. The dotted and solid lines indicate symmetric and antisymmetric waveguide modes that occur near the pole of $\epsilon(\omega)$. In thicker slabs, families of these solutions can be found with ϵ large and $q\tau$ close to an integral multiple of $i\pi$.

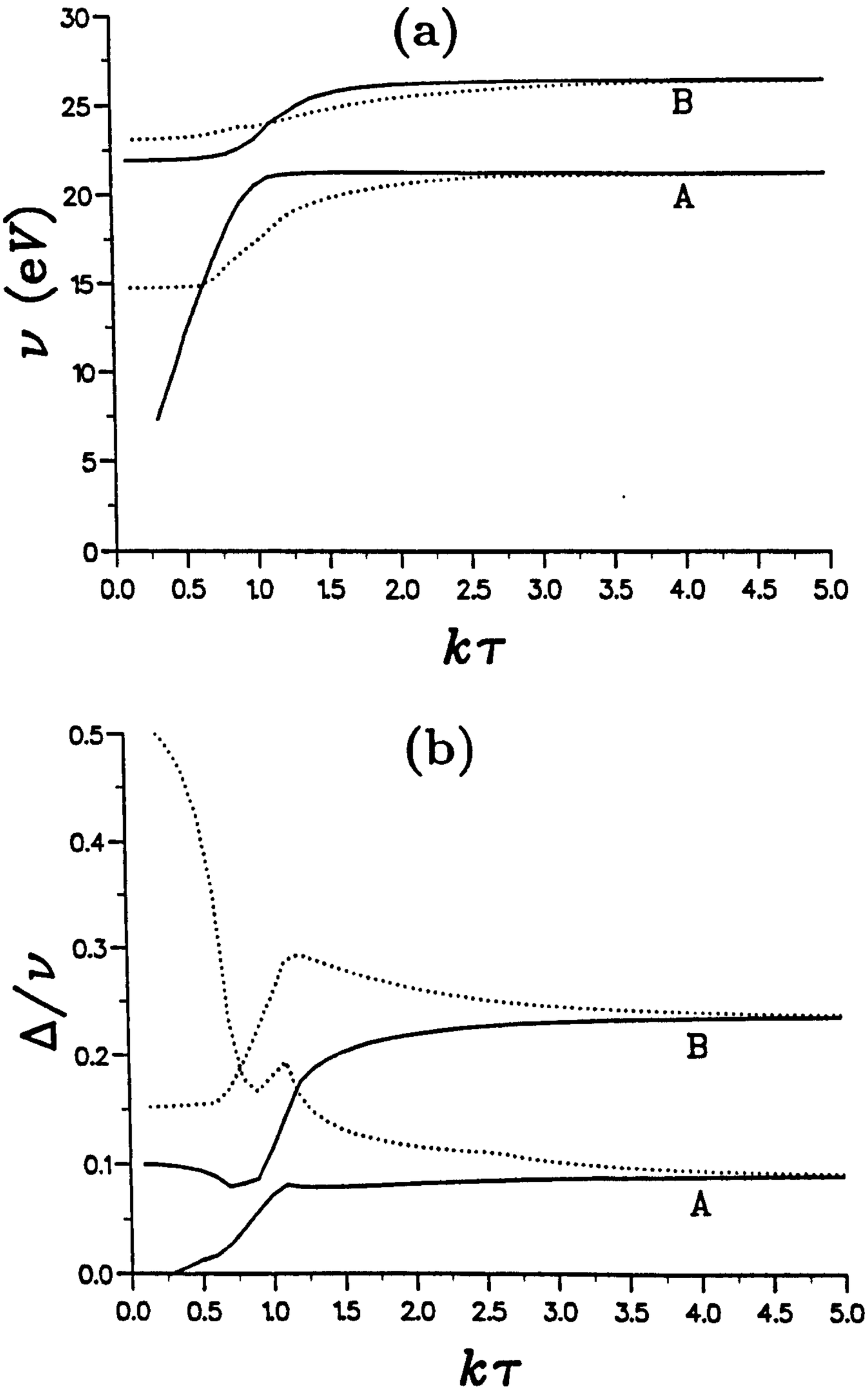

Figure 5.2 (a).Dispersion relations for transverse plasmons in a slab of type-I diamond of thickness $\tau = 80$ Å. Symmetric modes and antisymmetric modes are represented by dotted lines and solid lines respectively. *Two* characteristic energies are obtained as $k\tau \rightarrow \infty$, giving rise to two peaks in the plasmon density of states. (b).The ratio of Δ/ν for surface modes shown in Figure 5.2a.

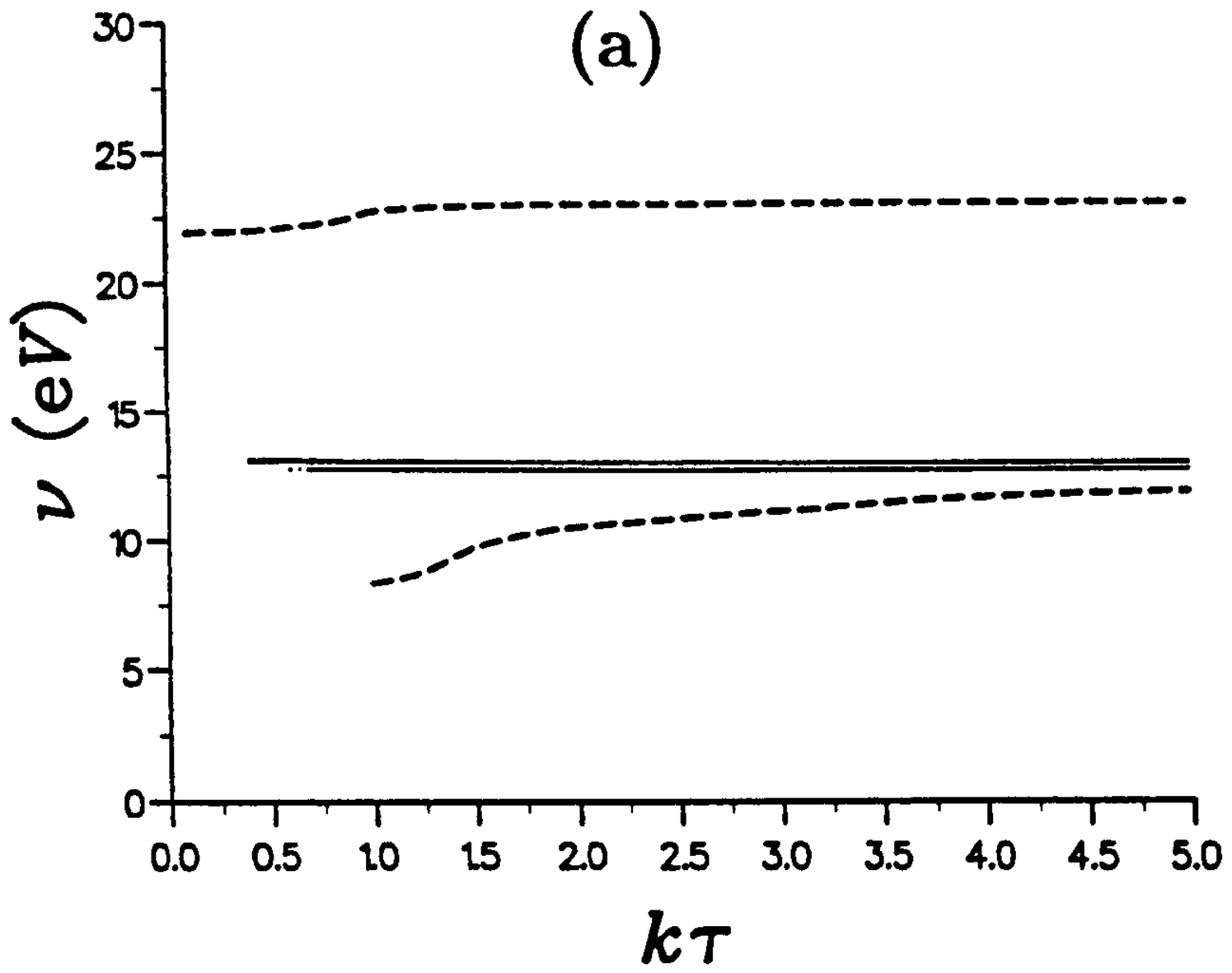

Figure 5.3 (a). Other solutions to equation 2.1: bulk transverse modes with $q' = 0$ (dashed lines) and waveguide modes with $\epsilon \rightarrow \infty$ (solid and dotted lines). (b). The ratio of Δ/ν for *other* modes shown in Figure 5.3a.

5.3. Excitation probability in thin slabs of diamond

When electrons interact with materials and excite plasmon modes, they are scattered and gain momentum $\hbar k$ in a direction perpendicular to their initial direction of motion and lose momentum $\hbar\omega/v$ parallel to their initial direction. The analytical expression for the energy loss function $\mathrm{d}^2P/\mathrm{d}(\hbar\omega)\mathrm{d}k$ can be integrated over transverse wavevectors to obtain the scattering probability per unit energy range, $I(\hbar\omega)$. If all the scattered electrons were collected, one would expect that

$$I(\hbar\omega) = 2\pi \int_0^\infty \mathrm{d}k\; k\, \frac{\mathrm{d}^2P}{\mathrm{d}(\hbar\omega)\mathrm{d}k} = \frac{Q^2}{2\pi^2\epsilon_0\hbar^2v^2} \int_0^\infty \mathrm{d}k\; k\, \mathrm{Im}(\chi_{\mathrm{bulk}} + \chi_{\mathrm{bdy}}).$$

where χ_{bulk} is given by Equation 3.36 and χ_{bdy} is given by Equation 3.37.

Unfortunately, as is always found in energy loss problems, the bulk term produces a logarithmic divergence at large k. On the other hand, Equation 3.30 shows that the terms due to surfaces and boundaries are well-behaved and produce no additional divergencies. The logarithmic divergence is dealt with as usual [14], by introducing an upper cut-off k_{c}. If all the scattered electrons were collected, $1/k_{\mathrm{c}}$ would set a minimum length scale for the validity of semiclassical continuum model.

In practice, k_{c} is often determined by the sizes of the objective aperture inside the electron microscope, which restricts the scattering angle. In the following examples the beam energy has been set at 100 keV and the cut–off wavevector has been chosen to be 15 nm^{-1} (corresponding to scattering through a maximum angle of 9 mrad).

5.3.1. Calculated energy loss spectra

Figure 5.4 show the energy loss spectrum for an electron travelling perpendicular to thin slabs of diamond with different thickness. The total energy loss intensity is decreased when the thickness of slabs is decreased. There are two peaks in the calculated loss spectra. The peak at 33.5 eV corresponds to bulk plasmons. The peak around 21–23 eV includes a direct gap optical absorption, which reflects the bulk diamond band structure and surface plasmon. When the thickness of the slab is decreased this peak is shifted to lower energy because of the contribution of the 21 eV surface plasmon becomes relatively more important for thinner slabs. The surface plasmon at 26.5 eV predicted from dispersion relation can not be seen because of its weak intensity compared with the nearby bulk plasmon.

In Figure 5.5, we present the surface plasmon contribution corresponding to Figure 5.4. Figure 5.5 shows that there are two surface plasmon peaks which are compariable with predicted surface plasmon dispersion relations above.

In order to obtain further evidence for the two predicted surface plasmons, an alternate method can be used.

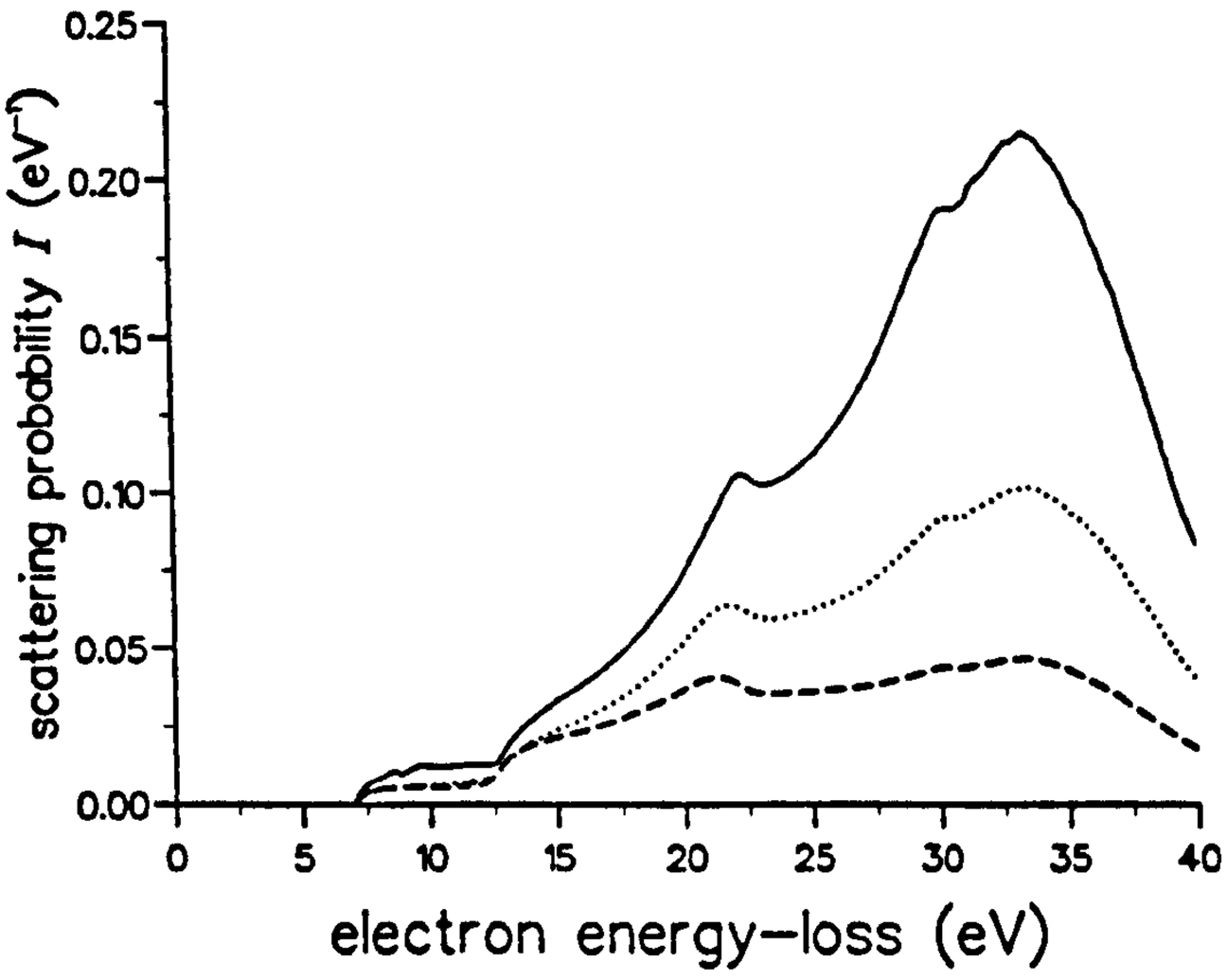

Figure 5.4 Electron energy-loss for normal incidence to different thickness slabs of diamond. Solid line: 200 Å. Dotted line: 100 Å. Dashed line: 50 Å.

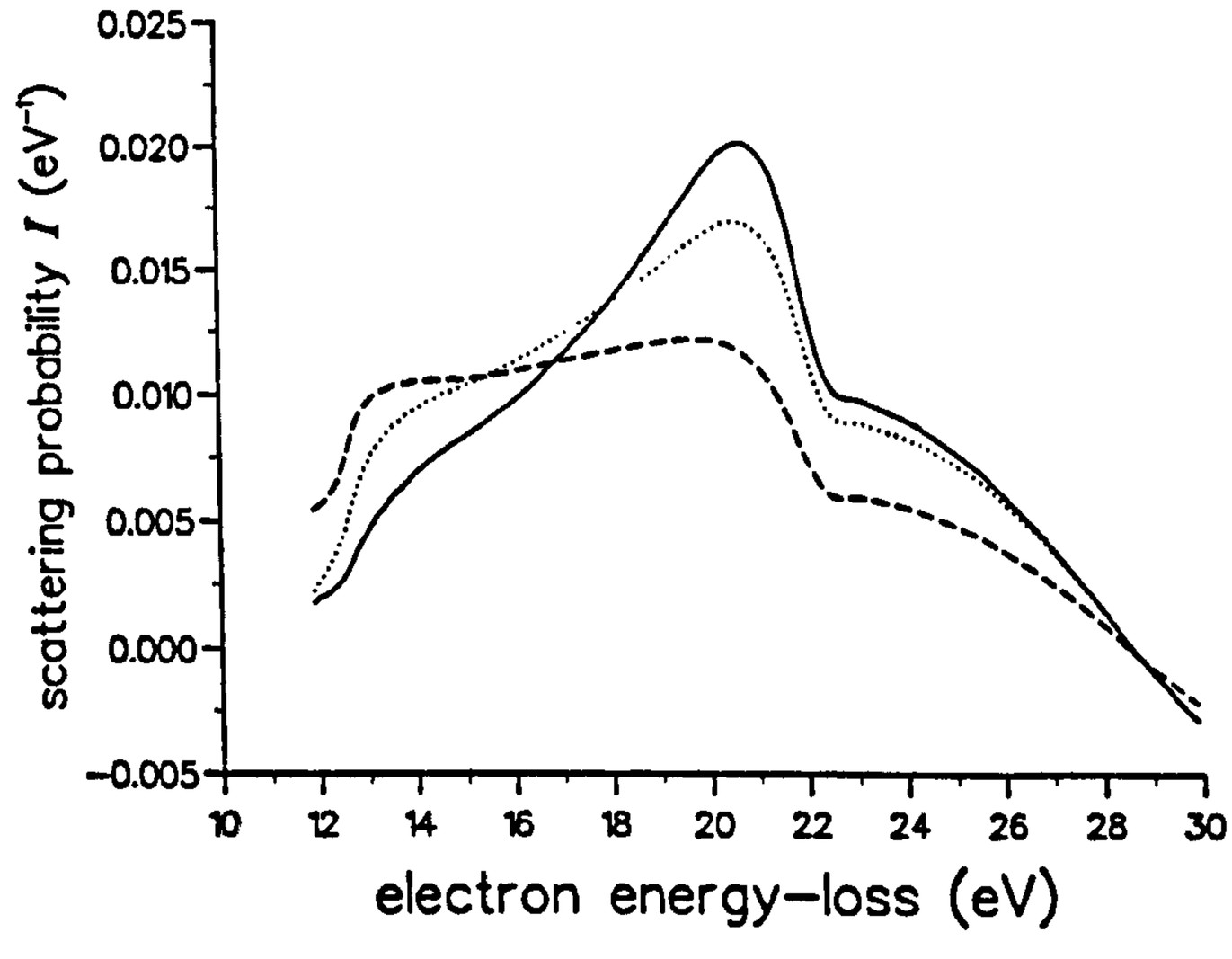

Figure 5.5 Surface contribution to electron energy-loss for normal incidence to different thickness slabs of diamond. Solid line: 200 Å. Dotted line: 100 Å. Dashed line: 50 Å.

In Figure 5.6, we present calculated energy-loss spectra for parallel incidence on a 80Å thickness slabs of diamond. When the beam is positioned at the centre of the slab, the spectrum (solid line) is similar to that of normal incidence. But whilst the beam is at surface, the surface plasmon at 21.2 eV is clearly shown. The shoulder between 22.5 and 26.5 eV corresponds to the second surface plasmon predicted from the dispersion relation. Similar features are observed in the spectrum for electron travelling outside the slab (dashed line in Figure 5.6).

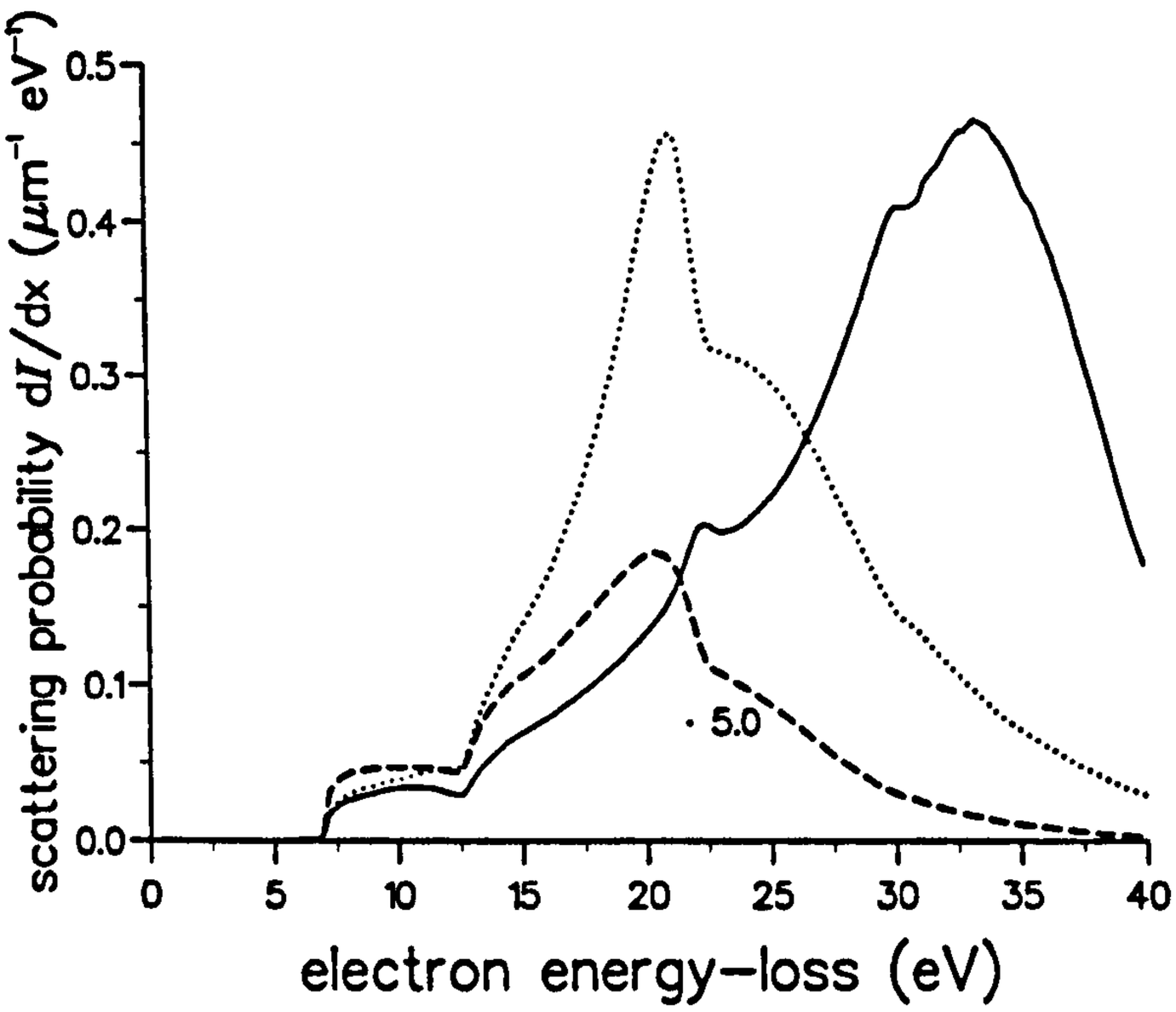

Figure 5.6 Electron energy-loss for parallel incidence to a slab of diamond. The thickness of the slab is 80 Å. The beam positions are taken to be 40 Å away from the surface in the slab (solid line), at the surface (dotted line) and 40 Å away from surface outside slab (dashed line). For improve visibility, the scale for the dashed line is 5 times greater than that indicated on the vertical scale.

5.3.2. Comparison with experimental energy-loss spectra

The results discussed above can be compared with experiments. I have taken a series of energy–loss spectra for a range of different thicknesses by varying the position of a STEM probe in a wedge–shaped sample of type-I diamond. Spectra were acquired beyond the edge of the wedge and then at regular intervals moving into the specimen. For each position of the probe, we can treat the wedge as being a slab of a given effective thickness, estimated using the relation [1];

$$\tau \approx (I_p/I_0)\lambda_p \tag{5.8}$$

where I_p is the area under the first plasmon peak, I_0 is the area under the zero loss peak, and λ_p is the inelastic mean free path (taken to be 70 nm). Away from the tip of the wedge, the effective thickness was found to be proportional to the distance moved into the specimen, consistent with a fixed wedge angle.

The loss spectra acquired in STEM includes both bulk and surface contributions. The bulk scattering probability is

$$\left(\frac{\mathrm{d}^2P}{\mathrm{d}(\hbar\omega)\mathrm{d}k}\right)_{\text{bulk}} = -\frac{Q^2}{4\pi^3\varepsilon_0\hbar^2v^2}\mathrm{Im}\left\{\frac{1}{\epsilon}\frac{1-\epsilon\beta^2}{k^2+\omega^2/v^2-\epsilon\omega^2/c^2}\right\}\tau$$

This contribution can be subtracted from the experimental intensities in order to obtain the surface contribution. Figure 5.7 shows the experimental loss spectra for various effective thicknesses and Figure 5.8 shows the corresponding surface contributions. One would expect to find features corresponding to the predicted peaks in plasmon density of states near 21.2 eV and 26.6 eV. The two peaks observed in Figure 5.8 may be interpreted in this way.

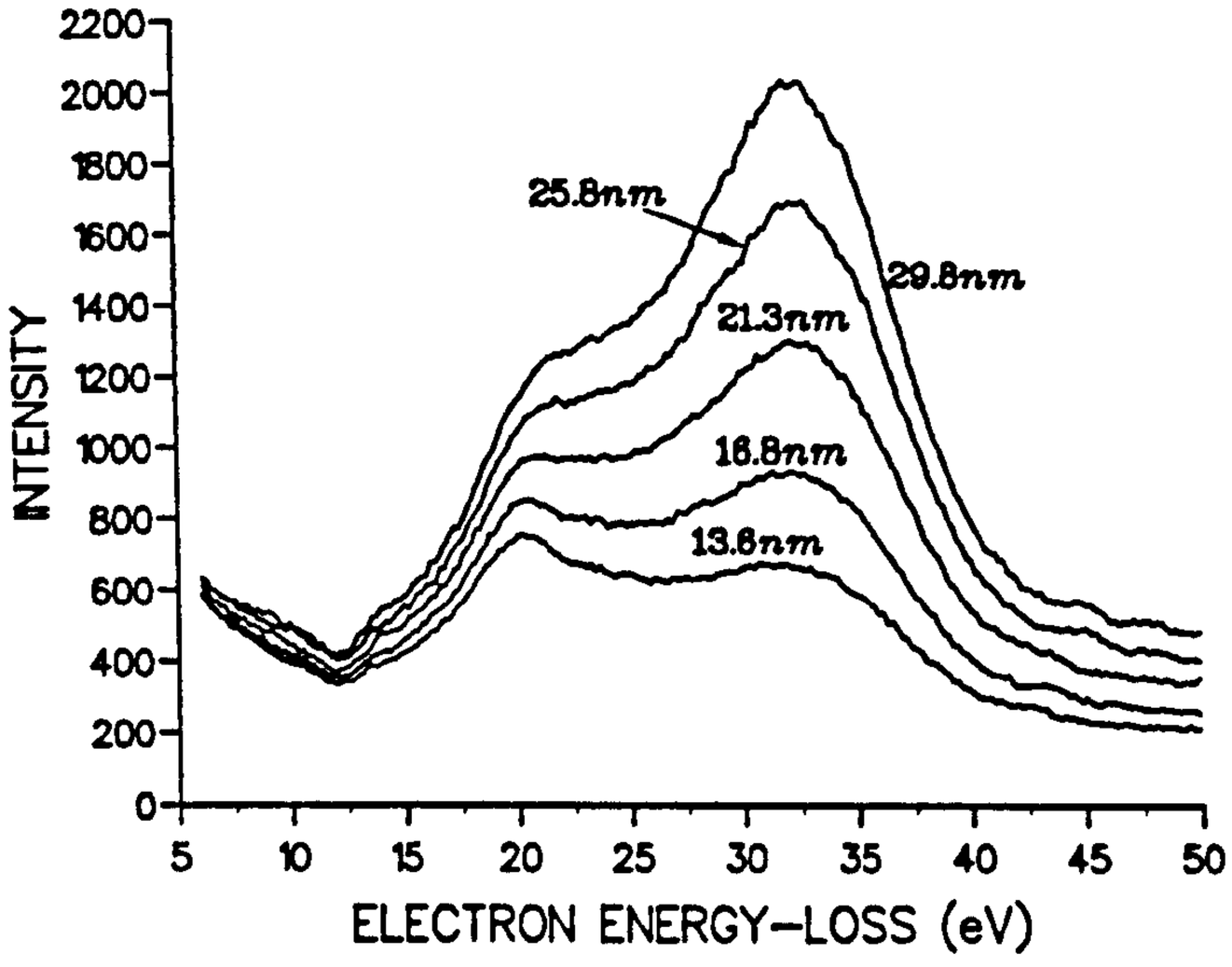

Figure 5.7 Experimental energy-loss spectra in a wedge-shaped sample of type-I diamond acquired in STEM. The effective thickness around the position of the probe is used to label each curve.

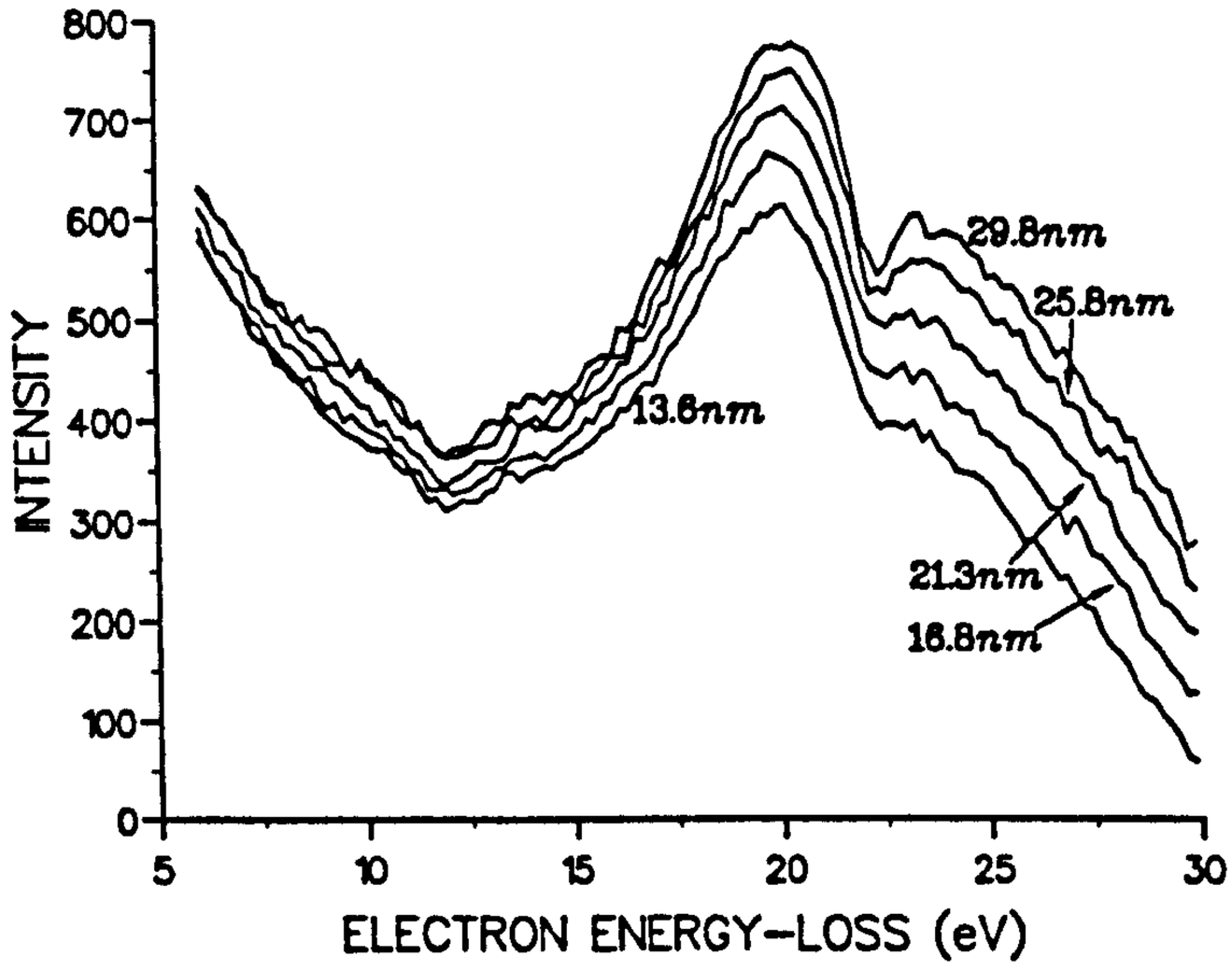

Figure 5.8 The surface contributions. Note that different scales are used for both axes in the two figures.

5.4. Summary

In summary, this chapter has developed a general method for predicting surface plasmon dispersion relations from dielectric functions that are known at real frequencies. This method has been tested on several trial dielectric functions and found to be more reliable than alternative approximations. It has been used to predict the dispersion relation for damped surface plasmons in thin slabs of diamond. Two pairs of symmetric and antisymmetric solutions were found. The density of states for surface plasmons is high at two loss characteristic energies (21.2 eV and 26.6 eV) and one expect to see features in energy–loss spectra near these energies.

These predictions are supported by the calculated energy loss spectra for normal and parallel incidence on a thin slab of diamond. Furthermore, a series of energy–loss spectra were acquired for a range of different effective thicknesses by varying the position of a STEM probe in a wedge–shaped sample of type-I diamond. It was found that the surface contribution to the energy–loss had peaks near the expected energies.

It is also necessary to note that the method described in Section 5.2 has its limitations. In particular, it is not easy to find the right solutions when the dielectric function changes rapidly. This is the case in many semiconductors such as Si and GaAs.

CHAPTER 6.

APPLICATIONS (II): MULTILAYERS

For multilayered systems, the theories developed in Chapters 3 and 4 are applied to Al/Mg, Al/Al_2O_3 and $Al/SiO_2/Si$ structures. This chapter calculates surface and interfacial plasmon dispersion relations and energy loss spectra in these systems.

6.1. Surface and interface plasmons

In Chapters 3 and 4, the general formula for the dispersion relation in an multilayers was derived. For TM modes, one has

$$[C_{n0}] = 0 \tag{6.1}$$

One interesting feature of Equation 6.1 is that additional bulk modes appear. Using Equation 3.38 it can be shown that the dispersion relation is satisfied by taking $q_i = 0$ for any i between 1 and n; these solutions correspond to transverse bulk modes in the various layers of slab. The remaining solutions of the dispersion relation correspond to true surface and interfacial modes.

In order to calculate the dispersion relation one needs explicit expressions for various systems. We have used REDUCE programs to produce these expressions for up to 15 layered films. The algebraic expressions were directly transferred to FORTRAN code for numerical computing.

6.1.1. Mg/Al structures

Surface and interfacial plasmons of Al/Mg double and triple slabs have be calculated by Richter and Geiger [25] in the electrostatic limit. Here we extend those calculations to include retardation for up to eleven layers. The dielectric behaviour of Mg and Al is modelled by dielectric functions of the form [25]

$$\epsilon_j(\omega) = 1 - \frac{\omega_{pj}^2}{\omega^2 + \mathrm{i}\omega\tau^{-1}} \tag{6.2}$$

where ω_p is the plasma frequency and τ a scattering time for electron–electron collisions. The parameters for Mg and Al are $\hbar\omega_{p1} = 10$ eV, $\hbar\omega_{p2} = 15$ eV and $\hbar\tau^{-1} = 0.6$ eV.

Following the method described in Chapter 5 the dispersion relation is calculated in the complex frequency plane. In each layer, the dielectric function is used to construct the function $f_j(\nu) = (\epsilon_j(\nu)+1)/(\epsilon_j(\nu)-1)$ which is then smoothed and extended into the lower-half frequency plane. Inversion is then used to obtain $\epsilon_j(\omega)$. The complete dispersion curves for double Al/Mg films are given in Figure 6.1. There are three main branches which can be interpreted as the surface plasmon of Mg (branch I), the surface plasmon of Al (branch II) and the interfacial plasmon (branch III). The transverse bulk mode of Mg (branch IV), transverse bulk mode of Al (branch V) and the light cone are also plotted.

In Figure 6.1, Branches I and II start from 0 at $k = 0$ and they behave like modes at a single surface. The transverse bulk mode corresponds to $q = 0$ and, for a Drude metal, has the following explicit form

$$\omega^2 = \omega_p^2 + k^2c^2$$

So the transverse bulk mode starts from bulk plasmon at $k = 0$ (see Branch IV and V) and approaches light cone as k increases.

For very large kd the dispersion relations for two layer system simplifies to

$$(\epsilon_1 + \epsilon_2)(\epsilon_1 + 1)(\epsilon_2 + 1) = 0$$

which is fulfilled by the frequencies

$$\mathrm{Re}\omega_{\mathrm{I}} = \sqrt{\frac{\omega_{p1}^2 - 1/2\tau^2}{2}}, \mathrm{Re}\omega_{\mathrm{II}} = \sqrt{\frac{\omega_{p2}^2 - 1/2\tau^2}{2}}, \mathrm{Re}\omega_{\mathrm{III}} = \sqrt{\frac{\omega_{p1}^2 + \omega_{p2}^2 - 1/2\tau^2}{2}}$$

So as $kd \to \infty$, the dispersion curves approache single surface or interfacial modes.

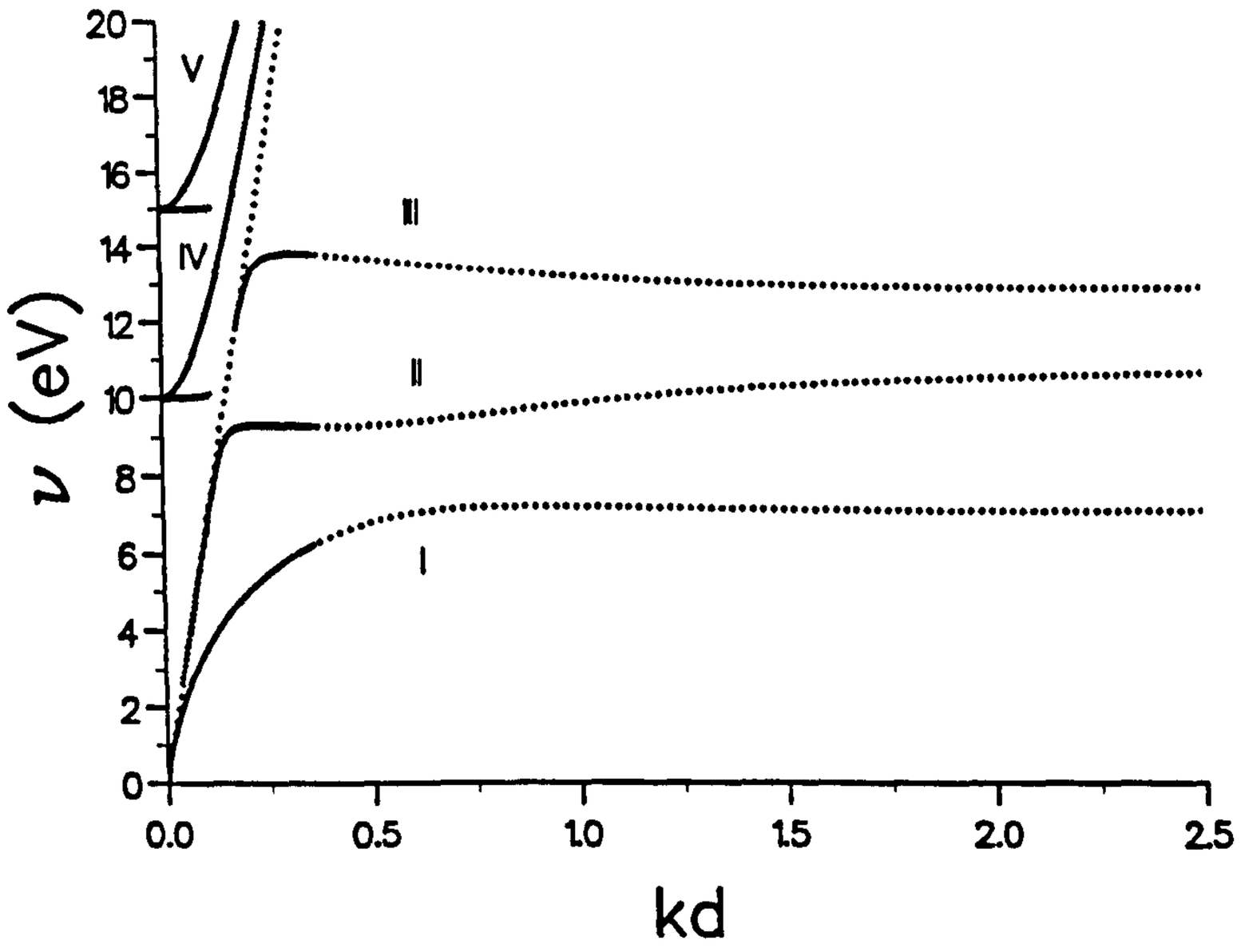

Figure 6.1 Dispersion relation of the surface and interfacial modes for a double Al/Mg film. The thickness of Al and Mg films is 30 Å.

Figures 6.2 to 6.4 show the dispersion curves for three, seven, and eleven layer systems. In all three systems, Mg forms the two outer layers of the multilayer, so there are only Mg surfaces. Surface plasmons of Mg are similar to those of single slabs of Mg[1]. For interfacial curves, there are more branches as the number of layers increases. All curves go to 12.7 eV at large k. There is always a branch which is similar to that of two layer systems. All other main branches start from bulk plasmons of Al and Mg respectively. As the number of layers increases, the interfacial plasmons appear to form a band as expected.

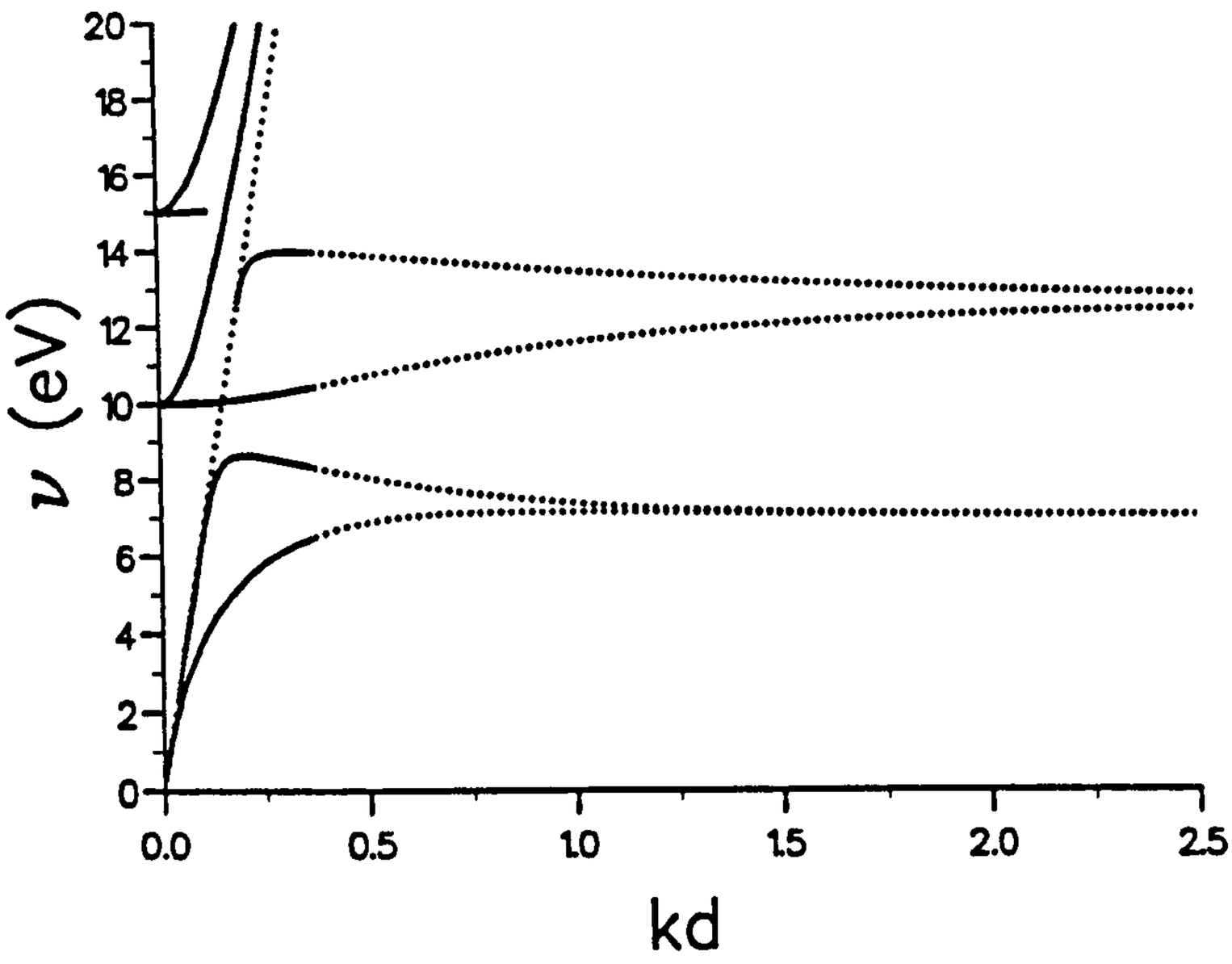

Figure 6.2 Dispersion relation of the surface and interfacial modes for three layer systems. The thickness of Al and Mg films is 30 Å.

[1]Dispersion curves for Drude metals have be extensively studies in various references (cf. [3]).

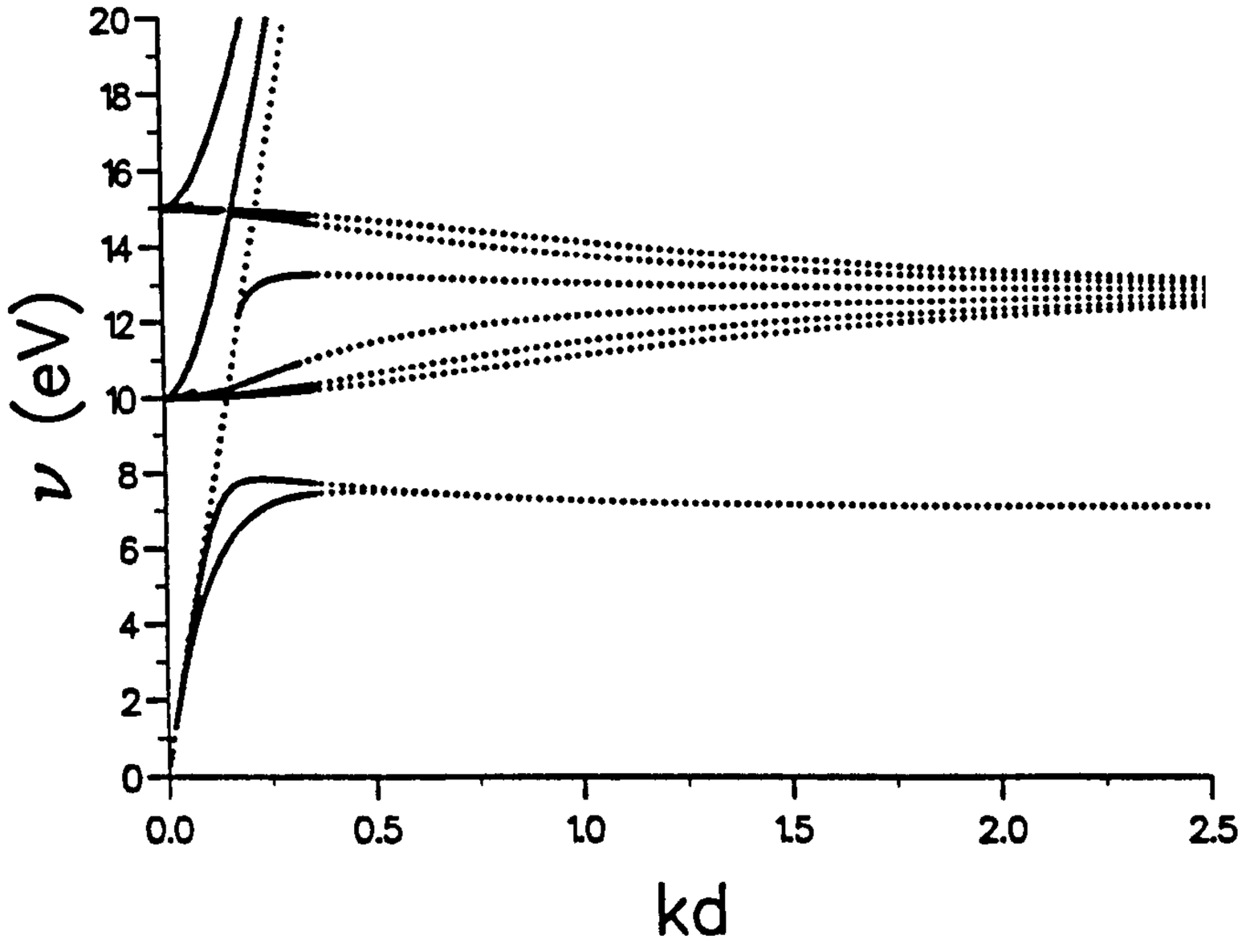

Figure 6.3 Dispersion relation of the surface and interfacial modes for seven layer systems. The thickness of Al and Mg films is 30 Å.

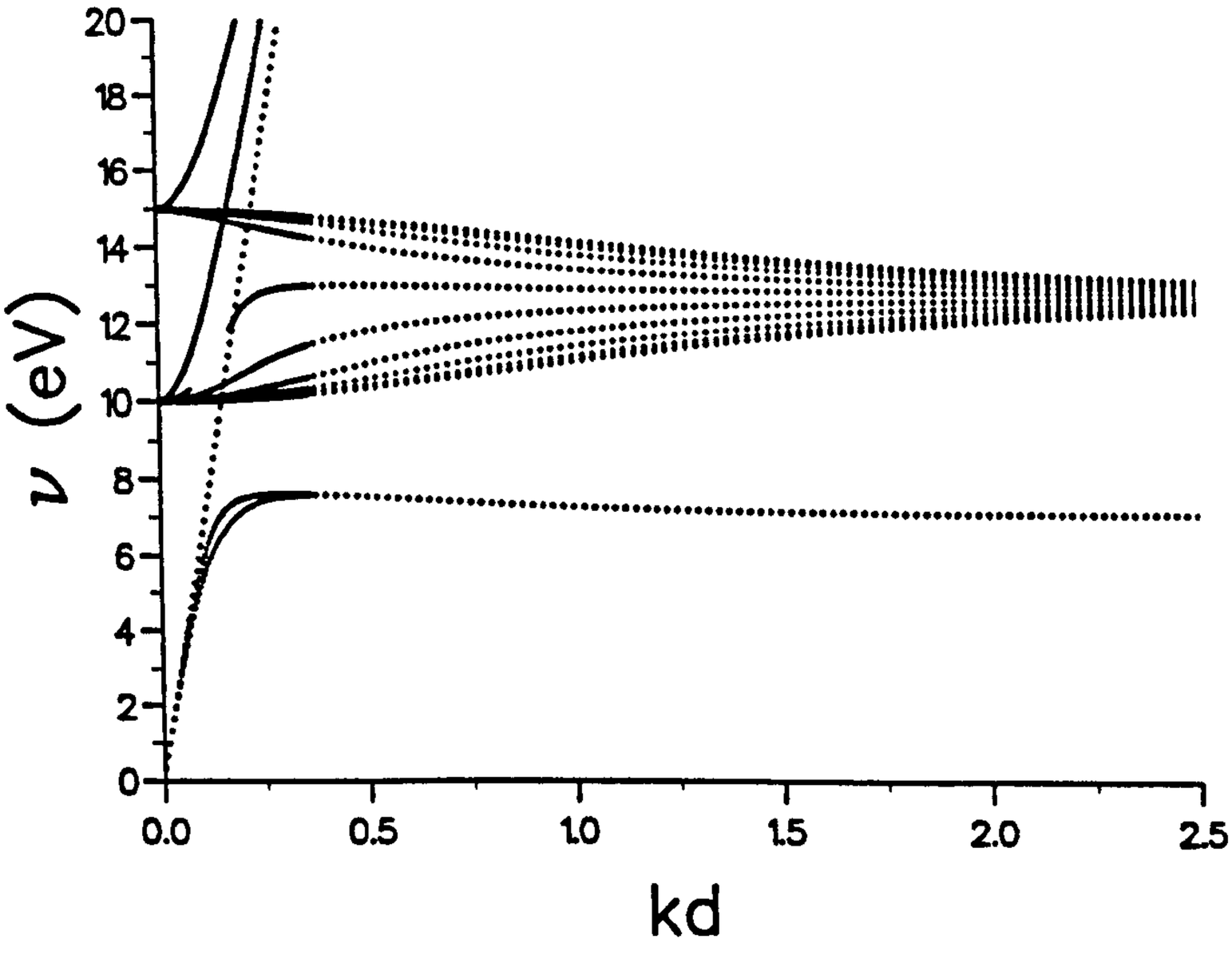

Figure 6.4 Dispersion relation of the surface and interfacial modes for eleven layer systems. The thickness of Al and Mg films is 30 Å.

6.1.2. Al/Al_2O_3 structures

Al and Al_2O_3 form a typical metal–insulator system. This study will illustrate the behavior of interfacial plasmons at the surface between metals and insulators. In order to illustrate typical behaviour, the dielectric function of aluminium is modelled by the Drude model with parameters as before. The dielectric function of Al_2O_3 is modelled by a constant, $\epsilon_{Al_2O_3} = 4$ (as in reference [25])[2].

Figure 6.5 shows the dispersion curves for two layered systems. Branch I is the interfacial plasmon and branch II is the surface plasmon of Al. Both branches start from 0 at $k = 0$. At large kd Branch I goes to 10.7 eV and Branch II goes to 6.5 eV. The surface plasmon of Al behaves like the plasmon at a single surface of Al. There are no surface plasmons of Al_2O_3 in our model because its dielectric function has been taken to be constant.

In Figure 6.5, transverse modes of Al (Branch IV) and Al_2O_3 (Branch III) are also plotted. The transverse mode of Al was discussed before. The transverse mode of Al_2O_3 is a straight line which behaves as $k = 2\omega/c$.

[2]After this work was finished, we became aware of the work by R. French who derived the dielectric function of Al_2O_3 from EELS, showing it to be non–constant. But as the bulk plasmon of Al_2O_3 is around 27.0 eV and beyond the region we are interested in, our dielectric constant model of Al_2O_3 is not unreasonable.

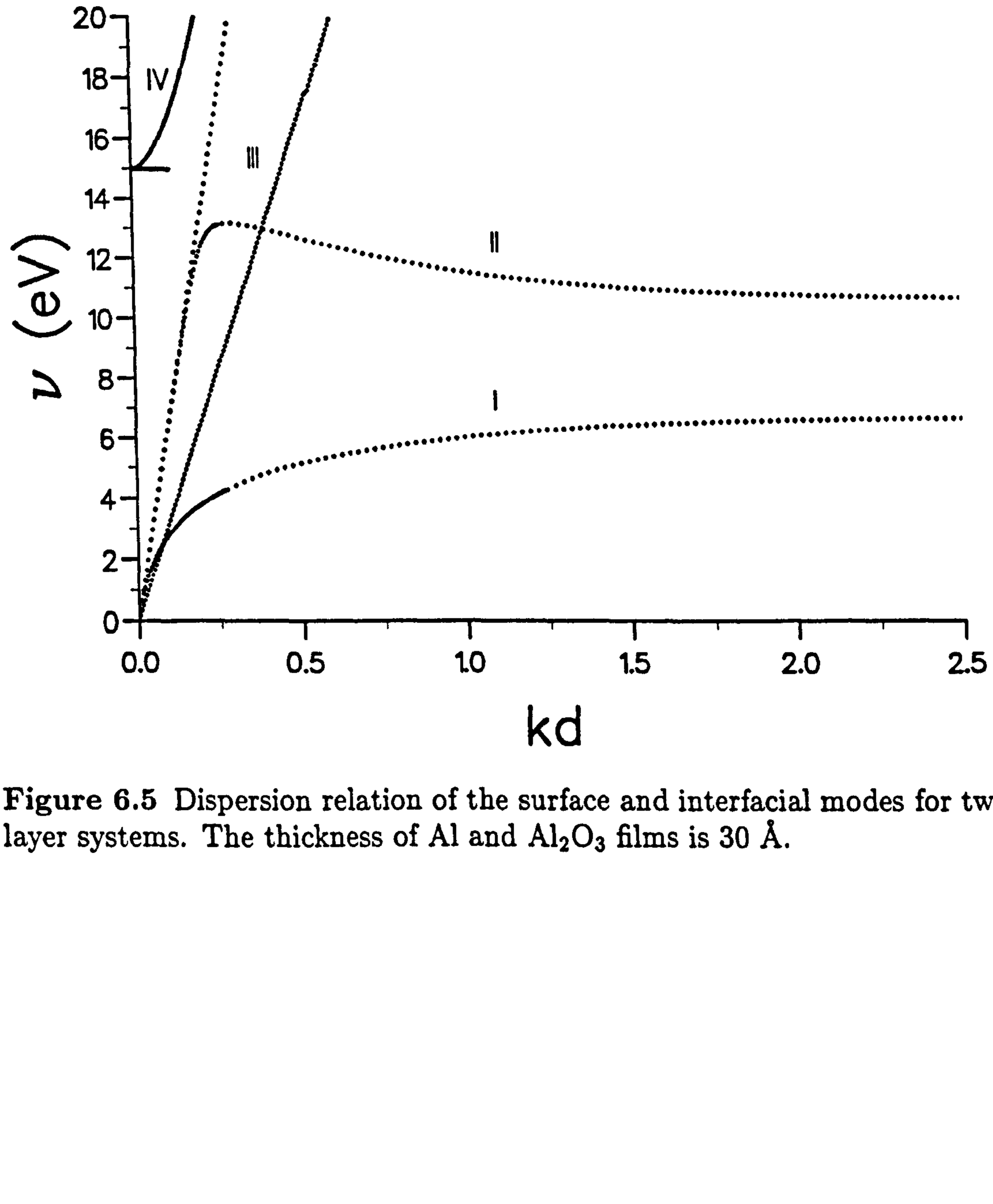

Figure 6.5 Dispersion relation of the surface and interfacial modes for two layer systems. The thickness of Al and Al_2O_3 films is 30 Å.

For multilayered slabs, Figures 6.6–6.8 show the dispersion curves of three, seven and eleven layered systems with Al_2O_3 outside. Corresponding interfacial modes are clearly shown. All branches approach 6.5 eV as k increases. In total, there are $n-1$ interfacial modes for n layered films.

In summary, we have calculated dispersion relation of surface and interface plasmons in two-, three-,seven-, and eleven-layer structures. In order to find out whether these modes can be in fact observed in energy loss spectra, the scattering probability must be calculated. In the following sections, the scattering formulae derived in Chapters 3 and 4 will be applied to study several systems of real materials.

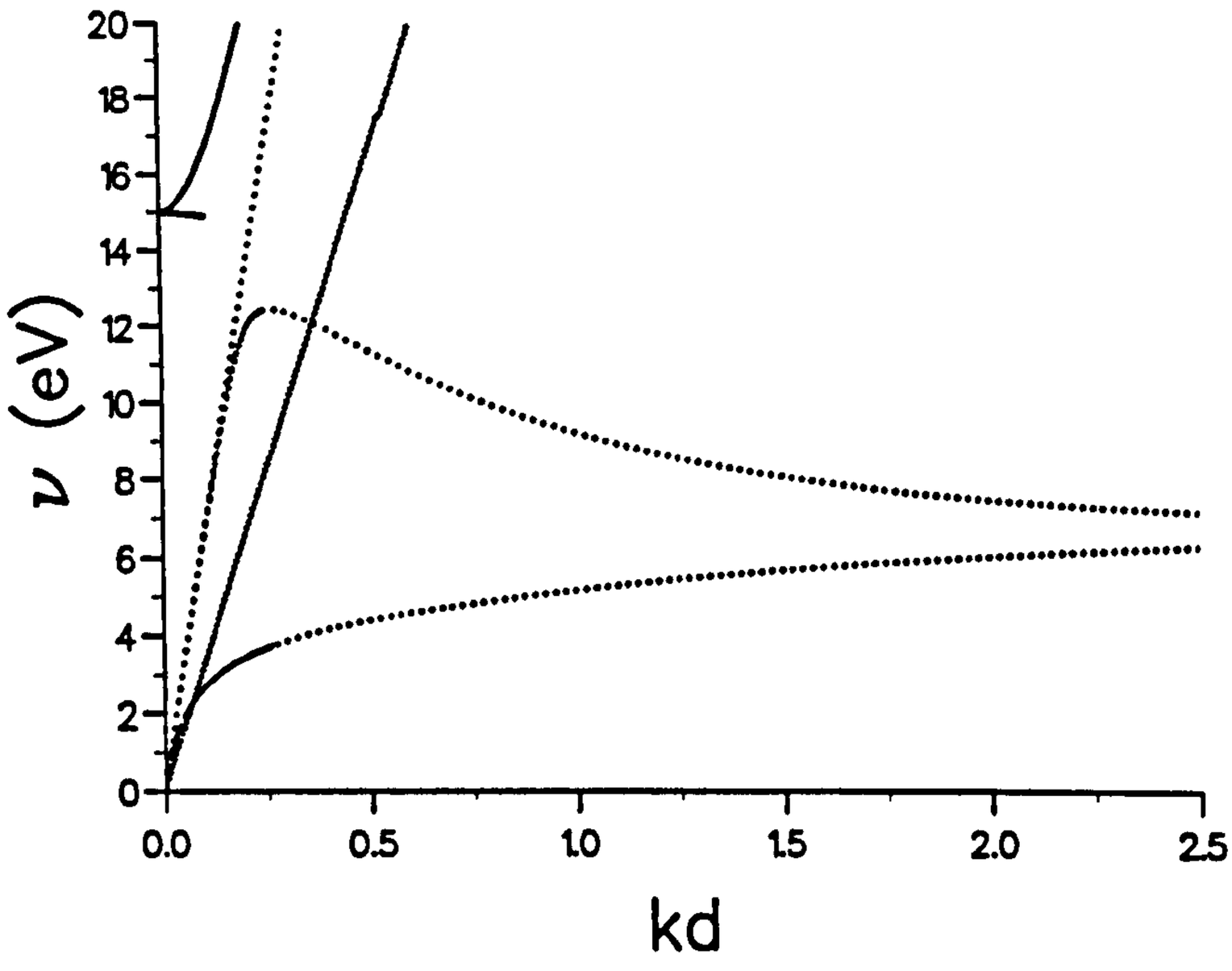

Figure 6.6 Dispersion relation of the surface and interfacial modes for three layer systems. The thickness of Al and Al_2O_3 films is 30 Å.

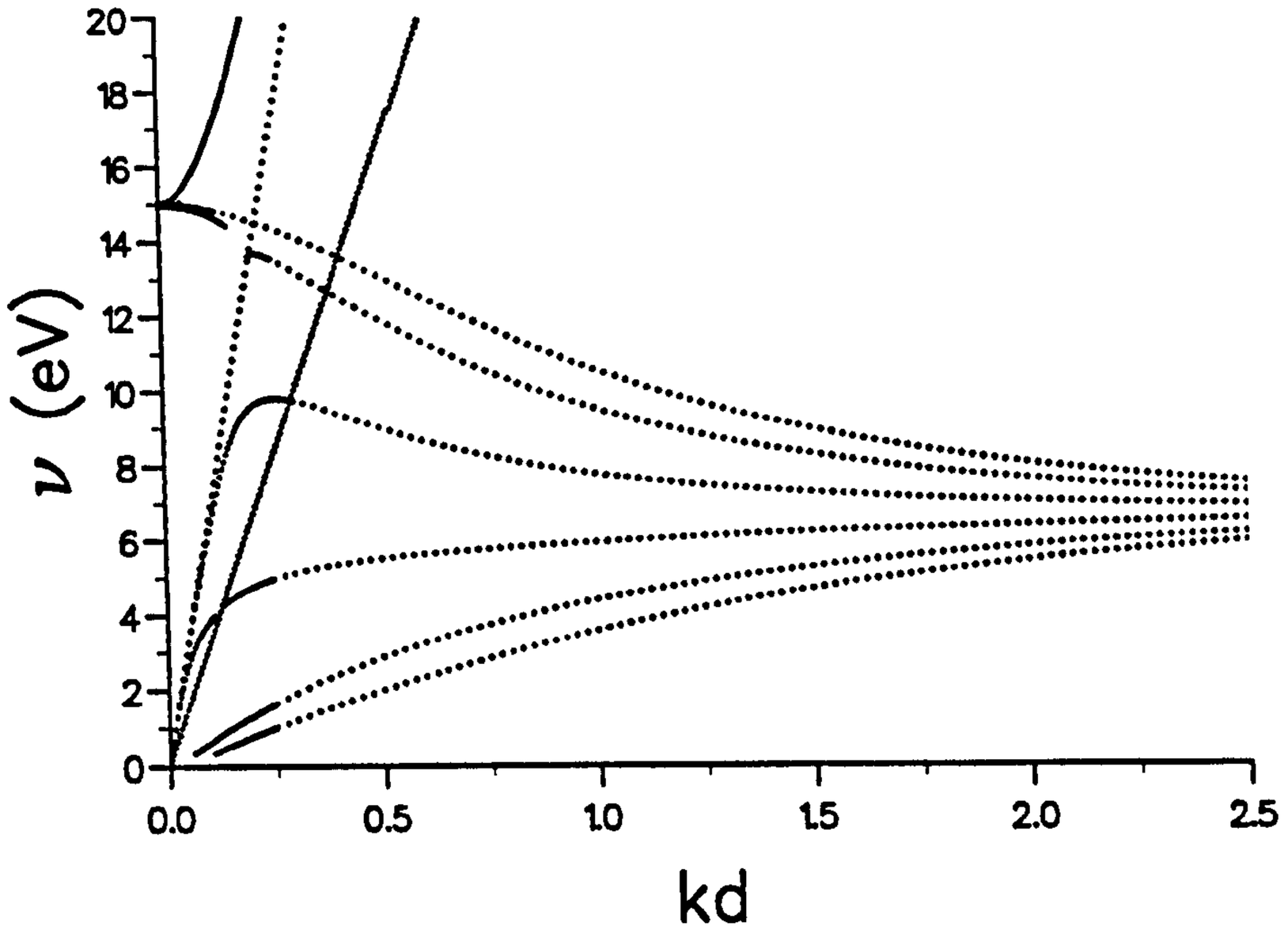

Figure 6.7 Dispersion relation of the surface and interfacial modes for seven layer systems. The thickness of Al and Al_2O_3 films is 30 Å.

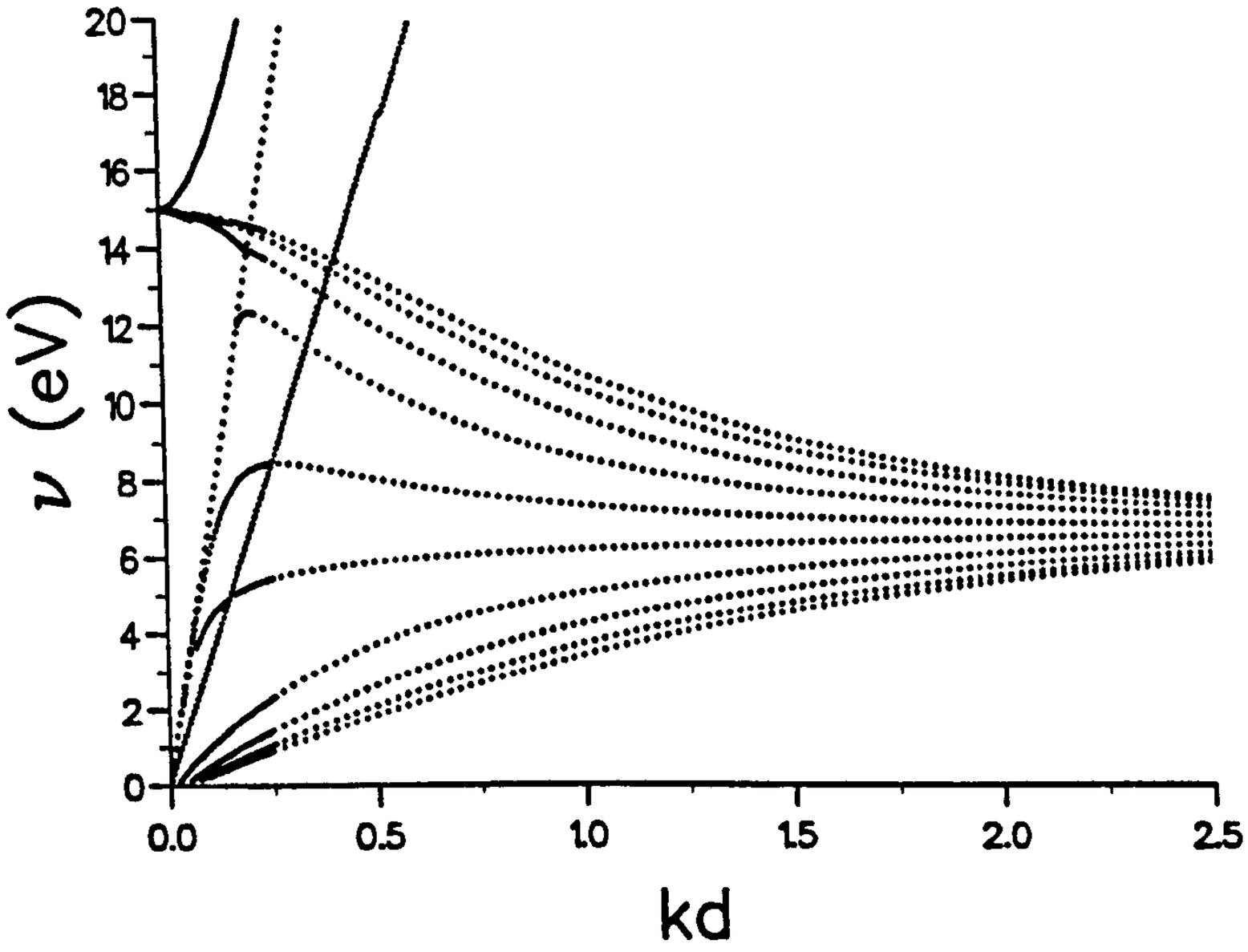

Figure 6.8 Dispersion relation of the surface and interfacial modes for eleven layer systems. The thickness of Al and Al_2O_3 films is 30 Å.

6.2. Loss spectra for normal incidence

The expressions for χ_{bulk} and χ_{bdy} derived in Chapter 3 provide a framework for interpreting energy-loss spectra for normal incidence in multilayered slabs. Equation 3.27 yields bulk peaks in the energy–loss spectrum when $\epsilon_i \simeq 0$ (bulk longitudinal plasmon in i^{th} layer) and when $p_i \simeq 0$ (Cherenkov radiation in i^{th} layer). However, the intensities of these peaks may be significantly modified by boundary effects, as Equation 3.30 shows that χ_{bdy} also has peaks at $\epsilon_i \simeq 0$ and $p_i \simeq 0$. It is natural to distinguish contributions to χ_{bdy} with $k < \omega/c$ (radiation modes) from those with $k > \omega/c$ (non-radiative modes). An interesting feature of Equation 3.30 is that there will be additional peaks corresponding to transverse bulk modes.

Equation 3.30 predicts a scattering probability that is proportional to products of differences of dielectric functions. The contribution of surface, interfacial and transverse modes will therefore be small if the materials involved have similar dielectric properties, as is the case for many common semiconductors. Extensive numerical calculations confirm this fact. The best chance of observing these modes arises if the materials have very different dielectric functions at frequencies for which $[C_{n0}]$ is close to zero (for typical values of k). This condition can often be met for metal-insulator and semiconductor-insulator interfaces.

6.2.1. Al/Mg structures

Al and Mg are good examples of materials that can be described by the Drude dielectric function, and they have been extensively studied in the literatures (cf. references [21, 25]). As the interfacial plasmon of Al/Mg is at around 12.7 eV, which is reasonably far away from the bulk and surface plasmons, there is good chance of seeing this interfacial plasmon in electron energy loss spectroscopy.

Figure 6.9 shows the calculated scattering probability of a Al/Mg double slab, with both layers of thickness $d = 100$ Å. The dielectric functions of Al and Mg are described by Equation 6.2. There are four peaks located around 7.1 eV, 10 eV, 12.4 eV and 15.0 eV which correspond to the surface and bulk plasmons of Mg, the interfacial plasmon, and the bulk plasmon of Al. The shoulder of the Mg bulk peak is due to the surface plasmon of Al. This interpretation is assisted by Figure 6.10, which shows how $2\pi k \mathrm{d}^2 P/\mathrm{d}(\hbar\omega)\mathrm{d}k$ varies as a function of k and $\hbar\omega$. The four main ridges on this diagram correspond to the dispersion relations for bulk, surface and interface modes. In our model, the bulk mode shows no dispersion. The surface and interfacial mode exhibits dispersion for $kd < 1$ but, because the scattering is dominated by the high k region, the surface and interfacial peaks in $I(\hbar\omega)$ remain narrow.

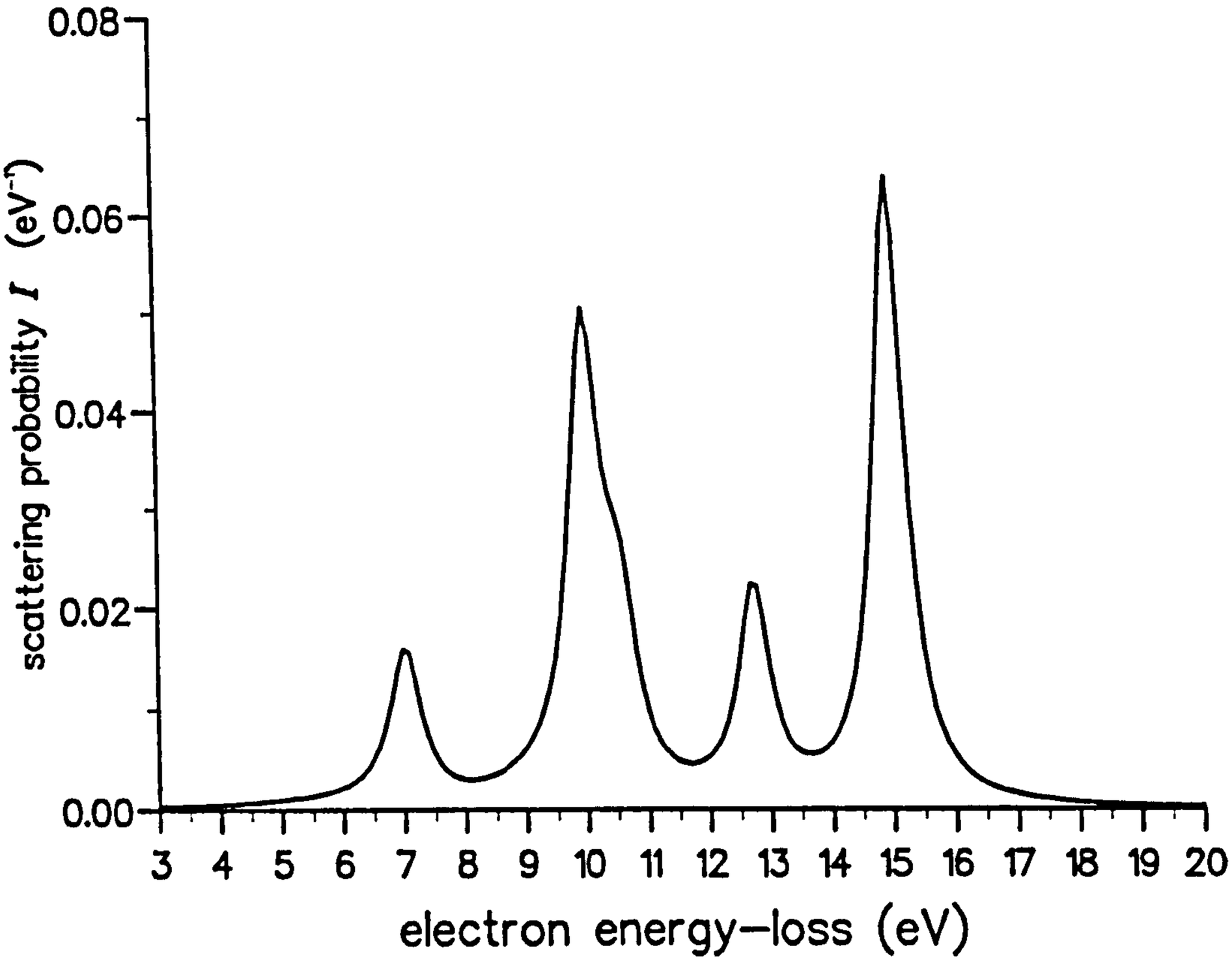

Figure 6.9 The scattering probability per unit energy range $I(\hbar\omega)$ for normal incidence on a Al/Mg double layer. The thickness of each layer is $d = 100$ Å. The bulk and surface plasmons of Mg are 10 eV and 7.1 eV. The bulk and surface plasmons of Mg are 15 eV and 10.2 eV. The interfacial plasmon peak is located at 12.7 eV.

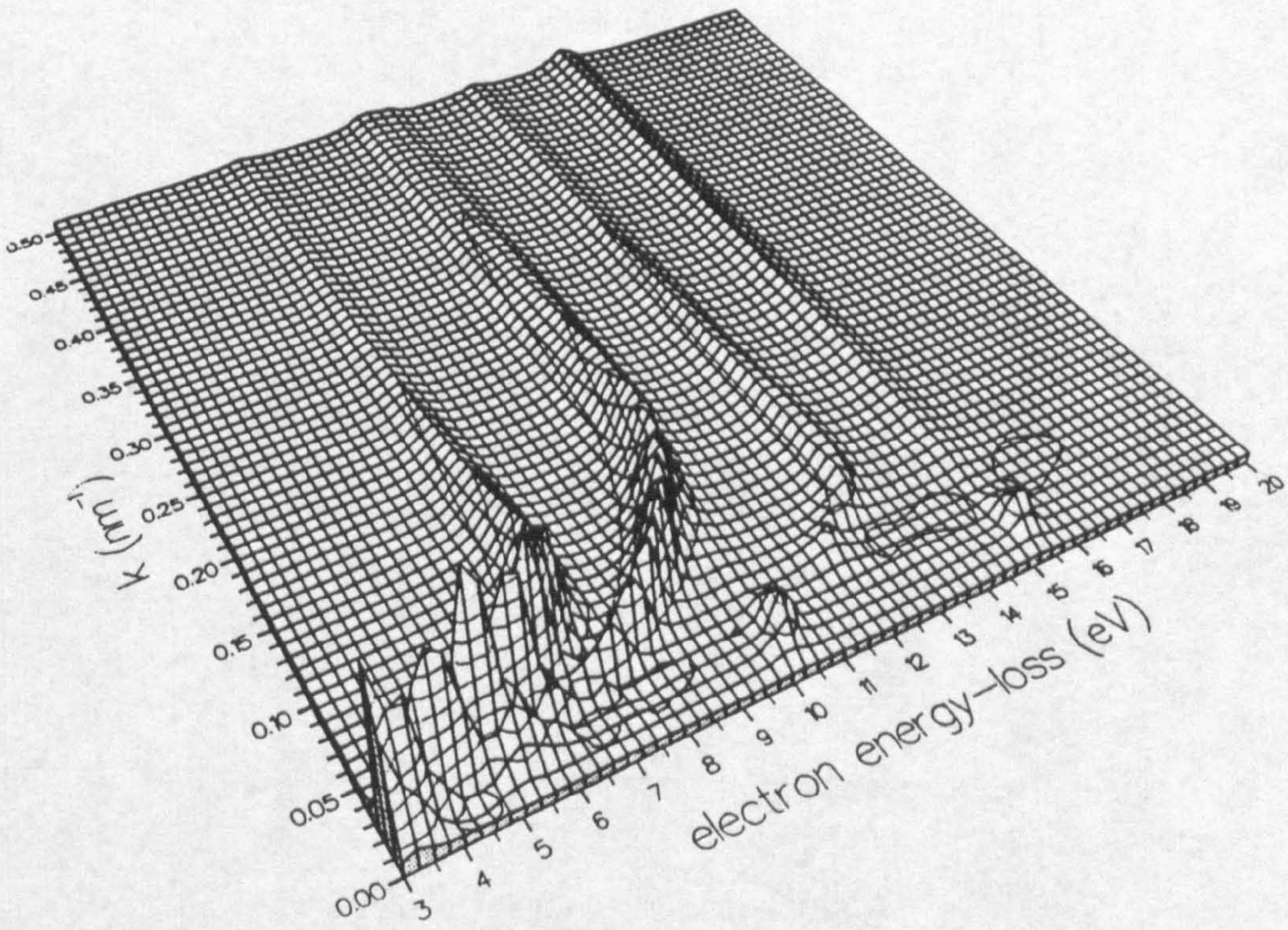

Figure 6.10 A three-dimensional plot of $2\pi k \mathrm{d}^2P/\mathrm{d}(\hbar\omega)\mathrm{d}k$ against k and $\hbar\omega$ for normal incidence on the Al/Mg double layer system of Figure 6.9. The four main ridges correspond to Mg surface, Mg bulk and Al surface, interfacial and Al bulk plasmons. The surface and the interfacial plasmons are broadened towards lower frequencies as a result of scattering at low k.

A slightly more complicated case arises when both sides of an aluminium slab are covered with layers of Mg. This geometry ensures that there is no surface of Al, but there are two surfaces of Mg. Figures 6.11 shows the calculated scattering probability $I(\hbar\omega)$ in this geometry. The four peaks, from left to right, correspond to surface Mg, bulk Mg, interfacial and bulk Al plasmons. Comparing with Figure 6.9, the shoulder at the Mg bulk peak does not exist in this structure.

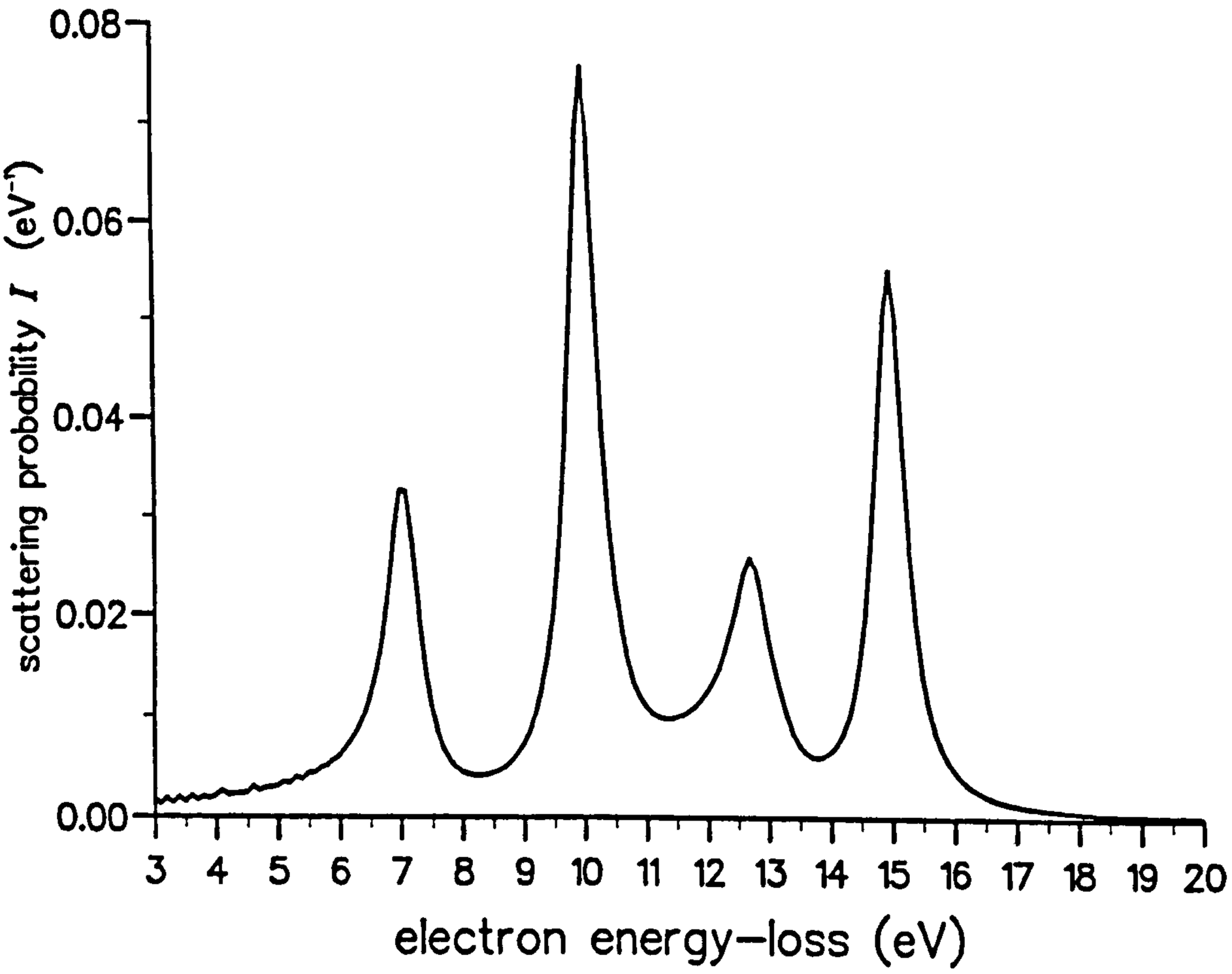

Figure 6.11 The scattering probability per unit energy range $I(\hbar\omega)$ for normal incidence on a Al/Mg three layer system. The thickness of each layer is $d = 100$ Å. The bulk and surface plasmons of Mg are at 10 eV and 7.1 eV. The bulk and surface plasmons of Mg are at 15 eV and 10.2 eV. The interfacial plasmon peak is located at 12.7 eV.

A three dimensional plot of $2\pi k \mathrm{d}^2 P/\mathrm{d}(\hbar\omega)\mathrm{d}k$ as a function of k and $\hbar\omega$ for a slab of aluminium covered on both sides with layers of Mg is plotted in Figure 6.12. The four main ridges correspond to the peaks in Figure 6.11. This figure shows the dispersion of the surface and interfacial plasmons. In comparison with Figure 6.10, the interfacial mode is split at small k because of the coupling between modes at the two Al/Mg interfaces. The surface mode of Mg is not split significantly because of the large distance between the two surfaces of Mg.

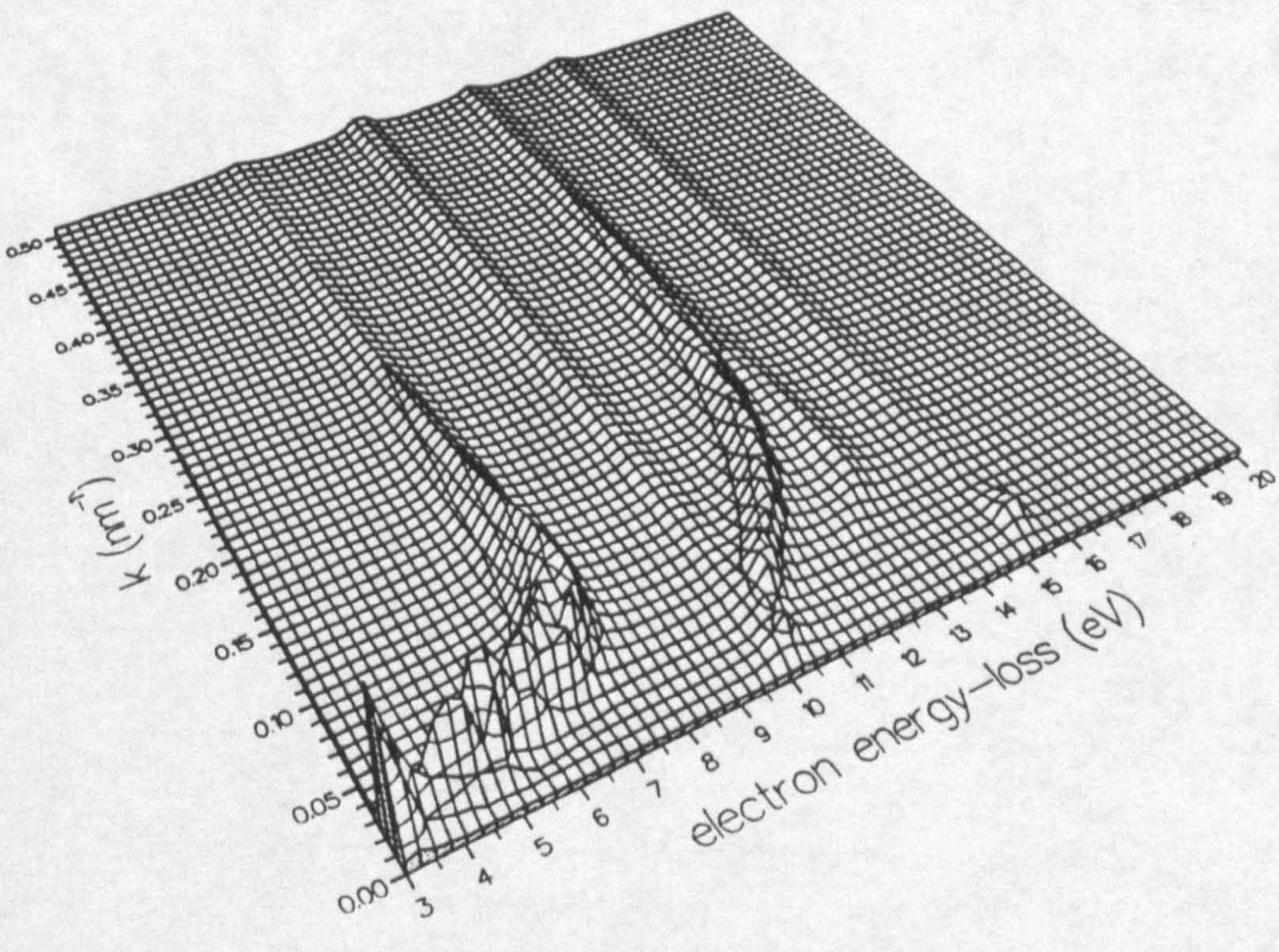

Figure 6.12 A three-dimensional plot of $2\pi k \mathrm{d}^2 P/\mathrm{d}(\hbar\omega)\mathrm{d}k$ against k and $\hbar\omega$ for normal incidence on the Mg/Al/Mg three layer system of Figure 6.11. The four main ridges correspond to Mg surface, Mg bulk, interfacial and Al bulk plasmons. The surface and (more importantly) the interfacial plasmons are broadened towards lower frequencies as a result of scattering at low k.

6.2.2. Al/Al_2O_3 structures

The next example is that of a Al/Al_2O_3 double slab, with both layers of thickness $d = 100$ Å. The calculated scattering probability per unit energy range is shown in Figure 6.13. There are two sharp peaks located around 15 eV and 10.7 eV and a much broader peak which reaches its maximum value at 6.5 eV, but which spreads to lower energies. These peaks correspond to bulk Al, surface Al and Al/Al_2O_3 interfacial plasmons. There are no bulk or surface losses due to Al_2O_3, because the dielectric function of this material has been taken to be real. Also, in terms of Equation 3.30, the factors of p_i^2 and $[C_{n0}]$ in the denominator of χ_{bdy} can both be small at low k and low ω, giving rise to significant scattering from relatively small regions of k-ω space.

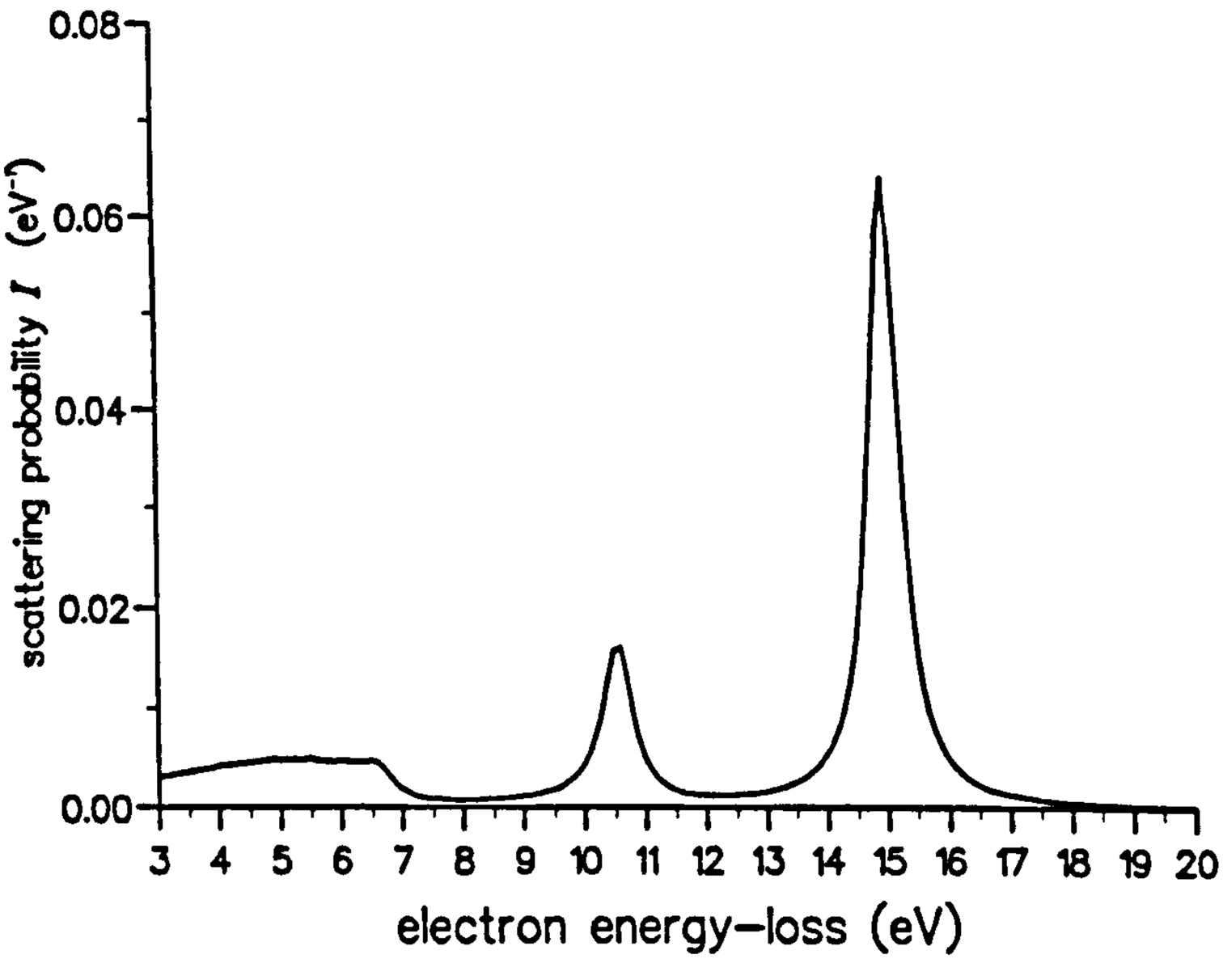

Figure 6.13 The scattering probability per unit energy range $I(\hbar\omega)$ for normal incidence on a Al/Al_2O_3 double layer. The thickness of each layer is $d = 100$ Å. The bulk Al, surface Al and Al/Al_2O_3 interface peaks are at 15 eV, 10.7 eV and at 6.5 eV and below.

Corresponding to Figure 6.13, a three dimensional plot of $2\pi k \mathrm{d}^2 P/\mathrm{d}(\hbar\omega)\mathrm{d}k$ varying as a function of k and $\hbar\omega$ is shown in Figure 6.14. The three main ridges on this diagram correspond to the dispersion relations for bulk, surface and interface modes. The two small peaks at about 17.5 eV and 19 eV show the transverse bulk mode of Al_2O_3. In our model, the bulk modes of Al and Al_2O_3 show no dispersion. The surface mode exhibits dispersion for $kd < 1$. The interface mode is broad because the high k region no longer dominates.

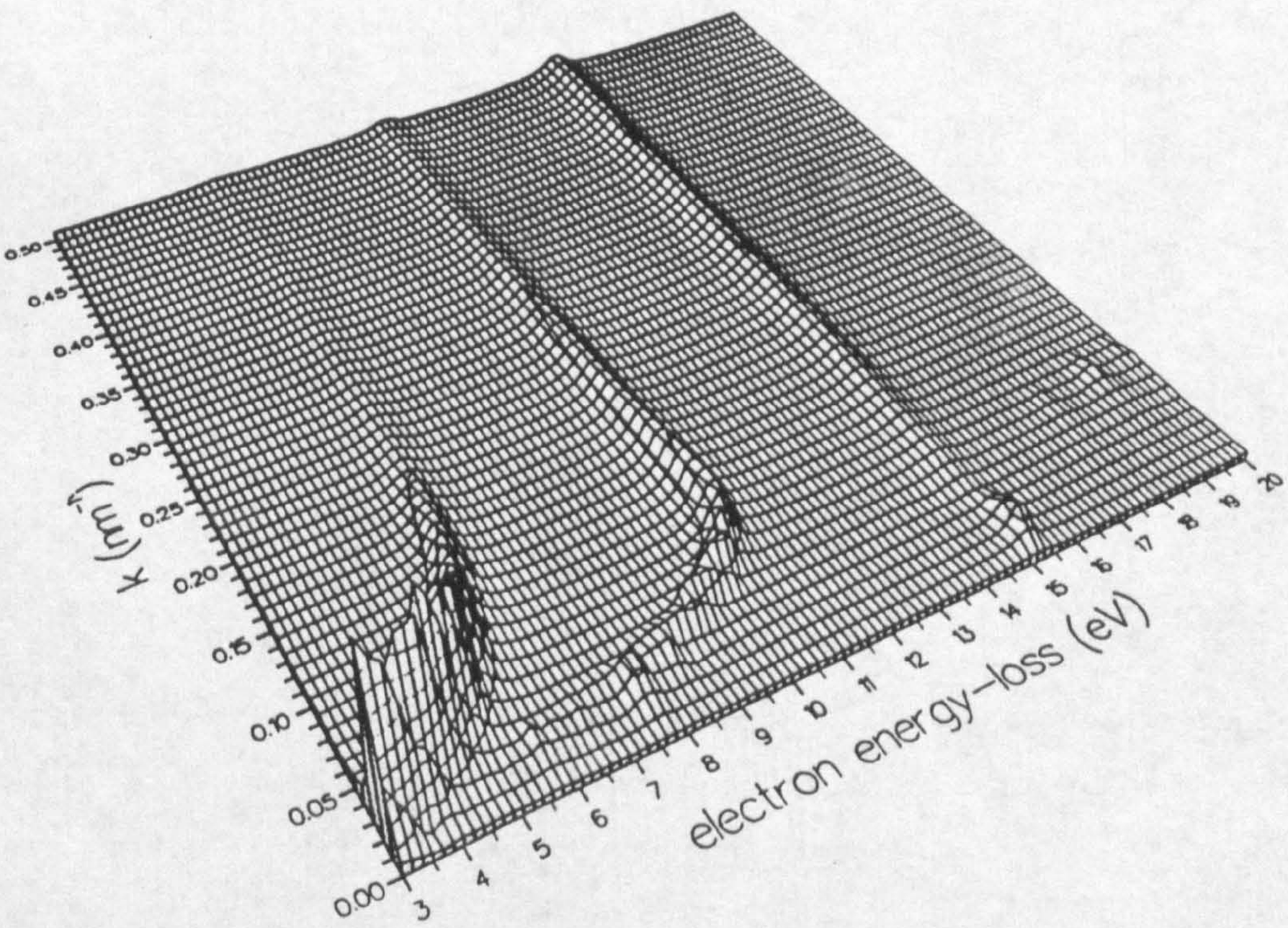

Figure 6.14 A three-dimensional plot of $2\pi k \mathrm{d}^2 P/\mathrm{d}(\hbar\omega)\mathrm{d}k$ against k and $\hbar\omega$ for normal incidence on the Al/Al_2O_3 double layer system of Figure 6.13. The three main ridges correspond to Al bulk, Al surface and interfacial plasmons. The surface and the interfacial plasmons are broadened towards lower frequencies as a result of dispersion low k.

A slightly more complicated case arises when both sides of an aluminium slab are tarnished with oxide. Figures 6.15 and 6.16 show $I(\hbar\omega)$ and $2\pi k \mathrm{d}^2 P/\mathrm{d}(\hbar\omega)\mathrm{d}k$ for a layer of aluminium covered on both sides with layers of Al_2O_3. This geometry ensures that there is no surface Al peak, but the peak due to interfacial plasmons now has a richer structure between 6 eV and 8 eV, because of the coupling between modes at the two metal-oxide interfaces.

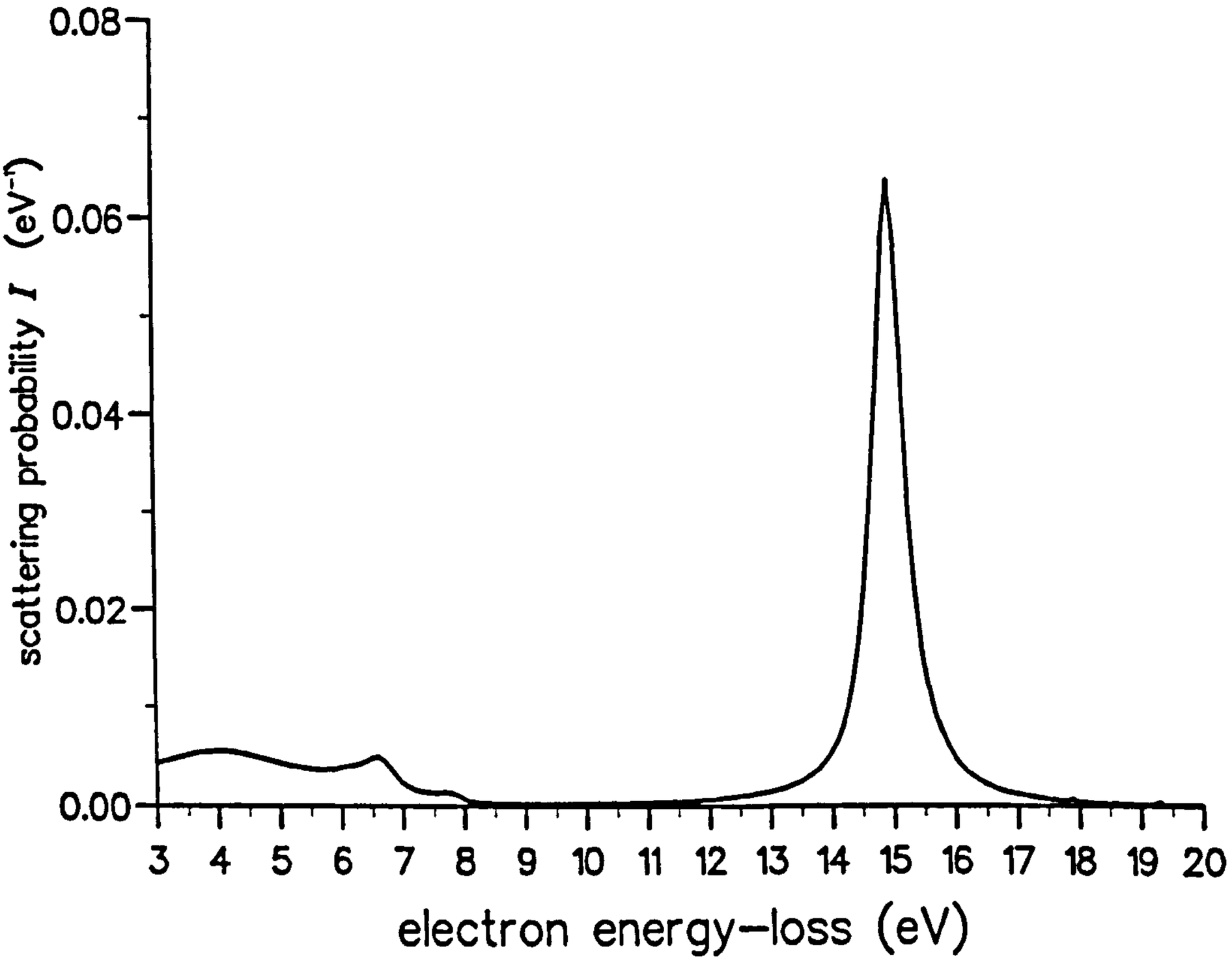

Figure 6.15 The scattering probability per unit energy range for normal incidence on a symmetric three-layer system $Al_2O_3/Al/Al_2O_3$. The thickness of each layer is taken to be 100 Å. The bulk Al peak is at 15 eV and the Al/Al_2O_3 interface modes are around 7 eV.

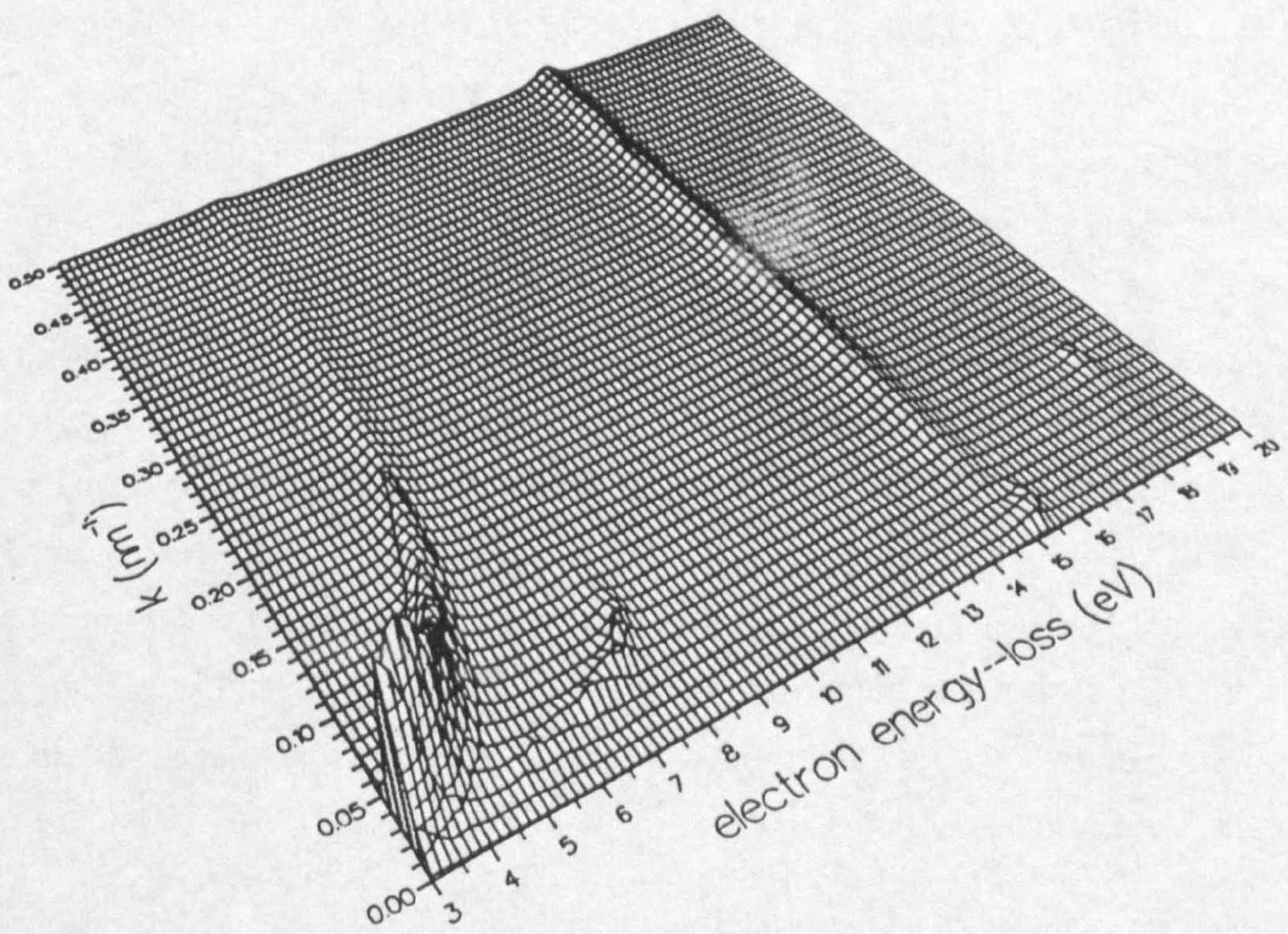

Figure 6.16 A three-dimensional plot of $2\pi k \mathrm{d}^2P/\mathrm{d}(\hbar\omega)\mathrm{d}k$ against k and $\hbar\omega$ for normal incidence on the $Al_2O_3/Al/Al_2O_3$ system of Figure 6.15. The three main ridges correspond to Al bulk plasmons, antisymmetric interfacial plasmons and symmetric interfacial plasmons.

6.2.3. $Al/SiO_2/Si$ structure

Finally, we study a three–layered $Al/SiO_2/Si$ (MOS) structure. $Al/SiO_2/Si$ heterostructures are typical of actual electronic devices, and can be studied with high spatial resolution scanning transmission electron microscopy. The dielectric functions of Si and SiO_2 taken from the *Handbook of Optical Constants* [83], and Al is represented by the model dielectric function as described above.

The scattering intensity $I(\hbar\omega)$ produced by this structure is shown in Figure 6.17 and the corresponding plot of $2\pi k \mathrm{d}^2P/\mathrm{d}(\hbar\omega)\mathrm{d}k$ given in Figure 6.18. The main features of this energy–loss spectrum are associated with Al and its surfaces and interfaces; bulk SiO_2 only contributes to the background, and the bulk and surface Si plasmons are obscured by the larger peaks due to Al. Bulk Al and surface Al peaks can be identified around 15.0 eV and 10.7 eV, as before. Above 15 eV, there is evidence for a transverse bulk mode in Al, given by $q_{Al} \simeq 0$. Equation 3.30 suggests that this mode is enhanced by the presence of bulk SiO_2 modes, which exist above 15 eV; this would explain why the transverse bulk modes in $Al/SiO_2/Si$ are much stronger than those in Al/Al_2O_3 or $Al_2O_3/Al/Al_2O_3$. Finally, note that the interfacial peak around 8 eV shows structure which can again be interpreted in terms of the splitting of two modes, although these will no longer be exactly symmetric or antisymmetric.

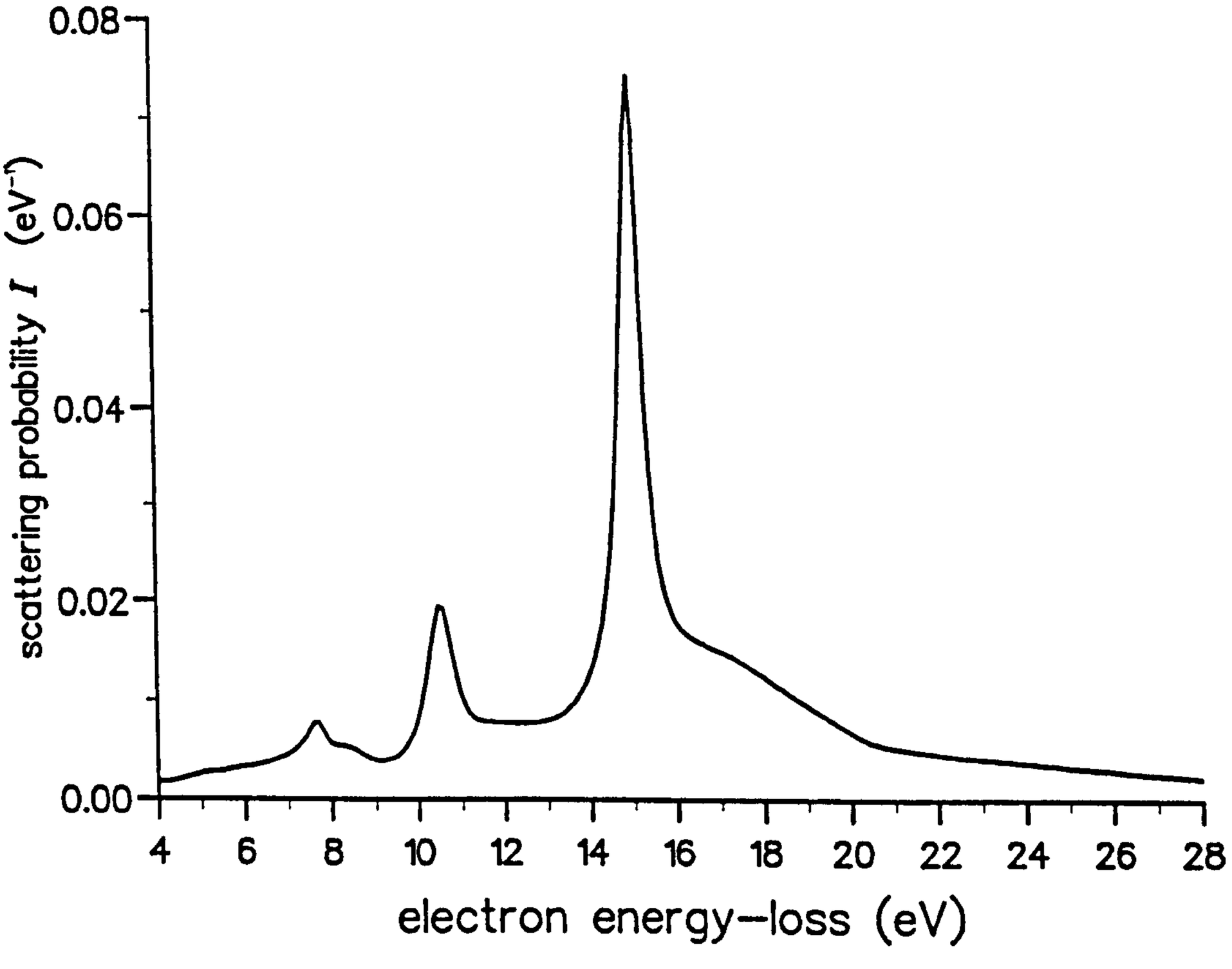

Figure 6.17 The scattering probability per unit energy range for normal incidence on a three–layer system Al/SiO_2/Si. All layers have thickness 100 Å. Bulk and surface Al peaks are at 15 eV and 10.7 eV. The transverse bulk mode in Al occurs above 15 eV (probably enhanced by Si and SiO_2 bulk plasmons) and Al/SiO_2 interface modes appear near 8 eV.

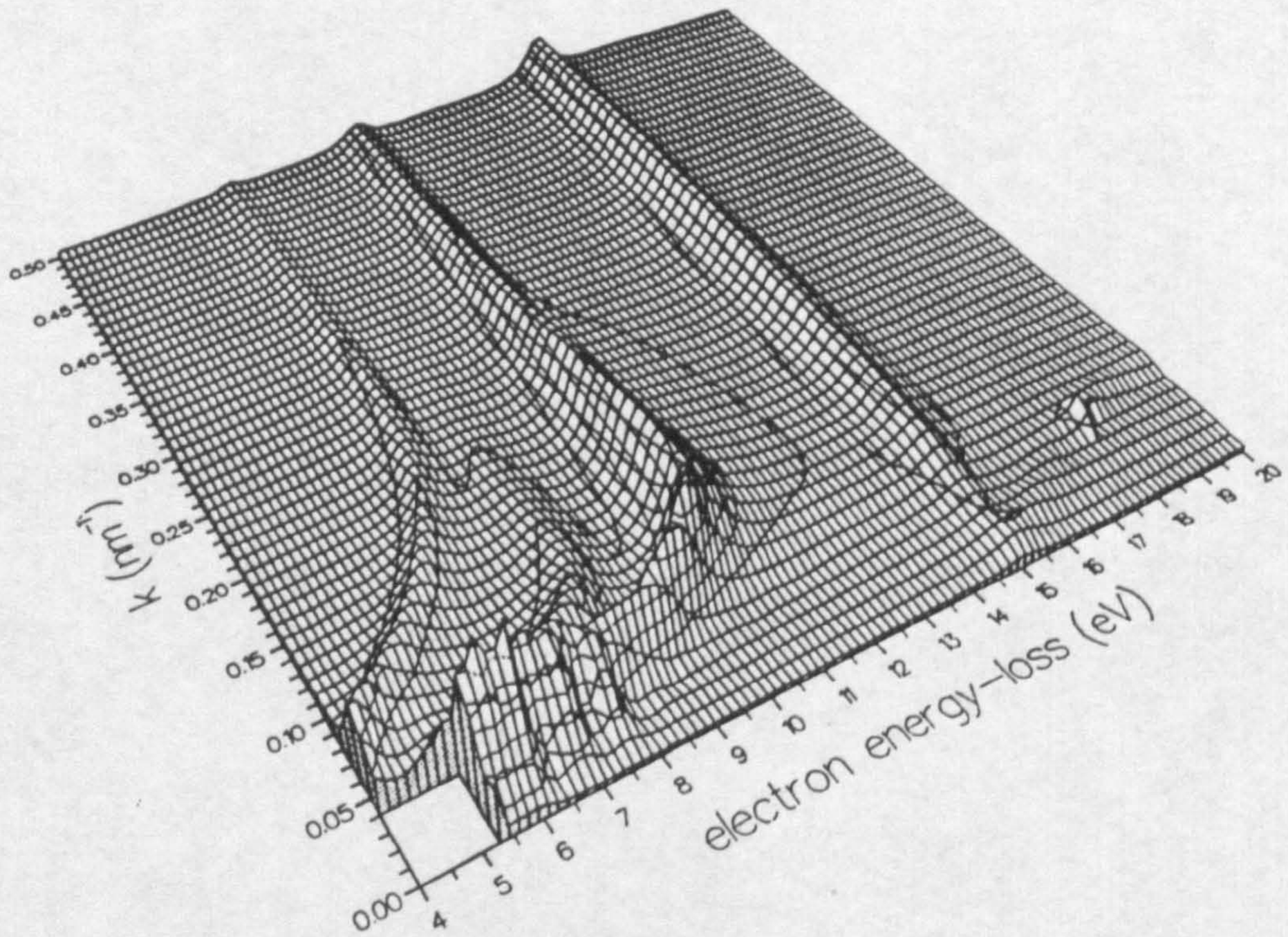

Figure 6.18 A three-dimensional plot of $2\pi k \mathrm{d}^2P/\mathrm{d}(\hbar\omega)\mathrm{d}k$ against k and $\hbar\omega$ for normal incidence on the $Al/SiO_2/Si$ system of Figure 6.17. From high to low energy, the main ridges correspond to the Al transverse bulk mode, the Al longitudinal bulk mode, the Al surface mode and two branches of interfacial plasmons. A narrow peak at low k and $\hbar\omega$ has been removed to reveal the detailed shape of these modes; the removed peak makes no significant contribution to $I(\hbar\omega)$.

6.3. Loss spectra for parallel incidence

This section uses the formulae developed in Chapter 4 to calculate energy loss spectra in a selection of model and real systems. It will concentrate on two main issues: the effect of changing the number of layers and the effect of changing the position of the beam. As in the case of normal incidence, I consider incident electrons of energy 100 keV and introduce a wavevector cut-off $k_c = 15\ \mathrm{nm}^{-1}$ in all integrals over k_y.

6.3.1. Mg/Al structures

A simple situation is that of a double slab. Figure 6.19 shows plots of energy loss probability per unit path length per unit energy range, $\mathrm{d}I(\hbar\omega)/\mathrm{d}x$, against energy and beam position for the two layer Al/Mg slab. The thickness of the Al and Mg layers is 30 Å. The beam position is moved from surface of Mg (−3 nm) , cross the interface (0 nm) and to the surface of Al (3 nm). We can unambiguously identify bulk, surface and interfacial plasmons from the positions of the peaks in energy/beam-position space.

Another interesting problem is how the spectrum changes when the number of layers is increased. Figure 6.20 shows the calculated scattering probabilities for three, seven, eleven, and fifteen layer Al/Mg systems. In Figure 6.20a, Al is in the centre of the slab and Mg is on the surface. In Figure 6.20b, Mg is in the centre of the slab and Al is on the surface. The thickness of each layer is 30 Å. The interfacial plasmon often occurs at a similar energy to bulk or surface plasmons and is not clearly resolved; nevertheless, its effects can be seen as a shift in the peaks of the energy loss spectrum. The middle peak in Figure 6.20a is due to a mixture of the bulk plasmon of Mg and the interfacial plasmon. The high energy peak in Figure 6.20b is due to a mixture of the bulk plasmon of Al and the interfacial plasmon. In both cases, the energy of the peak becomes closer to that of the interfacial plasmon as the number of layers increases, and approaches a limiting value (corresponding

to an infinite superlattice).

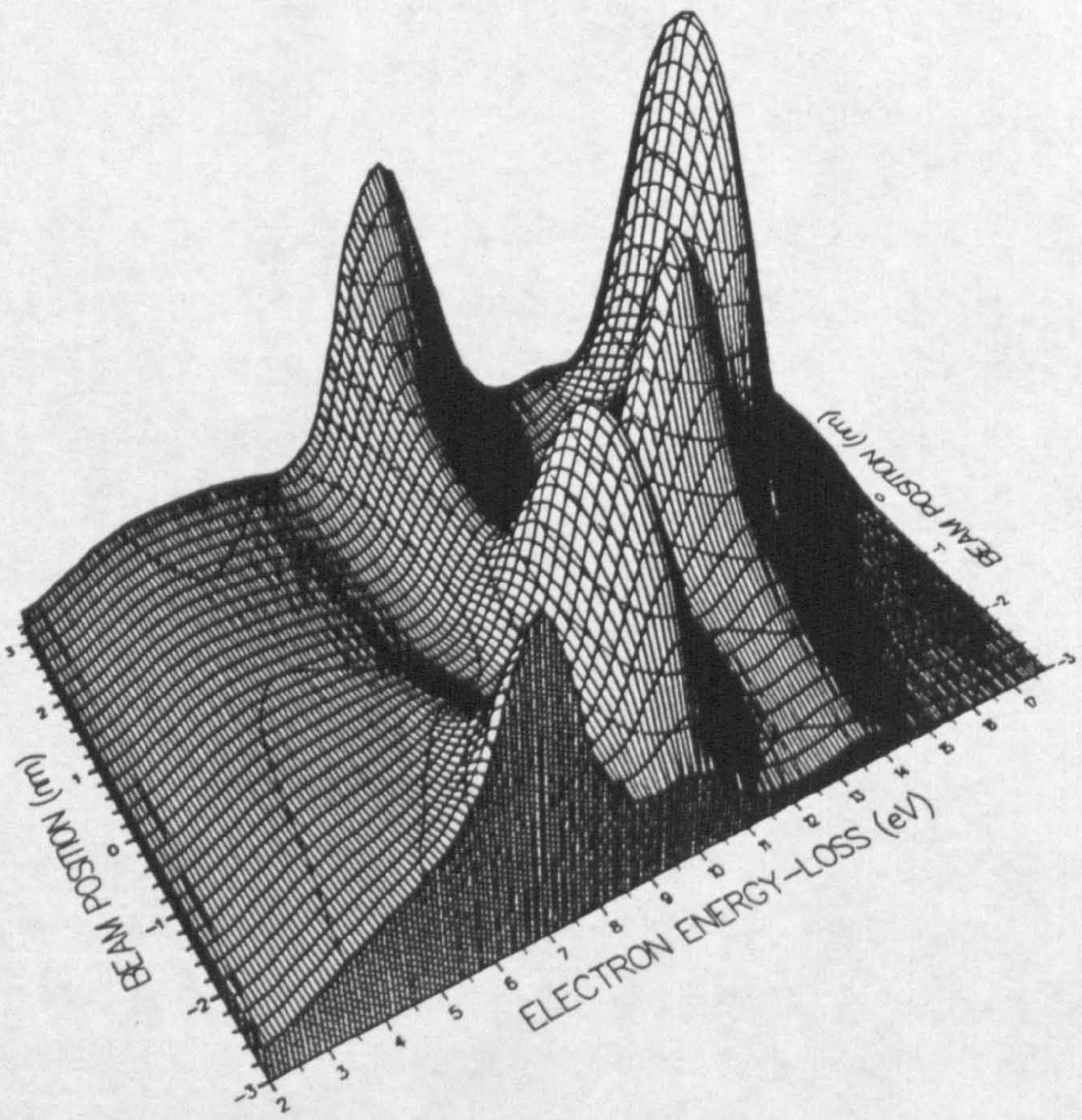

Figure 6.19 Three–dimensional plots of energy loss probability per unit path length per unit energy range, $\mathrm{d}I(\hbar\omega)/\mathrm{d}x$, against the energy and beam position for a Mg/Al double slab. Mg extends from –3 nm to 0 nm and Al from 0 nm to 3 nm.

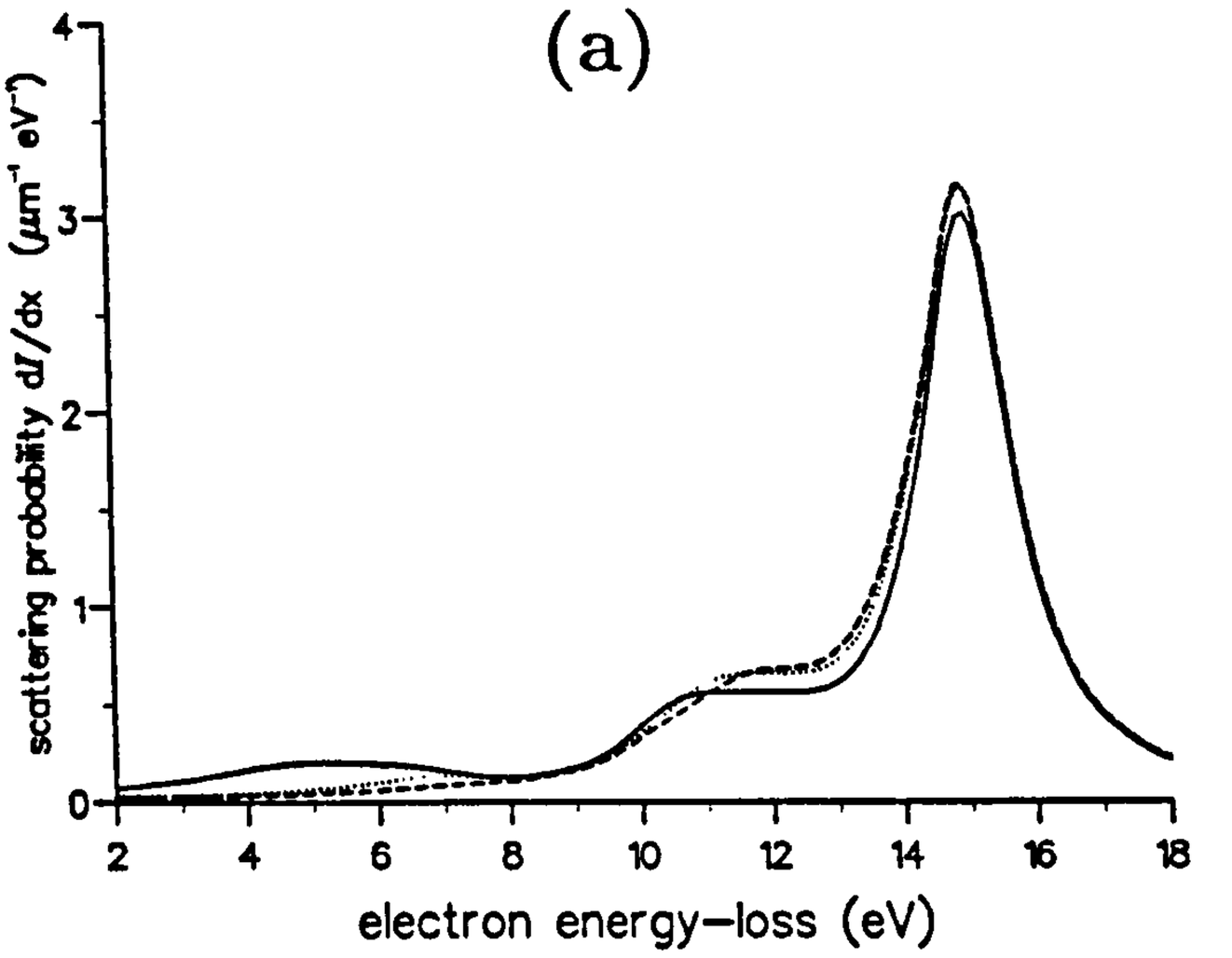

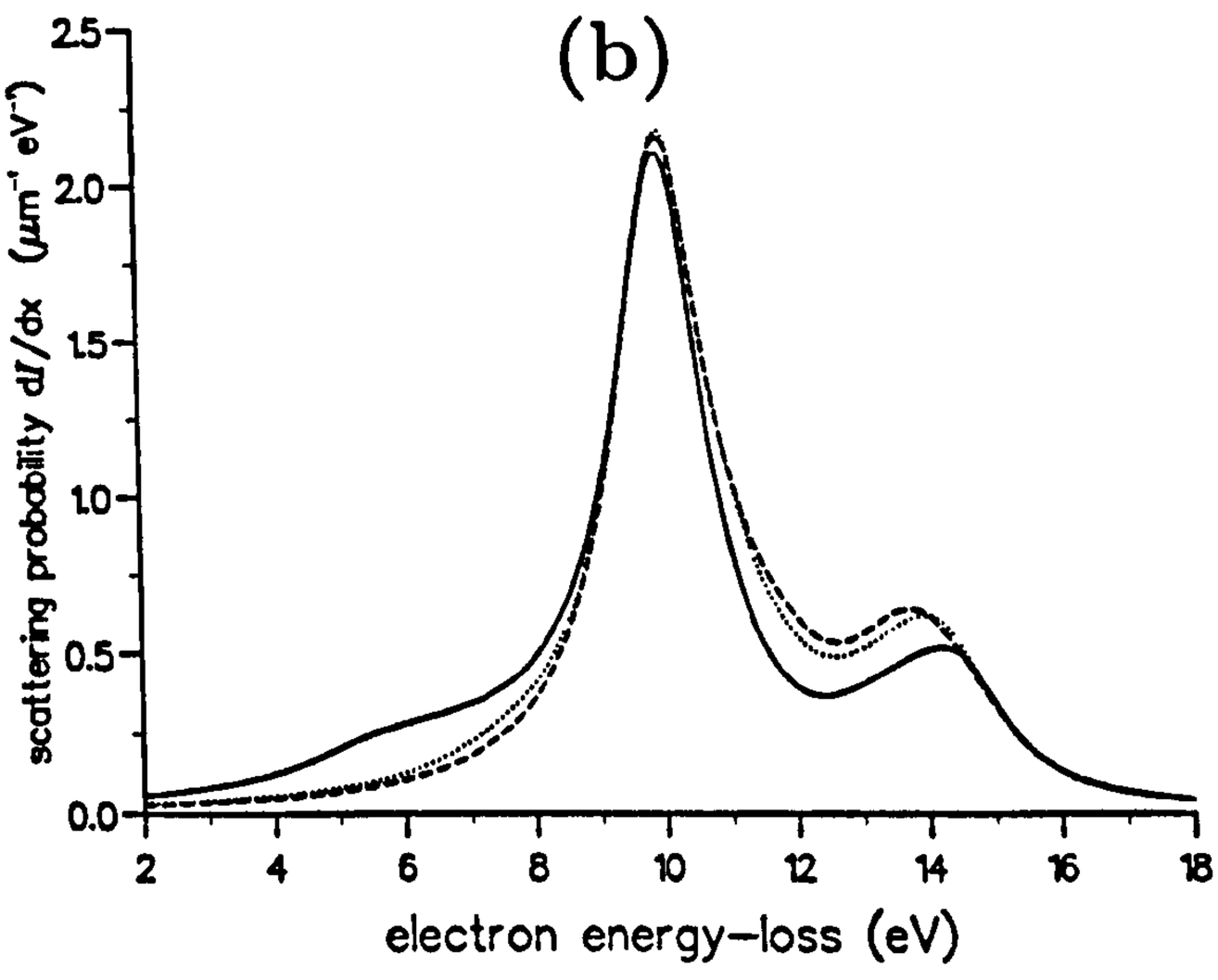

Figure 6.20 Energy loss probability for parallel incidence in the center of slabs composed of three layers (solid line), seven layers (dotted line), and eleven layers(dashed line). In Figure 6.20a Al is in the centre of the slab and Mg is on the surface. In Figure 6.20b Mg is in the centre of the slab and Al is on the surface.

6.3.2. Al_2O_3/Al structures

In the previous subsection, we calculated the energy loss spectra for an electron travelling normal to the interfaces of two and three layer systems of Al_2O_3/Al. We found an interfacial plasmon peak at 6.5eV. Here we carry out a similar calculation for parallel incidence on Al_2O_3/Al layer systems with increasing numbers of layers.

We discuss symmetrical multilayered slabs of Al and Al_2O_3, containing various numbers of layers. In each case, the central layer is Al and the outer layers are Al_2O_3. The dielectric functions for these materials are represented by the same models as in Section 6.2. Figure 6.21 shows the scattering probability per unit path length per unit energy range for symmetrical Al/Al_2O_3 slabs of 3, 7 and 11 layers. Each layer is 3 nm thick and the beam is in the middle of the central Al layer. The main loss feature in all cases is, of course, the Al bulk plasmon at 15 eV.

Because of the choice of geometry and dielectric functions, there are no surface plasmons due to Al or Al_2O_3. Cherenkov radiation, which would be associated with $p_m = 0$, is also suppressed below 15 eV because the dielectric function of Al has a negative real part in this region. The remaining peaks are associated with interfacial plasmons. They fall into two main groups: peaks below 7 eV and peaks above 10 eV. Note that the upper peak is missing in the 3-layer case and the positions of the peaks shift as the number of layers increases.

Figure 6.22 provides more detail of the solutions by plotting $\mathrm{d}^3P/\mathrm{d}(\hbar\omega)\mathrm{d}k_y\mathrm{d}x$ against k_y and $\hbar\omega$ for the 3, 7 and 11-layer slabs of Figure 6.21. In each case, scattering by the Al plasmon produces a ridge at 15 eV. The remaining ridges are due to interface modes. In Section 6.1, the dispersion dispersion relation (Equation 4.16) for the systems shown in Figure 6.22 was solved (Figures

6.6, 6.7 and 6.8) and it is found that the interfacial ridges correspond closely to the dispersion curves for *symmetric* TM modes. The antisymmetric TM modes are not excited because the slab is symmetrical and the beam occupies an exactly central position. The solutions to the dispersion relation show that the 7- and 11-layer systems have symmetric TM modes at both 'low' energy (< 7 eV)) and 'high' energy (> 10 eV), but the 3-layer system has only one symmetric TM mode, which occurs in the low energy region (cf. [80]); this explains the missing peak in the 3-layer slab. The shift in the peaks reflects the increasing complexity of mode structure that arises from coupling between different interfaces.

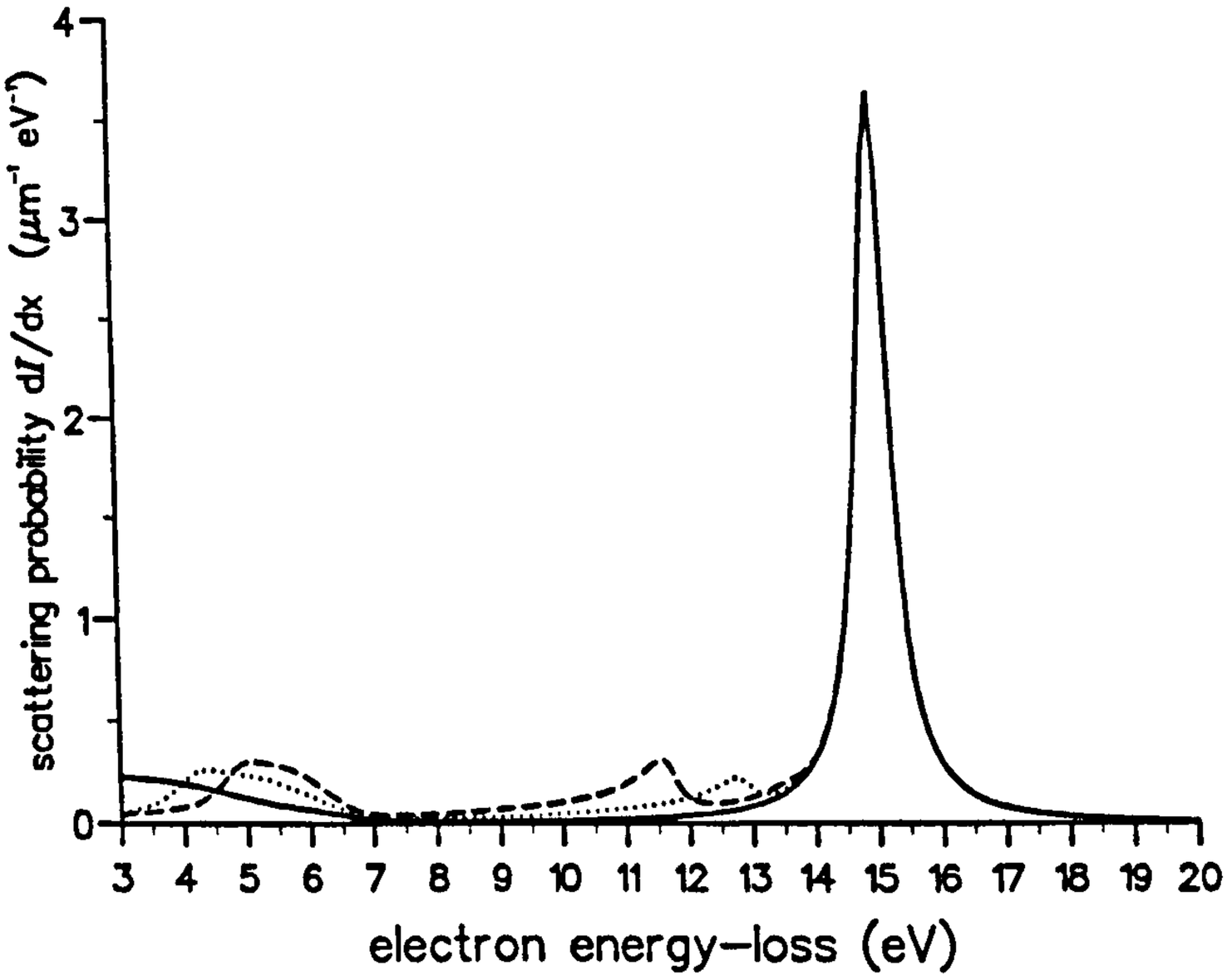

Figure 6.21 Scattering probability per unit path length per unit energy range, $\mathrm{d}I(\hbar\omega)/\mathrm{d}x$, for parallel incidence in the centre of Al/Al_2O_3 multilayers. The central layer is always Al, the outer layers Al_2O_3 and each layer is 3 nm thick. The scattering probability is shown for slabs composed of three layers (solid line), seven layers (dotted line), and eleven layers (dashed line).

Figure 6.22 shows no trace of a contribution due to TE modes. This can again be explained in terms of the dispersion relation for these modes. Although

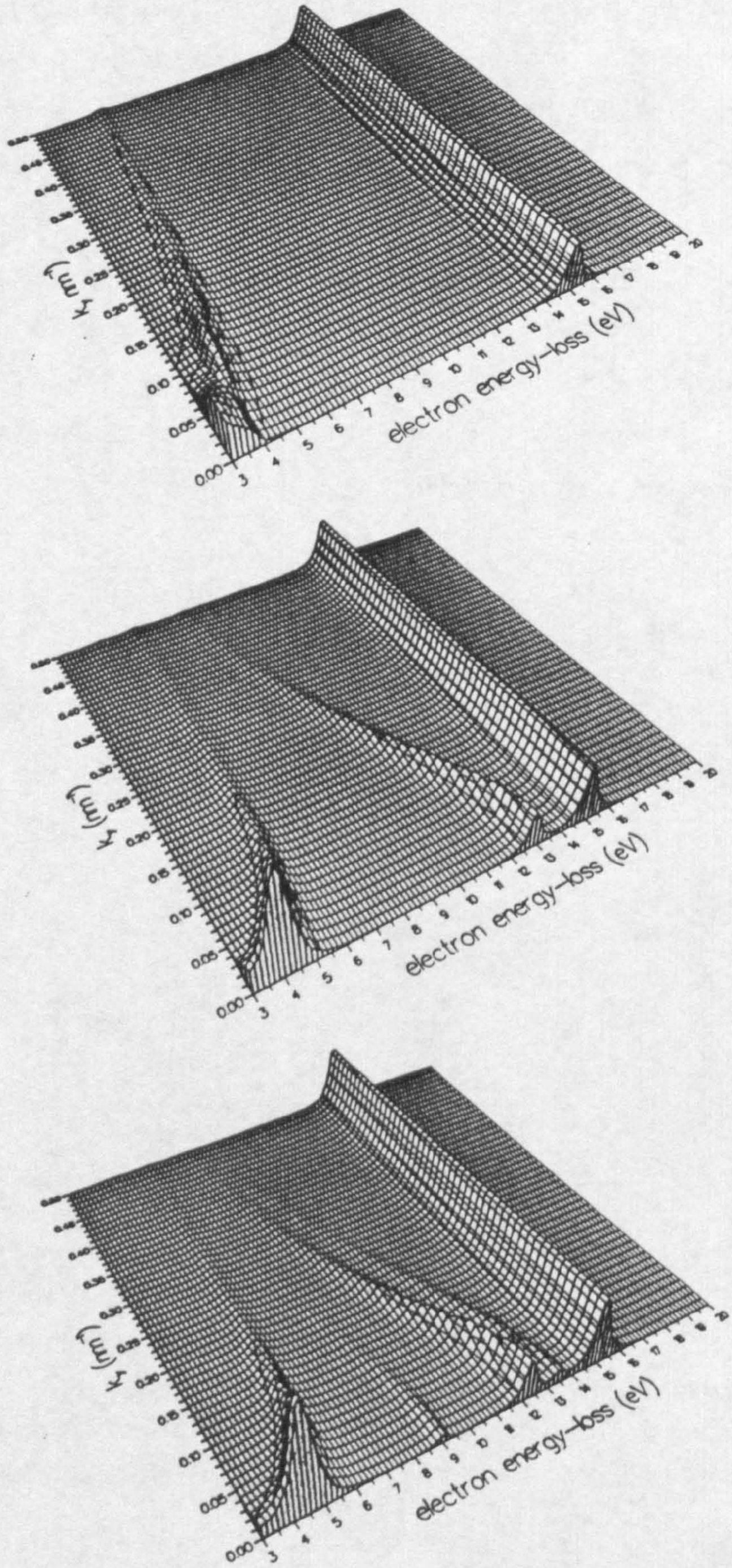

Figure 6.22 Three-dimensional plots of $\mathrm{d}^3P/\mathrm{d}(\hbar\omega)\mathrm{d}k_y\mathrm{d}x$ against k_y and $\hbar\omega$ for the Al/Al_2O_3 multilayers of Figure 6.21 with the beam in the centre of the slab. From top to bottom, the plots refer to 3-, 7- and 11-layer systems.

TE modes can be found as functions of k and $\hbar\omega$, no TE modes exist in the region $k > \omega/v$. As our energy-loss formula involves the substitution $k_x \to \omega/v$, there is no value of k_y that produces significant scattering by the TE modes.

Figure 6.23 shows the effect of moving the beam away from the central position in the case of the 7-layer Al/Al_2O_3 slab. This figure shows how $dI(\hbar\omega)/dx$ varies as the beam position is moved from the middle of the central Al layer to the first Al/Al_2O_3 interface. As might be expected, the structure in the interfacial modes becomes more evident as the beam approaches the interface, with both symmetric and antisymmetric TM modes being excited. However, the full structure only emerges when the beam (or part of it) is within a few Å of the interface!

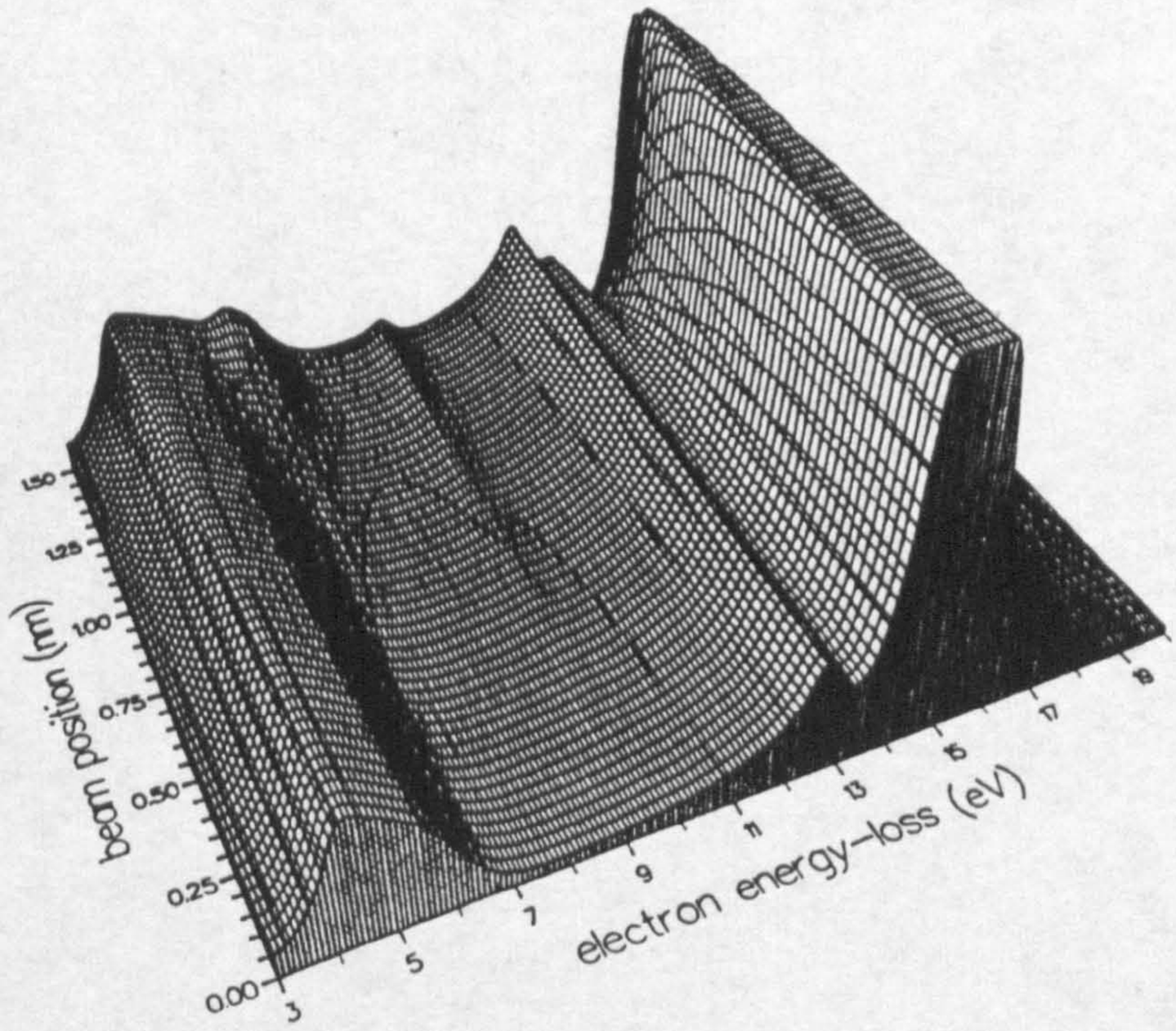

Figure 6.23 A three dimensional plot of scattering probability per unit path length per unit energy range, $(dI(\hbar\omega)/dx)$, against energy and beam position for the 7-layer Al/Al_2O_3 slab. The main Al peak has been truncated to reveal the other modes.

6.3.3. Al/SiO/Si structure

The next example revisits another system discussed in Section 6.2 in the context of normal incidence—a 3-layer MOS structure of Al/SiO_2/Si, modelled by the dielectric functions and data described above. Figure 6.24 displays $dI(\hbar\omega)/dx$ for this system as a function of beam position and energy loss. In this figure, the Si surface is at 0 nm, the Si/SiO_2 interface at 3 nm, the SiO_2/Al interface at 6 nm and the Al surface at 9 nm. The main features of this loss spectrum are clearly visible. The Si layer exhibits a bulk Si plasmon at 16.7 eV and a surface Si plasmon at 12.2 eV. An interfacial plasmon, at an energy of about 8.4 eV, is excited when the beam is close to the Si/SiO_2 boundary. The SiO_2 layer has only diffuse features, but a second interfacial plasmon at an energy of about 7.7 eV is excited when the beam is close to the SiO_2/Al boundary. The Al layer, of course, is dominated by the bulk Al plasmon at 15 eV and the surface Al plasmon at 10.7 eV. The SiO_2/Al interface exhibits structure above 15 eV agrees with our findings for normal incidence.

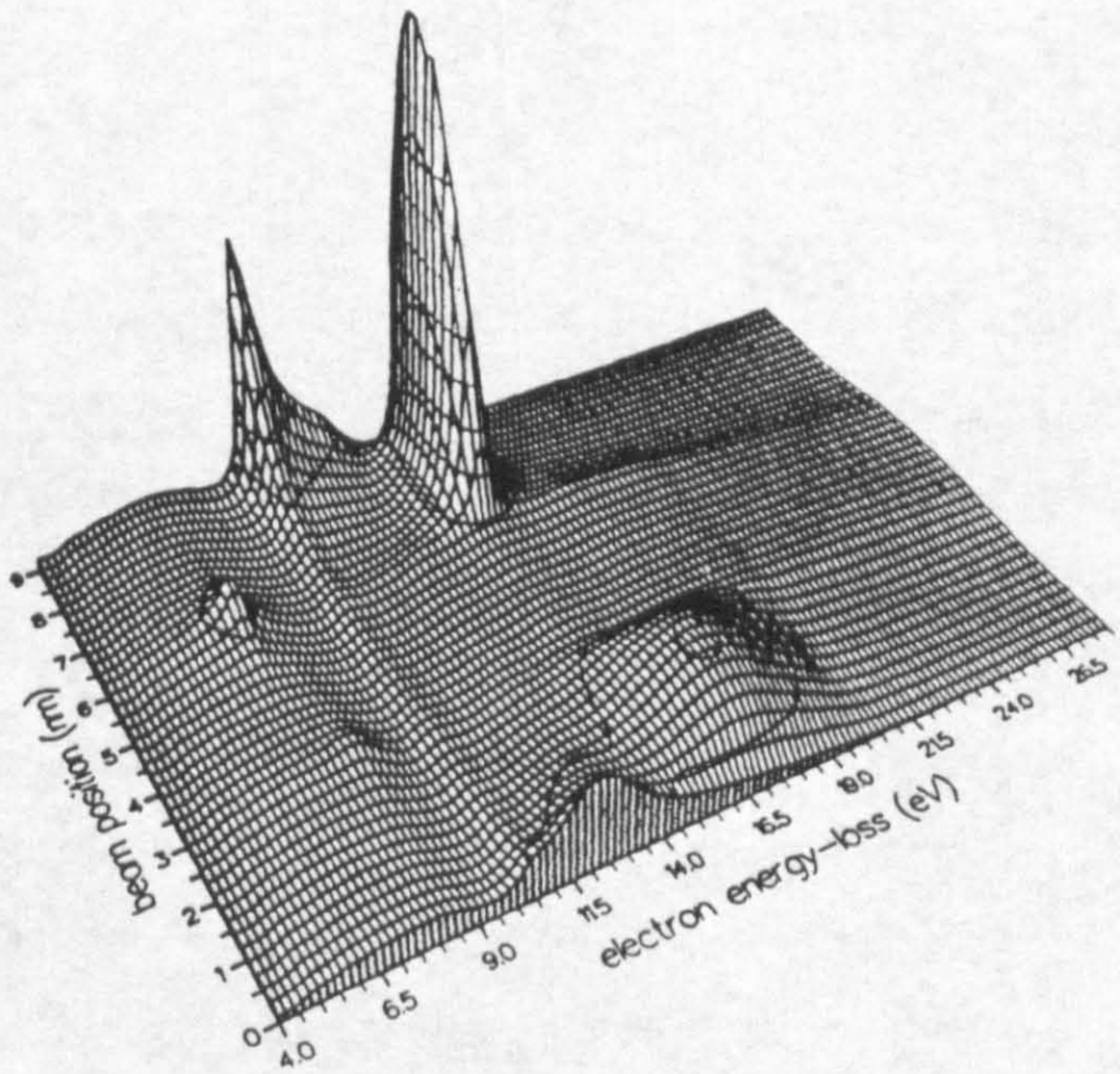

Figure 6.24 A three dimensional plot of scattering probability per unit path length per unit energy range, $(\mathrm{d}I(\hbar\omega)/\mathrm{d}x)$, against energy and beam position for a $Al/SiO_2/Si$ structure. Si extends from 0 nm to 3 nm, SiO_2 from 3 nm to 6 nm and Al from 6 nm to 9 nm.

6.3.4. InSb/GaP structure

Finally, we consider a semiconductor bilayer. As explained in Chapter 3, many semiconductors have dielectric functions that are broadly similar over the energy range of interest, making it difficult to observe interfacial plasmons at semiconductor/semiconductor boundaries. In Figure 6.25 we have deliberately chosen two semiconductors that are fairly dissimilar. The graph shows $\mathrm{d}I(\hbar\omega)/\mathrm{d}x$ as a function of beam position and energy loss for a two-layered slab of InSb (from 0 nm to 5 nm) and GaP (from 5 nm to 10 nm), with dielectric functions taken from reference [83]. The bulk plasmons for these two materials occur at 11.8 eV and 15.9 eV and surface plasmons are also visible. The main interest here, however, is the fact that an interfacial plasmon can be identified at about 13.4 eV, consistent with our feeling that parallel incidence gives the best chance of observing interfacial modes in difficult cases.

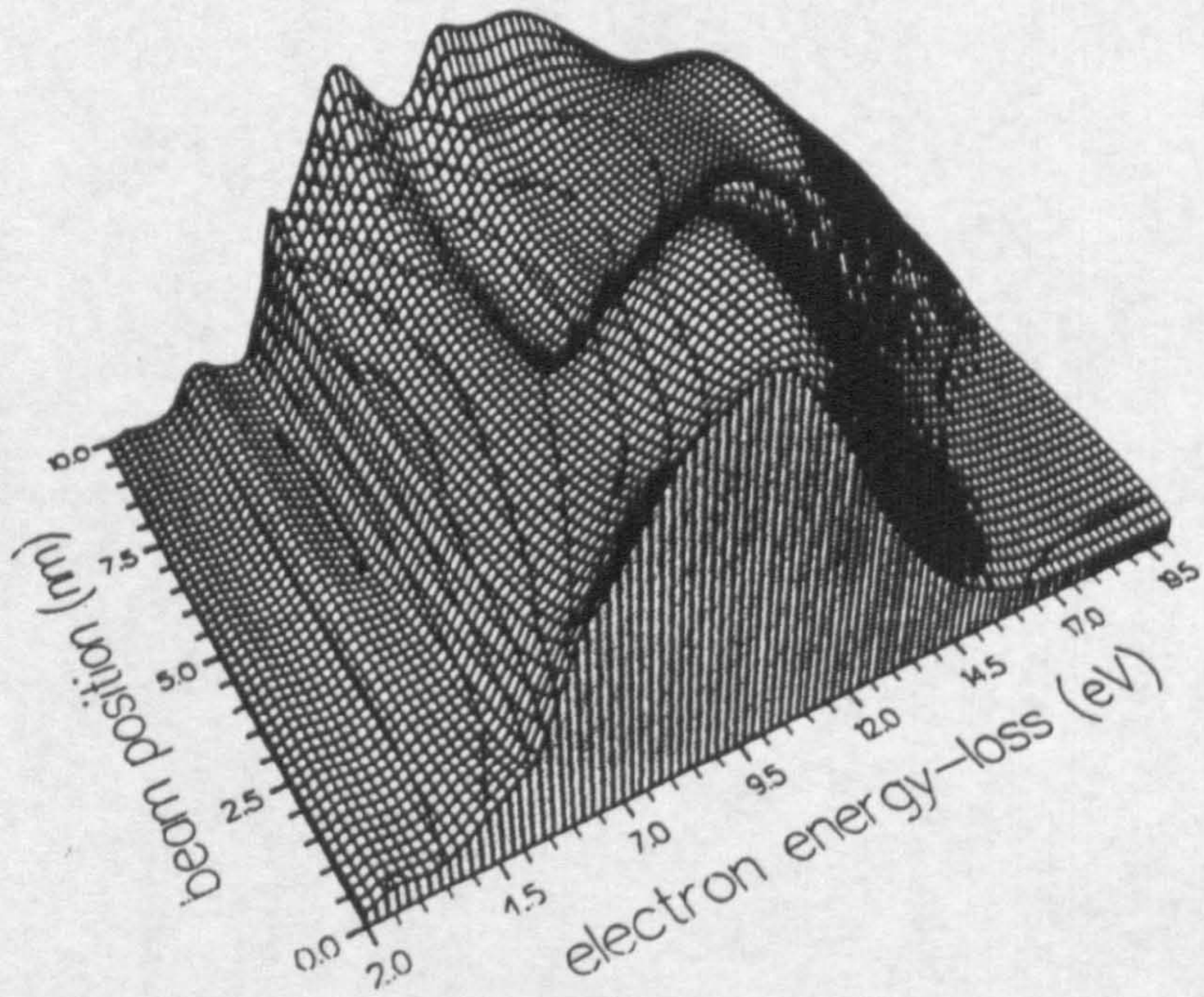

Figure 6.25 A three dimensional plot of scattering probability per unit path length per unit energy range, $(\mathrm{d}I(\hbar\omega)/\mathrm{d}x)$, against energy and beam position for a InSb/GaP double film. InSb extends from 0 nm to 5 nm and GaP from 5 nm to 10 nm.

6.4. Validation of abrupt dielectric model

To end this discussion, we will use the theory for multilayers in a slightly different way, to investigate whether it is reasonable to model a *single* interface by a sharp discontinuity in the dielectric function. We imagine a local dielectric function that varies smoothly near the interface between two materials, healing over a characteristic length of a few Å. We will assume that the scattering due to this dielectric function is very similar to that of a multilayered slab, formed by approximating the dielectric function by a series of step functions. We can then vary the thickness of the layers in the multilayered slab, mimicking the effect of smearing out the discontinuity at the interface. Figure 6.26 reveals the results of this procedure. It shows that the interfacial peak would be diminished by less than 30 % if the dielectric function healed over a distance of 15 Å or less. In practice, the dielectric function is expected to vary over just a few atomic layers so the model of a sharp discontinuity should provide a moderate overestimate of the losses due to interfacial plasmons, but remain reasonable to a first approximation.

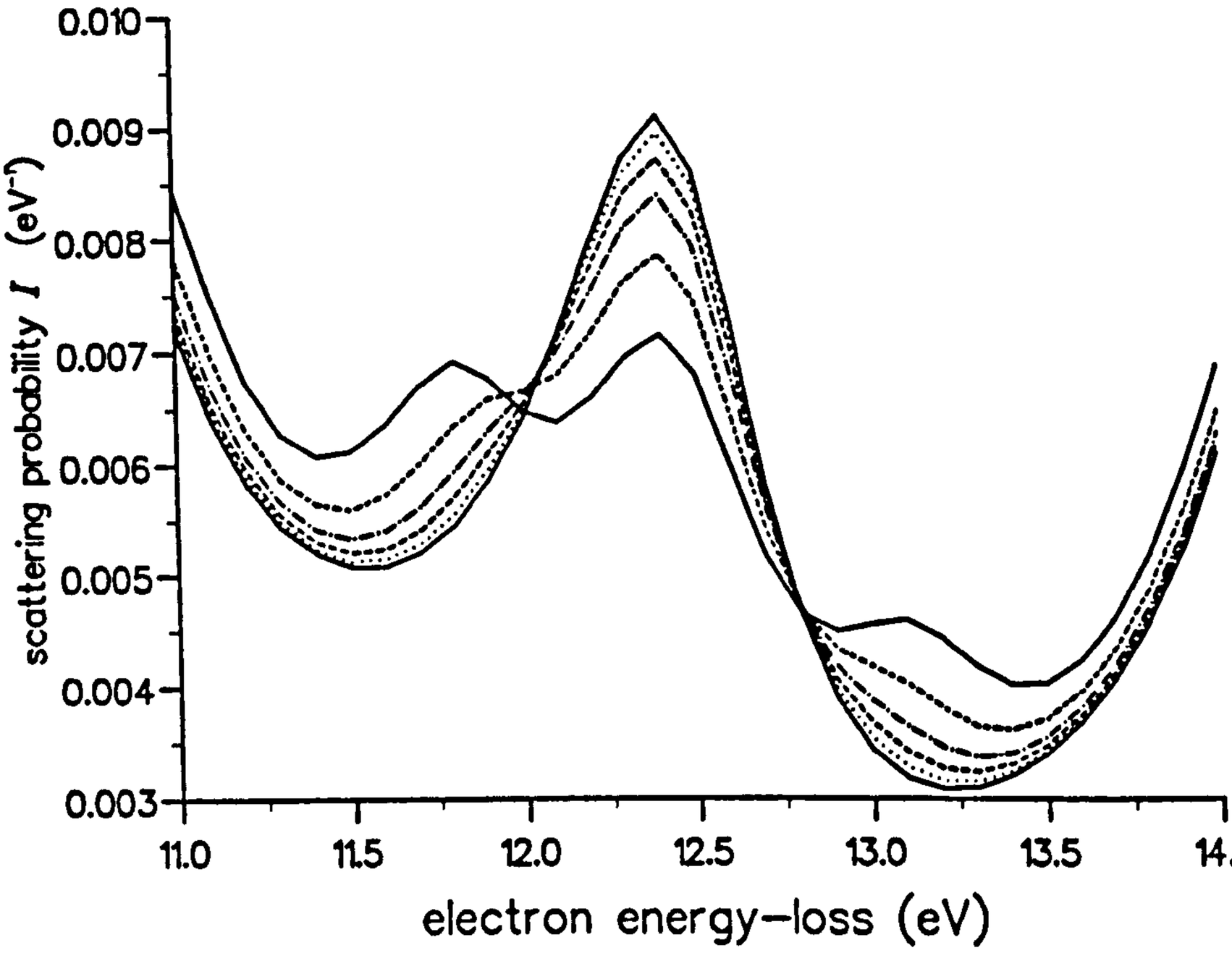

Figure 6.26 The scattering intensity for normal incidence on a Al/Mg bilayer in the region of the interfacial plasmon. Both layers are 100 Å thick. The dielectric function of Al is modelled by Equation 6.2 as explained above, while that of Mg is taken to have a similar form but with $\hbar\omega_p = 10.0$ eV. In the interfacial region the dielectric properties are varied from those of bulk Al to those of bulk Mg in five equal steps. The abruptness of the transition is explored by varying the thickness τ of the individual steps. The highest peak corresponds to an infinitely sharp boundary ($\tau = 0$). The remaining peaks are for $\tau = 0.2$ Å, 1.0 Å, 2.0 Å, 3.0 Å and 5.0 Å, corresponding to total healing lengths of 1.0 Å, 5.0 Å, 10.0 Å, 15.0 Å and 25.0 Å.

6.5. Summary

In summary, analytical expressions derived in Chapters 3 and 4 provide a convenient way of calculating the dispersion and the energy loss spectrum for any multilayered slab. Illustrative calculations for dispersion relation have been made for Al/Mg and Al/Al_2O_3 for up to 15 layers.

For normal incidence, the excitation probability has been calculated for two and three layer systems. For most metal/insulator interfaces or semiconductor/insulator interfaces, interfacial plasmons can be found below 10 eV. For most semiconductor/semiconductor interfaces, the interfacial plasmons are difficult to detect in normal incidence.

The excitation probability for parallel incidence has been calculated for various structures. For Al/Mg structure, calculations were carried out for up to 11 layers. Surface and interfacial plasmons were examined for various beam positions. The results also show that parallel incidence provides a better chance than normal incidence of observing interfacial plasmons in semiconductor systems.

Part III

Multilayered Anisotropic Media

Chapter 7.

Theory (iii): Anisotropic Slabs

This chapter develops a classical dielectric theory of electron energy loss in multilayered anisotropic slabs. Analytical expressions for the dispersion relation and energy loss function are obtained for normal and parallel incidence.

7.1. Introduction

As indicated in Chapter 2, one would expect the electron energy loss spectra for anisotropic materials to depend on the relative directions of electron beam and the anisotropy axes. Previous energy loss studies on graphite [70, 71, 72] and on the CuO-based high-temperature superconductors [73, 74] have shown that the fine structure of the loss spectrum does depend on the specimen orientation. The dielectric theory of the interaction of an electron beam with an anisotropic solid was initiated by Hubbard [11] and later expanded by several authors (cf. see [70, 75, 76]). But the algebra involved is complicated because one has to deal with a dielectric tensor rather than a scalar dielectric function. As a consequence, all theoretical analysis to date has concentrated on the classical bulk plasmon. The primary goal in this chapter is to derive formulae for Multilayered *anisotropic* media analogous to the results obtained in Chapters 3 and 4.

Chapters 3 and 4 have developed the dielectric theory of electron energy loss

in *isotropic* multilayered slabs. It turns out that the techniques of Chapters 3 and 4 can be carried over completely to the anisotropic non-retarded case. This chapter will therefore develop formulae that are valid for any number of anisotropic layers, with the anisotropy axes in arbitrary orientations. Both normal and parallel incidence will be discussed. Formulae for single slabs and interfaces, with the anisotropy axes oriented perpendicular or parallel to the beam and the faces of the slab, will then emerge as special cases of more general results. So far as possible, I will reuse the notation of Chapters and 4, including the square bracket convention for dispersion brackets.

This chapter is organised as follows. Section 7.2 defines the problem and introduces the potential equation. Section 7.3 develops the theory for normal incidence with similar methods to that of Chapter 3. We first derive the transfer matrix recurrence relation, and then obtain a complete solution of Poisson's equation, from which the dispersion relation, work done and loss probability are derived. Section 7.4 develops the dielectric theory for parallel incidence and derives the semiclassical energy loss spectrum and the dispersion relation. Finally, a short summary is presented in Section 7.5.

7.2. Anisotropic media

Media whose physical properties are dependent on their orientation with respect to either the electric or the magnetic field are called anisotropic. In an electrically anisotropic medium, the dielectric tensor is expressed as $\epsilon^{(ik)}$. The aim in this chapter is to develop classical dielectric theory in multilayered slabs for which the individual layers are characterised by such dielectric tensors. We consider a stratified slab which extends to infinity in the x- and y- directions and from $z = 0$ to $z = a$. The slab comprises n layers, labelled $1 \cdots n$. The j^{th} layer lies between z_{j-1} and z_j, has thickness $a_j = z_j - z_{j-1}$ and local dielectric tensor $\epsilon_j^{(ik)}(\omega)$. The external regions are labelled 0 and $n+1$ and extend from $z_{-1} = -\infty$ to $z_0 = 0$ and from $z_n = a$ to $z_{n+1} = \infty$.

The energy loss of electrons, in the classical approximation, is calculated by solving Poisson's equation to find the electric field at the position of the electron. In the j^{th} layer, the equation for the electric potential due to the polarization created by a point charge, Q, moving with uniform velocity $\mathbf{v}$, is given by

$$\sum_{ik} \epsilon_j^{(ik)}(\omega) \frac{\partial}{\partial x_i} \frac{\partial}{\partial x_k} \phi_j(\mathbf{r}, \omega) = -\rho_{\text{ext}}(\mathbf{r}, \omega)/\varepsilon_0 \tag{7.1}$$

Taking the Fourier transform of Equation 7.1 with respect to x and y then gives

$$\frac{\mathrm{d}^2}{\mathrm{d}z^2}\phi_j + 2\mathrm{i}\ell_j \frac{\mathrm{d}}{\mathrm{d}z}\phi_j - m_j^2 \phi_j = -\frac{\rho_{\text{ext}}(k_x, k_y, z, \omega)}{\varepsilon_0 \epsilon_j^{(33)}(\omega)} \tag{7.2}$$

where

$$m_j^2 = \left(\epsilon_j^{(11)} k_x^2 + 2\epsilon_j^{(12)} k_x k_y + \epsilon_j^{(22)} k_y^2\right) / \epsilon_j^{(33)} \tag{7.3}$$

and

$$\ell_j = \left(\epsilon_j^{(13)} k_x + \epsilon_j^{(23)} k_y\right) / \epsilon_j^{(33)}. \tag{7.4}$$

This chapter solves Equation 7.2 by using a transfer matrix recurrence relation to link the potentials in any two neighbouring regions. We then derive closed-form solutions for the potential and hence predict the energy-loss spectrum.

7.3. Normal incidence

The incident beam is assumed to travel at constant speed v in z- direction, ie. normal to the interfaces of layered slabs. The charge density is then given by

$$\rho_{\text{ext}} = Q\delta(x)\delta(y)\delta(z - vt)$$

The Fourier transformed charge density then takes the form

$$\rho_{\text{ext}}(k_x, k_y, \omega) = \frac{Q\mathrm{e}^{\mathrm{i}\omega z/v}}{v}$$

To apply the semiclassical dielectric formalism we must first solve Equation 7.2 with the above charge density.

7.3.1. Recurrence relation and solution

In order to make progress in this problem it is important to choose the right variables. Guided by explorations using computer algebra, the solution to Equation 7.2 is assumed to take the form

$$\phi_j(z, k_x, k_y, \omega) = \sum_{\sigma=\pm} A_j^\sigma \mathrm{e}^{q_j^\sigma z} + \frac{Q\mathrm{e}^{\mathrm{i}\omega z/v}}{\varepsilon_0 v \epsilon_j^{(33)} p_j^2} \tag{7.5}$$

where

$$q_j^\sigma = \sigma\kappa_j - \mathrm{i}\ell_j$$

$$\kappa_j = \sqrt{m_j^2 - \ell_j^2}$$

$$p_j^2 = \kappa_j^2 + \frac{\omega_j^2}{v^2} = m_j^2 + \frac{2\omega}{v}\ell_j + \frac{\omega^2}{v^2}$$

$$\omega_j = \omega + \ell_j v$$

The undetermined coefficients A_j^σ depend on ω, k_x, k_y. The boundary conditions at infinity require two of these coefficients to vanish, so there remain $2n+2$ undetermined coefficients. These coefficients can be found by using the boundary conditions at the $n+1$ interfaces. As in Chapter 3, the boundary conditions are most conveniently expressed in terms of a transfer matrix re-

currence relation. In order to express this recurrence relation in the simplest possible form we rescale the coefficients as follows:

$$\alpha_j^\sigma = \frac{\varepsilon_0 v}{Q} A_j^\sigma e^{(q^\sigma - i\omega/v)z_{j-1}} \qquad \text{with} \quad \alpha_0^\sigma = \frac{\varepsilon_0 v}{Q} A_0^\sigma$$

and then define the *coefficient vector* for the j^{th} layer

$$\boldsymbol{\alpha}_j = \begin{pmatrix} \alpha_j^+ \\ \alpha_j^- \end{pmatrix}$$

we also introduce the source terms

$$\hat{S}_{ji}^\sigma = \sigma \kappa_i \epsilon_i^{(33)} \left(\frac{1}{\epsilon_j^{(33)} p_j^2} - \frac{1}{\epsilon_i^{(33)} p_i^2} \right) + \frac{i}{v} \left(\frac{\omega_j}{p_j^2} - \frac{\omega_i}{p_i^2} \right) \tag{7.6}$$

and define the *source vector* for the j^{th} layer

$$\hat{\mathbf{S}}_j = \begin{pmatrix} \hat{S}_{j,j+1}^+ \\ -\hat{S}_{j,j+1}^- \end{pmatrix}.$$

Finally, we introduce two exponential factors

$$\hat{f}_j = e^{\kappa_j a_j} \qquad \text{with} \quad \hat{f}_0 = \hat{f}_{n+1} = 1 \tag{7.7}$$

$$\hat{b}_j^\sigma = e^{i\sigma\omega_j a_j/v} \qquad \text{with} \quad \hat{b}_0^\sigma = \hat{b}_{n+1}^\sigma = 1 \tag{7.8}$$

The boundary conditions at the interface between j^{th} and $(j+1)^{\text{th}}$ regions then lead the simple recurrence relation

Box 16. Recurrence relation for normal incidence

$$\hat{h}_{j+1,j+1}^+ \boldsymbol{\alpha}_{j+1} = \frac{1}{\hat{f}_j \hat{b}_j^+} \hat{\tau}^{(j+1,j)} \boldsymbol{\alpha}_j + \hat{\mathbf{S}}_j \tag{7.9}$$

where the *transfer matrix* is given by

$$\hat{\tau}^{(j+1,j)} = \begin{pmatrix} \hat{h}^{+}_{j+1,j}\hat{f}^{2}_{j} & \hat{h}^{-}_{j+1,j} \\ \hat{h}^{-}_{j+1,j}\hat{f}^{2}_{j} & \hat{h}^{+}_{j+1,j} \end{pmatrix}$$

and

$$\hat{h}^{\sigma}_{ji} = \epsilon^{(33)}_{j}\kappa_{j} + \sigma\epsilon^{(33)}_{i}\kappa_{i} \tag{7.10}$$

This recurrence relation is similar to that obtained for normal incidence through isotropic multilayers (Chapter 3, Equation 3.14). Differences lie beneath the surface, however, because the terms $\hat{S}^{\sigma}_{ji}$, $\hat{f}_{j}$, $\hat{b}^{\sigma}_{j}$ and $\hat{h}^{\sigma}_{ji}$ as defined above are slightly more complicated than the corresponding quantities in the isotropic case. In spite of these differences, we can still establish the analogue of Equation A.24 of Appendix A:

$$\hat{h}^{+}_{ji}\hat{S}^{\sigma}_{ij} + \hat{h}^{-}_{ji}\hat{S}^{-\sigma}_{ij} + \hat{h}^{+}_{jj}\hat{S}^{\sigma}_{ji} = 0$$

Using this identity and carrying out an inductive proof analogous to that given in Appendix A, one obtains the following general formula for the coefficient vector in the j^{th} region of an n layer slab:

Box 17. Solution for coefficients of electric potential in normal incidence

$$\alpha_{j} = \frac{1}{\left[\hat{C}_{n0}\right]}\left\{\hat{\mathrm{M}}_{nj}\sum_{k=0}^{j-1}\hat{\psi}^{-}_{k+1,j-1}\left[\hat{X}^{-}_{k0}\right] - \hat{\mathrm{N}}_{j-1,0}\hat{f}_{j}\hat{b}^{+}_{j}\sum_{k=j}^{n}\hat{\psi}^{+}_{j+1,k}\left[\hat{Y}^{+}_{kn}\right]\right\} \tag{7.11}$$

In comparison with Chapters 3 and 4, here, and throughout this chapter, we shall use a convenient shorthand: for any quantity X, we extend the hat notation of h_{ji}, f_{j}, b^{σ}_{j} and S^{σ}_{ji} so that $\hat{X}$ is defined by replacing each of these variables in X by corresponding $\hat{h}_{ji}$, $\hat{f}_{j}$, $\hat{b}^{\sigma}_{j}$ and $\hat{S}^{\sigma}_{ji}$. For example,

$$\hat{C}_{ji} = \hat{h}^{+}_{j+1,j}\hat{f}^{2}_{j}\hat{h}^{+}_{j,j-1}\cdots\hat{h}^{+}_{i+1,i}$$

We also reuse the square bracket notation for dispersion brackets, as explained in Chapter 3. This means, for example, that

$$\left[\hat{C}_{10}\right] = \left[\hat{h}_{21}^{+}\hat{f}_{1}^{2}\hat{h}_{10}^{+}\right] = \hat{h}_{21}^{+}\hat{f}_{1}^{2}\hat{h}_{10}^{+} + \hat{h}_{21}^{-}\hat{h}_{10}^{-}$$

Equation 7.11 provides a solution for the Fourier transformed potential in each region of the slab. The solution is only of passing interest in the context of energy-loss studies, but it is an important step towards finding the dispersion relation and the energy loss probability.

7.3.2. Dispersion relation and energy loss probability

The dispersion relation for excitations in an anisotropic multilayered slab can be found either directly from Equation 7.9 or from Equation 7.11. For an n-layered slab, we obtain

Box 18. Dispersion relation

$$\left[\hat{C}_{n0}\right] = 0 \tag{7.12}$$

which is directly analogous to Equation 3.19 of Chapter 3.

For example, the dispersion relation for a single anisotropic slab is obtained by substituting $n = 1$ in Equation 7.12. This gives

$$\begin{aligned}&(\epsilon_2^{(33)}\kappa_2 + \epsilon_1^{(33)}\kappa_1)\mathrm{e}^{2\kappa_1 a_1}(\epsilon_1^{(33)}\kappa_1 + \epsilon_0^{(33)}\kappa_0)\\ &+(\epsilon_2^{(33)}\kappa_2 - \epsilon_1^{(33)}\kappa_1)(\epsilon_1^{(33)}\kappa_1 - \epsilon_0^{(33)}\kappa_0) = 0\end{aligned} \tag{7.13}$$

In order to find the semiclassical energy loss spectrum we adopt a familiar strategy. The energy lost by an electron as it moves from $z = -\infty$ to $z =$

$+\infty$ is calculated from the solution for the potential (Equation 7.11). The resulting expression is simplified as far as possible, using methods developed in Chapter 3. The semiclassical energy loss spectrum is then obtained by interpreting the energy loss in terms of the exchange of individual quanta. Preceding as in Chapter 3, the work done for electron moving against electric field is expressed as

$$W = \frac{Q}{(2\pi)^3} \int \int_0^\infty \mathrm{d}k_x \mathrm{d}k_y \int_{-\infty}^\infty \mathrm{d}\omega \int_{-\infty}^\infty \mathrm{d}z \, E_z(k_x, k_y, k_z, \omega) \mathrm{e}^{-\mathrm{i}\omega z/v} \tag{7.14}$$

where

$$E_z = -\frac{\partial \phi}{\partial z}$$

The work done can be written in terms of the coefficients of electric potential

$$W = \frac{Q}{(2\pi)^3} \int \int \int_{-\infty}^\infty \mathrm{d}k_x \mathrm{d}k_y \mathrm{d}\omega \sum_{i=0}^{n+1} \int_{z_{i-1}}^{z_i} \mathrm{d}z \left(\sum_{\sigma=\pm} q_i^\sigma A_i^\sigma \mathrm{e}^{(q_i^\sigma - \mathrm{i}\omega/v)/z} + \frac{\mathrm{i}\omega}{v} \frac{Q}{\varepsilon_0 v \epsilon_j^{(33)} p_j^2} \right) \tag{7.15}$$

Substituting Equation 7.5 into Equation 7.14, with solution in Equation 7.11, one obtains

$$W = -\frac{Q^2}{4\pi^3 \varepsilon_0 \hbar v^2} \int_{-\infty}^\infty \mathrm{d}k_x \int_{-\infty}^\infty \mathrm{d}k_y \int_0^\infty (\hbar\omega) \mathrm{d}\omega \frac{\mathrm{d}^3 P}{\mathrm{d}(\hbar\omega)\mathrm{d}k_x \mathrm{d}k_y} \tag{7.16}$$

where the scattering probability is

$$\frac{\mathrm{d}^3 P}{\mathrm{d}(\hbar\omega)\mathrm{d}k_x \mathrm{d}k_y} = -\frac{Q^2}{4\pi^3 \varepsilon_0 \hbar^2 v^2} \mathrm{Im}(\chi_{\mathrm{bulk}} + \chi_{\mathrm{bdy}}) \tag{7.17}$$

where χ_{bulk} represents the bulk contribution and χ_{bdy} represents the boundary contributions, which are

Box 19. Bulk and boundary contributions to energy loss function

$$\chi_{\text{bulk}} = \sum_{k=1}^{n} \frac{a_k}{\epsilon_k^{(33)} p_k^2} \tag{7.18}$$

and

$$\chi_{\text{bdy}} = \frac{1}{\left[\hat{C}_{n0}\right]} \sum_{\sigma=\pm} \sum_{k=0}^{n} \sum_{j=k}^{n} z_{kj} \hat{\psi}_{k+1,j}^{\sigma} \left[\hat{X}_{k0}^{\sigma}\right] \left[\hat{Y}_{jn}^{\sigma}\right] \tag{7.19}$$

where

$$z_{ij} = \begin{cases} \frac{1}{2} & \text{if} \quad i = j \\ 1 & \text{otherwise.} \end{cases}$$

A detailed derivation of Equation 7.19 will be given in Appendix E.

As expected, the bulk contribution is a sum over layers, with the j^{th} layer contributing an amount equal to its thickness times the energy loss per unit length in an infinite anisotropic medium with dielectric tensor $\epsilon_j^{(ik)}(\omega)$ (see [69]). The boundary contribution can be interpreted as a sum of couplings between pairs of interfaces. Although more complicated than χ_{bulk}, it is still remarkably simple, bearing in mind the complexity of the problem.

Equations 7.18 and 7.19 are the main theoretical results for normal incidence on anisotropic multilayers. They provide a natural extension of the previous work on isotropic multilayers. It is also worth noting that the final results are unchanged by the transformation $\kappa_j \longrightarrow -\kappa_j$, for any $1 \leq j \leq n$. This means that the choice of square root of κ is immaterial.

For a single anisotropic slab, the above equations reduce to

$$\chi^{(1)}_{\text{bulk}} + \chi^{(1)}_{\text{bdy}} = -\frac{a_1}{\epsilon_1^{(33)} p_1^2} - \frac{1}{\left[\hat{C}_{n0}\right]} \sum_{\sigma=\pm} \hat{S}^{\sigma}_{10} \left(\left[\hat{Y}^{\sigma}_{01}\right] + \hat{\psi}^{\sigma}_{11} \hat{S}^{\sigma}_{12} \right) \tag{7.20}$$

Equation 7.20 will be applied to a graphite slab in Chapter 8.

7.3.3. Comparison with retarded isotropic calculation

In comparison with retarded isotropic calculation, one major point to be in mind is that

$$\lim_{c\to\infty} \left(h^{\pm}_{ij} \right) = k \left(\epsilon_j \pm \epsilon_i \right)$$

while

$$\lim_{\text{isotropic}} \left(\hat{h}^{\pm}_{ij} \right) = k \left(\epsilon_i \pm \epsilon_j \right)$$

so

$$\lim_{c\to\infty} \left(h^{\sigma}_{ij} \right) = \sigma \lim_{\text{isotropic}} \left(\hat{h}^{\sigma}_{ij} \right)$$

Because contractions occur in pairs we also have

$$\lim_{c\to\infty} \left[C_{ij} \right] = \lim_{\text{isotropic}} \left[\hat{C}_{ij} \right]$$

$$\lim_{c\to\infty} \left[D_{ij} \right] = - \lim_{\text{isotropic}} \left[\hat{D}_{ij} \right]$$

$$\lim_{c\to\infty} \left[E_{ij} \right] = - \lim_{\text{isotropic}} \left[\hat{E}_{ij} \right]$$

$$\lim_{c\to\infty} \left[F_{ij} \right] = \lim_{\text{isotropic}} \left[\hat{F}_{ij} \right]$$

Moreover, for source terms, we have

$$\lim_{c\to\infty} \left(S^{\sigma}_{ij} \right)_{\text{retarded}} = \frac{\epsilon_i - \epsilon_j}{\epsilon_i (k^2 + \omega^2/v^2)}$$

$$\lim_{\text{isotropic}} \left(\hat{S}^{\sigma}_{ij}\right)_{\text{anisotropic}} = \frac{\sigma k(\epsilon_j - \epsilon_i)}{\epsilon_i(k^2 + \omega^2/v^2)}$$

so

$$k \lim_{c\to\infty} \left(S^{\sigma}_{i,i+1}\right)_{\text{retarded}} = -\sigma \lim_{\text{isotropic}} \left(\hat{S}^{\sigma}_{i,i+1}\right)_{\text{anisotropic}}$$

Hence we can show that

$$k \lim_{c\to\infty} \left[X^{\sigma}_{ji}\right] = -\sigma \lim_{\text{isotropic}} \left[\hat{X}^{\sigma}_{ji}\right]$$

and

$$k \lim_{c\to\infty} \left[Y^{\sigma}_{ij}\right] = -\sigma \lim_{\text{isotropic}} \left[\hat{Y}^{\sigma}_{ij}\right]$$

So finally we obtain

$$\lim_{c\to\infty} k^2 \left(\left[X^{\sigma}_{i0}\right]\left[Y^{\sigma}_{jn}\right]\right) = \lim_{\text{isotropic}} \left(\left[\hat{X}^{\sigma}_{i0}\right]\left[\hat{Y}^{\sigma}_{jn}\right]\right)$$

We therefore do get agreement between Equation 3.35 and Equation 7.19, including checking the signs of the terms in our normal isotropic calculations. The bulk contribution are easily shown to be consistent too.

7.4. Parallel incidence

This section derives energy loss formulae for an electron that travels parallel to the interfaces of the slab. We suppose that the electron travels in the m^{th} region, parallel to the x-axis, with $y = 0$ and $z = z_b$. Primes are used to distinguish subregions on either side of the beam: m' lies between z_{m-1} and z_b, while m'' lies between z_b and z_m. The charge density for an electron travelling with constant speed v along the x- direction is then given by

$$\rho_{\text{ext}} = Q\delta(x - vt)\delta(y)\delta(z)$$

Its Fourier transformed form is

$$\rho(k_x, k_y, z, \omega) = 2\pi Q \delta(\omega - k_x v)\delta(z - z_b)$$

7.4.1. Recurrence relation and solution

The particular solution of Equation 7.2 in region j is written as

$$\phi_j(z, k_x, k_y, \omega) = \tilde{\phi}_j \delta(k_x v - \omega) \tag{7.21}$$

where

$$\tilde{\phi}_j = \sum_{\sigma=\pm} B_j^\sigma \mathrm{e}^{q_j^\sigma z} \tag{7.21a}$$

where the B_j^σ are undetermined coefficients. In the beam layer, this satisfies the boundary conditions

$$\tilde{\phi}_{m''}\Big|_{z_b^+} - \tilde{\phi}_{m'}\Big|_{z_b^-} = 0 \tag{7.22}$$

and

$$\frac{\mathrm{d}\tilde{\phi}_{m''}}{\mathrm{d}z}\bigg|_{z_b^+} - \frac{\tilde{\phi}_{m'}}{\mathrm{d}z}\bigg|_{z_b^-} = -\frac{2\pi Q}{\varepsilon_0 \epsilon_m^{(33)}} \tag{7.23}$$

We rescale the variables

$$\beta_i^\sigma = -\frac{\varepsilon_0 \epsilon_m^{(33)} \kappa_m}{\pi Q} B_i^\sigma \mathrm{e}^{q_i^\sigma z_{i-1}} \qquad \text{with} \quad \beta_0^\sigma = -\frac{\varepsilon_0 \epsilon_m^{(33)} \kappa_m}{\pi Q} B_0^\sigma \tag{7.24}$$

and define the *coefficient vector*

$$\beta_j = \begin{pmatrix} \beta_j^+ \\ \beta_j^- \end{pmatrix}$$

and *source vector*

$$\hat{\mathbf{G}}_m = \begin{pmatrix} 1/\hat{g}_m^+ \\ -1/\hat{g}_m^- \end{pmatrix}$$

where

$$\hat{g}_m^\sigma = \mathrm{e}^{q_m^\sigma (z_b - z_{m-1})}$$

The boundary conditions at the j^{th} interfaces then produce following recurrence relation

$$\hat{h}_{j+1,j+1}\beta_{j+1} = \frac{1}{\hat{f}_j \lambda_j} \hat{\tau}^{(j+1,j)} \beta_j \tag{7.25}$$

where

$$\lambda_j = \mathrm{e}^{\mathrm{i}\ell_j a_j}$$

Applying boundary conditions at the level of the beam, one one has

$$\beta_{m''} = \beta_{m'} + \hat{\mathbf{G}}_m \tag{7.26}$$

So combining Equations 7.25 and 7.26 leads to the recurrence relation

Box 20. Recurrence relation for parallel incidence

$$\beta_{j+1} = T^{(j+1,j)} \left(\beta_j + \delta_{jm'} \mathbf{G}_m \right) \tag{7.27}$$

where

$$T^{(j+1,j)} = \frac{\tau^{(j+1,j)}}{\hat{h}_{j+1,j+1}^+ \hat{f}_j \lambda_j} \qquad \text{for} \quad j \neq m'$$

and

$$T^{(m'',m')} = I$$

This recurrence relation looks similar to that obtained for parallel incidence through isotropic multilayers in classical approximation (Appendix D). There is an extra factor λ_j in Equation 7.27 but, as will seen shortly this factor cancels out of the energy loss spectrum. The other differences are that the terms $\hat{h}^{\sigma}_{ji}$, $\hat{f}_j$ and $\hat{g}_j$ as defined above are slightly more complicated that the corresponding quantities in the isotropic case.

The recurrence relation 7.27 can be solved to find the coefficient vector in the beam layer:

Box 21. Coefficients of electric potential in the beam layer

$$\beta_{m'} = -\frac{\hat{\gamma}^{-}_{nm}}{\left[\hat{C}_{n0}\right]}\hat{\mathrm{N}}_{m-1,0} \tag{7.28}$$

$$\beta_{m''} = -\frac{\hat{\zeta}^{+}_{m-1,0}}{g^{+}_{m}g^{-}_{m}\left[\hat{C}_{n0}\right]}\hat{\mathrm{M}}_{nm} \tag{7.29}$$

where

$$\hat{\gamma}^{\sigma}_{ji} = \left[\hat{C}_{ji}\right]/g^{+}_{i} + \sigma\left[\hat{D}_{ji}\right]/g^{-}_{i}$$

$$\hat{\zeta}^{\sigma}_{ji} = \left[\hat{C}_{ji}\right]g^{+}_{j+1} + \sigma\left[\hat{E}_{ji}\right]g^{-}_{j+1}$$

These results for the potential will now be used to find the dispersion relation, the work done by the beam and hence the semiclassical energy loss spectrum.

7.4.2. Dispersion relation and energy loss

The dispersion relation derived from Equations 7.28, 7.29 or 7.27 takes the same form as for normal incidence (Equation 7.12). This is unlike our previous findings in Chapter 4, where additional TE modes were found in parallel incidence that were not excited by normal incidence. These modes do not appear in the present calculation because we are working in the non-retarded limit.

One can calculate the work done on the incoming electron by the electric field induced in its polarized surroundings. The work done in the parallel case is expressed as

$$\frac{\mathrm{d}W}{\mathrm{d}x} = -\frac{Q}{(2\pi)^3 v}\int\int_{-\infty}^{\infty}\tilde{E}_x^{(m)}(k_x,k_y,z_b,\omega)\mathrm{d}k_y\mathrm{d}\omega\Big|_{k_x\to\omega/v}$$

where

$$\tilde{E}_x^{(m)} = -\frac{\partial}{\partial x}\tilde{\phi} = -\mathrm{i}k_x\left(B_m^+\mathrm{e}^{q_m^+ z_b} + B_m^-\mathrm{e}^{q_m^- z_b}\right)$$

Substituting B_m^σ into $\tilde{E}_x^{(m)}$, one obtains the work done per unit path length

$$\frac{\mathrm{d}W}{\mathrm{d}x} = \frac{Q^2}{2\pi^2\varepsilon_0\hbar v^2}\int_0^\infty \hbar\omega\mathrm{d}\omega\int_{-\infty}^{\infty}\mathrm{d}k_y\mathrm{Im}\left(\chi_m^{(n)}\right) \tag{7.30}$$

So the energy loss probability is described by function

$$\frac{\mathrm{d}^3P}{\mathrm{d}(\hbar\omega)\mathrm{d}k_y\mathrm{d}x} = \frac{Q^2}{2\pi^2\varepsilon_0\hbar^2v^2}\mathrm{Im}\left\{\chi_m^{(n)}\right\}_{k_x\to\omega/v} \tag{7.31}$$

where

$$\chi_m^{(n)} = \frac{1}{\kappa_m}\left(\beta_m^+\hat{g}_m^+ + \beta_m^-\hat{g}_m^-\right) \tag{7.32}$$

Using our solutions for the coefficient vector in the beam region (either Equation 7.28 or 7.29) we finally obtain

Box 22. The energy loss function for parallel incidence

$$\chi_m^{(n)} = -\frac{1}{\epsilon_m^{(33)} \kappa_m \left[\hat{C}_{n0}\right]} \hat{\gamma}_{nm}^{-} \hat{\zeta}_{m-1,0}^{+} \tag{7.33}$$

Equation 7.33 is our main theoretical result for parallel incidence in or near anisotropic multilayers. It extends our previous work on isotropic multilayers and, although the proof is not as obvious as for normal incidence, we have checked that the isotropic limit of Equation 7.33 is the same as the isotropic limit of Equation 4.27 in Chapter 4.

7.4.3. Special cases

Our initial purpose in carrying out these calculations was to obtain formulae for single anisotropic interfaces and slabs. With this aim in mind, we now consider some special cases, beginning with that of a bulk medium, for which the number of interfaces $(n+1)$ is equal to zero. Thus, $n = -1$ and Equation 7.33 gives

$$\chi_0^{(-1)} = \frac{1}{\epsilon_0^{(33)} \kappa_0} \tag{7.34}$$

which is consistent with the results of reference [76] for energy loss in a bulk anisotropic medium.

Next, we take $n = 0$, corresponding to single interface at $z = 0$. With the beam in region 0, we obtain

$$\chi_0^{(0)} = \frac{1}{\epsilon_0^{(33)} \kappa_0} \left(1 - \frac{\hat{h}_{10}^{-}}{\hat{h}_{10}^{+}} e^{2\kappa_0 z_b}\right) \tag{7.35}$$

and with the beam in region 1, we obtain

$$\chi_1^{(0)} = \frac{1}{\epsilon_1^{(33)}\kappa_1}\left(1 + \frac{\hat{h}_{10}^-}{\hat{h}_{10}^+}e^{-2\kappa_1 z_b}\right) \tag{7.36}$$

As expected, Equations 7.35 and 7.36 transform into one another if we make the replacements $0 \leftrightarrow 1$ and $z_b \leftrightarrow -z_b$. Also, at the interface itself, $\chi_0^0 = \chi_1^0$.

Finally, consider the case of a single slab. On substituting $n = 1$ and $m = 1$ in Equation 7.33, we obtain the loss function for an internal beam:

$$\chi_1^{(1)} = \frac{1}{\epsilon_1^{(33)}\kappa_1\,[C_{10}]}\left(\hat{h}_{21}^+ e^{2\kappa_1(a_1 - z_b)} - \hat{h}_{21}^-\right)\left(\hat{h}_{10}^+ e^{2\kappa_1 z_b} + \hat{h}_{10}^-\right) \tag{7.37}$$

while, substituting $n = 1$ and either $m = 0$ or $m = 2$ gives the expressions for an external beam:

$$\chi_0^{(1)} = \frac{1}{\epsilon_0^{(33)}\kappa_0}\left(1 - \frac{\hat{h}_{21}^+ f_1^2 \hat{h}_{10}^- + \hat{h}_{21}^- \hat{h}_{10}^+}{\hat{h}_{21}^+ f_1^2 \hat{h}_{10}^+ + \hat{h}_{21}^- \hat{h}_{10}^-}e^{2\kappa_0 z_b}\right) \tag{7.38}$$

$$\chi_2^{(1)} = \frac{1}{\epsilon_2^{(33)}\kappa_2}\left(1 + \frac{\hat{h}_{21}^- f_1^2 \hat{h}_{10}^+ + \hat{h}_{21}^+ \hat{h}_{10}^-}{\hat{h}_{21}^+ f_1^2 \hat{h}_{10}^+ + \hat{h}_{21}^- \hat{h}_{10}^-}e^{-2\kappa_2(z_b - a_1)}\right) \tag{7.39}$$

Equations 7.38 and 7.39 transform into one another if we make the replacements $0 \leftrightarrow 2$ and $z_b \leftrightarrow a_1 - z_b$. Also, Equation 7.37 agrees with Equation 7.38 when $z_b = 0$ and agrees with Equation 7.39 when $z_b = a_1$. In the next section, these equations will be applied to graphite slabs surrounded by vacuum and diamond.

7.5. Summary

This chapter develops dielectric theory in multilayers composed of anisotropic media. Starting from Poisson's equation and using a recursive transfer matrix method, the energy loss spectra for electrons travelling normal and parallel to the interfaces of multilayered anisotropic slabs were derived. These results are valid for any number of anisotropic slabs. Basically, this chapter has solved some algebraic problems in the calculation of EELS spectra in

anisotropic media; these problems would be very hard if one had to rely on hand calculation. The results obtained in this chapter will now be applied to study bulk, surface and interface plasmons in graphite slabs.

Chapter 8.

Applications (iii): Anisotropic Slabs

The theory developed in Chapter 7 is used to study bulk, surface and interface plasmons in graphite slabs. For normal incidence, the energy loss spectrum is calculated for single graphite slabs, varying the choice of the anisotropic axis. For parallel incidence, we first study a semi-infinite graphite medium and then a graphite slab sandwiched between semi-infinite diamond and vacuum regions.

8.1. Introduction

In recent years the study of graphite has received much attention in the literature. This crystal exhibits unique electronic properties of interest to the theoretical, as well as the experimental physicist. The electronic structure of graphite is well understood [87].

Energy loss studies in graphite have also received considerable attention [70, 23, 85]. Since graphite is anisotropic, the EELS spectra depend on the graphite crystallographic orientation relative to the momentum transfer [23]. This is a result of the optical selection rules being direction dependent. These studies have shown that the graphite $\sigma + \pi$ bulk plasmon excitation has an energy of 27 eV for wavevector transfer $\mathbf{q}$ perpendicular to the anisotropic axis and 19 eV for $\mathbf{q}$ parallel to anisotropic axis [70]. The π-plasmon peak is at an energy of 6 eV for $\mathbf{q}$ perpendicular to the anisotropic axis and 4 eV for

q parallel to the anisotropic axis [85]. In this chapter, the theory developed in Chapter 7 will be applied to study energy loss spectra of graphite, a typical uniaxial material.

Surface and interface plasmons on graphite have not been studied both theoretically or experimentally to date. As this is the first analysis that includes surface and interface terms for anisotropic materials, we concentrate on the simplest geometries — a single slab, a single interface and a surface coating of graphite on diamond. This chapter will be organised as follows. Section 8.2 defines orientations. Section 8.3 calculates electron energy loss for normal incidence on single slabs of graphite. Section 8.4 studies a single interface of graphite for parallel incidence on the surface. A more complicated situation of a graphite slab sandwiched between semi-infinite diamond and vacuum regions is also discussed. Finally, a short summary is presented in Section 8.5.

8.2. Orientations

We consider three different orientations, with the anisotropy axis (or c-axis) aligned along the x-, y- and z-axes. For brevity, these will be referred to as the $\hat{x}$-, $\hat{y}$- and $\hat{z}$-orientations. In all the graphs that follow, a solid line will be used for the $\hat{z}$-orientation, a dashed line for the $\hat{y}$-orientation and a dotted line for the $\hat{x}$-orientation. The dielectric tensors for these orientations are

$$\hat{\epsilon}_x = \begin{pmatrix} \epsilon^{\parallel} & 0 & 0 \\ 0 & \epsilon^{\perp} & 0 \\ 0 & 0 & \epsilon^{\perp} \end{pmatrix}, \quad \hat{\epsilon}_y = \begin{pmatrix} \epsilon^{\perp} & 0 & 0 \\ 0 & \epsilon^{\parallel} & 0 \\ 0 & 0 & \epsilon^{\perp} \end{pmatrix}, \quad \hat{\epsilon}_z = \begin{pmatrix} \epsilon^{\perp} & 0 & 0 \\ 0 & \epsilon^{\perp} & 0 \\ 0 & 0 & \epsilon^{\parallel} \end{pmatrix}$$

where $\epsilon^{\parallel}$ is the dielectric function when the electric field is parallel to the c-axis and $\epsilon^{\perp}$ is the dielectric function when the electric field is perpendicular to the c-axis.

Numerical values of these dielectric functions are taken from the *Handbook of Optical Constants of Solids II* by Palik [88]. Figure 8.1 shows the real and imaginary parts of $\epsilon^{\perp}$ and $\epsilon^{\parallel}$ of graphite.

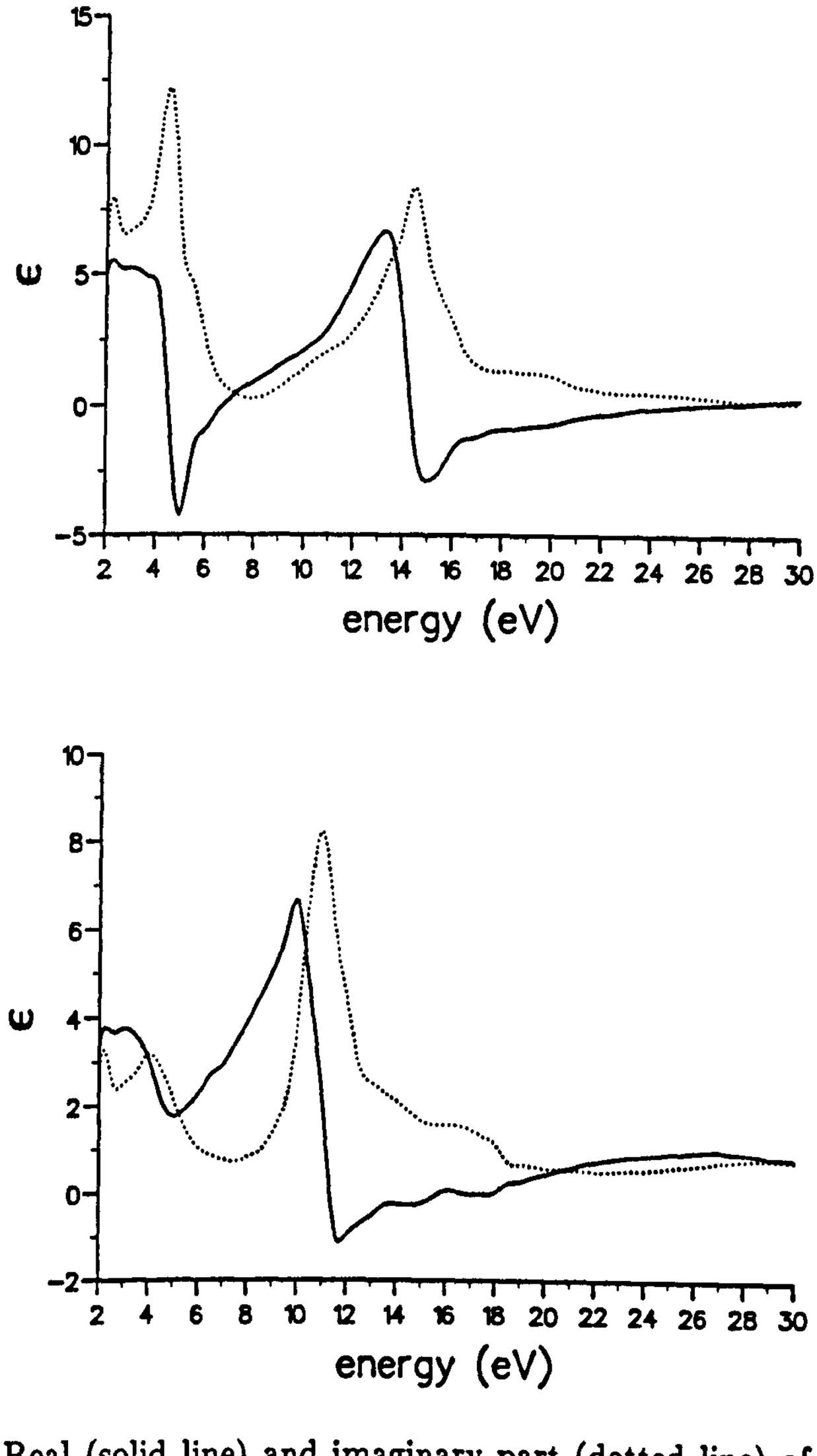

Figure 8.1 Real (solid line) and imaginary part (dotted line) of the dielectric constant in graphite for $\epsilon^{\perp}$ (above) and $\epsilon^{\parallel}$ (below).

The beam will be taken to be either parallel or normal to the slab. Figure 8.2 shows these two cases. In Case I, the beam is parallel to anisotropic axis, so the momentum transfer, **q**, is practically perpendicular to anisotropic axis or parallel to graphite planes. In Case II, the beam is perpendicular to anisotropic axis, so the momentum transfer can be either parallel or perpendicular to anisotropic axis.

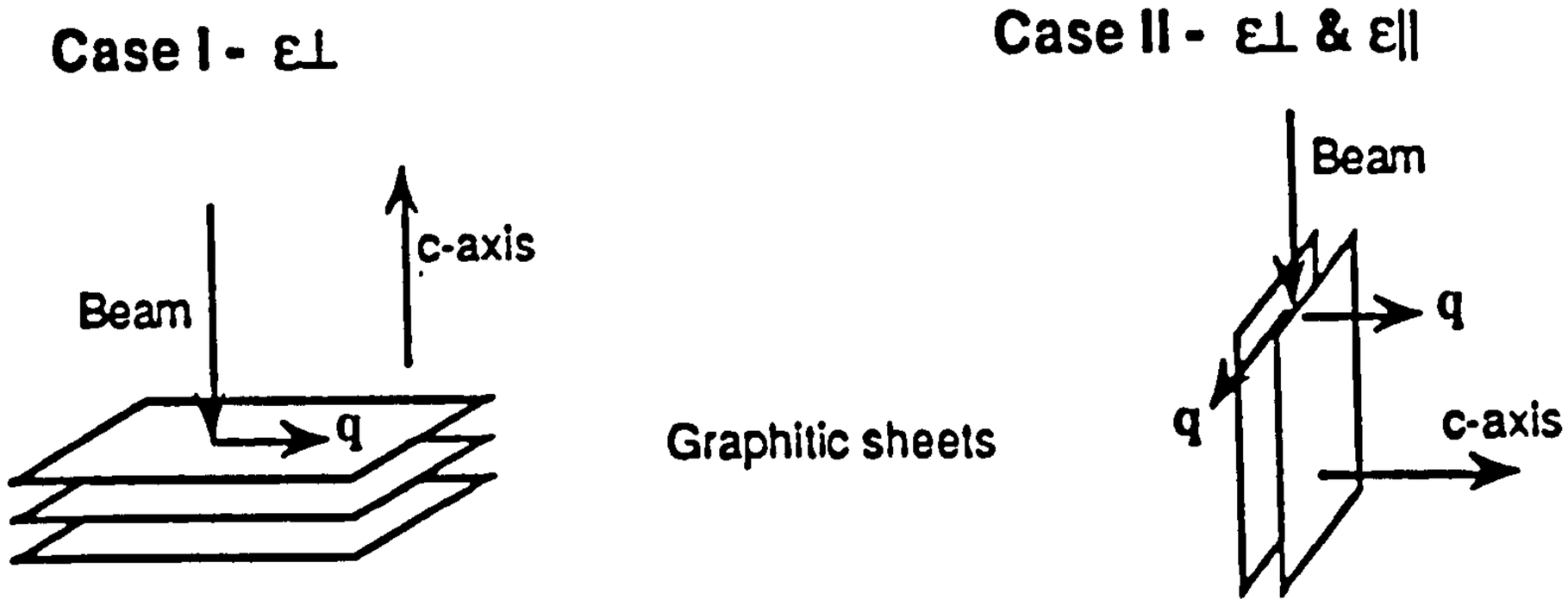

Figure 8.2 Relations between beam direction and anisotropic orientation.

The intensity of an energy-resolved STEM image is proportional to the scattering probability per unit energy range, $I(\hbar\omega)$, which is obtained by integrating Equations 7.17 or 7.31 over wavevectors. To avoid the logarithmic divergence that always accompanies the bulk losses it is necessary to introduce an upper wavenumber cut-off, k_c. For normal incidence we take

$$I(\hbar\omega) = \int_{-k_c}^{k_c} \mathrm{d}k_x \int_{-\sqrt{k_c^2-k_x^2}}^{\sqrt{k_c^2-k_x^2}} \mathrm{d}k_y \, \frac{\mathrm{d}^3P}{\mathrm{d}(\hbar\omega)\mathrm{d}k_x\mathrm{d}k_y} \tag{8.1}$$

and for parallel incidence

$$\frac{\mathrm{d}I(\hbar\omega)}{\mathrm{d}x} = \int_{-k_c}^{k_c} \mathrm{d}k_y \, \frac{\mathrm{d}^3P}{\mathrm{d}(\hbar\omega)\mathrm{d}k_y\mathrm{d}x} \tag{8.2}$$

In practice, k_c is often determined by the size of the objective aperture which restricts the scattering angle, so it is appropriate to impose the cut-off isotopically as in Equation 8.1; in any case, $I(\hbar\omega)$ is fairly insensitive to the cut-off and Equation 8.1 provides a simple and convenient choice. In the following examples the beam energy has been set at 100 keV and the cut-off wavevector has been chosen to be 15 nm^{-1} (corresponding to scattering through a maximum angle of 9 mrad).

8.3. Normal incidence on graphite slabs

The first example is that of normal incidence on a single graphite slab of thickness $d = 100$ Å (Figure 8.3). The effects of anisotropy are clearly seen in the differences between the energy-loss spectra for the $\hat{z}$-orientation (solid line) and the two equivalent $\hat{x}$- and $\hat{y}$-orientations (dotted line). The interpretation of these spectra is aided by plotting the bulk and surface contributions separately (Figures 8.4 and 8.5).

In general agreement with previous work [70, 85], the bulk contributions have significant features at 5 eV, 6.5 eV, 19 eV and below 28 eV (Figure 8.4). The 5 eV shoulder and the 6.5 eV peak are associated with π plasmons (strictly speaking, combinations of collective and single-particle excitations of the π electrons). The 5 eV mode is excited only by momentum transfers parallel to the c-axis, while the 6.5 eV mode requires the momentum transfer to be perpendicular to the c-axis. The shoulder at 19 eV and the peaks below 28 eV are associated with coupled $\sigma + \pi$ plasmons. These modes are excited by momentum transfers that are, respectively, parallel and perpendicular to the c-axis. It follows from the geometry of the scattering process that the $\hat{z}$-orientation should strongly suppress the 5 eV and 19 eV plasmons but moderately favour the 6.5 eV and 28 eV plasmons. Figure 8.4 agrees with this prediction.

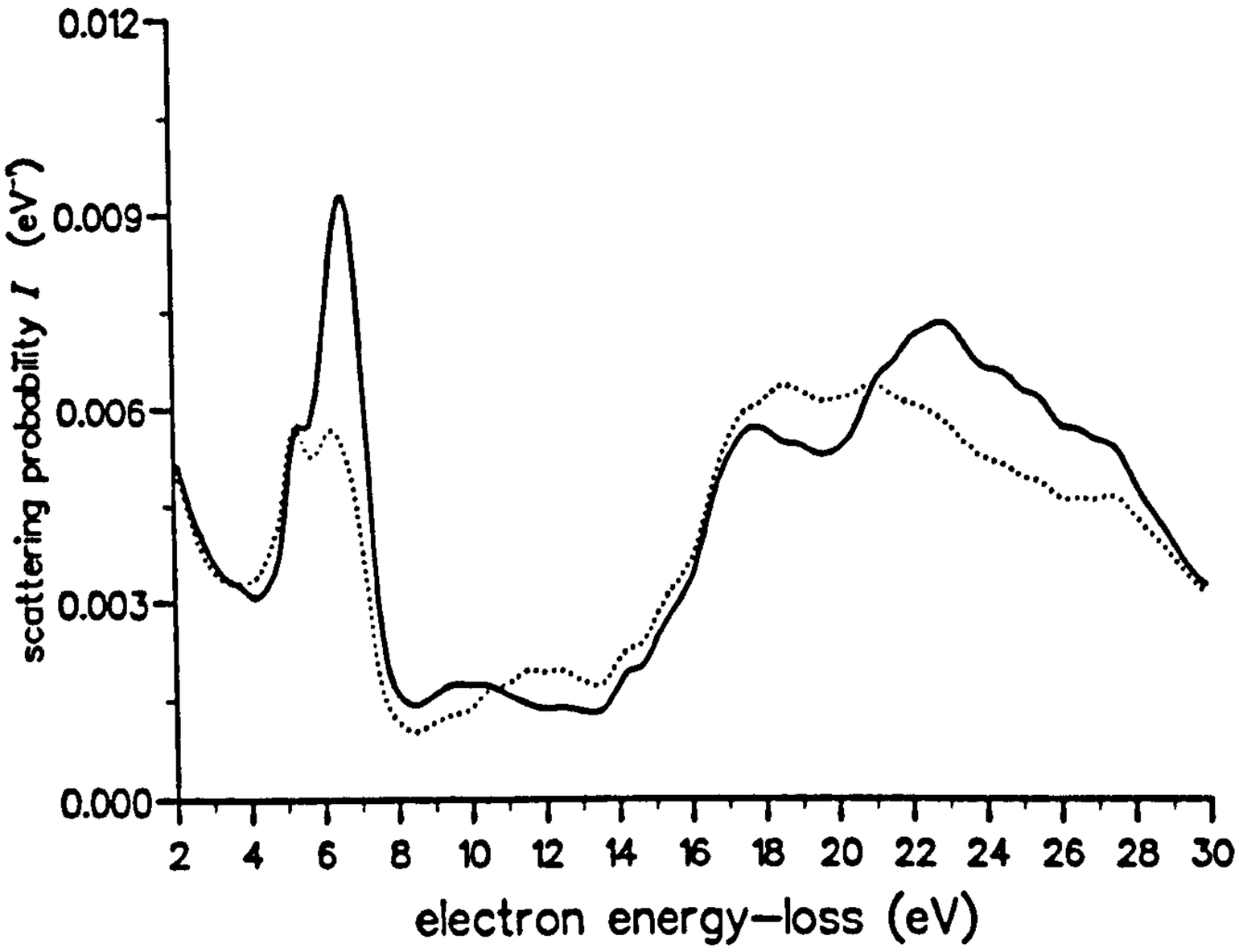

Figure 8.3 The scattering probability per unit energy range $I(\hbar\omega)$ for normal incidence on a single graphite slab of thickness $d = 100$ Å. The solid line corresponds the $\hat{z}$-orientation and the dotted line to the equivalent $\hat{x}$- and $\hat{y}$-orientations.

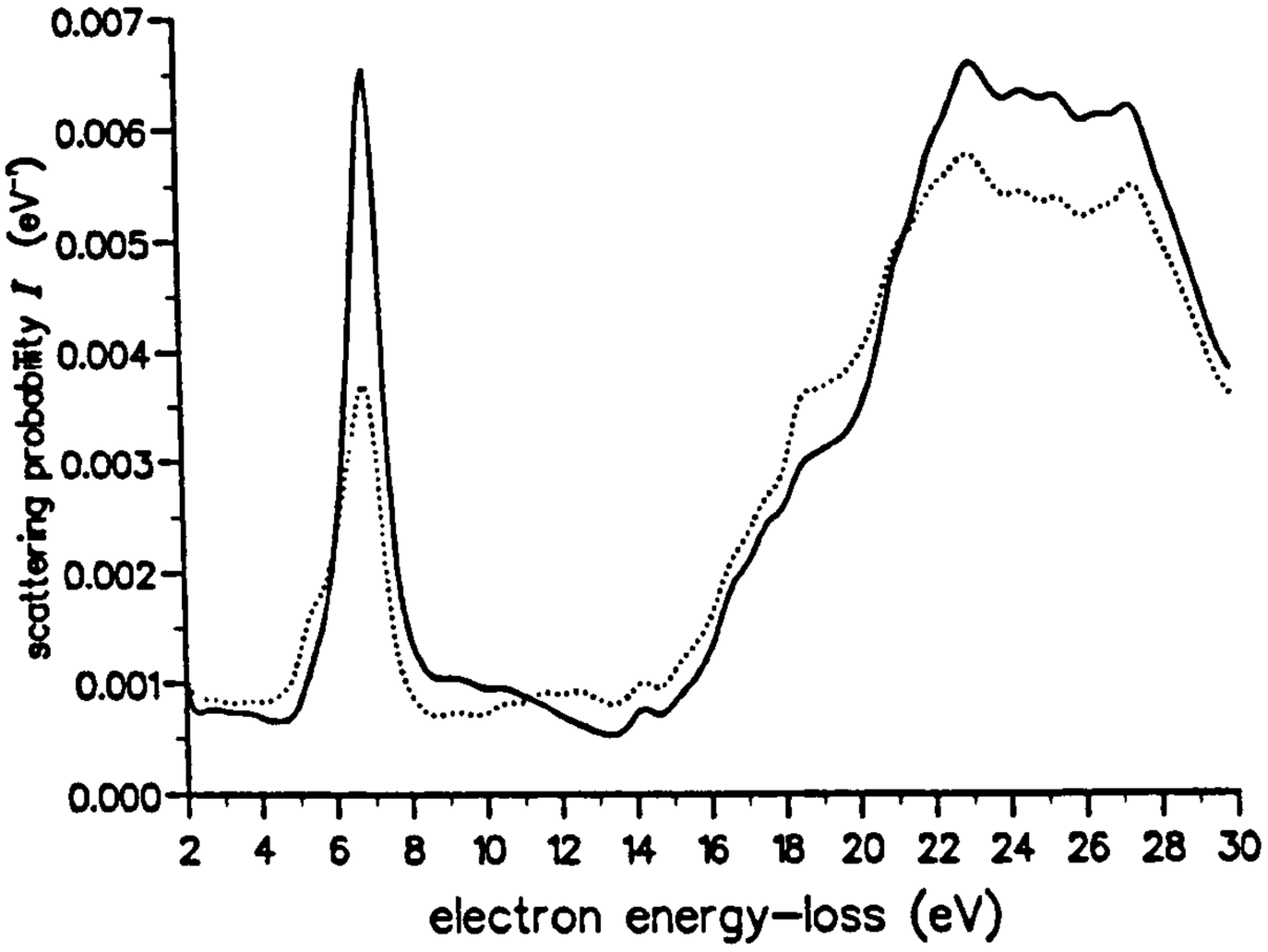

Figure 8.4 Bulk contributions to the energy-loss spectra of Figure 8.3.

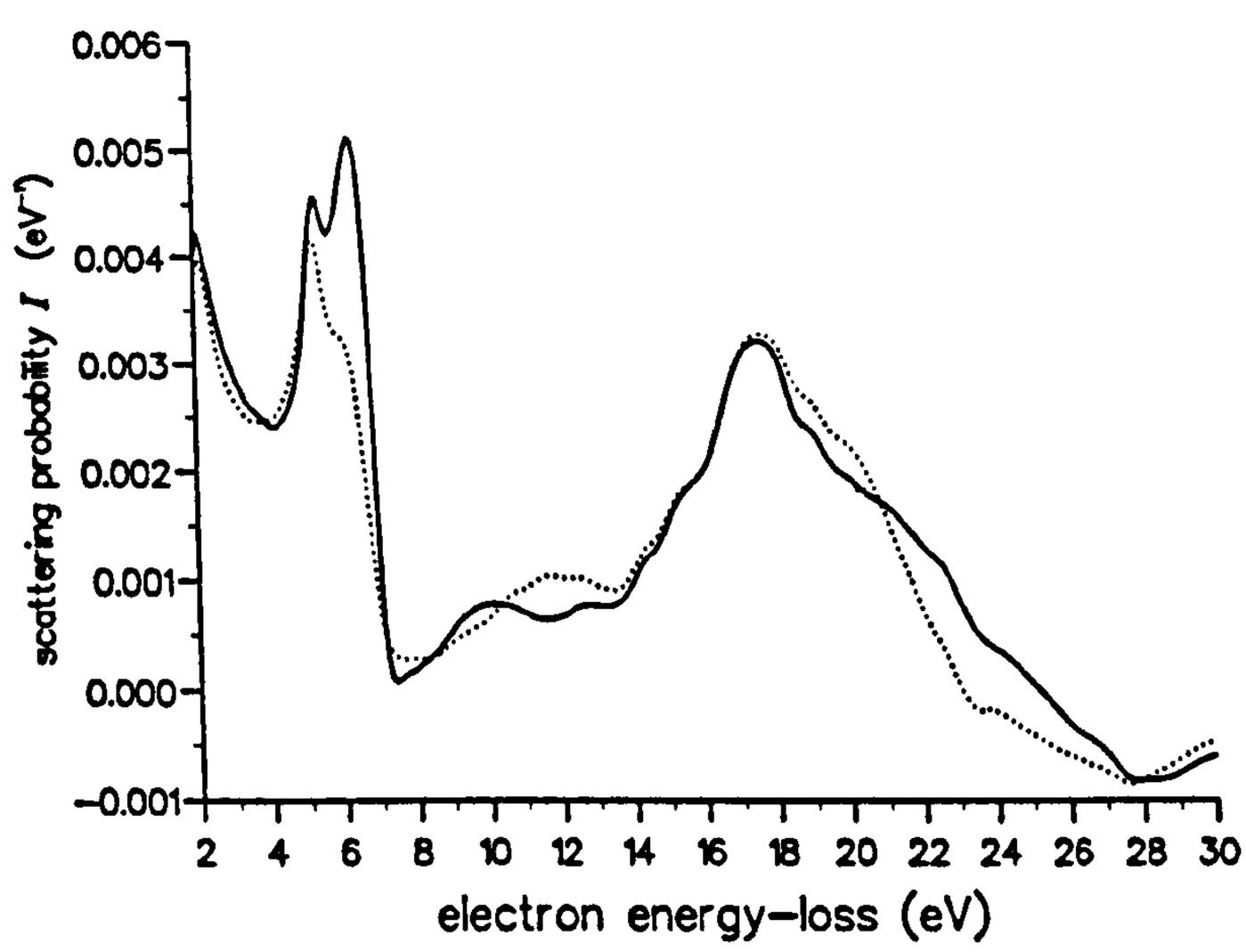

Figure 8.5 Surface contributions to the energy-loss spectra of Figure 8.3.

The surface contributions, shown in Figure 8.5, are dominated by surface plasmons around 6 eV and 18 eV. The low-energy surface plasmon modes are broader for the $\hat{z}$-orientation than for the other orientations. This offsets the narrowness of the low-energy bulk mode in the $\hat{z}$-orientation and explains why the 6 eV peak in Figure 8.3 has a similar width for all orientations of the c-axis. The surface mode at 18 eV is not very sensitive to the direction of the c-axis and is evident in all the energy-loss spectra of Figure 8.3. The $\hat{x}$ and $\hat{y}$ orientations produce slightly greater energy-loss in this region because the 18 eV surface mode merges with the 19 eV bulk mode that exists for these orientations. The 18 eV surface plasmon is broad enough to modify the shape of the loss spectrum above 20 eV; the peaks are shifted to lower energies than in the bulk spectrum because the surface contribution decreases with increasing energy. Finally, note that the weak structure in the spectrum between 9 eV and 13 eV is largely due to surface contributions, but these losses are best described as background because analysis of the dispersion relation $\left[\hat{C}_{10}\right] = 0$ shows that there are no self-sustaining surface plasmon modes in this range.

8.4. Parallel incidence on bounded graphite regions

As described in previous chapters, parallel incidence generally provides more insight in observing surface and interfacial plasmons. Here the theory developed in Chapter 7 is applied to study graphite surface mode.

Our first example is that of parallel incidence near a graphite–vacuum interface. Figure 8.6 shows $\mathrm{d}I(\hbar\omega)/\mathrm{d}x$, the scattering probability per unit energy range per unit path length for an electron travelling in the graphite region, 15 Å away from the interface. The usual bulk modes can be identified at 5 eV, 7 eV, 19 eV and 27.5 eV. In the $\hat{x}$-orientation, the c-axis is parallel to the beam, so the 5 eV and 19 eV modes are strongly suppressed and the 7 eV and 27.7 eV modes moderately enhanced in this orientation. With the beam

in this position (i.e. inside the graphite region) the surface contributions are much smaller than those due to the bulk, but a detailed analysis shows that they increase the effects of anisotropy for the 27.5 eV mode and decrease them for the 5–7 eV modes.

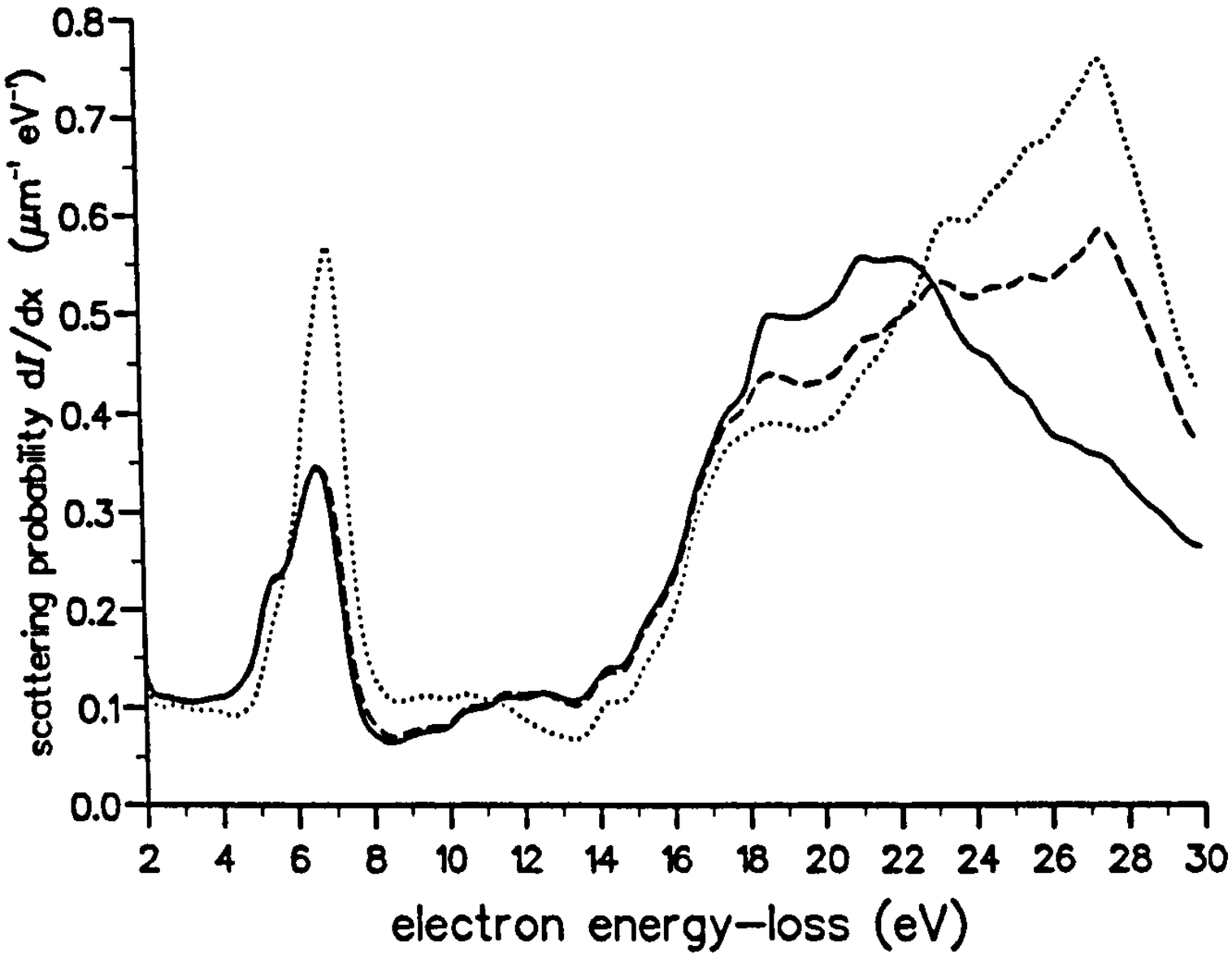

Figure 8.6 Scattering probability per unit energy range per unit path length , $\mathrm{d}I(\hbar\omega)/\mathrm{d}x$, for an electron in the graphite region, travelling parallel to, and 15 Å away from the interface between semi-infinite graphite and vacuum regions.

Very different results are obtained when the beam is outside the graphite region. Figure 8.7 shows $\mathrm{d}I(\hbar\omega)/\mathrm{d}x$ for an electron travelling in the vacuum region, 15 Å away from the interface. This spectrum is dominated by surface effects so there are no features at 28 eV. There are significant effects due to anisotropy in the surface modes. In comparison with the $\hat{z}$-orientation, the $\hat{x}$ and $\hat{y}$-orientations produce broader modes around 18–20 eV and narrower modes around 5–7 eV. Figure 8.8 shows the energy-loss spectrum when the beam is at the interface. This is quite similar to Figure 8.7, but the 18–20 eV modes are now more pronounced, particularly in the case of the $\hat{x}$-orientation.

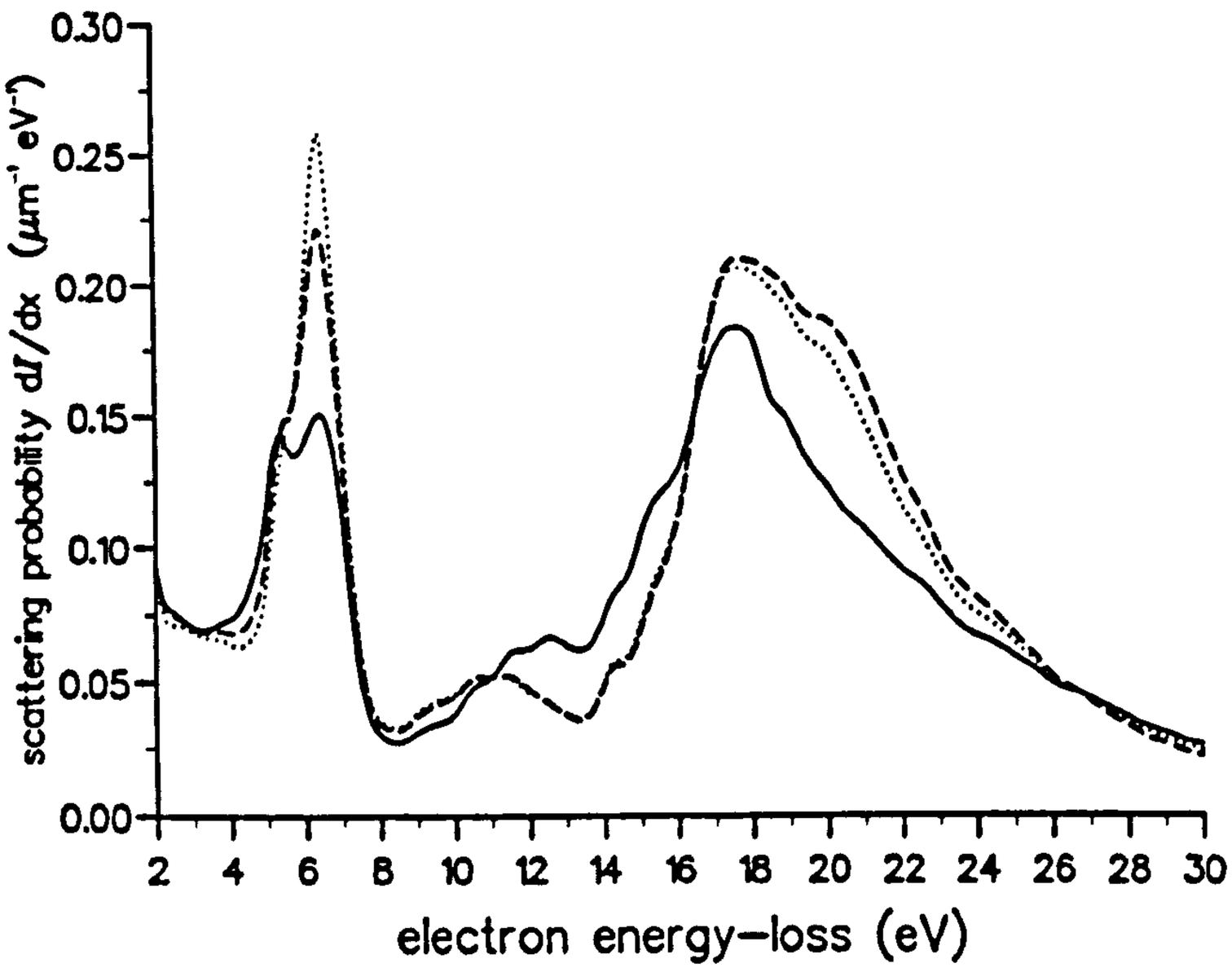

Figure 8.7 Scattering probability per unit energy range per unit path length, $\mathrm{d}I(\hbar\omega)/\mathrm{d}x$, for an electron in the vacuum region, travelling parallel to, and 15 Å away from the interface between semi-infinite graphite and vacuum regions.

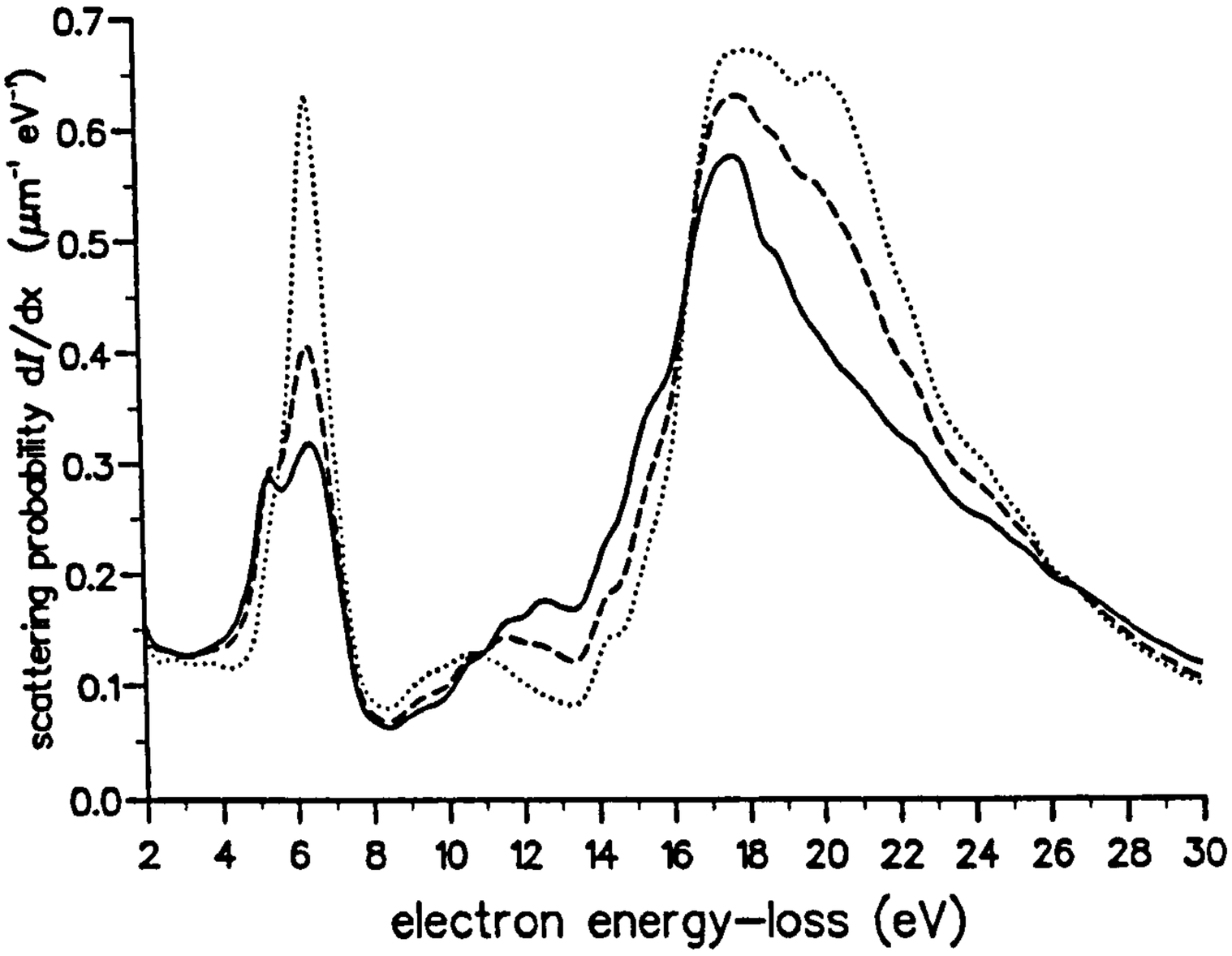

Figure 8.8 Scattering probability per unit energy range per unit path length, $\mathrm{d}I(\hbar\omega)/\mathrm{d}x$, for an electron travelling at the surface between semi-infinite vacuum and graphite regions.

The final example considers a thin graphite slab of thickness 30Å, sandwiched between semi-infinite vacuum and diamond regions. Figure 8.9 shows the energy-loss spectrum calculated for an electron in the middle of the graphite slab The main features of this spectrum are similar to those of Figure 8.6. When the electron beam is moved to the graphite-diamond interface, the spectrum alters considerably (Figure 8.10). Diamond-graphite interface modes are found at 14 eV and possibly at 22 eV and the modes between 28 eV and 30 eV can be interpreted as a combination bulk graphite and bulk diamond modes.

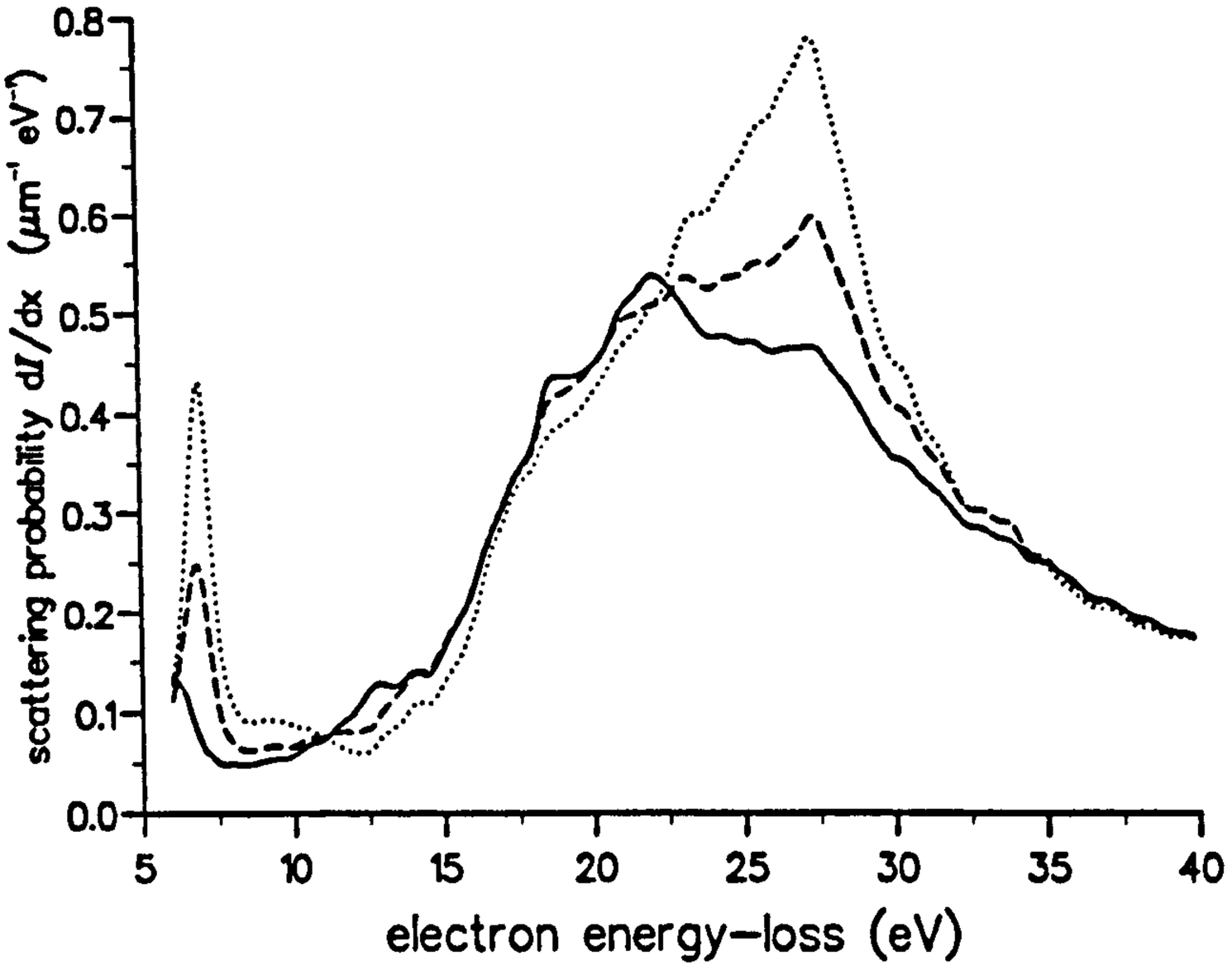

Figure 8.9 Scattering probability per unit energy range per unit path length, $dI(\hbar\omega)/dx$, for an electron travelling in the middle of the graphite region in a diamond/graphite/vacuum sandwich structure.

In summary, this chapter has developed FORTRAN codes to calculate the energy loss function for graphite single slabs, graphite single interfaces, and graphite slab sandwiched by diamond and vacuum. Comparison was made by changing the direction of anisotropic axis.

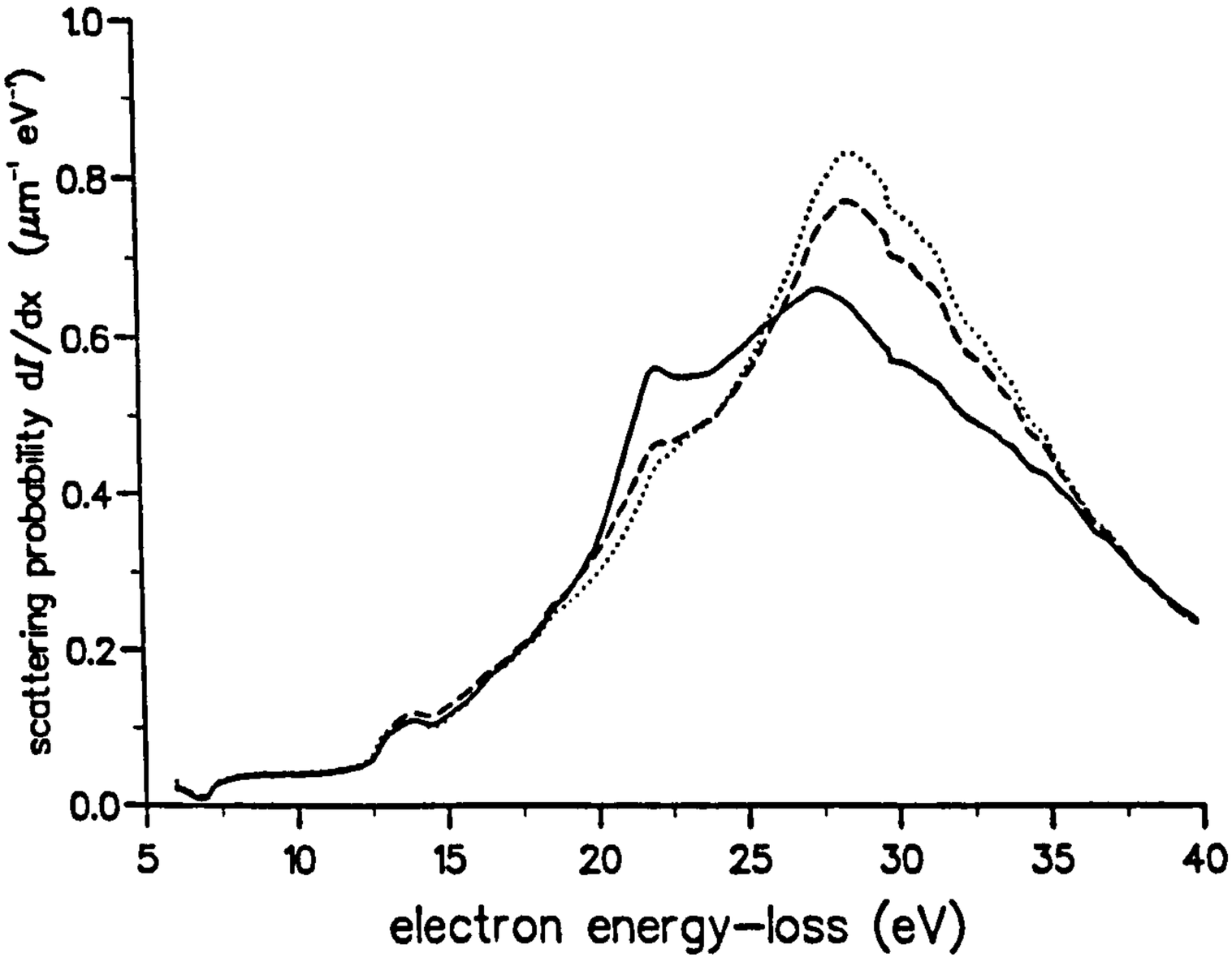

Figure 8.10 Scattering probability per unit energy range per unit path length, $\mathrm{d}I(\hbar\omega)/\mathrm{d}x$, for an electron travelling at the diamond-graphite interface of a diamond/graphite/vacuum sandwich structure.

Part IV

Conclusions

CHAPTER 9.

CONCLUSIONS

In this chapter, the main results of this research are summarised and possible prospects of applications of computer algebra to surface and interface polaritons are predicted.

9.1. Work done in this thesis

The main objective of this work has been to develop the dielectric theory of electron energy loss in multilayered slabs, composed of either isotropic or anisotropic media. Chapter 3 and 4 developed the semiclassical dielectric theory of energy loss. including retardation effects, for electrons travelling normal and parallel to a stratified slab composed of a finite number of isotropic layers. Starting from a transfer matrix formulation and using computer algebra, closed formulae for the Hertz vector, the dispersion relation and the energy loss spectrum were obtained, valid for any number of layers. Equations 3.30 and 3.35 derived in Chapter 3 provide a straightforward way of calculating the dispersion relation and energy loss spectrum for normal incidence on a multilayered slab. Equation 4.27 derived in Chapter 4 provides the basis for calculating the energy loss spectrum of an electron travelling parallel to the interfaces of a multilayered slab. This equation is valid for an arbitrary position of the electron beam and any number of layers. The analytical expressions of these results have been expressed in as a simple form as possible and checked against known results. The symmetries of the

solutions have also been examined.

Chapters 5 and 6 applied these analytical results to simple model of dielectric media and to real materials. In order to solve the dispersion relation for real materials we developed a procedure for extending the dielectric function into the lower-half complex frequency plane. This enabled us to explore the damping of surface plasmons. The expansion method used minimised problems caused by poles in the dielectric function, but it only works successfully if the dielectric function is fairly smooth.

The energy loss formulae were applied to various multilayered systems, namely, Mg/Al, Al/Al_2O_3, Al/SiO_2/Si and InSb/GaP. These calculations showed that for most metal/insulator interfaces or semiconductor/insulator interfaces, interfacial plasmons can be found below 10 eV. For semiconductor/semiconductor interfaces, the interfacial plasmons are difficult to detect in normal incidence, but parallel incidence provides a better chance to see for these modes.

Chapters 7 and 8 extended non-retarded dielectric theory to the case of multilayered anisotropic slabs. Starting from Poisson's equation and using a transfer matrix method, the dispersion relation was derived and the energy loss spectrum obtained for both normal and parallel incidence. The theory for multilayered anisotropic slabs is similar to that for multilayered isotropic slabs, except that the dielectric tensor has to be considered in the anisotropic case. The energy-loss formula was used to study bulk, surface and interfacial plasmons of graphite. The results showed that anisotropic effects are important for not only the bulk plasmon, but also for surface and interfacial plasmons.

In addition to the main text, a series of appendices was given to clarify and

extend the basic. These appendices not only give the detailed derivations of analytical expressions, but also offer some useful results not contained in main text. For example, Appendix D presents the classical theory of parallel incidence, which gives the much more simple form of loss probability of retarded theory of parallel incidence.

9.2. Computer algebra

The fundamental problem in macroscopic dielectric theory of electron energy loss consists of solving Maxwell's equations (or Poisson's equation in classical approximation) subject to appropriate boundary conditions. The algebra involved in such calculations is very cumbersome and time-consuming if done by hand and mistakes are easily made. Indeed, many papers have appeared containing algebraic or typographical errors , including the pioneering paper by Ritchie[6] and the well known paper by Kröger[21]. By contrast, computer algebra programs are convenient, safe and sure. Moreover, the analytical solutions can be written directly into a FORTRAN program for numerical calculation. This is more accurate and much faster than any method based on a direct numerical integration of Maxwell's equations.

Computer algebra can perform large analytical computations, such as solving linear equations, doing differentiation and integration etc. A computer algebra program consists of a set of functional commands which are evaluated sequential by the computer. To my best knowledge, this thesis is first to apply computer algebra to the study of electron energy loss. The basic framework of the computer algebra codes in this research consists of the following:

- Solving the Maxwell's (or Poisson's) equations to obtain the coefficients of Hertz vector or the electrostatic potential.

- Producing the electric and magnetic fields.
- Checking that these fields satisfy Maxwell's (or Poisson's) equations and the boundary conditions.
- Fourier transforming to produce expressions for the work done and then the energy loss probability.
- Simplifying all expressions as much as possible.

Computer algebra is powerful tool for mathematical analysis, but must be used with care if the results are not to be of unmanageable length. With care it is possible to obtain compact answers in specific cases (for example, multilayers of one, two or three layers). However, it is difficult to see how computer algebra could obtain more general results, valid for arbitrary number of layers. A combination of computer algebra and hand calculation has proved to be more effective than using either technique by itself. Throughout this work, computer algebra code has produced results for small numbers of layers (from $n = 1$ to 3). From these specific results, we have guessed the probable expression for any number of layers (arbitrary n). Then we have used mathematical induction to prove that these guesses are correct. Finally, computer algebra programs have checked the final formulae for higher values of n (from 4 to 10), and we have checked the symmetry and limiting behaviour of our answers.

One of the most important things in the 'guess–compute–compare' business is to know when you are right. Even before all the checks were complete, we were confident that out results were correct. Truth can often be recognised by its simplicity and relatively simple formulae, valid for a wide range of solutions, encouraged us to believe that our results were right.

Computer algebra has been a popular tool in theoretical particle physics, but

has not been widely used in theoretical condensed matter physics. I believe that this situation will be changed very rapidly. In particular, I would like to point out that the codes developed in this work can be used not only in the dielectric theory of electron energy loss, but also in other similar problems in surface and interfacial polaritons, such as

- *Electromagnetic transmission and reflection characteristics* in multilayered structures, leading to the derivation of Raman intensities and comparison with Raman scattering experiments.

- *Surface polaritons in ferromagnetic and antiferromagnetic multilayers.*

- *Magnetoplasmons in semiconducting multilayers* in the presence of an external magnetic field.

9.3. Future directions

The theory and methods developed in this work can be extended in many ways. Table 9.1 gives the topics directly related this work. The ticks show the cases dealt with in this thesis, while the blank spaces show possible directions of future work.

The simplest unexplored situation in Table 9.1 is oblique incidence on multilayered isotropic slabs in the classical approximation. The complexity of the transfer matrix and the source term, and hence of the recurrence relation in this calculation will be similar to the retarded normal calculation, but with slightly different forms. However, the work done and the energy loss probability will be complicated because one has to consider components of the the electric fields in both the x- and z- directions.

The retarded oblique calculation combines the difficulties of retarded parallel incidence and normal incidence. The transfer matrix is same as that of parallel incidence (4×4) but the source terms are complicated and vary from

	Normal		Parallel		Oblique	
	Classical	Retarded	Classical	Retarded	Classical	Retarded
Isotropic	√	√	√	√		
Anisotropic	√		√			

Table 9.1 Table of completed and suggested research on multilayered structures.

layer to layer. The sum over layers will, in the first instance, lead to very complicated formulae and effort will be needed to simplify the final answer.

For multilayered anisotropic slabs, classical oblique incidence will be a little harder than that of multilayered isotropic slabs because one has to consider the dielectric tensor. The most difficult part of these studies is considering retardation effects. The Hertz vector no longer exists in anisotropic media so one has to work with electric field and magnetic field directly. In this calculation, the recurrence relation will become much more complicated, and it is expected that the analytical expressions will be complicated too.

The theory described here could also extended to study other geometries, such as wire-like and dot-like structures of one polar semiconductor material within another (i.e. quantum wires and quantum dots). Such studies would help to understand the effects of confinement and decreased dimensionality on the electronic and optical properties of semiconductor systems.

To conclude, the results in this work not only solve some difficult theoretical problems but also offer the theoretical basis for future EELS analysis

in a STEM, especially in multilayers, superlattices and anisotropic media. The use of computer algebra in the theory of electron energy loss has been demonstrated as a useful and powerful technique. I believe that the theories, methods and philosophies developed in this work will be valuable in many other contexts.

APPENDIX A.

TRANSFER MATRIX AND DISPERSION BRACKETS

In Chapters 3 and 4, we introduced dispersion brackets. The solutions for Hertz vector, the dispersion relation, and the scattering probability were given in terms of dispersion brackets. In this appendix, the properties of dispersion brackets are studied.

A.1. Transfer matrices in terms of dispersion brackets

A.1.1. 2×2 transfer matrix for normal incidence

In Chapter 3, we introduced the transfer matrix between the j^{th} and $(j+1)^{\text{th}}$ layers:

$$\tau^{(j+1,j)} = \begin{pmatrix} h^{+}_{j+1,j} f_j^2 & h^{-}_{j+1,j} \\ h^{-}_{j+1,j} f_j^2 & h^{+}_{j+1,j} \end{pmatrix} \tag{A.1}$$

Here we generalize Equation A.1 to obtain the transfer matrix between i^{th} and j^{th} layers. That is we wish prove that the matrix product

$$\tau^{(ji)} = \prod_{k=i}^{j-1} \tau^{(k+1,k)}$$

(with successive terms ordered from right to left) is given by

$$\tau^{(ji)} = \begin{pmatrix} [C_{j-1,i}] & [D_{j-1,i}] \\ [E_{j-1,i}] & [F_{j-1,i}] \end{pmatrix} \tag{A.2}$$

where $[C_{ji}]$, $[D_{ji}]$, $[E_{ji}]$ and $[F_{ji}]$ were defined in the main text.

To prove that Equation A.2 is true, we proceed by induction. Setting $j = i+1$ gives

$$\tau^{(i+1i)} = \begin{pmatrix} h^+_{i+1,i} f_i^2 & h^-_{i+1,i} \\ h^-_{i+1,i} f_i^2 & h^+_{i+1,i} \end{pmatrix} = \begin{pmatrix} [C_{ii}] & [D_{ii}] \\ [E_{ii}] & [F_{ii}] \end{pmatrix}$$

So Equation A.2 is true for this case. We shall assume that Equation A.2 is true for a given $\tau^{(ji)}$ and then prove that it is true for $\tau^{(j+1,i)}$. This requires us to prove that

$$\begin{pmatrix} h^+_{j+1,j} f_j^2 & h^-_{j+1,j} \\ h^-_{j+1,j} f_j^2 & h^+_{j+1,j} \end{pmatrix} \begin{pmatrix} [C_{j-1,i}] & [D_{j-1,i}] \\ [E_{j-1,i}] & [F_{j-1,i}] \end{pmatrix} = \begin{pmatrix} [C_{ji}] & [D_{ji}] \\ [E_{ji}] & [F_{ji}] \end{pmatrix}$$

For example, it is necessary to show that

$$[C_{ji}] = h^+_{j+1,j} f_j^2 \, [C_{j-1,i}] + h^-_{j+1,j} \, [E_{j-1,i}]$$

The proof can be carried out by noting that $[C_{ji}]$ can be split into terms that involve $h^+_{j+1,j} f_j^2$ and terms that involve $h^-_{j+1,j}$:

$$[C_{ji}] = h^+_{j+1,j} \alpha + h^-_{j+1,j} \beta$$

The terms involving $h^+_{j+1,j}$ are those for which $h^+_{j+1,j}$ is uncontracted in $[C_{ji}]$. All other contractions are possible so

$$\alpha = f_j^2 \, [C_{j-1,i}]$$

The terms involving $h^-_{j+1,j}$ are those for which $h^+_{j+1,j}$ is contracted with another term in $[C_{ji}]$. Noting that

$$\overbrace{h^+_{j+1,j} f_j^2 h^+_{j,j-1} f^2_{j-1} \cdots h^+_{k+1,k}} f_k^2 \cdots h^+_{i+1,i} f_i^2$$
$$= h^-_{j+1,j} \overbrace{h^-_{j,j-1} f^2_{j-1} \cdots h^+_{k+1,k}} f_k^2 \cdots h^+_{i+1,i} f_i^2$$

and that

$$\overbrace{h^+_{j+1,j} f_j^2 h^+_{j,j-1}} f^2_{j-1} \cdots h^+_{k+1,k} f_k^2 \cdots h^+_{i+1,i} f_i^2$$
$$= h^-_{j+1,j} h^-_{j,j-1} f^2_{j-1} \cdots h^+_{k+1,k} f_k^2 \cdots h^+_{i+1,i} f_i^2$$

and allowing for all other contractions (i.e. those not involving $h^+_{j+1,j}$), we conclude that

$$\beta = [E_{j-1,i}]$$

which completes the proof by induction. Exactly similar proofs can easily be constructed for the other matrix elements.

A.1.2. 4×4 transfer matrix for parallel incidence

In Chapter 4, we gave a generalised transfer matrix without detailed derivation. Here we wish prove that Equation 4.17 is true by induction.

First from Equation 4.17, we have

$$T^{(j+1,j)} = \frac{1}{\kappa_{jj}} \begin{pmatrix} \eta_{jj}\tilde{\tau}^{(j+1,j)} & 0 \\ \chi^{(j+1,j)} & \tau^{(j+1,j)} \end{pmatrix}$$

It can be shown that this equation is same as Equation 4.9. So Equation 4.17 is true for for the special case of neighbouring regions. We now show that if Equation 4.17 is true for $T^{(ji)}$, then it is also true for $T^{(j+1,i)}$. We start from

$$T^{(j+1,i)} = T^{(j+1,j)}T^{(ji)}$$

Because $T^{(j+1,j)}$ and $T^{(ji)}$ are block triangular, it is easy to show that $T^{(j+1,i)}$ is block triangular and

$$\begin{pmatrix} T_{11}^{(j+1,i)} & T_{12}^{(j+1,i)} \\ T_{21}^{(j+1,i)} & T_{22}^{(j+1,i)} \end{pmatrix} = \frac{\eta_{ij}}{\kappa_{ij}} \tilde{T}^{(j+1,i)}$$

$$\begin{pmatrix} T_{33}^{(j+1,i)} & T_{34}^{(j+1,i)} \\ T_{43}^{(j+1,i)} & T_{44}^{(j+1,i)} \end{pmatrix} = \frac{1}{\kappa_{ij}} T^{(j+1,i)}$$

by arguments similar to those given for normal incidence. These results are of the expected form. The remaining task is to evaluate the matrix

$$T_{\text{lower left}}^{(j+1,i)} = \begin{pmatrix} T_{31}^{(j+1,i)} & T_{32}^{(j+1,i)} \\ T_{41}^{(j+1,i)} & T_{42}^{(j+1,i)} \end{pmatrix}$$

where

$$T_{31}^{(j+1,i)} = \sum_{k=1}^{4} T_{3k}^{(j+1,j)} T_{k1}^{(jk)}, \quad T_{32}^{(j+1,i)} = \sum_{k=1}^{4} T_{3k}^{(j+1,j)} T_{k2}^{(jk)}$$

$$T_{41}^{(j+1,i)} = \sum_{k=1}^{4} T_{4k}^{(j+1,j)} T_{k1}^{(jk)}, \quad T_{42}^{(j+1,i)} = \sum_{k=1}^{4} T_{4k}^{(j+1,j)} T_{k2}^{(jk)}$$

Taking the column vectors of $T_{\text{lower left}}^{(j+1,i)}$ and substituting for all above matrix elements involving, we have

$$\begin{pmatrix} T_{31}^{(j+1,i)} \\ T_{41}^{(j+1,i)} \end{pmatrix} = \frac{1}{\kappa_{ij}} \left\{ d_{j+1,j}\eta_{i,j-1} \begin{pmatrix} \left[\tilde{C}_{j-1,i}\right] f_j^2 + \left[\tilde{E}_{j-1,i}\right] \\ -\left[\tilde{C}_{j-1,i}\right] f_j^2 - \left[\tilde{E}_{j-1,i}\right] \end{pmatrix} \right.$$
$$\left. + \sum_{k=i}^{j-1} d_{k+1,k}\eta_{i,k-1}\tilde{\Lambda}_{ki}^{+} \begin{pmatrix} h_{j+1,j}^{+} f_j^2 \Theta_{j-1,k}^{-} + h_{j+1,j}^{-} \Phi_{j-1,k}^{-} \\ h_{j+1,j}^{-} f_j^2 \Theta_{j-1,k}^{-} + h_{j+1,j}^{+} \Phi_{j-1,k}^{-} \end{pmatrix} \right\}$$

and

$$\begin{pmatrix} T_{32}^{(j+1,i)} \\ T_{42}^{(j+1,i)} \end{pmatrix} = \frac{1}{\kappa_{ij}} \left\{ d_{j+1,j}\eta_{i,j-1} \begin{pmatrix} \left[\widetilde{D}_{j-1,i}\right] f_j^2 + \left[\tilde{F}_{j-1,i}\right] \\ -\left[\widetilde{D}_{j-1,i}\right] f_j^2 - \left[\tilde{F}_{j-1,i}\right] \end{pmatrix} \right.$$
$$\left. + \sum_{k=i}^{j-1} d_{k+1,k}\eta_{i,k-1}\tilde{\Omega}_{ki}^{+} \begin{pmatrix} h_{j+1,j}^{+} f_j^2 \Theta_{j-1,k}^{-} + h_{j+1,j}^{-} \Phi_{j-1,k}^{-} \\ h_{j+1,j}^{-} f_j^2 \Theta_{j-1,k}^{-} + h_{j+1,j}^{+} \Phi_{j-1,k}^{-} \end{pmatrix} \right\}$$

It can be shown that

$$h_{j+1,j}^{+} f_j^2 \Theta_{j-1,k}^{-} + h_{j+1,j}^{-} \Phi_{j-1,k}^{-} = \Theta_{jk}^{-}$$

$$h_{j+1,j}^{-} f_j^2 \Theta_{j-1,k}^{-} + h_{j+1,j}^{+} \Phi_{j-1,k}^{-} = \Phi_{jk}^{-}$$

$$\left[\tilde{E}_{j-1,i}\right] + \left[\tilde{C}_{j-1,i}\right] f_j^2 = \Theta_{jj}^{-}\tilde{\Lambda}_{ji}^{+} = -\Phi_{jj}^{-}\tilde{\Lambda}_{ji}^{+}$$

and

$$\left[\tilde{F}_{j-1,i}\right] + \left[\widetilde{D}_{j-1,i}\right] f_j^2 = \Theta_{jj}^{-}\tilde{\Omega}_{ji}^{+} = -\Phi_{jj}^{-}\tilde{\Omega}_{ji}^{+}$$

So we have

$$\begin{pmatrix} T_{31}^{(j+1,i)} \\ T_{41}^{(j+1,i)} \end{pmatrix} = \frac{1}{\kappa_{ij}} \left\{ \sum_{k=i}^{j-1} d_{k+1,k}\eta_{i,k-1} \begin{pmatrix} \Theta_{jk}^{-}\tilde{\Lambda}_{ki} \\ \Phi_{jk}^{-}\tilde{\Lambda}_{ki}^{+} \end{pmatrix} + d_{j+1,j}\eta_{i,j-1} \begin{pmatrix} \Theta_{jj}^{-}\tilde{\Lambda}_{ji}^{+} \\ \Phi_{jj}^{-}\tilde{\Lambda}_{ji}^{+} \end{pmatrix} \right\}$$
$$= \frac{1}{\kappa_{ij}} \sum_{k=i}^{j} d_{k+1,k}\eta_{i,k-1} \begin{pmatrix} \Theta_{jk}^{-}\tilde{\Lambda}_{ki}^{+} \\ \Phi_{jk}^{-}\tilde{\Lambda}_{ki}^{+} \end{pmatrix} = \frac{1}{\kappa_{ij}} \begin{pmatrix} \chi_{11}^{(j+1,i)} \\ \chi_{21}^{(j+1,i)} \end{pmatrix}$$

and

$$\begin{pmatrix} T_{32}^{(j+1,i)} \\ T_{42}^{(j+1,i)} \end{pmatrix} = \frac{1}{\kappa_{ij}} \left\{ \sum_{k=i}^{j-1} d_{k+1,k}\eta_{i,k-1} \begin{pmatrix} \Theta_{jk}^{-}\tilde{\Omega}_{ki} \\ \Phi_{jk}^{-}\tilde{\Omega}_{ki}^{+} \end{pmatrix} + d_{j+1,j}\eta_{i,j-1} \begin{pmatrix} \Theta_{jj}^{-}\tilde{\Omega}_{ji}^{+} \\ \Phi_{jj}^{-}\tilde{\Omega}_{ji}^{+} \end{pmatrix} \right\}$$
$$= \frac{1}{\kappa_{ij}} \sum_{k=i}^{j} d_{k+1,k}\eta_{i,k-1} \begin{pmatrix} \Theta_{jk}^{-}\tilde{\Omega}_{ki}^{+} \\ \Phi_{jk}^{-}\tilde{\Omega}_{ki}^{+} \end{pmatrix} = \frac{1}{\kappa_{ij}} \begin{pmatrix} \chi_{12}^{(j+1,i)} \\ \chi_{22}^{(j+1,i)} \end{pmatrix}$$

which completes the proof by induction.

A.2. Properties of dispersion brackets

According to the definition

$$_{T}^{(j+1,i)} = {}_{T}^{(j+1,k)}{}_{T}^{(k,i)}$$

One immediately obtains

$$\begin{pmatrix} [C_{ji}] & [D_{ji}] \\ [E_{ji}] & [F_{ji}] \end{pmatrix} = \begin{pmatrix} [C_{jk}] & [D_{jk}] \\ [E_{jk}] & [F_{jk}] \end{pmatrix} \begin{pmatrix} [C_{k-1i}] & [D_{k-1i}] \\ [E_{k-1i}] & [F_{k-1i}] \end{pmatrix} \tag{A.3}$$

which can be written as

$$[C_{ji}] = [C_{jk}]\,[C_{k-1,i}] + [D_{jk}]\,[E_{k-1,i}] \tag{A.3a}$$

$$[D_{ji}] = [C_{jk}]\,[D_{k-1,i}] + [D_{jk}]\,[F_{k-1,i}] \tag{A.3b}$$

$$[E_{ji}] = [E_{jk}]\,[C_{k-1,i}] + [F_{jk}]\,[E_{k-1,i}] \tag{A.3c}$$

and

$$[F_{ji}] = [E_{jk}]\,[D_{k-1,i}] + [F_{jk}]\,[F_{k-1,i}] \tag{A.3d}$$

Using Equations A.3a and A.3b and expanding $[C_{nj}]$ and $[D_{nj}]$ in terms of $[C_{nj+1}]$ and $[D_{nj+1}]$ it follows that

$$[C_{jj}]\,[D_{nj}] - [D_{jj}]\,[C_{nj}] = h_{jj}^{+} h_{j+1,j+1}^{+} f_j^2\,[D_{n,j+1}] \tag{A.4}$$

and

$$[E_{jj}]\,[D_{nj}] - [F_{jj}]\,[C_{nj}] = -h_{jj}^{+} h_{j+1,j+1}^{+} f_j^2\,[C_{n,j+1}] \tag{A.5}$$

For $j \geq k \geq i$, from Equation A.3, we have

$$\begin{pmatrix} [C_{jk}] & [D_{jk}] \\ [E_{jk}] & [F_{jk}] \end{pmatrix}^{-1} \begin{pmatrix} [C_{ji}] & [D_{ji}] \\ [E_{ji}] & [F_{ji}] \end{pmatrix} = \begin{pmatrix} [C_{k-1,i}] & [D_{k-1,i}] \\ [E_{k-1}] & [F_{j-1,i}] \end{pmatrix} \tag{A.6}$$

where

$$\begin{pmatrix} [C_{jk}] & [D_{jk}] \\ [E_{jk}] & [F_{jk}] \end{pmatrix}^{-1} = \frac{1}{\Delta_{kj}} \begin{pmatrix} [F_{jk}] & -[D_{jk}] \\ -[E_{jk}] & [C_{jk}] \end{pmatrix}$$

and

$$\Delta_{kj} = \begin{vmatrix} [C_{jk}] & [D_{jk}] \\ [E_{jk}] & [F_{jk}] \end{vmatrix} \tag{A.7}$$

So from Equation A.6, we have following identities:

$$[C_{ji}]\,[E_{jk}] - [C_{jk}]\,[E_{ji}] = -\Delta_{kj}\,[E_{k-1,i}] \tag{A.6a}$$

$$[C_{ji}]\,[F_{jk}] - [D_{jk}]\,[E_{ji}] = \Delta_{kj}\,[C_{k-1,i}] \tag{A.6b}$$

$$[D_{ji}]\,[F_{jk}] - [D_{jk}]\,[F_{ji}] = \Delta_{kj}\,[D_{k-1,i}] \tag{A.6c}$$

$$[D_{ji}]\,[E_{jk}] - [C_{jk}]\,[F_{ji}] = -\Delta_{kj}\,[F_{k-1,i}] \tag{A.6d}$$

It can be shown that

$$\Delta_{kj} = \prod_{i=k}^{j} \Delta_i = \prod_{i=k}^{j} \left(4\varepsilon_i\varepsilon_{i+1}q_iq_{i+1}f_i^2\right)$$

Furthermore, using Equations A.3a, A.6a and A.6b, we can show

$$[C_{n0}]\,[C_{jk}] - [C_{j0}]\,[C_{nk}] = \Delta_{kj}\,[D_{n,j+1}]\,[E_{k-1,0}] \tag{A.8}$$

$$[C_{n0}]\,[D_{jk}] - [C_{j0}]\,[D_{nk}] = -\Delta_{kj}\,[D_{n,j+1}]\,[C_{k-1,0}] \tag{A.9}$$

$$[C_{n0}]\,[E_{jk}] - [E_{j0}]\,[C_{nk}] = -\Delta_{kj}\,[C_{n,j+1}]\,[E_{k-1,0}] \tag{A.10}$$

and

$$[C_{n0}]\,[F_{jk}] - [E_{j0}]\,[D_{nk}] = \Delta_{kj}\,[C_{n,j+1}]\,[C_{k-1,0}] \tag{A.11}$$

We defined following variables in Chapter 4:

$$\Theta^{\sigma}_{ji} = [C_{j,i+1}] + \sigma\,[D_{j,i+1}] \tag{A.12}$$

$$\Phi^{\sigma}_{ji} = [E_{j,i+1}] + \sigma\,[F_{j,i+1}] \tag{A.13}$$

$$\Lambda^{\sigma}_{ji} = [C_{j-1,i}]\,f_j^2 + \sigma\,[E_{j-1,i}] \tag{A.14}$$

$$\Omega^{\sigma}_{ji} = [D_{j-1,i}]\,f_j^2 + \sigma\,[F_{j-1,i}] \tag{A.15}$$

Using Equation A.3, one has follows

$$[C_{ji}] + [E_{ji}] = \left(h^{+}_{j+1,j} + h^{-}_{j+1,j}\right)\Lambda^{+}_{ji} \tag{A.16}$$

$$[C_{ji}] - [E_{ji}] = \left(h^{+}_{j+1,j} - h^{-}_{j+1,j}\right)\Lambda^{-}_{ji} \tag{A.17}$$

$$[C_{ji}] + [D_{ji}]\,f_i^2 = \left(h^{+}_{i+1,i} + h^{-}_{i+1,i}\right) f_i^2\Theta^{+}_{ji} \tag{A.18}$$

$$[C_{ji}] - [D_{ji}]\,f_i^2 = \left(h^{+}_{i+1,i} - h^{-}_{i+1,i}\right) f_i^2\Theta^{-}_{ji} \tag{A.19}$$

$$[D_{ji}] + [F_{ji}] = \left(h^{+}_{j+1,j} + h^{-}_{j+1,j}\right)\Omega^{+}_{ji} \tag{A.20}$$

$$[D_{ji}] - [F_{ji}] = \left(h^{+}_{j+1,j} - h^{-}_{j+1,j}\right)\Omega^{-}_{ji} \tag{A.21}$$

Equations A.3–A.21 are true for the dispersion brackets with tilde~and hat ˆ. The exceptions are

$$\tilde{\Delta}_{kj} = \prod_{i=k}^{j}\left(4q_iq_{i+1}f_i^2\right)$$

and

$$\hat{\Delta}_{kj} = \prod_{i=k}^{j} \left(4\epsilon_i^{(33)} \epsilon_{i+1}^{(33)} \kappa_i \kappa_{i+1} \hat{f}_i^2 \right)$$

Furthermore, it is easy to show that

$$\left[X_{ji}^{\sigma} \right] = S_{j+1,j}^{\sigma} f_j^2 \left[C_{j-1,i} \right] + S_{j+1,j}^{-\sigma} \left[E_{j-1,i} \right] \tag{A.22}$$

$$\left[Y_{ij}^{\sigma} \right] = S_{i,i+1}^{\sigma} \left[C_{j,i+1} \right] - S_{i,i+1}^{-\sigma} \left[D_{j,i+1} \right] \tag{A.23}$$

and

$$h_{ii}^{+} S_{ij}^{\sigma} + h_{ij}^{+} S_{ji}^{\sigma} + h_{ij}^{-} S_{ji}^{-\sigma} = 0. \tag{A.24}$$

APPENDIX B.

DERIVATION OF FORMULA FOR NORMAL INCIDENCE

In Chapter 3, solutions for Hertz vector, the dispersion relation, and the scattering probability were given and their symmetrical properties were examined. In this appendix, general proofs of these results will be sketched.

B.1. Proof of Equation 3.23 for the Hertz vector

Substituting $j = 0$ in Equation 3.23, one has

$$\boldsymbol{\alpha}_0 = -\frac{1}{[C_{n0}]} \begin{pmatrix} 1 \\ 0 \end{pmatrix} \sum_{k=0}^{n} \psi_{1k}^{+} \left[Y_{kn}^{+} \right]$$

which recovers Equation 3.15.

Now we can try a general proof of Equation 3.23 by induction. Starting from Equation 3.14, one has

$$\boldsymbol{\alpha}_{j+1} = \frac{1}{h_{j+1j+1}^{+} f_j b_j^{+}} \begin{pmatrix} [C_{jj}]\, \alpha_j^{+} + [D_{jj}]\, \alpha_j^{-} \\ [E_{jj}]\, \alpha_j^{+} + [F_{jj}]\, \alpha_j^{-} \end{pmatrix} + \frac{1}{h_{j+1j+1}^{+}} \mathbf{S}_j \tag{B.1}$$

Substituting for α_j^{+} and α_j^{-} from Equation 3.23 and rearranging terms, Equation B.1 can be written as three terms

$$\alpha_{j+1} = \mathbf{A}_1 + \mathbf{A}_2 + \mathbf{A}_3 \tag{B.2}$$

where

$$\mathbf{A}_1 = \frac{1}{h^+_{j+1,j+1}} \mathbf{S}_j$$

$$\mathbf{A}_2 = -\frac{1}{h^+_{j+1,j+1} f_j b^+_j} \frac{1}{[C_{n0}]} \begin{pmatrix} [C_{jj}][D_{nj}] - [D_{jj}][C_{nj}] \\ [E_{jj}][D_{nj}] - [F_{jj}][C_{nj}] \end{pmatrix} \sum_{k=0}^{j-1} \psi^-_{k+1,j-1} \left[X^-_{k0}\right]$$

$$\mathbf{A}_3 = -\frac{1}{h^+_{j+1,j+1}} \frac{1}{[C_{n0}]} \begin{pmatrix} [C_{jj}][C_{j-1,0}] + [D_{jj}][E_{j-1,0}] \\ [E_{jj}][C_{j-1,0}] + [F_{jj}][E_{j-1,0}] \end{pmatrix} \sum_{k=j}^{n} \psi^+_{j+1,k} \left[Y^+_{kn}\right]$$

Using Equations A.4 and A.5 $\mathbf{A}_2$ can be further simplified as

$$\mathbf{A}_2 = \frac{1}{[C_{n0}]} \begin{pmatrix} -[D_{n,j+1}] \\ [C_{n,j+1}] \end{pmatrix} \sum_{k=0}^{j-1} \psi^-_{k+1,j} \left[X^-_{k0}\right]$$

as expected. Using Equations A.3a and A.3c, $\mathbf{A}_3$ can be simplified as

$$\mathbf{A}_3 = -\frac{1}{h^+_{j+1,j+1}} \frac{1}{[C_{n0}]} \begin{pmatrix} [C_{j0}] \\ [E_{j0}] \end{pmatrix} \sum_{k=j}^{n} \psi^+_{j+1,k} \left[Y^+_{kn}\right]$$

$\mathbf{A}_3$ can be further split up into

$$\mathbf{A}_{31} = -\frac{1}{h^+_{j+1,j+1}} \frac{1}{[C_{n0}]} \begin{pmatrix} [C_{j0}] \\ [E_{j0}] \end{pmatrix} \psi^+_{j+1,j} \left[Y^+_{jn}\right]$$

and

$$\mathbf{A}_{32} = -\frac{1}{[C_{n0}]} f_{j+1} b^+_{j+1} \begin{pmatrix} [C_{j0}] \\ [E_{j0}] \end{pmatrix} \sum_{k=j+1}^{n} \psi^+_{j+2,k} \left[Y^+_{kn}\right]$$

where we used Equation 3.16.

Finally, using Equations A.3, A.22, A.23 and A.24, we add $\mathbf{A}_1$ and $\mathbf{A}_{31}$ to obtain

$$\mathbf{A}_1 + \mathbf{A}_{31} = \frac{1}{h^+_{j+1,j+1}\,[C_{n0}]} \left\{ \begin{pmatrix} S^+_{j,j+1} \\ -S^-_{j,j+1} \end{pmatrix} [C_{n0}] - \begin{pmatrix} [C_{j0}] \\ [E_{j0}] \end{pmatrix} \left[Y^+_{jn}\right] \right\}$$

Using Equation A.23 and reorganising terms we have

$$\mathbf{A}_1 + \mathbf{A}_{31} = \frac{1}{h^+_{j+1,j+1}\,[C_{n0}]} \times \begin{pmatrix} S^+_{j,j+1}\left([C_{n0}] - [C_{n,j+1}]\,[C_{j0}]\right) + [C_{j0}]\,S^-_{j,j+1}\,[D_{n,j+1}] \\ -S^-_{j,j+1}\left([C_{n0}] - [D_{n,j+1}]\,[E_{j0}]\right) - [E_{j0}]\,S^-_{j,j+1}\,[C_{n,j+1}] \end{pmatrix}$$

Then using Equation A.3a, we obtain

$$\mathbf{A}_1 + \mathbf{A}_{31} = -\frac{1}{h^+_{j+1,j+1}\,[C_{n0}]} \begin{pmatrix} -[D_{n,j+1}] \\ [C_{n,j+1}] \end{pmatrix} \left(S^+_{j,j+1}\,[E_{j0}] + S^-_{j,j+1}\,[C_{j0}]\right)$$

Collecting all terms together, one obtains

$$\boldsymbol{\alpha}_{j+1} = \frac{1}{[C_{n0}]} \left\{ \mathbf{M}_{n,j+1} \sum_{k=0}^{j} \psi^-_{k+1,j} \left[X^-_{k0}\right] - \mathbf{N}_{j0} f_{j+1} b^+_{j+1} \sum_{k=j+1}^{n} \psi^+_{j+2,k} \left[Y^+_{kn}\right] \right\}$$

which completes the the proof that leads from $\boldsymbol{\alpha}_j$ to $\boldsymbol{\alpha}_{j+1}$.

In summary, we have used mathematical induction to prove that the solution (Equation 3.23) is general true. Throughout this proof, we have use various identities involving dispersion brackets.

B.2. Derivation of the loss function

In Chapter 3, Equation 3.25 represented the work done in terms of Hertz coefficients and source terms. Here we start from Equation 3.28 and the solution for the Hertz vector coefficients to derive the energy loss function.

It is convenient to start from the quantity $[C_{n0}]\,\chi_{\text{bdy}}/k^2$. Expanding Equation 3.28, this can be written as

$$[C_{n0}]\,\chi_{\text{bdy}}/k^2 = \frac{iv}{\omega}\left\{\frac{q_0\alpha_0^+}{p_0^2}[C_{n0}] + \sum_{j=1}^{n}\frac{q_j}{p_j^2}R_j^- + \frac{q_{n+1}\alpha_{n+1}^-}{p_{n+1}^2}[C_{n0}]\right\}$$
$$- \left\{\frac{\alpha_0^+}{p_0^2}[C_{n0}] + \sum_{j=1}^{n}\frac{1}{p_j^2}R_j^+ - \frac{\alpha_{n+1}^-}{p_{n+1}^2}[C_{n0}]\right\}$$

where

$$R_j^\sigma = [C_{n0}]\left(\frac{\alpha_j^+ f_j^2 + \sigma\alpha^-}{f_j b_j^+} - \left(\alpha_j^+ + \sigma\alpha_j^-\right)\right)$$

Substituting α_i^+ and α_i^- into R_j^σ and using Equations A.12–A.19 together with the notation

$$r_j^\sigma = \begin{cases} \epsilon_j & \text{if} \quad \sigma = + \\ q_j & \text{if} \quad \sigma = - \end{cases}$$

one obtains

$$R_j^\sigma = \sigma\left(\frac{r_{j+1}^\sigma}{r_j^\sigma}\psi_{jj}^-\Theta_{nj}^{-\sigma} - \Theta_{n,j-1}^{-\sigma}\right)\sum_{k=0}^{j-1}\psi_{k+1,j-1}^-\left[X_{k0}^-\right]$$
$$+ \left(\frac{r_{j-1}^\sigma}{r_j^\sigma}\psi_{jj}^+\Lambda_{j-1,0}^\sigma - \Lambda_{j0}^\sigma\right)\sum_{k=j}^{n}\psi_{j+1,k}^+\left[Y_{kn}^+\right]$$

We now define

$$A_j^\sigma = \Theta_{nj}^\sigma\sum_{k=0}^{j-1}\psi_{k+1,j}^-\left[X_{k0}^-\right]$$

and

$$B_j^\sigma = \Lambda_{j-1,0}^\sigma\sum_{k=j}^{n}\psi_{jk}^+\left[Y_{kn}^+\right]$$

So R_j^σ can be written as

$$R_j^\sigma = \sigma\left(\frac{r_{j+1}^\sigma}{r_j^\sigma}A_j^{-\sigma} - A_{j-1}^{-\sigma} - \Theta_{n,j-1}^{-\sigma}\left[X_{j-1,0}^-\right]\right) + \left(\frac{r_{j-1}^\sigma}{r_j^\sigma}B_j^\sigma - B_{j+1}^\sigma - \Lambda_{j0}^\sigma\left[Y_{jn}^+\right]\right)$$

Now we can split R_j^σ as

$$R_j^\sigma = \frac{\sigma U_j^\sigma - V_j^\sigma}{r_j^\sigma}$$

where

$$U_j^\sigma = r_{j+1}^\sigma A_j^{-\sigma} - r_j^\sigma A_{j-1}^{-\sigma} - r_j^\sigma \Theta_{n,j-1}^{-\sigma}\left[X_{j-1,0}^-\right]$$

and

$$V_j^\sigma = r_j^\sigma B_{j+1}^\sigma - r_{j-1}^\sigma B_j^\sigma + r_j^\sigma \Lambda_{j0}^\sigma\left[Y_{jn}^+\right]$$

So

$$[C_{n0}]\,\chi_{\text{bdy}}/k^2 = \frac{\mathrm{i}v}{\omega}\left\{\frac{q_0\alpha_0^+}{p_0^2}[C_{n0}] - \sum_{j=1}^n \frac{V_j^-}{p_j^2} + \frac{\alpha_{n+1}^- q_{n+1}}{p_{n+1}^2}[C_{n0}] - \sum_{j=1}^n \frac{U_j^-}{p_j^2}\right\}$$
$$- \left\{\frac{\alpha_0^+}{p_0^2}[C_{n0}] - \sum_{j=1}^n \frac{V_j^+}{\epsilon_j p_j^2} + \sum_{j=1}^n \frac{U_j^+}{\epsilon_j p_j^2} - \frac{\alpha_{n+1}^-}{p_{n+1}^2}[C_{n0}]\right\}$$

Now

$$\sum_{j=1}^n \frac{q_{j+1}A_j^+ - q_j A_{j-1}^+}{p_j^2} = \sum_{j=1}^{n-1} q_{j+1}A_j^+\left(\frac{1}{p_j^2} - \frac{1}{p_{j+1}^2}\right) + \frac{q_{n+1}A_n^+}{p_n^2}$$

$$\sum_{j=1}^n \frac{q_j B_{j+1}^- - q_{j-1}B_j^-}{p_j^2} = \sum_{j=1}^{n-1} q_j B_{j+1}^-\left(\frac{1}{p_j^2} - \frac{1}{p_{j+1}^2}\right) - \frac{q_0 B_1^-}{p_1^2}$$

$$\sum_{j=1}^n \frac{\epsilon_{j+1}A_j^- - \epsilon_j A_{j-1}^-}{\epsilon_j p_j^2} = \sum_{j=1}^{n-1} \epsilon_{j+1}A_j^-\left(\frac{1}{\epsilon_j p_j^2} - \frac{1}{\epsilon_{j+1}p_{j+1}^2}\right) + \frac{\epsilon_{n+1}A_n^+}{\epsilon_n p_n^2}$$

$$\sum_{j=1}^n \frac{\epsilon_j B_{j+1}^+ - \epsilon_{j-1}B_j^+}{\epsilon_j p_j^2} = \sum_{j=1}^{n-1} \epsilon_j B_{j+1}^+\left(\frac{1}{\epsilon_j p_j^2} - \frac{1}{\epsilon_j p_{j+1}^2}\right) - \frac{\epsilon_0 B_1^+}{\epsilon_1 p_1^2}$$

Also, from Equation 3.23, we have

$$\alpha_0^+ = -\frac{1}{[C_{n0}]}\left(B_1^{\pm} + \left[Y_{0n}^+\right]\right)$$

and

$$\alpha_{n+1}^- = \frac{1}{[C_{n0}]}\left(A_n^{\pm} + \left[X_{n0}^-\right]\right) .$$

So, substituting α_0^+ and α_{n+1}^- and using

$$\frac{1}{p_{j+1}^2} - \frac{1}{p_j^2} = \frac{d_{j,j+1}\omega^2}{c^2 p_j^2 p_{j+1}^2}$$

and

$$\frac{1}{\epsilon_{j+1}p_{j+1}^2} - \frac{1}{\epsilon_j p_j^2} = \frac{d_{j,j+1}p_{j,j+1}^2}{\epsilon_j \epsilon_{j+1} p_j^2 p_{j+1}^2}$$

we obtain

$$\frac{q_0\alpha_0^+}{p_0^2}[C_{n0}] - \sum_{j=1}^{n}\frac{V_j^-}{p_j^2} = -\sum_{j=1}^{n}\frac{d_{j-1,j}q_{j-1}\omega^2}{c^2 p_{j-1}^2 p_j^2}B_j^- - \sum_{j=0}^{n}\frac{q_j}{p_j^2}\Lambda_{j0}^-\left[Y_{jn}^+\right]$$

$$\frac{\alpha_{n+1}^- q_{n+1}}{p_{n+1}^2}[C_{n0}] - \sum_{j=1}^{n}\frac{U_j^-}{p_j^2} = -\sum_{j=2}^{n+1}\frac{d_{j-1,j}q_j\omega^2}{c^2 p_{j-1}^2 p_j^2}A_{j-1}^+ + \sum_{j=1}^{n+1}\frac{q_j}{p_j^2}\Theta_{n,j-1}^+\left[X_{j-1,0}^-\right]$$

$$\frac{\alpha_0^+}{p_0^2}[C_{n0}] - \sum_{j=1}^{n}\frac{V_j^+}{\epsilon_j p_j^2} = \sum_{j=1}^{n}\frac{d_{j-1,j}p_{j-1,j}^2}{\epsilon_j p_{j-1}^2 p_j^2}B_j^+ - \sum_{j=1}^{n}\frac{1}{p_j^2}\Lambda_{j0}^+\left[Y_{jn}^+\right]$$

and

$$\sum_{j=1}^{n}\frac{U_j^+}{\epsilon_j p_j^2} - \frac{\alpha_{n+1}^-}{p_{n+1}^2}[C_{n0}] = -\sum_{j=2}^{n+1}\frac{d_{j-1,j}p_{j-1,j}^2}{\epsilon_{j-1}p_{j-1}^2 p_j^2}A_{j-1}^- - \sum_{j=1}^{n+1}\frac{1}{p_j^2}\Theta_{n,j-1}^-\left[X_{j-1,0}^-\right]$$

Collecting all terms together, we have

$$[C_{n0}]\,\chi_{\text{bdy}}/k^2 = \frac{1}{[C_{n0}]}\left(\chi_{\text{double}} + \chi_{\text{single}}\right)$$

where χ_{double} is consists of "double sum terms" and χ_{single} "single sum terms". For χ_{double}, we can further split it into two terms

$$\chi_{\text{double}} = \left(\chi^{(1)}_{\text{double}} + \chi^{(2)}_{\text{double}}\right)$$

where

$$\chi^{(1)}_{\text{double}} = -\sum_{j=1}^{n} \frac{d_{j-1,j}}{p^2_{j-1}p^2_j}\left(\frac{p^2_{j-1,j}}{\varepsilon_j}B^+_j + \frac{\mathbf{i}v}{\omega}q_{j-1}\frac{\omega^2}{c^2}B^-_j\right)$$

and

$$\chi^{(2)}_{\text{double}} = \sum_{j=2}^{n+1} \frac{d_{j-1,j}}{p^2_{j-1}p^2_j}\left(\frac{p^2_{j-1,j}}{\varepsilon_{j-1}}A^-_{j-1} - \frac{\mathbf{i}v}{\omega}q_j\frac{\omega^2}{c^2}A^+_{j-1}\right)$$

Similarly, we split χ_{single} into terms

$$\chi_{\text{single}} = \left(\chi^{(1)}_{\text{single}} + \chi^{(2)}_{\text{single}}\right)$$

where

$$\chi^{(1)}_{\text{single}} = \sum_{j=0}^{n} \frac{1}{p^2_j}\Lambda^+_{j0}\left[Y^+_{jn}\right] + \sum_{j=1}^{n+1} \frac{1}{p^2_j}\Theta^-_{n,j-1}\left[X^-_{j-1,0}\right]$$

and

$$\chi^{(2)}_{\text{single}} = -\frac{\mathbf{i}v}{\omega}\left\{\sum_{j=0}^{n} \frac{q_j}{p^2_j}\Lambda^-_{j0}\left[Y^+_{jn}\right] - \sum_{j=1}^{n+1} \frac{q_j}{p^2_j}\Theta^+_{n,j-1}\left[X^-_{j-1,0}\right]\right\}$$

Now we need to look at each of the four terms separately. Substituting B^σ_j and using the definitions of $\Lambda^\sigma_{j-1,0}$ and S^σ_{ij}, we have

$$\chi^{(1)}_{\text{double}} = -\sum_{j=1}^{n}\left(\left[C_{j-2,0}\right]f^2_{j-1}S^+_{j,j-1} + \left[E_{j-2,0}\right]S^-_{j,j-1}\right)\sum_{k=j}^{n}\psi^+_{jk}\left[Y^+_{kn}\right]$$

According to Equation A.23 and the definitions of $S^\sigma_{j,j+1}$ and $S^\sigma_{j,j+1}$, we have

$$\chi^{(1)}_{\text{double}} = \sum_{j=0}^{n-1} \sum_{k=j+1}^{n} \psi^{+}_{j+1,k} \left[X^{+}_{j0}\right] \left[Y^{+}_{kn}\right] \tag{B.3}$$

Similarly,

$$\chi^{(2)}_{\text{double}} = -\sum_{j=1}^{n} \left([C_{j-2,0}]\, f^2_{j-1} S^{-}_{j,j-1} + [E_{j-2,0}]\, S^{+}_{j,j-1} \right) \sum_{k=j}^{n} \psi^{-}_{jk} \left[Y^{-}_{kn}\right]$$

which simplifies to

$$\chi^{(2)}_{\text{double}} = \sum_{j=0}^{n-1} \sum_{k=j+1}^{n} \psi^{-}_{j+1,k} \left[X^{-}_{j0}\right] \left[Y^{-}_{kn}\right] \tag{B.4}$$

Adding both contributions together gives

$$\chi_{\text{double}} = \sum_{j=0}^{n-1} \sum_{k=j+1}^{n} \sum_{\sigma=\pm} \psi^{\sigma}_{j+1,k} \left[X^{\sigma}_{j0}\right] \left[Y^{\sigma}_{kn}\right] \tag{B.5}$$

This is very close to our final result; it just lacks the "diagonal terms" with $j = k$. We will now show that χ_{single} reduces to these diagonal terms.

Now we look at the χ_{single}. Substituting Equations A.12, A.14, A.22, and A.23 into $\chi^{(1)}_{\text{single}}$, we obtain

$$\begin{aligned}
\chi^{(1)}_{\text{single}} = \sum_{j=0}^{n} \Bigg\{ & [C_{j-1,0}]\, f^2_j\, [C_{n,j+1}] \left(\frac{S^{+}_{j,j+1}}{p^2_j} + \frac{S^{-}_{j+1,j}}{p^2_{j+1}} \right) \\
& - [C_{j-1,0}]\, f^2_j\, [D_{n,j+1}] \left(\frac{S^{-}_{j,j+1}}{p^2_j} + \frac{S^{-}_{j+1,j}}{p^2_{j+1}} \right) \\
& + [E_{j-1,0}]\, [C_{n,j+1}] \left(\frac{S^{+}_{j,j+1}}{p^2_j} + \frac{S^{+}_{j+1,j}}{p^2_{j+1}} \right) \\
& - [E_{j-1,0}]\, [D_{n,j+1}] \left(\frac{S^{-}_{j,j+1}}{p^2_j} + \frac{S^{+}_{j+1,j}}{p^2_{j+1}} \right) \Bigg\}
\end{aligned}$$

and

$$\chi^{(2)}_{\text{single}} = \frac{\mathrm{i}v}{\omega}\sum_{j=0}^{n}\Bigg\{-[C_{j-1,0}]\,f_j^2\,[C_{n,j+1}]\left(\frac{q_j}{p_j^2}S^{+}_{j,j+1}-\frac{q_{j+1}}{p_{j+1}^2}S^{-}_{j+1,j}\right)$$
$$+[C_{j-1,0}]\,f_j^2\,[D_{n,j+1}]\left(\frac{q_j}{p_j^2}S^{-}_{j,j+1}+\frac{q_{j+1}}{p_{j+1}^2}S^{-}_{j+1,j}\right)$$
$$+[E_{j-1,0}]\,[C_{n,j+1}]\left(\frac{q_j}{p_j^2}S^{+}_{j,j+1}+\frac{q_{j+1}}{p_{j+1}^2}S^{+}_{j+1,j}\right)$$
$$-[E_{j-1,0}]\,[D_{n,j+1}]\left(\frac{q_j}{p_j^2}S^{-}_{j,j+1}-\frac{q_{j+1}}{p_{j+1}^2}S^{+}_{j+1,j}\right)\Bigg\}$$

Now

$$\frac{S^{\sigma}_{j,j+1}}{p_j^2}+\frac{S^{\sigma}_{j+1,j}}{p_{j+1}^2}=G_j\left\{-Z_j-\sigma d_{j,j+1}\mathrm{i}\omega v\left(\frac{q_j}{p_{j+1}^2}-\frac{q_{j+1}}{p_j^2}\right)\right\} \tag{B.6}$$

$$\frac{S^{\sigma}_{j,j+1}}{p_j^2}+\frac{S^{-\sigma}_{j+1,j}}{p_{j+1}^2}=G_j\left\{-Z_j+\sigma d_{j,j+1}\mathrm{i}\omega v\left(\frac{q_j}{p_{j+1}^2}+\frac{q_{j+1}}{p_j^2}\right)\right\} \tag{B.7}$$

$$\frac{q_jS^{\sigma}_{j,j+1}}{p_j^2}+\frac{q_{j+1}S^{\sigma}_{j+1,j}}{p_{j+1}^2}=G_j\left\{Z'_j+\sigma d_{j,j+1}c^2p^2_{j,j+1}\left(\frac{q_j}{\epsilon_jp_j^2}-\frac{q_{j+1}}{\epsilon_{j+1}p_{j+1}^2}\right)\right\} \tag{B.8}$$

$$\frac{q_jS^{\sigma}_{j,j+1}}{p_j^2}-\frac{q_{j+1}S^{-\sigma}_{j+1,j}}{p_{j+1}^2}=G_j\left\{Z'_j+\sigma d_{j,j+1}c^2p^2_{j,j+1}\left(\frac{q_j}{\epsilon_jp_j^2}+\frac{q_{j+1}}{\epsilon_{j+1}p_{j+1}^2}\right)\right\} \tag{B.9}$$

where

$$G_j=\frac{Q}{c^2\epsilon_0 v p_j^2p_{j+1}^2}$$

$$Z_j=-\frac{c^2p^4_{j,j+1}d^2_{j,j+1}}{\epsilon_j\epsilon_{j+1}p_j^2p_{j+1}^2}$$

and

$$Z'_j=\frac{\omega^2}{c^2}\frac{\mathrm{i}\omega v d^2_{j,j+1}q_jq_{j+1}}{p_j^2p_{j+1}^2}$$

Substituting Equations B.6–B.9 into $\chi^{(1)}_{\text{single}}$ and $\chi^{(2)}_{\text{single}}$ and adding them together will give a lengthy expression of χ_{single}. We then split χ_{single} into two

terms

$$\chi_{\text{single}} = \chi^{(a)}_{\text{single}} + \chi^{(b)}_{\text{single}}$$

where $\chi^{(a)}_{\text{single}}$ is the terms involving $d^2_{j,j+1}$ and $\chi^{(b)}_{\text{single}}$ is the terms only involving $d_{j,j+1}$. It is easy to see that

$$\begin{aligned}\chi^{(a)}_{\text{single}} = -\frac{\mathrm{i}\omega}{v}\sum_{j=0}^{n} G_j Z_j \Big\{ &- [C_{j-1,0}]\, f_j^2\, [C_{n,j+1}] + [C_{j-1,0}]\, f_j^2\, [D_{n,j+1}] \\ &- [E_{j-1,0}]\, [C_{n,j+1}] + [E_{j-1,0}]\, [D_{nj+1}] \Big\} \\ + \sum_{j=0}^{n} G_j Z'_j \Big\{ &- [C_{j-1,0}]\, f_j^2\, [C_{n,j+1}] - [C_{j-1,0}]\, f_j^2\, [D_{n,j+1}] \\ &+ [E_{j-1,0}]\, [C_{n,j+1}] + [E_{j-1,0}]\, [D_{nj+1}] \Big\}\end{aligned}$$

Substituting Z_j and Z'_j into $\chi^{(a)}_{\text{single}}$, we have

$$\begin{aligned}\chi^{(a)}_{\text{single}} = \frac{\mathrm{i}\omega}{v}\sum_{j=0}^{n} \frac{G_j d^2_{j,j+1}}{c^2 \varepsilon_j \varepsilon_{j+1} p_j^2 p_{j+1}^2} \times \\ \Big\{ \Big([C_{j-1,0}]\, f_j^2\, [C_{n,j+1}] - [E_{j-1,0}]\, [D_{n,j+1}] \Big) \Big(c^4 p^4_{j,j+1} - \varepsilon_j \varepsilon_{j+1} q_j q_{j+1} v^2 \omega^2 \Big) \\ - \Big([C_{j-1,0}]\, f_j^2\, [D_{n,j+1}] - [E_{j-1,0}]\, [C_{n,j+1}] \Big) \Big(c^4 p^4_{j,j+1} + \varepsilon_j \varepsilon_{j+1} q_j q_{j+1} v^2 \omega^2 \Big) \Big\}\end{aligned}$$

As

$$s^-_{j,j+1} s^-_{j+1,j} + s^+_{j,j+1} s^+_{j+1,j} = 2 \left(c^4 p^4_{j,j+1} - \varepsilon_j \varepsilon_{j+1} q_j q_{j+1} v^2 \omega^2 \right)$$

and

$$s^-_{j,j+1} s^+_{j+1,j} + s^+_{j,j+1} s^-_{j+1,j} = 2 \left(c^4 p^4_{j,j+1} + \varepsilon_j \varepsilon_{j+1} q_j q_{j+1} v^2 \omega^2 \right)$$

we then have

$$\chi^{(a)}_{\text{single}} = \frac{1}{2}\sum_{j=0}^{n}\sum_{\sigma=\pm}\left[X^{\sigma}_{j0}\right]\left[Y^{\sigma}_{jn}\right] \tag{B.10}$$

So

$$\chi_{\text{double}} + \chi^{(a)}_{\text{single}} = \sum_{j=0}^{n}\sum_{k=j}^{n}\sum_{\sigma=\pm} z_{jk}\psi^{\sigma}_{j+1,k}\left[X^{\sigma}_{j0}\right]\left[Y^{\sigma}_{kn}\right] \tag{B.11}$$

where

$$z_{ij} = 1 - \frac{1}{2}\delta_{ij} = \begin{cases} \frac{1}{2} & \text{if} \quad i = j \\ 1 & \text{otherwise.} \end{cases}$$

The right-hand side of Equation B.11 is, in fact, our final result for χ. But to prove this, it is now necessary to show that $\chi^{(b)}_{\text{single}} = 0$. From our expressions for $\chi^{(1)}_{\text{single}}$ and $\chi^{(2)}_{\text{single}}$, we have

$$\begin{aligned}
\chi^{(b)}_{\text{single}} = -\frac{\mathrm{i}\omega}{v}\sum_{j=0}^{n}\Bigg\{ & \left[C_{j-1,0}\right] f_j^2 \left[C_{n,j+1}\right] G_j d_{j,j+1}\mathrm{i}\omega v\left(\frac{q_j}{p^2_{j+1}} + \frac{q_{j+1}}{p^2_j}\right) \\
& - \left[C_{j-1,0}\right] f_j^2 \left[D_{n,j+1}\right] G_j d_{j,j+1}\mathrm{i}\omega v\left(\frac{q_j}{p^2_{j+1}} - \frac{q_{j+1}}{p^2_j}\right) \\
& - \left[E_{j-1,0}\right]\left[C_{n,j+1}\right] G_j d_{j,j+1}\mathrm{i}\omega v\left(\frac{q_j}{p^2_{j+1}} - \frac{q_{j+1}}{p^2_j}\right) \\
& + \left[E_{j-1,0}\right]\left[D_{nj+1}\right] G_j d_{j,j+1}\mathrm{i}\omega v\left(\frac{q_j}{p^2_{j+1}} + \frac{q_{j+1}}{p^2_j}\right)\Bigg\} \\
+ \sum_{j=0}^{n}\Bigg\{ & - \left[C_{j-1,0}\right] f_j^2 \left[C_{n,j+1}\right] G_j d_{j,j+1} c^2 p^2_{j,j+1}\left(\frac{q_j}{\varepsilon_j p^2_j} + \frac{q_{j+1}}{\varepsilon_{j+1} p^2_{j+1}}\right) \\
& + \left[C_{j-1,0}\right] f_j^2 \left[D_{n,j+1}\right] G_j d_{j,j+1} c^2 p^2_{j,j+1}\left(\frac{q_j}{\varepsilon_j p^2_j} - \frac{q_{j+1}}{\varepsilon_{j+1} p^2_{j+1}}\right) \\
& - \left[E_{j-1,0}\right]\left[C_{n,j+1}\right] G_j d_{j,j+1} c^2 p^2_{j,j+1}\left(\frac{q_j}{\varepsilon_j p^2_j} - \frac{q_{j+1}}{\varepsilon_{j+1} p^2_{j+1}}\right) \\
& + \left[E_{j-1,0}\right]\left[D_{nj+1}\right] G_j d_{j,j+1} c^2 p^2_{j,j+1}\left(\frac{q_j}{\varepsilon_j p^2_j} + \frac{q_{j+1}}{\varepsilon_{j+1} p^2_{j+1}}\right)\Bigg\}
\end{aligned}$$

Substituting G_j into $\chi^{(b)}_{\text{single}}$, using the definitions of Λ^{σ}_{ji} and Θ^{σ}_{ji} and making a rearrangement we have

$$\chi^{(b)}_{\text{single}} = \frac{Q}{\epsilon_0 v}\sum_{j=0}^{n}\left(\frac{\varepsilon_{j+1}p_{j+1}^4 - \epsilon_j p_j^4}{p_j^4 p_{j+1}^4}\right)\left(\frac{q_j}{\varepsilon_j}\Lambda^-_{j0}\Theta^-_{nj} + \frac{q_{j+1}}{\varepsilon_{j+1}}\Lambda^+_{j0}\Theta^+_{nj}\right)$$

Finally, substituting Λ^σ_{j0} and Θ^σ_{nj} and using Equation A.3a, we obtain

$$\chi^{(b)}_{\text{single}} = \frac{Q}{\epsilon_0 v}\sum_{j=0}^{n}\left(\frac{1}{\varepsilon_j p_j^4} - \frac{1}{\varepsilon_{j+1}p_{j+1}^4}\right)[C_{n0}] = 0 \tag{B.12}$$

So χ is given by the expression on the right hand side of Equation B.11. That answer can be rewritten by using the definitions of x^σ_{ji} and y^σ_{ij}, to obtain

$$\chi_{\text{bdy}} = \frac{k^2}{[C_{n0}]}\sum_{i=0}^{n}\sum_{j=i}^{n}\frac{d_{i,i+1}d_{j,j+1}T^{(n)}_{ij}}{\epsilon_{i+1}\epsilon_j p_i^2 p_{i+1}^2 p_j^2 p_{j+1}^2}$$

where we have defined

$$T^{(n)}_{ij} = \sum_{\sigma=\pm} z_{ij}\psi^\sigma_{i+1,j}\left[x^\sigma_{i0}\right]\left[y^\sigma_{jn}\right] \tag{B.13}$$

This recovers Equation 3.30.

B.3. Proofs of symmetries

In Chapter 3, I presented symmetry relations for the dispersion relation, the Hertz vector and the energy loss function. Here, a detailed proof of those symmetries is given.

B.3.1. Symmetries of dispersion relation

We wish to prove following symmetry relation:

$$\hat{\mathcal{P}}_k\,[C_{n0}] = -\,[C_{n0}]\,/\,f_k^2 \qquad \text{for} \quad k = 1\ldots n \tag{B.14}$$

The contractions in the dispersion bracket $[C_{n0}]$ can be divided into eight classes, according to their position relative to the factors $h^+_{k+1,k}f_k^2 h^+_{k,k-1}$ that

involve q_k. These classes are labelled $T_1, \cdots, T_8$ below. Only the most important contractions are shown explicitly. In each case, additional contractions may occur within each segment denoted by dots $(\cdots)$. The labels i and j are arbitrary.

$$
\begin{aligned}
(T_1): &\quad \cdots h^+_{j+1,j} \cdots h^+_{k+1,k} f_k^2 h^+_{k,k-1} \cdots h^+_{i+1,i} \cdots \\
(T_2): &\quad \cdots \overbrace{h^+_{j+1,j} \cdots h^+_{k+1,k}} f_k^2 h^+_{k,k-1} \cdots h^+_{i+1,i} \cdots \\
(T_3): &\quad \cdots \overbrace{h^+_{j+1,j} \cdots h^+_{k+1,k} f_k^2 h^+_{k,k-1}} \cdots h^+_{i+1,i} \cdots \\
(T_4): &\quad \cdots h^+_{j+1,j} \cdots \overbrace{h^+_{k+1,k} f_k^2 h^+_{k,k-1}} \cdots h^+_{i+1,i} \cdots \\
(T_5): &\quad \cdots h^+_{j+1,j} \cdots \overbrace{h^+_{k+1,k} f_k^2 h^+_{k,k-1} \cdots h^+_{i+1,i}} \cdots \\
(T_6): &\quad \cdots h^+_{j+1,j} \cdots h^+_{k+1,k} f_k^2 \overbrace{h^+_{k,k-1} \cdots h^+_{i+1,i}} \cdots \\
(T_7): &\quad \cdots \overbrace{h^+_{j+1,j} \cdots h^+_{k+1,k}} f_k^2 \overbrace{h^+_{k,k-1} \cdots h^+_{i+1,i}} \cdots \\
(T_8): &\quad \cdots h^+_{j+1,j} \cdots h^+_{k+1,k} f_k^2 h^+_{k,k-1} \cdots h^+_{i+1,i} \cdots
\end{aligned}
$$

Applying the definition of a contraction, the eight classes can be written as:

$$
\begin{aligned}
(T_1): &\quad \Longleftrightarrow h^+_{j+1,j} \Longleftrightarrow h^+_{k+1,k} f_k^2 h^+_{k,k-1} \Longleftrightarrow h^+_{i+1,i} \Longleftrightarrow \\
(T_2): &\quad \Longleftrightarrow h^-_{j+1,j} \longleftrightarrow h^-_{k+1,k} f_k^2 h^+_{k,k-1} \Longleftrightarrow h^+_{i+1,i} \Longleftrightarrow \\
(T_3): &\quad \Longleftrightarrow h^-_{j+1,j} \longleftrightarrow h^+_{k+1,k} h^-_{k,k-1} \Longleftrightarrow h^+_{i+1,i} \Longleftrightarrow \\
(T_4): &\quad \Longleftrightarrow h^+_{j+1,j} \Longleftrightarrow h^-_{k+1,k} h^-_{k,k-1} \Longleftrightarrow h^+_{i+1,i} \Longleftrightarrow \\
(T_5): &\quad \Longleftrightarrow h^+_{j+1,j} \Longleftrightarrow h^-_{k+1,k} h^+_{k,k-1} \longleftrightarrow h^-_{i+1,i} \Longleftrightarrow \\
(T_6): &\quad \Longleftrightarrow h^+_{j+1,j} \Longleftrightarrow h^+_{k+1,k} f_k^2 h^-_{k,k-1} \longleftrightarrow h^-_{i+1,i} \Longleftrightarrow \\
(T_7): &\quad \Longleftrightarrow h^-_{j+1,j} \longleftrightarrow h^+_{k+1,k} h^+_{k,k-1} \longleftrightarrow h^-_{i+1,i} \Longleftrightarrow \\
(T_8): &\quad \Longleftrightarrow h^-_{j+1,j} \longleftrightarrow h^-_{k+1,k} f_k^2 h^-_{k,k-1} \longleftrightarrow h^-_{i+1,i} \Longleftrightarrow
\end{aligned}
$$

where $\Longleftrightarrow$ indicates a segment where all (f^2)'s are present, while $\longleftrightarrow$ indicated a region where all the (f^2)'s are absent. Using the identities

$$\hat{P}_k h^{\sigma}_{k,k+1} = -h^{-\sigma}_{k,k+1}$$

$$\hat{P}_k h^{\sigma}_{k,k-1} = h^{-\sigma}_{k,k-1}$$

and

$$\hat{P}_k f_k = 1/f_k$$

we then have

$$\hat{\mathcal{P}}_k(T_1) = -T_4/f_k^2, \qquad \hat{\mathcal{P}}_k(T_4) = -T_1/f_k^2$$
$$\hat{\mathcal{P}}_k(T_2) = -T_3/f_k^2, \qquad \hat{\mathcal{P}}_k(T_3) = -T_2/f_k^2$$
$$\hat{\mathcal{P}}_k(T_5) = -T_6/f_k^2, \qquad \hat{\mathcal{P}}_k(T_6) = -T_5/f_k^2$$
$$\hat{\mathcal{P}}_k(T_7) = -T_8/f_k^2, \qquad \hat{\mathcal{P}}_k(T_8) = -T_7/f_k^2$$

Finally, Equation B.14 is proved by collecting together all the contractions. It is easy to see that $[C_{n0}]$ is invariant under $\hat{T}_v$ and $\hat{S}$. The effect of $\hat{T}_\omega$ is slightly more complicated because

$$\hat{T}_\omega \epsilon(\omega) = \epsilon(-\omega) = \epsilon^*(\omega)$$

A decision must be made about how to define the effect of $\hat{T}_\omega$ on variables like q_k which involve square roots of function of $\epsilon(\omega)$. Consistent with our choice for q_k we take $\hat{T}_\omega(q_k)$ to have a positive real part[1]. Then

$$\hat{T}_\omega(q_k) = q_k^*$$

From this equation it follows immediately that

[1]The opposite choice could also be made: relative to our definitions this would correspond to a composite operation $\hat{P}_k \hat{T}_\omega(q_k) = -q_k^*$.

$$\hat{T}_\omega [C_{n0}] = [C_{n0}]^*$$

B.3.2. Symmetries of Hertz vector

We first look at the operator $\hat{P}_k$. Before applying $\hat{P}_k$ to Hertz vector, we first look at its effect on simpler expressions. It is easy to see that

$$\mathcal{P}_i(s_{ij}^\sigma) = s_{ij}^\sigma \qquad \text{and} \quad \mathcal{P}_j(s_{ij}^\sigma) = s_{ij}^{-\sigma}$$

$$\mathcal{P}_i(S_{ij}^\sigma) = S_{ij}^\sigma \qquad \text{and} \quad \mathcal{P}_j(S_{ij}^\sigma) = S_{ij}^{-\sigma}$$

and

$$\mathcal{P}_k(\psi_{ij}^\sigma) = \begin{cases} -\psi_{ij}^\sigma / f_k^2 & \text{if} \quad i \le k \le j \qquad \text{and} \quad i \neq j+1 \\ \\ \psi_{ij}^\sigma & \text{otherwise} \end{cases}$$

Then, Using similar methods similar to those used in the proof of Equation B.14, we can show that

$$\mathcal{P}_k [C_{ji}] = \begin{cases} -[E_{ji}] & \text{if} \quad k = j+1 \\ \\ -[C_{ji}] / f_k^2 & \text{if} \quad i+1 \le k \le j \\ \\ [D_{ji}] / f_k^2 & \text{if} \quad k = i \\ \\ [C_{ji}] & \text{if} \quad k \le i-1 \qquad \text{or} \quad k \ge j+2 \end{cases}$$

$$\mathcal{P}_k\,[D_{ji}] = \begin{cases} -\,[F_{ji}] & \text{if} \quad k = j+1 \\ -\,[D_{ji}]\,/f_k^2 & \text{if} \quad i+1 \le k \le j \\ [C_{ji}]\,/f_k^2 & \text{if} \quad k = i \\ [D_{ji}] & \text{if} \quad k \le i \end{cases}$$

$$\mathcal{P}_k\,[E_{ji}] = \begin{cases} -\,[C_{ji}] & \text{if} \quad k = j+1 \\ -\,[E_{ji}]\,/f_k^2 & \text{if} \quad i+1 \le k \le j \\ [F_{ji}]\,/f_k^2 & \text{if} \quad k = i \\ [E_{ji}] & \text{if} \quad k \le i \end{cases}$$

$$\mathcal{P}_k\left[X_{ji}^{\sigma}\right] = \begin{cases} -\left[X_{ji}^{\sigma}\right]/f_k^2 & \text{if} \quad i < k \le j \\ \left[X_{ji}^{\sigma}\right] & \text{if} \quad k \ge j+1 \end{cases}$$

and

$$\mathcal{P}_k\left[Y_{ij}^{\sigma}\right] = \begin{cases} -\left[Y_{ij}^{\sigma}\right]/f_k^2 & \text{if} \quad i+1 < k \le j \\ \left[Y_{ij}^{\sigma}\right] & \text{if} \quad k \le i \end{cases}$$

So with above operations, we can show that the Hertz vector coefficients, calculated from Equation 3.23, obey the identities

$$\hat{\mathcal{P}}_k \alpha_j^{\sigma} = \begin{cases} \alpha_j^{-\sigma} & \text{if} \quad k = j \\ \alpha_j^{\sigma} & \text{if} \quad k \ne j \end{cases}$$

Now we look at the operator $\hat{T}_v\hat{S}$. As the $\hat{S}$ is an operator that reverses the

order of indices through the stack of slabs so that $i \to n-i+1$:

$$\hat{\mathcal{S}}\left[C_{ji}\right] = \frac{f_{n+1-i}^2}{f_{n-j}^2}\left[C_{n-i,n-j}\right]$$

$$\hat{\mathcal{S}}\left[D_{ji}\right] = -\frac{1}{f_{n-j}^2}\left[E_{n-i,n-j}\right]$$

$$\hat{\mathcal{S}}\left[E_{ji}\right] = -f_{n+1-i}^2\left[D_{n-i,n-j}\right]$$

$$\hat{\mathcal{S}}\left(\left[X_{ji}^{\sigma}\right]\right) = \left[Y_{n-j,n-i}^{\sigma}\right] f_{n+1-i}^2$$

$$\hat{\mathcal{S}}\left(\left[Y_{ij}^{\sigma}\right]\right) = \left[X_{n-i,n-j}^{\sigma}\right] / f_{n-j}^2$$

and

$$\hat{\mathcal{S}}\left(\psi_{i+1,j}^{\sigma}\right) = \psi_{n+1-j,n-i}^{\sigma}$$

The $\hat{T}_v$ is an operator that reverses the sign of v. So there are following simple operations:

$$\hat{T}_v b_i^{\sigma} = b_i^{-\sigma}$$

$$\hat{T}_v\left[Y_{jn}^{\sigma}\right] = \left[Y_{jn}^{-\sigma}\right]$$

and

$$\hat{T}_v\left[X_{j0}^{\sigma}\right] = \left[Y_{j0}^{-\sigma}\right]$$

Using all above operations, we finally have

$$\hat{\mathcal{S}}\hat{T}_v(\alpha_j^{\sigma}) = -\mathrm{e}^{-(\sigma q_{n+1-j}+\mathrm{i}\omega/v)a_{n+1-j}}\alpha_{n+1-j}^{-\sigma}$$

where a is the total thickness of the slab.

Finally, the solution can be checked by considering two neighbouring regions coalesce. Using n and $n-1$ to denote the number of layers in the slab, Equation 3.23 gives

$$\hat{\mathcal{J}}_{k,k+1} A_j^\sigma(n) = A_j^\sigma(n-1) \qquad \text{for} \quad 1 \le j \le k-1$$

$$\mathcal{J}_{k,k+1} A_j^\sigma(n) = A_{j-1}^\sigma(n-1) \qquad \text{for} \quad k+1 \le j \le n.$$

as expected.

B.3.3. Symmetries of energy loss function

Using the basic operations above, we immediately have

$$\mathcal{P}_k(\chi_{\text{bdy}}) = \chi_{\text{bdy}}$$

and

$$\hat{\mathcal{T}}_v(\chi_{\text{bdy}}) = \chi_{\text{bdy}}$$

As the operator $\hat{\mathcal{T}}_\omega$ reverses the sign of ω. It is obviously that

$$\hat{\mathcal{T}}_\omega(b_j^\sigma) = b_j^*$$

$$\hat{\mathcal{T}}_\omega(s_{ij}^\sigma) = s_{ij}^*$$

$$\hat{\mathcal{T}}_\omega(S_{ij}^\sigma) = S_{ij}^*$$

$$\hat{\mathcal{T}}_\omega(X_{ij}^\sigma) = X_{ij}^*$$

$$\hat{\mathcal{T}}_\omega(Y_{ij}^\sigma) = Y_{ij}^*$$

and

$$\hat{\mathcal{T}}_\omega(\psi_{i+1,j}^\sigma) = \psi_{i+1,j}^*$$

therefore,

$$\hat{\mathcal{T}}_\omega(\chi_{\text{bdy}}) = -\left(\frac{k^2}{[C_{n0}]}\sum_{i=0}^{n}\sum_{j=i}^{n}\sum_{\sigma=\pm} z_{ij}\psi^\sigma_{i+1,j}\left[X^\sigma_{i0}\right]\left[Y^\sigma_{jn}\right]\right)^* = \chi^*_{\text{bdy}}$$

Finally,

$$\hat{\mathcal{S}}(\chi_{\text{bdy}}) = -\frac{k^2}{[C_{n0}]}\sum_{i=0}^{n}\sum_{j=i}^{n}\sum_{\sigma=\pm} z_{ij}\psi^\sigma_{n+1-j,n-i}\left[Y^\sigma_{n-i,n}\right]\left[X^\sigma_{0,n-j}\right]$$

We substitute $i' = n - j$ and $j' = n - i$ to obtain

$$\hat{\mathcal{S}}(\chi_{\text{bdy}}) = -\frac{k^2}{[C_{n0}]}\sum_{j'=0}^{n}\sum_{i'=0}^{j'}\sum_{\sigma=\pm} z_{i'j'}\psi^\sigma_{i'+1,j'}\left[Y^\sigma_{j',n}\right]\left[X^\sigma_{0,i'}\right] = \chi_{\text{bdy}}$$

APPENDIX C.

DERIVATION OF FORMULA FOR PARALLEL INCIDENCE

In Chapter 4, we gave the solution for Hertz coefficients for parallel incidence. This appendix will derive those expressions.

In order to obtain explicit solutions for the Hertz vector, we need to solve Equation 4.13, using the generalised transfer matrix $T^{(ji)}$ derived in Appendix A.1.2 and the boundary conditions

$$\alpha_0^- = \beta_0^- = \alpha_{n+1}^+ = \beta_{n+1}^+ = 0$$

We calculate the coefficients in two stages–first for layers $j \leq m'$ and then for layers $j \geq m''$. The coefficients for $j \leq m'$ are easier to calculate (especially if we require solutions in the most compact form). They are also sufficient to determine the energy loss spectrum. The coefficients for $j \geq m''$ are more of a luxury, but they allow us to check that our answer is self-consistent.

C.1. Coefficients for $j \leq m'$

C.1.1. Coefficients α_0^σ and β_0^σ

In order to use Equation 4.13 to determine the Hertz vector coefficients in any layer $j \leq m'$, we must first find the coefficients in one of the external

regions ($j = 0$). Starting from Equation 4.13 with j replaced by $n+1$ and applying the boundary at infinity, we have

$$T_{11}^{(n+1,0)}\alpha_0^+ + T_{11}^{(n+1,m)}g_m^- - T_{12}^{(n+1,m)}g_m^+ = 0 \tag{C.1}$$

$$T_{31}^{(n+1,0)}\alpha_0^+ + T_{33}^{(n+1,0)}\beta_0^+ + T_{31}^{(n+1,m)}g_m^- - T_{32}^{(n+1,m)}g_m^+ = 0 \tag{C.2}$$

Starting from Equation C.1, one obtains

$$\alpha_0^+ = -\frac{1}{T_{11}^{(n+1,0)}}\left(T_{11}^{(n+1,m)}g_m^- - T_{12}^{(n+1,m)}g_m^+\right)$$

Substituting the elements of T, one immediately has

$$\alpha_0^+ = -\frac{1}{\left[\tilde{C}_{n0}\right]}\frac{\eta_{mn}}{\eta_{0n}}\frac{\kappa_{0n}}{\kappa_{mn}}\left(\left[\tilde{C}_{nm}\right]g_m^- - \left[\tilde{D}_{nm}\right]g_m^+\right)$$

$$= -\frac{q_m\epsilon_m}{q_0\epsilon_0}\rho_{0,m-1}\frac{\tilde{\gamma}_{nm}^-}{\left[\tilde{C}_{n0}\right]}$$

Since

$$\alpha_0^- = 0$$

we have

$$\begin{pmatrix} \alpha_0^+ \\ \alpha_0^- \end{pmatrix} = -\frac{q_m\epsilon_m}{q_0\epsilon_0}\rho_{0,m-1}\frac{\tilde{\gamma}_{nm}^-}{\left[\tilde{C}_{n0}\right]}\begin{pmatrix} 1 \\ 0 \end{pmatrix} \tag{C.3}$$

β_0^+ can be then expressed in term of α_0^+, using Equation C.2. This gives

$$\begin{pmatrix} \beta_0^+ \\ \beta_0^- \end{pmatrix} = -\frac{1}{[C_{n0}]}\left(T_{31}^{(n+1,0)}\alpha_0^+ + T_{31}^{(n+1,m)}g_m^- - T_{32}^{(n+1,m)}g_m^+\right)\begin{pmatrix} 1 \\ 0 \end{pmatrix} \tag{C.4}$$

C.1.2. Coefficients α_j^σ and β_j^σ

Applying Equation 4.13, we obtain

$$\begin{pmatrix} \alpha_j^+ \\ \alpha_j^- \end{pmatrix} = -\frac{q_m \epsilon_m}{q_j \epsilon_j} \rho_{j,m-1} \frac{\tilde{\gamma}_{nm}^-}{\left[\tilde{C}_{n0}\right]} \begin{pmatrix} \left[\tilde{C}_{j-1,0}\right] \\ \left[\tilde{E}_{j-1,0}\right] \end{pmatrix} \tag{C.5}$$

As in main text, we can write Equation C.5 as

$$\boldsymbol{\alpha}_j = -\frac{q_m \epsilon_m}{q_j \epsilon_j} \rho_{j,m-1} \frac{\tilde{\gamma}_{nm}^-}{\left[\tilde{C}_{n0}\right]} \widetilde{\mathbf{N}}_{j-1,0}$$

Now we look at β_j^σ. From Equation 4.13, we have

$$\beta_j^+ = T_{31}^{(j0)} \alpha_0^+ + T_{33}^{(j0)} \beta_0^+$$

and

$$\beta_j^- = T_{41}^{(j0)} \alpha_0^+ + T_{43}^{(j0)} \beta_0^+$$

Using Equation C.2 and substituting the elements of T, and for α_0^σ from Equation C.3 and β_0^σ from Equation C.4, we obtain

$$\begin{pmatrix} \beta_j^+ \\ \beta_j^- \end{pmatrix} = \frac{1}{\left[C_{n0}\right]\left[\tilde{C}_{n0}\right]} \frac{\kappa_{0,m-1}}{\kappa_{0,j-1}} \left\{ \begin{pmatrix} u_j \\ v_j \end{pmatrix} \frac{-\tilde{\gamma}_{nm}^-}{\eta_{0,m-1}} + \left[\tilde{C}_{n0}\right] w_{n+1,m} \begin{pmatrix} \left[C_{j-1,0}\right] \\ \left[E_{j-1,0}\right] \end{pmatrix} \right\} \tag{C.6}$$

where we have defined

$$u_j = \left[C_{n0}\right] \chi_{11}^{j0} - \left[C_{j-1,0}\right] \chi_{11}^{n+1,0} \tag{C.7}$$

$$v_j = \left[C_{n0}\right] \chi_{21}^{j0} - \left[E_{j-1,0}\right] \chi_{11}^{n+1,0} \tag{C.8}$$

$$w_{ji} = \chi_{12}^{ji} g_m^+ - \chi_{11}^{ji} g_m^- \tag{C.9}$$

For future use, we also define

$$x_{ji} = \chi_{22}^{ji} g_m^+ - \chi_{21}^{ji} g_m^- \tag{C.10}$$

Now we try to simplify the β_j^σ terms. First look at u_j and v_j. Substituting $\chi_{11}^{(j0)}$, $\chi_{11}^{(n+1,0)}$, and $\chi_{21}^{(j0)}$, one obtains

$$\begin{aligned}
\begin{pmatrix} u_j \\ v_j \end{pmatrix} &= [C_{n0}] \sum_{k=1}^{j} \tilde{A}_{0k} \begin{pmatrix} \Theta^-_{j-1,k-1} \\ \Phi^-_{j-1,k-1} \end{pmatrix} - \begin{pmatrix} [C_{j-1,0}] \\ [E_{j-1,0}] \end{pmatrix} \sum_{k=1}^{n+1} \tilde{A}_{0k} \Theta^-_{n,k-1} \\
&= \sum_{k=1}^{j} \tilde{A}_{0k} \left\{ [C_{n0}] \begin{pmatrix} \Theta^-_{j-1,k-1} \\ \Phi^-_{j-1,k-1} \end{pmatrix} - \Theta^-_{n.k-1} \begin{pmatrix} [C_{j-1,0}] \\ [E_{j-1,0}] \end{pmatrix} \right\} \\
&\quad - \sum_{k=j+1}^{n+1} \tilde{A}_{0k} \Theta^-_{n,k-1} \begin{pmatrix} [C_{j-1,0}] \\ [E_{j-1,0}] \end{pmatrix}
\end{aligned}$$

where

$$\tilde{A}_{0k} = d_{k,k-1} \tilde{\Lambda}^+_{k-1,0} \eta_{0,k-2}$$

We need to simplify the quantity

$$\mathbf{X_j} = [C_{n0}] \begin{pmatrix} \Theta^-_{j-1,k-1} \\ \Phi^-_{j-1,k-1} \end{pmatrix} - \Theta^-_{n,k-1} \begin{pmatrix} [C_{j-1,0}] \\ [E_{j-1,0}] \end{pmatrix}$$

Substituting for Θ^-_{ij} and Φ^-_{ij}, we obtain

$$\mathbf{X_j} = \begin{pmatrix} \big([C_{n0}]\,[C_{j-1,k}] - [C_{j-1,0}]\,[C_{nk}]\big) - \big([C_{n0}]\,[D_{j-1,k}] - [C_{j-1,0}]\,[D_{nk}]\big) \\ \big([C_{n0}]\,[E_{j-1,k}] - [E_{j-1,0}]\,[C_{nk}]\big) - \big([C_{n0}]\,[F_{j-1,k}] - [E_{j-1,0}]\,[D_{nk}]\big) \end{pmatrix}$$

Using Equations A.8–A.11, we have

$$\mathbf{X_j} = \begin{pmatrix} \Delta_{k,j-1}\big([C_{k-1,0}] + [E_{k-1,0}]\big)\,[D_{nj}] \\ -\Delta_{k,j-1}\big([C_{k-1,0}] + [E_{k-1,0}]\big)\,[C_{nj}] \end{pmatrix} = -2q_k \epsilon_{k-1} \Delta_{k,j-1} \Lambda^+_{k-1,0} \mathbf{M}_{nj}$$

So

$$\begin{pmatrix} u_j \\ v_j \end{pmatrix} = -2\mathrm{M}_{nj} \sum_{k=1}^{j} q_k \epsilon_{k-1} \Delta_{k,j-1} \tilde{A}_{0k} \Lambda^{+}_{k-1,0} - \mathrm{N}_{j-1,0} \sum_{k=j+1}^{n+1} \tilde{A}_{0k} \Theta^{-}_{n,k-1} \quad \text{(C.11)}$$

Now

$$\begin{aligned} w_{n+1,m} &= \sum_{k=m}^{n} d_{k+1,k} \eta_{m,k-1} \left(\Theta^{-}_{nk} \tilde{\Omega}^{+}_{km} g^{+}_{m} - \Theta^{-}_{nk} \tilde{\Lambda}^{+}_{km} g^{-}_{m} \right) \\ &= \sum_{k=m+1}^{n+1} d_{k,k-1} \eta_{m,k-2} \tilde{\Gamma}_{k-1,m} \Theta^{-}_{n,k-1} \end{aligned}$$

where

$$\tilde{\Gamma}_{k-1,m} = \tilde{\Omega}^{+}_{k-1,m} g^{+}_{m} - \tilde{\Lambda}^{+}_{k-1,m} g^{-}_{m}$$

Therefore, β^{σ}_{j} can be written as

$$\beta_j = \frac{\kappa_{0,m-1}}{\kappa_{0,j-1}} \frac{1}{\eta_{0,m-1} \left[C_{n0} \right] \left[\tilde{C}_{n0} \right]} \left(\mathbf{A_1} + \mathbf{A_2} + \mathbf{A_3} \right)$$

where

$$\mathbf{A_1} = \mathrm{M}_{nj} \tilde{\gamma}^{-}_{nm} \sum_{k=1}^{j} d_{k,k-1} \eta_{0,k-2} \Delta_{k,j-1} 2 q_k \epsilon_{k-1} \tilde{\Lambda}^{+}_{k-1,0} \Lambda^{+}_{k-1,0}$$

$$\mathbf{A_2} = \mathrm{N}_{j-1,0} \tilde{\gamma}^{-}_{nm} \sum_{k=j+1}^{m} d_{k,k-1} \eta_{0,k-2} \tilde{\Lambda}^{+}_{k-1,0} \Theta^{-}_{n,k-1}$$

and

$$\begin{aligned} \mathbf{A_3} = \sum_{k=m+1}^{n+1} & d_{k,k-1} \eta_{0,k-2} \Theta^{-}_{n,k-1} \mathrm{N}_{j-1,0} \times \\ & \left\{ \left[\tilde{C}_{n0} \right] \left(\tilde{\Omega}^{+}_{k-1,m} g^{+}_{m} - \tilde{\Lambda}^{+}_{k-1,m} g^{-}_{m} \right) - \tilde{\Lambda}^{+}_{k-1,0} \left(\left[\widetilde{D}_{nm} \right] g^{+}_{m} - \left[\tilde{C}_{nm} \right] g^{-}_{m} \right) \right\} \end{aligned}$$

The $\mathbf{A_1}$ and $\mathbf{A_2}$ can be simplified as

$$\mathbf{A_1} = 2\mathbf{M}_{nj}\tilde{\gamma}^{-}_{nm}\eta_{0,j-1}q_j\sum_{k=1}^{j}\eta_{k+1,j}V_{k,j-1}\tilde{\Lambda}^{+}_{k-1,0}\Lambda^{+}_{k-1,0}$$

$$\mathbf{A_2} = \mathbf{N}_{j-1,0}\tilde{\gamma}^{-}_{nm}\eta_{0,j-1}\sum_{k=j+1}^{m}d_{k,k-1}\eta_{j,k-2}\tilde{\Lambda}^{+}_{k-1,0}\Theta^{-}_{n,k-1}$$

where

$$V_{ij} = \prod_{k=i}^{j}\left(4q_k^2 f_k^2\right)$$

In order to obtain $\mathbf{A_1}$ and $\mathbf{A_2}$, we have used identity

$$\Delta_{ij} = \eta_{ij}\eta_{i+1,j+1}V_{ij}\frac{q_{j+1}}{q_j} \tag{C.12}$$

For the vector $\mathbf{A_3}$, we need to calculate the quantity

$$A_{31} = \left[\tilde{C}_{n0}\right]\left(\tilde{\Omega}^{+}_{k-1,m}g^{+}_{m} - \tilde{\Lambda}^{+}_{k-1,m}g^{-}_{m}\right) - \tilde{\Lambda}^{+}_{k-1,0}\left(\left[\widetilde{D}_{nm}\right]g^{+}_{m} - \left[\tilde{C}_{nm}\right]g^{-}_{m}\right)$$

Substituting $\tilde{\Omega}^{+}_{k-1,m}$, $\tilde{\Lambda}^{+}_{k-1,m}$ and $\tilde{\Lambda}^{+}_{k-1,0}$ into A_{31}, we have

$$\begin{aligned}
A_{31} = &-f^2_{k-1}g^{+}_{m}\left(\left[\tilde{C}_{k-2,0}\right]\left[\widetilde{D}_{nm}\right] - \left[\tilde{C}_{n0}\right]\left[\widetilde{D}_{k-2,m}\right]\right)\\
&-g^{+}_{m}\left(\left[\tilde{E}_{k-2,0}\right]\left[\widetilde{D}_{nm}\right] - \left[\tilde{C}_{n0}\right]\left[\tilde{F}_{k-2,m}\right]\right)\\
&+f^2_{k-1}g^{-}_{m}\left(\left[\tilde{C}_{k-2,0}\right]\left[\tilde{C}_{nm}\right] - \left[\tilde{C}_{n0}\right]\left[\tilde{C}_{k-2,m}\right]\right)\\
&+g^{-}_{m}\left(\left[\tilde{E}_{k-2,0}\right]\left[\tilde{C}_{nm}\right] - \left[\tilde{C}_{n0}\right]\left[\tilde{E}_{k-2,m}\right]\right)
\end{aligned}$$

Using Equation A.5 and making a rearrangement, we obtain

$$A_{31} = \Delta_{m,k-2}\left(\left[\tilde{C}_{m-1,0}\right]g^{+}_{m} + \left[\tilde{E}_{m-1,0}\right]g^{-}_{m}\right)\left(\left[\tilde{C}_{n,k-1}\right] - \left[\widetilde{D}_{n,k-1}\right]f^2_{k-1}\right)$$

Using Equation A.19, we have

$$A_{31} = 2q_{k-1}f^2_{k-1}\Delta_{m,k-2}\tilde{\zeta}^{+}_{m-1,0}\tilde{\Theta}^{-}_{n,k-1}$$

where

$$\zeta_{ji}^{\sigma} = [C_{ji}]\, g_{j+1}^{+} + \sigma\, [E_{ji}]\, g_{j+1}^{-}$$

So

$$\mathbf{A_3} = \frac{1}{2q_m}\mathbf{N}_{j-1,0}\eta_{0,m-1}\tilde{\zeta}_{m-1,0}^{+}\sum_{k=m+1}^{n+1} d_{k,k-1}\eta_{m,k-2}V_{m,k-1}\Theta_{n,k-1}^{-}\tilde{\Theta}_{n,k-1}^{-}$$

Now we conclude that

$$\beta_j = \frac{q_m\epsilon_m}{q_j\epsilon_j}\frac{\rho_{j,m-1}}{[C_{n0}]\,[\tilde{C}_{n0}]}\Big\{2q_j\epsilon_j\tilde{\gamma}_{nm}^{-}W_{0,j-1}\mathbf{M}_{nj} + (\tilde{\gamma}_{nm}^{-}X_{j,m-1} + 2q_m f_m^2\tilde{\zeta}_{m-1,0}^{+}\eta_{jm}Z_{mn})\mathbf{N}_{j-1,0}\Big\} \tag{C.13}$$

where

$$W_{ij} = \sum_{k=i}^{j}\left(\frac{\epsilon_{k+1}-\epsilon_k}{\epsilon_{k+1}}\right)\nu_{k+1,j}\tilde{\Lambda}_{ki}^{+}\Lambda_{ki}^{+} \tag{C.14}$$

$$X_{ij} = \sum_{k=i}^{j}(\epsilon_{k+1}-\epsilon_k)\eta_{i,k-1}\Theta_{nk}^{-}\tilde{\Lambda}_{k0}^{+} \tag{C.15}$$

$$Z_{ij} = \sum_{k=i}^{j}\left(\frac{\epsilon_{k+1}-\epsilon_k}{\epsilon_k}\right)\nu_{i+1,k}\tilde{\Theta}_{jk}^{-}\Theta_{jk}^{-} \tag{C.16}$$

and

$$\nu_{ij} = \prod_{k=i}^{j} h_{kk}^{+}\tilde{h}_{kk}^{+}f_k^2 = \prod_{k=i}^{j} 4q_k^2 f_k^2\epsilon_k \qquad \text{with} \quad \nu_{i+1,i} = 1. \tag{C.17}$$

This concludes our calculation of the coefficients for $j \leq m'$. Since our main result for the energy loss spectrum requires only the Hertz vector coefficients in the beam layer, these calculations cover all required oefficients in energy loss study, which are

$$\begin{pmatrix} \alpha^+_{m'} \\ \alpha^-_{m'} \end{pmatrix} = -\frac{\tilde{\gamma}^-_{nm}}{[\tilde{C}_{n0}]} \begin{pmatrix} [\tilde{C}_{m-1,0}] \\ [\tilde{E}_{m-1,0}] \end{pmatrix} \tag{C.18}$$

and

$$\begin{pmatrix} \beta^+_{m'} \\ \beta^-_{m'} \end{pmatrix} = \frac{2q_m\epsilon_m}{[\tilde{C}_{n0}]\,[C_{n0}]} \left\{ \tilde{\gamma}^-_{nm} W_{0,m-1} \begin{pmatrix} -[D_{nm}] \\ [C_{nm}] \end{pmatrix} + f_m^2 \tilde{\zeta}^+_{m-1,0} Z_{mn} \begin{pmatrix} [\tilde{C}_{m-1,0}] \\ [\tilde{E}_{m-1,0}] \end{pmatrix} \right\} \tag{C.19}$$

C.2. Coefficients for $j \geq m''$

For $j = m''$, from Equation 4.13, we immediately have

$$\begin{pmatrix} \alpha^+_{m''} \\ \alpha^-_{m''} \end{pmatrix} = -\frac{\tilde{\gamma}^-_{nm}}{[\tilde{C}_{n0}]} \begin{pmatrix} [\tilde{C}_{m-1,0}] \\ [\tilde{E}_{m-1,0}] \end{pmatrix} + \begin{pmatrix} g^-_m \\ -g^+_m \end{pmatrix}$$

and

$$\begin{pmatrix} \beta^+_{m''} \\ \beta^-_{m''} \end{pmatrix} = \begin{pmatrix} \beta^+_{m'} \\ \beta^-_{m'} \end{pmatrix} = \frac{2q_m\epsilon_m}{[\tilde{C}_{n0}]\,[C_{n0}]} \left\{ \tilde{\gamma}^-_{nm} W_{0,m-1} \begin{pmatrix} -[D_{nm}] \\ [C_{nm}] \end{pmatrix} + f_m^2 \tilde{\zeta}^+_{m-1,0} Z_{mn} \begin{pmatrix} [\tilde{C}_{m-1,0}] \\ [\tilde{E}_{m-1,0}] \end{pmatrix} \right\}$$

C.2.1. α^σ_j for $j \geq m''$

For $j \geq m''$, we have

$$\alpha^+_j = T^{(jm)}_{11} \alpha^+_{m''} + T^{(jm)}_{12} \alpha^-_{m''}$$

Substituting $T^{(jm)}_{11}, T^{(jm)}_{12}, \alpha^+_{m''}$, and $\alpha^-_{m''}$, we obtain

$$T_{11}^{(jm)}\alpha_{m''}^{+} = -\frac{\eta_{nm}}{\kappa_{nm}}\frac{\tilde{\gamma}_{nm}^{-}}{\left[\tilde{C}_{n0}\right]}\left(\left[\tilde{C}_{j-1,m}\right]\left[\tilde{C}_{m-1,0}\right] + \left[\tilde{D}_{j-1,m}\right]\left[\tilde{E}_{m-1,0}\right]\right)$$
$$= -\frac{\eta_{nm}}{\kappa_{nm}}\frac{\tilde{\gamma}_{nm}^{-}}{\left[\tilde{C}_{n0}\right]}\left[\tilde{C}_{j-1,0}\right]$$

and

$$T_{11}^{(jm)}\alpha_{m''}^{-} = \frac{\eta_{nm}}{\kappa_{nm}}\left(\left[\tilde{C}_{j-1,m}\right]g_{m}^{-} - \left[\tilde{D}_{j-1,m}\right]g_{m}^{+}\right)$$
$$= \frac{\eta_{nm}}{\kappa_{nm}}\tilde{\gamma}_{j-1,m}^{-}$$

So

$$\alpha_{j}^{+} = -\frac{\eta_{nm}}{\kappa_{nm}}\left(\frac{\tilde{\gamma}_{nm}^{-}}{\left[\tilde{C}_{n0}\right]}\left[\tilde{C}_{j-1,0}\right] - \tilde{\gamma}_{j-1,m}^{-}\right)$$

Similarly,

$$\alpha_{j}^{-} = -\frac{\eta_{nm}}{\kappa_{nm}}\left(\frac{\tilde{\gamma}_{nm}^{-}}{\left[\tilde{C}_{n0}\right]}\left[\tilde{E}_{j-1,0}\right] - \tilde{\mu}_{j-1,m}^{-}\right)$$

where

$$\tilde{\mu}_{ij}^{\sigma} = \left[\tilde{E}_{ij}\right]g_{m}^{-} + \sigma\left[\tilde{F}_{ij}\right]g_{m}^{+}$$

Then we have

$$\boldsymbol{\alpha}_{j} = -\frac{1}{\left[\tilde{C}_{n0}\right]}\frac{\eta_{nm}}{\kappa_{nm}}\left\{\tilde{\gamma}_{nm}^{-}\begin{pmatrix}\left[\tilde{C}_{j-1,0}\right]\\ \left[\tilde{E}_{j-1,0}\right]\end{pmatrix} - \left[\tilde{C}_{n0}\right]\begin{pmatrix}\tilde{\gamma}_{j-1,m}^{-}\\ \tilde{\mu}_{j-1,m}^{-}\end{pmatrix}\right\} \qquad \text{(C.20)}$$

The remining task is to simplify the Equation C.20 as Equation C.5. In Equation C.20, $\boldsymbol{\alpha}_j$ involves

$$\mathbf{W_j} = \tilde{\gamma}_{nm}^{-}\begin{pmatrix}\left[\tilde{C}_{j-1,0}\right]\\ \left[\tilde{E}_{j-1,0}\right]\end{pmatrix} - \left[\tilde{C}_{n0}\right]\begin{pmatrix}\tilde{\gamma}_{j-1,m}^{-}\\ \tilde{\mu}_{j-1,m}^{-}\end{pmatrix}$$

So

$$\mathbf{W_j} = \mathbf{W_j}^{(1)} g_m^+ - \mathbf{W_j}^{(2)} g_m^-$$

where

$$\mathbf{W_j}^{(1)} = \left[\tilde{C}_{n0}\right] \begin{pmatrix} \left[\widetilde{D}_{j-1,m}\right] \\ \left[\tilde{F}_{j-1,m}\right] \end{pmatrix} - \left[\widetilde{D}_{nm}\right] \begin{pmatrix} \left[\tilde{C}_{j-1,0}\right] \\ \left[\tilde{E}_{j-1,0}\right] \end{pmatrix}$$

$$\mathbf{W_j}^{(2)} = \left[\tilde{C}_{n0}\right] \begin{pmatrix} \left[\tilde{C}_{j-1,m}\right] \\ \left[\tilde{E}_{j-1,m}\right] \end{pmatrix} - \left[\tilde{C}_{nm}\right] \begin{pmatrix} \left[\tilde{C}_{j-1,0}\right] \\ \left[\tilde{E}_{j-1,0}\right] \end{pmatrix}$$

Using Equations A.8–A.11, we have

$$\begin{aligned} \mathbf{W_j}^{(1)} &= \begin{pmatrix} -\tilde{\Delta}_{m,j-1} \left[\widetilde{D}_{nj}\right] \left[\tilde{C}_{m-1,0}\right] \\ \tilde{\Delta}_{m,j-1} \left[\tilde{C}_{nj}\right] \left[\tilde{C}_{m-1,0}\right] \end{pmatrix} \\ &= \tilde{\Delta}_{m,j-1} \left[\tilde{C}_{m-1,0}\right] \mathbf{M}_{nj} \end{aligned}$$

$$\begin{aligned} \mathbf{W_j}^{(2)} &= -\begin{pmatrix} -\tilde{\Delta}_{m,j-1} \left[\widetilde{D}_{nj}\right] \left[\tilde{E}_{m-1,0}\right] \\ \tilde{\Delta}_{m,j-1} \left[\tilde{C}_{nj}\right] \left[\tilde{E}_{m-1,0}\right] \end{pmatrix} \\ &= -\tilde{\Delta}_{m,j-1} \left[\tilde{E}_{m-1,0}\right] \mathbf{M}_{nj} \end{aligned}$$

So

$$\mathbf{W_j} = \tilde{\Delta}_{m,j-1} \left(\left[\tilde{C}_{m-1,0}\right] g_m^+ + \left[\tilde{E}_{m-1,0}\right] g_m^- \right) \mathbf{M}_j$$

We then obtain

$$\alpha_j = -\frac{\epsilon_m}{\epsilon_j} \rho_{m,j-1} \frac{\tilde{\zeta}_{m-1,0}^+}{\left[\tilde{C}_{n0}\right]} \mathbf{M}_{nj}$$

C.2.2. β_j^σ for $j \geq m''$

From Equation 4.13, we have

$$\begin{pmatrix} \beta_j^+ \\ \beta_j^- \end{pmatrix} = \frac{1}{[C_{n0}]\,[\tilde{C}_{n0}]} \frac{\kappa_{m-1,0}}{\kappa_{j-1,0}} \left\{ \begin{pmatrix} u_j \\ v_j \end{pmatrix} \frac{-\tilde{\gamma}_{nm}^-}{\eta_{m-1,0}} + w_{n+1,m}\,[\tilde{C}_{n0}] \begin{pmatrix} [C_{j-1,0}] \\ [E_{j-1,0}] \end{pmatrix} - [C_{n0}]\,[\tilde{C}_{n0}] \begin{pmatrix} w_{jm} \\ x_{jm} \end{pmatrix} \right\} \quad \text{(C.21)}$$

Equation C.21 involves

$$\mathbf{Y_j} = w_{n+1,m} \begin{pmatrix} [C_{j-1,0}] \\ [E_{j-1,0}] \end{pmatrix} - \begin{pmatrix} w_{jm} \\ x_{jm} \end{pmatrix} [C_{n0}]$$

Now

$$\begin{pmatrix} w_{jm} \\ x_{jm} \end{pmatrix} = \sum_{k=m}^{j-1} d_{k+1,k}\eta_{m,k-1} \begin{pmatrix} \Theta_{j-1,k}^- \tilde{\Omega}_{km}^+ g_m^+ - \Theta_{j-1,k}^- \tilde{\Lambda}_{km}^+ g_m^- \\ \Phi_{j-1,k}^- \tilde{\Omega}_{km}^+ g_m^+ - \Phi_{j-1,k}^- \tilde{\Lambda}_{km}^+ g_m^- \end{pmatrix}$$

$$= \sum_{k=m+1}^{j} d_{k,k-1}\eta_{m,k-2}\tilde{\Gamma}_{k-1,m} \begin{pmatrix} \Theta_{j-1,k-1}^- \\ \Phi_{j-1,k-1}^- \end{pmatrix}$$

Substituting w_{ji} and x_{ji} into $\mathbf{Y_j}$ to obtain

$$\mathbf{Y_j} = \sum_{k=m+1}^{j} d_{k,k-1}\tilde{\Gamma}_{k-1,m}\eta_{m,k-2} \begin{pmatrix} [C_{j-1,0}]\,\Theta_{n,k-1}^- - [C_{n0}]\,\Theta_{j-1,k-1}^- \\ [E_{j-1,0}]\,\Theta_{n,k-1}^- - [C_{n0}]\,\Phi_{j-1,k-1}^- \end{pmatrix}$$

$$+ \sum_{k=j+1}^{n+1} d_{k,k-1}\eta_{m,k-2}\tilde{\Gamma}_{k-1,m}\Theta_{n,k-1}^- \begin{pmatrix} [C_{j-1,0}] \\ [E_{j-1,0}] \end{pmatrix}$$

The first matrix in $\mathbf{Y_j}$ is $-\mathbf{X_j}$. So we have

$$\mathbf{Y_j} = 2q_j\eta_{m,j-1}\left(\sum_{k=m+1}^{j} d_{k,k-1}\eta_{k+1,j}\tilde{\Gamma}_{k-1,m}V_{k,j-1}\Lambda^{+}_{k-1,0}\right)\mathbf{M}_{nj} + \left(\sum_{k=j+1}^{n+1} d_{k,k-1}\eta_{k-1,m}\tilde{\Gamma}_{k-1,m}\Theta^{-}_{n,k-1}\right)\mathbf{N}_{j-1,0}$$

Then Equation C.21 is written as

$$\beta_j = \frac{\kappa_{0,m-1}}{\kappa_{0,j-1}}\frac{1}{\eta_{0,m-1}}\frac{1}{\left[C_{n0}\right]\left[\tilde{C}_{n0}\right]}\mathbf{Z_j}$$

where

$$\mathbf{Z_j} = -\begin{pmatrix} u_j \\ v_j \end{pmatrix}\tilde{\gamma}^{-}_{nm} + \eta_{0,m-1}\left[\tilde{C}_{n0}\right]\mathbf{Y_j}$$

Using Equation C.11, we split $\mathbf{Z_j}$ into three parts:

$$\mathbf{Z_j} = \mathbf{Z_j}^{(1,m)} + \mathbf{Z_j}^{(m+1,j)} + \mathbf{Z_j}^{(j+1,n+1)}$$

where

$$\mathbf{Z_j}^{(1,m)} = 2\mathbf{M}_{nj}\tilde{\gamma}^{-}_{nm}\sum_{k=1}^{m} d_{k,k-1}q_k\epsilon_{k-1}\eta_{0,k-2}\Delta_{k,j-1}\tilde{\Lambda}^{+}_{k-1,0}\Lambda^{+}_{k-1,0}$$

$$\mathbf{Z_j}^{(m+1,j)} = 2\mathbf{M}_{nj}\tilde{\gamma}^{-}_{nm}\sum_{k=m+1}^{j} d_{k,k-1}q_k\epsilon_{k-1}\eta_{0,k-2}\Delta_{k,j-1}\tilde{\Lambda}^{+}_{k-1,0}\Lambda^{+}_{k-1,0} + 2q_j\eta_{0,m-1}\eta_{m,j-1}\left[\tilde{C}_{n0}\right]\mathbf{M}_{nj}\sum_{k=m+1}^{j} d_{k,k-1}\tilde{\Gamma}_{k-1,m}\eta_{k+1,j}V_{k,j-1}\Lambda^{+}_{k-1,0}$$

$$\mathbf{Z_j}^{(j+1,n+1)} = \mathbf{N}_{j-1,0}\tilde{\gamma}^{-}_{nm}\sum_{k=j+1}^{n+1} d_{k,k-1}\eta_{0,k-2}\tilde{\Lambda}^{+}_{k-1,0}\Theta^{-}_{n,k-1} + \eta_{0,m-1}\left[\tilde{C}_{n0}\right]\mathbf{N}_{j-1,0}\sum_{k=j+1}^{n+1} d_{k,k-1}\eta_{m,k-2}\tilde{\Gamma}_{k-1,m}\Theta^{-}_{n,k-1}$$

The $\mathbf{Z_j}^{(m+1,j)}$ and $\mathbf{Z_j}^{(j+1,n+1)}$ are still complicated. We now further simplify them. Combining terms, we have

$$\mathbf{Z_j}^{(m+1,j)} = 2q_j\eta_{0,j-1}\mathbf{M}_{nj} \times \sum_{k=m+1}^{j} d_{k,k-1}\eta_{k+1,j}V_{k,j-1}\Lambda^{+}_{k-1,0}\left(\tilde{\gamma}^{-}_{nm}\tilde{\Lambda}^{+}_{k-1,0} + \left[\tilde{C}_{n0}\right]\tilde{\Gamma}_{k-1,m}\right)$$

and

$$\mathbf{Z_j}^{(j+1,n+1)} = \mathbf{N}_{j-1,0}\sum_{k=j+1}^{n+1} d_{k,k-1}\eta_{0,k-2}\Theta^{-}_{n,k-1}\left(\tilde{\gamma}^{-}_{nm}\tilde{\Lambda}^{+}_{k-1,0} + \left[\tilde{C}_{n0}\right]\tilde{\Gamma}_{k-1,m}\right)$$

The terms in brackets above can be simplified by substituting $\tilde{\gamma}^{-}_{nm}$, $\tilde{\Lambda}^{+}_{k-1,0}$ and $\tilde{\Gamma}_{k-1,m}$ and using Equations A.8–A.11:

$$\tilde{\gamma}^{-}_{nm}\tilde{\Lambda}^{+}_{k-1,0} + \left[\tilde{C}_{n0}\right]\tilde{\Gamma}_{k-1,m} = \frac{1}{2q_m}V_{m,k-1}\tilde{\zeta}^{+}_{m-1,0}\tilde{\Theta}^{-}_{n,k-1}$$

So we obtain

$$\mathbf{Z_j}^{(m+1,j)} = \frac{q_j}{q_m}\mathbf{M}_{nj}\eta_{0,j-1}V_{m,j-1}\tilde{\zeta}^{+}_{m-1,0}\sum_{k=m+1}^{j} d_{k,k-1}\eta_{k+1,j}\Lambda^{+}_{k-1,0}\tilde{\Theta}^{-}_{n,k-1}$$

and

$$\mathbf{Z_j}^{(j+1,n+1)} = \frac{1}{2q_m}\mathbf{N}_{j-1,0}\tilde{\zeta}^{+}_{m-1,0}\sum_{k=j+1}^{n+1} d_{k,k-1}\eta_{0,k-2}V_{m,k-1}\Theta^{-}_{n,k-1}\tilde{\Theta}^{-}_{n,k-1}$$

Collecting together all terms gives for $j \geq m''$

$$\beta_j = \frac{\epsilon_m}{\epsilon_j}\frac{\rho_{m,j-1}}{\left[\tilde{C}_{n0}\right]\left[C_{n0}\right]}\left\{2q_j\epsilon_j f_j^2\tilde{\zeta}^{+}_{m-1,0}Z_{jn}\mathbf{N}_{j-1,0} + \left(2q_m\tilde{\gamma}^{-}_{nm}\eta_{mj}W_{0,m-1} + \tilde{\zeta}^{+}_{m-1,0}Y_{m,j-1}\right)\mathbf{M}_{nj}\right\} \quad \text{(C.22)}$$

where Z_{ij} and W_{ij} are defined by Equations C.16 and C.14 and

$$Y_{ij} = \sum_{k=i}^{j} (\epsilon_{k+1} - \epsilon_k) \eta_{k+2,j+1} \tilde{\Theta}^{-}_{nk} \Lambda^{+}_{k0}$$

We have therefore obtained all the Hertz coefficients (both for $j \leq m'$ and $j \geq m''$) and simplified them as far as possible.

APPENDIX D.

NON-RELATIVISTIC CASE FOR PARALLEL INCIDENCE

In Chapter 4, the retarded dielectric theory for parallel incidence was developed. Here, we carry out a classical calculation in order to obtain a simplified expression for work done.

D.1. Scattering geometry and potential equation

The scattering geometry is similar to that described in Chapter 4. Starting from Maxwell's equation

$$\nabla \cdot \mathbf{D} = \rho/\varepsilon_0$$

one obtains the potential equation in the i^{th} region

$$\nabla^2 \phi_i = -\frac{\rho}{\varepsilon_0 \epsilon_i} \tag{D.1}$$

If the electron travels in the x direction, the charge density is

$$\rho(x, y, z, t) = Q\delta(x - vt)\delta(y)\delta(z - z_b)$$

Fourier transforming Equation D.1 with respect to x y and t, one obtains

$$\frac{\mathrm{d}^2\phi_i}{\mathrm{d}z^2} - k^2\phi_i = \frac{2\pi Q}{\varepsilon_0 \epsilon_i}\delta(\omega - k_x v)\delta(z - z_b) \tag{D.2}$$

The solution of this equation can be written as

$$\phi_i = \hat{\phi}_i \delta(k_x v - \omega)$$

where

$$\hat{\phi}_i = A_i^+ \mathrm{e}^{kz} + A_i^- \mathrm{e}^{-kz} \tag{D.3}$$

where the coefficients A_i^σ are to be determined from the boundary conditions at surfaces and interfaces. Moreover, the boundary conditions at the position of the beam are

$$\hat{\phi}_{m''}\Big|_{z_b^+} = \hat{\phi}_{m'}\Big|_{z_b^-}$$

and

$$\frac{\mathrm{d}\hat{\phi}_{m''}}{\mathrm{d}z}\bigg|_{z_b^+} - \frac{\mathrm{d}\hat{\phi}_{m'}}{\mathrm{d}z}\bigg|_{z_b^-} = -\frac{2\pi Q}{\epsilon_0 \epsilon_m}$$

D.2. Recurrence relation

We rescale the coefficients A_i^σ as follows:

$$\alpha_i^\sigma = -\frac{k\epsilon_0\epsilon_m}{Q\pi} A_i^\sigma \mathrm{e}^{\sigma k z_{i-1}} \qquad \text{with} \quad \alpha_0^\sigma = -\frac{k\epsilon_0\epsilon_0}{Q\pi} A_0^\sigma$$

Then, applying boundary conditions at $(i-1)^{\text{th}}$ interface we obtain a recurrence relation between $j-1^{\text{th}}$ and j^{th} layers in the form

$$\begin{pmatrix} \alpha_i^+ \\ \alpha_i^- \end{pmatrix} = \frac{1}{\check{h}_{ii}^+ \check{f}_{i-1}} \begin{pmatrix} \check{h}_{ii-1}^+ \check{f}_{i-1}^2 & \check{h}_{ii-1}^- \\ \check{h}_{ii-1}^- \check{f}_{i-1}^2 & \check{h}_{ii-1}^+ \end{pmatrix} \begin{pmatrix} \alpha_{i-1}^+ \\ \alpha_{i-1}^- \end{pmatrix} \tag{D.4}$$

where

$$\check{h}_{ij}^\sigma = \epsilon_i + \sigma\epsilon_j \qquad \text{and} \quad \check{f}_i = \mathrm{e}^{ka_i}$$

Note that the accent ˇ is used in order to distinguish the classical quantities from similar ones used in the normal and parallel retarded calculations and the anisotropic calculation. The coefficients in the subregions on either side of the beam are related by

$$\begin{pmatrix} \alpha_{m''}^{+} \\ \alpha_{m''}^{-} \end{pmatrix} = \begin{pmatrix} \alpha_{m'}^{+} \\ \alpha_{m''}^{-} \end{pmatrix} + \begin{pmatrix} \mathrm{e}^{-k(z_b - z_{m-1})} \\ -\mathrm{e}^{k(z_b - z_{m-1})} \end{pmatrix} \tag{D.5}$$

So combining Equations D.4 and D.5 to obtain

$$\begin{pmatrix} \alpha_i^{+} \\ \alpha_i^{-} \end{pmatrix} = \frac{1}{\check{h}_{ii}^{+} \check{f}_{i-1}} \begin{pmatrix} \check{h}_{ii-1}^{+} \check{f}_{i-1}^{2} & \check{h}_{ii-1}^{-} \\ \check{h}_{ii-1}^{-} \check{f}_{i-1}^{2} & \check{h}_{ii-1}^{+} \end{pmatrix} \begin{pmatrix} \alpha_{i-1}^{+} \\ \alpha_{i-1}^{-} \end{pmatrix} + \delta_{im''} \begin{pmatrix} \check{g}_m^{-} \\ \check{g}_m^{+} \end{pmatrix} \tag{D.6}$$

where

$$\check{g}_m^{\sigma} = \mathrm{e}^{\sigma k(z_b - z_{m-1})}$$

D.3. Scattering probability

As in Section 4.5, the work done for electron travelling in m^{th} layer in x direction against electric field is

$$\frac{\mathrm{d}W}{\mathrm{d}x} = -\frac{Q}{(2\pi)^3 v} \int\int \tilde{E}_x(k_x, k_y, z_b, \omega)\Big|_{k_x = \omega/v} dk_y d\omega$$

where

$$\tilde{E}_x(k_x, k_y, z_b, \omega) = -ik_x \left(A_m^{+} \mathrm{e}^{kz_b} + A_m^{-} \mathrm{e}^{-kz_b} \right)$$

so

$$\frac{\mathrm{d}W}{\mathrm{d}x} = \frac{Q^2}{2\pi^2 \epsilon_0 \hbar v^2} \int_0^{\infty} \hbar\omega \mathrm{d}\omega \int_0^{\infty} \mathrm{Im} \left(\frac{\alpha_m^{+} \check{g}_m^{+} + \alpha_m^{-} \check{g}_m^{-}}{k\epsilon_m} \right) \tag{D.7}$$

For an n–layered slab, with the beam in the m^{th} layer, the scattering probability is expressed as

$$\frac{\mathrm{d}^2P}{\mathrm{d}(\hbar\omega)\mathrm{d}x} = \frac{Q^2}{2\pi^2\epsilon_0\hbar^2v^2}\int_0^\infty \mathrm{Im}(\chi_m^{(n)}) \tag{D.8}$$

where

$$\chi_m^{(n)} = \frac{\alpha_m^+\check{g}_m^+ + \alpha_m^-\check{g}_m^-}{k\epsilon_m} \tag{D.9}$$

The remaining task is to find the coefficients α_m^+ and α_m^-. Repeatedly applying recurrence relation D.6 from external region 0 to external region $n+1$, and using the boundary conditions at infinity, one obtains

$$\alpha_0^+ = (\check{h}_{mm}^+\cdots\check{h}_{11}^-)(\check{f}_{m-1}\cdots\check{f}_0)\left(\frac{\left[\check{D}_{nm}\right]\check{g}_m^+ - \left[\check{C}_{nm}\right]\check{g}_m^-}{\left[\check{C}_{n0}\right]}\right)$$

Then, applying recurrence relation D.6 from region 0 to the layer of the beam and substituting α_0^+, we obtain

$$\begin{pmatrix}\alpha_m^+\\ \alpha_m^-\end{pmatrix} = \frac{\left[\check{D}_{nm}\right]\check{g}_m^+ - \left[\check{C}_{nm}\right]\check{g}_m^-}{\left[\check{C}_{n0}\right]}\begin{pmatrix}\left[\check{C}_{m-10}\right]\\ \left[\check{E}_{m-10}\right]\end{pmatrix}$$

so

$$\alpha_m^+\check{g}_m^+ + \alpha^-\check{g}_m^- = \frac{1}{\left[\check{C}_{n0}\right]}\left(\left[\check{D}_{nm}\right]\check{g}_m^+ - \left[\check{C}_{nm}\right]\check{g}_m^-\right)\left(\left[\check{C}_{m-10}\right]\check{g}_m^+ + \left[\check{E}_{m-10}\right]\check{g}_m^-\right)$$

Defining

$$\check{\gamma}_{nm}^- = \left[\check{C}_{nm}\right]\check{g}_m^- - \left[\check{D}_{nm}\right]\check{g}_m^+$$

and

$$\check{\zeta}_{m-10}^+\left[\check{E}_{m-10}\right]\check{g}_m^- + \left[\check{C}_{m-10}\right]\check{g}_m^+$$

then

$$\sum_\sigma \alpha_m^\sigma\check{g}_m^+ = -\frac{1}{\left[\check{C}_{n0}\right]}\check{\gamma}_{nm}^-\check{\zeta}_{m-10}^+$$

So the energy loss function can be written as

$$\chi_m^{(n)} = \frac{\check{\gamma}_{nm}^{-}\check{\zeta}_{m-10}^{+}}{k\epsilon_m\left[\check{C}_{n0}\right]} \tag{D.10}$$

D.4. Comparison with retarded case

We first rearrange the classical answer. Substituting $\tilde{\gamma}_{nm}^{+}$ and $\tilde{\zeta}_{m-10}^{+}$ into Equation D.10 and expanding it, one obtains

$$\left(\chi_m^{(n)}\right)_{\text{classical}} = \frac{1}{k\epsilon_m}\left(-1 + \frac{\check{g}_m^{+}\left[\check{D}_{nm}\right]\check{\zeta}_{m-10}^{+} - \check{g}_m^{-}\left[\check{E}_{m-10}\right]\check{\gamma}_{nm}^{-}}{\left[\check{C}_{n0}\right]}\right) \tag{D.11}$$

Now we can attempt the $c \to \infty$ check of the relativistic answer (see Equation 4.28):

$$\begin{aligned}\chi_m^{(n)} = &\left(\frac{v^2}{c^2} - \frac{1}{\epsilon_m}\right)\frac{\tilde{\gamma}_{nm}^{-}\tilde{\zeta}_{m-10}^{+}}{q_m\left[\tilde{C}_{n0}\right]} \\ &+ \frac{2q_m}{\left[\tilde{C}_{n0}\right]\left[C_{n0}\right]}\left(f_m^2\tilde{\zeta}_{m-1,0}^{+}\zeta_{m-1,0}^{-}Z_{mn} - \tilde{\gamma}_{nm}^{-}\gamma_{nm}^{+}W_{0m-1}\right)\end{aligned} \tag{D.12}$$

Taking the limit $c \to \infty$, first term becomes $-1/k\epsilon_m$ as found in Equation D.11. Therefore,

$$\left(\chi_m^{(n)}\right)_{c\to\infty} = -\frac{1}{k\epsilon_m} + A_1 + A_2$$

where

$$A_1 = \frac{2k}{F_{0n}(2k)^{n+1}k^{n+1}\left[\check{C}_{n0}\right]}\check{f}_m^2\left\{F_{0m-1}(2k)^m\check{g}_m^{+}\right\}\left\{k^m\check{\zeta}_{m-1,0}^{+}\right\}Z'_{mn}$$

and

$$A_2 = -\frac{2k}{F_{0n}(2k)^{n+1}k^{n+1}\left[\check{C}_{n0}\right]}\left\{F_{mn}(2k)^{n+1-m}\check{g}_m^{-}\right\}\left\{k^{n+1-m}\check{\gamma}_{nm}^{-}\right\}W'_{0,m-1}$$

where

$$F_{ij} = \prod_{k=i}^{j} \check{f}_k^2$$

Z'_{nm} and $W'_{0,m-1}$ are the $c \to \infty$ limits of Z_{mn} and W_{0m-1}, which are

$$Z'_{mn} = \frac{1}{\epsilon_m} 2^{n-m} k^{2(n-m)} F_{m+1,n} \left[\check{D}_{nm}\right]$$

and

$$W'_{0,m-1} = \frac{1}{\epsilon_m} 2^{m-1} k^{2m-2} F_{0m-1} \left[\check{E}_{m-1,0}\right]$$

So

$$A_1 = \frac{\left[\check{D}_{nm}\right] \check{g}_m^+ \check{\zeta}_{m-1,0}^+}{k\epsilon_m \left[\check{C}_{n0}\right]}$$

and

$$A_2 = -\frac{\left[\check{E}_{m-1,0}\right] \check{g}_m^- \check{\gamma}_{nm}^-}{k\epsilon_m \left[\check{C}_{n0}\right]}$$

Thus

$$\lim_{c\to\infty} \chi_m^{(n)} = \left(\chi_m^{(n)}\right)_{\text{classical}}$$

APPENDIX E.

DERIVATION OF LOSS FUNCTION FOR ANISOTROPIC SLABS

This appendix will derive the energy loss function for an electron travelling normal to the interfaces of anisotropic slabs.

In Chapter 7, "simplified" expression for work done (Equation 7.16) and the scattering probability (Equations 7.17 and 7.19) was given without any details. Calculation of the bulk contributions is straightforward and need not be given here. In this appendix, we will derive the contributions from surfaces and interfaces starting from Equation 7.15.

$$W_{\text{bdy}} = \frac{Q}{(2\pi)^3} \int\int\int_{-\infty}^{\infty} \mathrm{d}\omega \mathrm{d}k_x \mathrm{d}k_y \sum_{i=0}^{n+1} \int_{z_{i-1}}^{z_i} \mathrm{d}z \left(\sum_{\sigma=\pm} q_i^\sigma A_i^\sigma \mathrm{e}^{(q_i^\sigma - \mathrm{i}\omega/v)z} \right) \quad \text{(E.1)}$$

is boundary contribution. The work done can be written in terms of energy loss function,

$$W_{\text{bdy}} = -\frac{Q^2}{4\pi^3 \varepsilon_0 \hbar v^2} \int_{-\infty}^{\infty} \mathrm{d}k_x \int_{-\infty}^{\infty} \mathrm{d}k_y \int_0^{\infty} (\hbar\omega)\, \mathrm{d}\omega \mathrm{Im}\chi_{\text{bdy}}$$

where

$$\chi_{\text{bdy}} = \frac{\mathrm{i}v}{\omega} \left\{ \left[\alpha_0^+ + \sum_{j=1}^{n} \left(\frac{\alpha_j^+ \hat{f}_j^2 + \alpha_j^-}{\hat{f}_j \hat{b}_j^+} - (\alpha_j^+ + \alpha_j^-) \right) - \alpha_{n+1}^- \right] \right.$$

$$- \frac{\omega}{v^2}\left[\frac{\omega_0}{p_0^2}\alpha_0^+ + \sum_{j=1}^{n}\frac{\omega_j}{p_j^2}\left(\frac{\alpha_j^+\hat{f}_j^2 + \alpha_j^-}{\hat{f}_j\hat{b}_j^+} - (\alpha_j^+ + \alpha_j^-)\right) - \frac{\omega_{n+1}}{p_{n+1}^2}\alpha_{n+1}^-\right]$$
$$+ \frac{i\omega}{v}\left[\frac{\kappa_0}{p_0^2}\alpha_0^+ + \sum_{j=1}^{n}\frac{\kappa_j}{p_j^2}\left(\frac{\alpha_j^+\hat{f}_j^2 - \alpha_j^-}{\hat{f}_j\hat{b}_j^+} - (\alpha_j^+ - \alpha_j^-)\right) + \frac{\kappa_{n+1}}{p_{n+1}^2}\alpha_{n+1}^-\right]\Bigg\}$$

It is convenient to start from the quantity $\chi_{\text{bdy}}\left[\hat{C}_{n0}\right] \mathrm{i}\omega/v$. To calculate this quantity we need to add together contributions from external and internal regions. Starting from Equation E.1, we have

$$\chi_{\text{bdy}}\left[\hat{C}_{n0}\right] \mathrm{i}\omega/v = \chi_1 - \frac{\omega}{v^2}\chi_2 + \frac{\mathrm{i}\omega}{v}\chi_3$$

where

$$\chi_1 = \left[\hat{C}_{n0}\right]\alpha_0^+ + \sum_{j=1}^{n} R_j^+ - \left[\hat{C}_{n0}\right]\alpha_{n+1}^-$$

$$\chi_2 = \left[\hat{C}_{n0}\right]\frac{\omega_0\alpha_0^+}{p_0^2} + \sum_{j=1}^{n}\frac{\omega_j}{p_j^2}R_j^+ - \left[\hat{C}_{n0}\right]\frac{\omega_{n+1}}{p_{n+1}^2}$$

and

$$\chi_3 = \left[\hat{C}_{n0}\right]\frac{\kappa_0}{p_0^2}\alpha_0^+ + \sum_{j=1}^{n}\frac{\kappa_j}{p_j^2}R_j^- - \left[\hat{C}_{n0}\right]\frac{\kappa_{n+1}}{p_{n+1}^2}$$

where

$$\hat{R}_j^\sigma = \left[\hat{C}_{n0}\right]\left\{\frac{\alpha_j^+\hat{f}_j^2 + \sigma\alpha_j^-}{\hat{f}_j\hat{b}_j^+} - \left(\alpha_j^+ + \sigma\alpha_j^-\right)\right\}$$

Substituting α_j^+ and α_j^- into R_j^σ and using Equations A.12–A.19 together with the notation

$$\hat{\tau}_j^\sigma = \begin{cases} 1 & \text{if} \quad \sigma = + \\ \epsilon_j^{(33)}\kappa_j & \text{if} \quad \sigma = - \end{cases}$$

one obtains

$$\hat{R}_j^\sigma = \sigma\left(\frac{\hat{r}_{j+1}^\sigma}{\hat{r}_j^\sigma}\hat{A}_j^{-\sigma} - \hat{A}_{j-1}^{-\sigma} - \hat{\Theta}_{n,j-1}^{-\sigma}\left[\hat{X}_{j-1,0}^-\right]\right) + \left(\frac{\hat{r}_{j-1}^\sigma}{\hat{r}_j^\sigma}\hat{B}_j^\sigma - \hat{B}_{j+1}^\sigma - \hat{\Lambda}_{j0}^\sigma\left[\hat{Y}_{jn}^+\right]\right)$$

where

$$\hat{A}_j^\sigma = \hat{\Theta}_{nj}^\sigma \sum_{k=0}^{j-1} \hat{\psi}_{k+1,j}^- \left[\hat{X}_{k0}^-\right]$$

and

$$\hat{B}_j^\sigma = \hat{\Lambda}_{j-1,0}^\sigma \sum_{k=j}^{n} \hat{\psi}_{jk}^+ \left[\hat{Y}_{kn}^+\right]$$

Now we can split $\hat{R}_j^\sigma$ as

$$\hat{R}_j^\sigma = \frac{\sigma\hat{U}_j^\sigma - \hat{V}_j^\sigma}{\hat{r}_j^\sigma}$$

where

$$\hat{U}_j^\sigma = \hat{r}_{j+1}^\sigma \hat{A}_j^{-\sigma} - \hat{r}_j^\sigma \hat{A}_{j-1}^{-\sigma} - r_j^\sigma \hat{\Theta}_{n,j-1}^{-\sigma}\left[\hat{X}_{j-1,0}^-\right]$$

and

$$\hat{V}_j^\sigma = \hat{r}_j^\sigma \hat{B}_{j+1}^\sigma - \hat{r}_{j-1}^\sigma \hat{B}_j^\sigma + \hat{r}_j^\sigma \hat{\Lambda}_{j0}^\sigma\left[\hat{Y}_{jn}^+\right]$$

So we have

$$\chi_1 = \left(\left[\hat{C}_{n0}\right]\alpha_0^+ - \sum_{j=1}^{n}\hat{V}_j^+\right) + \left(\sum_{j=1}^{n}\hat{U}_j^+ - \left[\hat{C}_{n0}\right]\alpha_{n+1}^-\right)$$

$$\chi_2 = \left(\left[\hat{C}_{n0}\right]\frac{\omega_0\alpha_0^+}{p_0^2} - \sum_{j=1}^{n}\frac{\omega_j}{p_j^2}\hat{V}_j^+\right) + \left(\sum_{j=1}^{n}\frac{\omega_j}{p_j^2}\hat{U}_j^+ - \left[\hat{C}_{n0}\right]\frac{\omega_{n+1}}{p_{n+1}^2}\alpha_{n+1}^-\right)$$

and

$$\chi_3 = \left(\left[\hat{C}_{n0}\right]\frac{\kappa_0}{p_0^2}\alpha_0^+ - \sum_{j=1}^{n}\frac{1}{\epsilon_j^{(33)}p_j^2}\hat{V}_j^-\right) - \left(\sum_{j=1}^{n}\frac{1}{\epsilon_j^{(33)}p_j^2}\hat{U}_j^- - \left[\hat{C}_{n0}\right]\frac{\kappa_{n+1}}{p_{n+1}^2}\alpha_{n+1}^-\right)$$

Following similar methods as isotropic normal calculations, we obtain

$$\left[\hat{C}_{n0}\right]\alpha_0^+ - \sum_{j=1}^{n}\hat{V}_j^+ = -\sum_{j=0}^{n}\hat{\Lambda}_{j0}^+\left[\hat{Y}_{jn}^+\right]$$

$$\sum_{j=1}^{n}\hat{U}_j^+ - \left[\hat{C}_{n0}\right]\alpha_{n+1}^- = -\sum_{j=0}^{n}\hat{\Theta}_{nj}^-\left[\hat{X}_{j0}^-\right]$$

$$\left[\hat{C}_{n0}\right]\frac{\omega_0\alpha_0^+}{p_0^2} - \sum_{j=1}^{n}\frac{\omega_j}{p_j^2}\hat{V}_j^+ = \sum_{j=1}^{n}\hat{B}_j^+ t_{j,j-1} - \sum_{k=0}^{n}\left[\hat{Y}_{kn}^+\right]\hat{\Lambda}_{k0}^+\frac{\omega_k}{p_k^2}$$

$$\sum_{j=1}^{n}\frac{\omega_j}{p_j^2}\hat{U}_j^+ - \left[\hat{C}_{n0}\right]\frac{\omega_{n+1}\alpha_{n+1}^-}{p_{n+1}^2} = -\sum_{j=1}^{n}\hat{A}_j^- t_{j+1,j} - \sum_{k=1}^{n+1}\left[\hat{X}_{k-1,0}^-\right]\hat{\Theta}_{n,k-1}^-\frac{\omega_k}{p_k^2}$$

$$\left[\hat{C}_{n0}\right]\frac{\kappa_0}{p_0^2}\alpha_0^+ + \sum_{j=1}^{n}\frac{1}{\epsilon_j^{(33)}p_j^2}\hat{V}_j^- = \sum_{j=0}^{n-1}\hat{B}_{j+1}^- r_{j+1,j} - \sum_{k=0}^{n}\frac{\kappa_k}{p_k^2}\hat{\Lambda}_{k0}^+\left[\hat{Y}_{kn}^+\right]$$

and

$$\sum_{j=1}^{n}\frac{1}{\epsilon_j^{(33)}p_j^2}\hat{U}_j^- - \left[\hat{C}_{n0}\right]\frac{\kappa_{n+1}}{p_{n+1}^2} = -\sum_{j=1}^{n}\hat{A}_j^+ r_{j+1,j} - \sum_{k=1}^{n+1}\frac{\kappa_k}{p_k^2}\hat{\Theta}_{n,k-1}^+\left[\hat{X}_{k-1,0}^-\right]$$

where

$$t_{ji} = \frac{\omega_j}{p_j^2} - \frac{\omega_i}{p_i^2}$$

and

$$r_{ji} = \epsilon_i^{(33)}\kappa_i\left(\frac{1}{\epsilon_j^{(33)}p_j^2} - \frac{1}{\epsilon_i^{(33)}p_i^2}\right)$$

Collecting all terms together, we have

$$\chi_{\text{bdy}}\left[\hat{C}_{n0}\right]\mathrm{i}\omega/v = \chi_{\text{double}} + \chi_{\text{single}}$$

where χ_{double} is consists of "double sum terms" and χ_{single} "single sum terms". For χ_{double} we can further split it into two terms

$$\chi_{\text{double}} = \chi^{(1)}_{\text{double}} + \chi^{(2)}_{\text{double}}$$

where

$$\chi^{(1)}_{\text{double}} = -\frac{\omega}{v^2}\left\{\sum_{j=1}^{n}\sum_{k=j}^{n}\hat{\psi}^{+}_{jk}\left[\hat{Y}^{+}_{kn}\right]\left(\hat{\Lambda}^{+}_{j-1,0}t_{j,j-1} - \mathrm{i}v\hat{\Lambda}^{-}_{j-1,0}r_{j,j-1}\right)\right\}$$

and

$$\chi^{(2)}_{\text{double}} = \frac{\omega}{v^2}\left\{\sum_{j=1}^{n}\sum_{k=0}^{j-1}\hat{\psi}^{-}_{k+1,j}\left[\hat{X}^{-}_{k0}\right]\left(\hat{\Theta}^{-}_{nj}t_{j+1,j} + \mathrm{i}v\hat{\Theta}^{+}_{nj}r_{j+1,j}\right)\right\}$$

Similarly, we split χ_{single} into terms

$$\chi_{\text{single}} = \chi^{(1)}_{\text{single}} + \chi^{(2)}_{\text{single}}$$

where

$$\chi^{(1)}_{\text{single}} = \frac{\omega}{v^2}\left\{\left(\sum_{k=0}^{n}\left[\hat{Y}^{+}_{kn}\right]\hat{\Lambda}^{+}_{k0}\frac{\omega_k}{p_k^2} + \sum_{k=1}^{n+1}\left[\hat{X}^{-}_{k-1,0}\right]\hat{\Theta}^{-}_{n,k-1}\frac{\omega_k}{p_k^2}\right)\right.$$
$$\left. -iv\left(\sum_{k=0}^{n}\left[\hat{Y}^{+}_{kn}\right]\hat{\Lambda}^{-}_{k0}\frac{\kappa_k}{p_k^2} - \sum_{k=1}^{n+1}\left[\hat{X}^{-}_{k-1,0}\right]\hat{\Theta}^{+}_{n,k-1}\frac{\kappa_k}{p_k^2}\right)\right\}$$

and

$$\chi^{(2)}_{\text{single}} = -\sum_{k=0}^{n}\left(\left[\hat{X}^{-}_{k0}\right]\hat{\Theta}^{-}_{nk} + \left[\hat{Y}^{+}_{kn}\right]\hat{\Lambda}^{+}_{k0}\right)$$

We first look at the χ_{double}. It can be shown that

$$\hat{\Lambda}^{+}_{j-1,0}t_{j,j-1} - \mathrm{i}v\hat{\Lambda}^{-}_{j-1,0}r_{j,j-1} = -(\mathrm{i}v)\left[\hat{X}^{+}_{j-1,0}\right]$$

and

$$\hat{\Theta}^{-}_{nj}t_{j+1,j} + \mathrm{i}v\hat{\Theta}^{+}_{nj}r_{j+1,j} = (\mathrm{i}v)\left[\hat{Y}^{-}_{jn}\right]$$

So we have

$$\chi^{(1)}_{\text{double}} = \frac{\mathrm{i}\omega}{v} \sum_{j=1}^{n} \sum_{k=j}^{n} \hat{\psi}^{+}_{jk} \left[\hat{Y}^{+}_{kn}\right] \left[\hat{X}^{+}_{j-1,0}\right]$$

and

$$\chi^{(2)}_{\text{double}} = \frac{\mathrm{i}\omega}{v} \sum_{j=1}^{n} \sum_{k=0}^{j-1} \hat{\psi}^{-}_{k+1,j} \left[\hat{X}^{-}_{k0}\right] \left[\hat{Y}^{-}_{jn}\right]$$

Changing the indices, we finally obtain

$$\chi_{\text{double}} = \frac{\mathrm{i}\omega}{v} \sum_{k=0}^{n-1} \sum_{j=k+1}^{n} \sum_{\sigma=\pm} \hat{\psi}^{\sigma}_{k+1,j} \left[\hat{X}^{\sigma}_{k0}\right] \left[\hat{Y}^{\sigma}_{jn}\right]$$

This is very close to our final result; it just lacks the "diagonal terms" with $j = k$. We will now show that χ_{single} reduces to these diagonal terms. We split $\chi^{(1)}_{\text{single}}$ as

$$\chi^{(1)}_{\text{single}} = \frac{\omega}{v^2} \left(\chi^{(11)}_{\text{single}} - \mathrm{i}v\chi^{(12)}_{\text{single}}\right)$$

where

$$\chi^{(11)}_{\text{single}} = \sum_{k=0}^{n} \left[\hat{Y}^{+}_{kn}\right] \hat{\Lambda}^{+}_{k0} \frac{\omega_k}{p_k^2} + \sum_{k=1}^{n+1} \left[\hat{X}^{-}_{k-1,0}\right] \hat{\Theta}^{-}_{n,k-1} \frac{\omega_k}{p_k^2}$$

and

$$\chi^{(12)}_{\text{single}} = \sum_{k=0}^{n} \left[\hat{Y}^{+}_{kn}\right] \hat{\Lambda}^{-}_{k0} \frac{\kappa_k}{p_k^2} - \sum_{k=1}^{n+1} \left[\hat{X}^{-}_{k-1,0}\right] \hat{\Theta}^{+}_{n,k-1} \frac{\kappa_k}{p_k^2}$$

Substituting $\left[\hat{X}^{-}_{k-1,0}\right]$, $\left[\hat{Y}^{+}_{kn}\right]$, $\hat{\Lambda}^{\pm}_{k0}$ and $\hat{\Theta}^{\pm}_{n,k-1}$, we have

$$\begin{aligned}\chi^{(11)}_{\text{single}} = \sum_{k=0}^{n} \Bigg\{ & \left[\hat{C}_{n,k+1}\right] \hat{f}_k^2 \left[\hat{C}_{k-1,0}\right] \left(\frac{\hat{S}^{+}_{k,k+1}\omega_k}{p_k^2} + \frac{\hat{S}^{-}_{k+1,k}\omega_{k+1}}{p_{k+1}^2}\right) \\ & - \left[\hat{D}_{n,k+1}\right] \hat{f}_k^2 \left[\hat{C}_{k-1,0}\right] \left(\frac{\hat{S}^{-}_{k,k+1}\omega_k}{p_k^2} + \frac{\hat{S}^{-}_{k+1,k}\omega_{k+1}}{p_{k+1}^2}\right)\end{aligned}$$

$$+\left[\hat{C}_{n,k+1}\right]\left[\hat{E}_{k-1,0}\right]\left(\frac{\hat{S}^{+}_{k,k+1}\omega_k}{p_k^2}+\frac{\hat{S}^{+}_{k+1,k}\omega_{k+1}}{p_{k+1}^2}\right)$$
$$\left.-\left[\hat{D}_{n,k+1}\right]\left[\hat{E}_{k-1,0}\right]\left(\frac{\hat{S}^{-}_{k,k+1}\omega_k}{p_k^2}+\frac{\hat{S}^{+}_{k+1,k}\omega_{k+1}}{p_{k+1}^2}\right)\right\}$$

and

$$\chi^{(12)}_{\text{single}}=\sum_{k=0}^{n}\left\{\left[\hat{C}_{n,k+1}\right]\hat{f}_k^2\left[\hat{C}_{k-1,0}\right]\left(\frac{\hat{S}^{+}_{k,k+1}\kappa_k}{p_k^2}-\frac{\hat{S}^{-}_{k+1,k}\kappa_{k+1}}{p_{k+1}^2}\right)\right.$$
$$-\left[\hat{D}_{n,k+1}\right]\hat{f}_k^2\left[\hat{C}_{k-1,0}\right]\left(\frac{\hat{S}^{-}_{k,k+1}\kappa_k}{p_k^2}+\frac{\hat{S}^{-}_{k+1,k}\kappa_{k+1}}{p_{k+1}^2}\right)$$
$$-\left[\hat{C}_{n,k+1}\right]\left[\hat{E}_{k-1,0}\right]\left(\frac{\hat{S}^{+}_{k,k+1}\kappa_k}{p_k^2}+\frac{\hat{S}^{+}_{k+1,k}\kappa_{k+1}}{p_{k+1}^2}\right)$$
$$\left.+\left[\hat{D}_{n,k+1}\right]\left[\hat{E}_{k-1,0}\right]\left(\frac{\hat{S}^{-}_{k,k+1}\kappa_k}{p_k^2}-\frac{\hat{S}^{+}_{k+1,k}\kappa_{k+1}}{p_{k+1}^2}\right)\right\}$$

It can be shown that

$$\frac{\hat{S}^{\sigma}_{k,k+1}\omega_k}{p_k^2}+\frac{\hat{S}^{\sigma}_{k+1,k}\omega_{k+1}}{p_{k+1}^2}=\frac{\mathrm{i}}{v}t^2_{k,k+1}+\sigma\frac{\omega_k r_{k,k+1}}{p_k^2}+\sigma\frac{\omega_{k+1}r_{k+1,k}}{p_{k+1}^2}$$

$$\frac{\hat{S}^{\sigma}_{k,k+1}\omega_k}{p_k^2}+\frac{\hat{S}^{-\sigma}_{k+1,k}\omega_{k+1}}{p_{k+1}^2}=\frac{\mathrm{i}}{v}t^2_{k,k+1}+\sigma\frac{\omega_k r_{k,k+1}}{p_k^2}-\sigma\frac{\omega_{k+1}r_{k+1,k}}{p_{k+1}^2}$$

$$\frac{\hat{S}^{\sigma}_{k,k+1}\kappa_k}{p_k^2}+\frac{\hat{S}^{\sigma}_{k+1,k}\kappa_{k+1}}{p_{k+1}^2}=\frac{\mathrm{i}}{v}t_{k,k+1}\left(\frac{\kappa_k}{p_k^2}-\frac{\kappa_{k+1}}{p_{k+1}^2}\right)-\sigma r_{k,k+1}r_{k+1,k}$$

and

$$\frac{\hat{S}^{\sigma}_{k,k+1}\kappa_k}{p_k^2}-\frac{\hat{S}^{-\sigma}_{k+1,k}\kappa_{k+1}}{p_{k+1}^2}=\frac{\mathrm{i}}{v}t_{k,k+1}\left(\frac{\kappa_k}{p_k^2}+\frac{\kappa_{k+1}}{p_{k+1}^2}\right)-\sigma r_{k,k+1}r_{k+1,k}$$

Adding together $\chi^{(11)}_{\text{single}}$ and $-\mathrm{i}v\chi^{(12)}_{\text{single}}$ and we have

$$\frac{v^2}{\omega}\chi^{(1)}_{\text{single}}=\chi^{(1a)}_{\text{single}}+\chi^{(1b)}_{\text{single}}$$

where

$$\chi_{\text{single}}^{(1a)} = \frac{\mathrm{i}}{v}\sum_{k=0}^{n} t_{k,k+1}^2\Big(\big[\hat{C}_{n,k+1}\big]\,\hat{f}_k^2\,\big[\hat{C}_{k-1,0}\big] - \big[\hat{D}_{n,k+1}\big]\,\hat{f}_k^2\,\big[\hat{C}_{k-1,0}\big] + \big[\hat{C}_{n,k+1}\big]\big[\hat{E}_{k-1,0}\big] - \big[\hat{D}_{n,k+1}\big]\big[\hat{E}_{k-1,0}\big]\Big)$$

$$\mathrm{i}v\sum_{k=0}^{n} r_{k,k+1}r_{k+1,k}\Big(-\big[\hat{C}_{n,k+1}\big]\,\hat{f}_k^2\,\big[\hat{C}_{k-1,0}\big] - \big[\hat{D}_{n,k+1}\big]\,\hat{f}_k^2\,\big[\hat{C}_{k-1,0}\big] + \big[\hat{C}_{n,k+1}\big]\big[\hat{E}_{k-1,0}\big] + \big[\hat{D}_{n,k+1}\big]\big[\hat{E}_{k-1,0}\big]\Big)$$

and

$$\chi_{\text{single}}^{(1b)} = \sum_{k=0}^{n}\Big\{\Big(\big[\hat{C}_{n,k+1}\big]\,\hat{f}_k^2\,\big[\hat{C}_{k-1,0}\big] + \big[\hat{D}_{n,k+1}\big]\big[\hat{E}_{k-1,0}\big]\Big)I_k + \Big(\big[\hat{D}_{n,k+1}\big]\,\hat{f}_k^2\,\big[\hat{C}_{k-1,0}\big] + \big[\hat{C}_{n,k+1}\big]\big[\hat{E}_{k-1,0}\big]\Big)J_k\Big\}$$

with

$$I_k = \left(\frac{\omega_k r_{k,k+1}}{p_k^2} - \frac{\omega_{k+1}r_{k+1,k}}{p_{k+1}^2}\right) + t_{k,k+1}\left(\frac{\kappa_k}{p_k^2} + \frac{\kappa_{k+1}}{p_{k+1}^2}\right)$$

and

$$J_k = \left(\frac{\omega_k r_{k,k+1}}{p_k^2} + \frac{\omega_{k+1}r_{k+1,k}}{p_{k+1}^2}\right) - t_{k,k+1}\left(\frac{\kappa_k}{p_k^2} - \frac{\kappa_{k+1}}{p_{k+1}^2}\right)$$

According to the definitions of S_{ji}^{σ}, t_{ji} and r_{ji}, we have

$$S_{ji}^{\sigma} = \frac{\mathrm{i}}{v}t_{ji} + \sigma r_{ji}$$

It can be shown that

$$\frac{1}{v^2}t_{k,k+1}^2 + \sigma r_{k,k+1}r_{k+1,k} = \tfrac{1}{2}\left(S_{k+1,k}^{+}S_{k,k+1}^{\sigma} + S_{k+1,k}^{-}S_{k,k+1}^{-\sigma}\right)$$

So we obtain

$$\chi_{\text{single}}^{(1a)} = \mathrm{i}v \sum_{k=0}^{n} \tfrac{1}{2} \left(\left[\hat{X}_{k0}^{+} \right] \left[Y_{kn}^{+} \right] + \left[\hat{X}_{k0}^{-} \right] \left[\hat{Y}_{kn}^{-} \right] \right)$$

This is the term we were aiming for. So

$$\frac{v}{\mathrm{i}\omega} \left(\chi_{\text{double}} + \frac{\omega}{v^2} \chi_{\text{single}}^{(1a)} \right) = \sum_{k=0}^{n} \sum_{j=k}^{n} \sum_{\sigma=\pm} z_{kj} \hat{\psi}_{k+1,j}^{\sigma} \left[\hat{X}_{k0}^{\sigma} \right] \left[\hat{Y}_{jn}^{\sigma} \right] \tag{E.2}$$

The right hand side of Equation E.2 is, in fact, our final result for χ_{bdy}. But to prove this, it is now necessary to show that $\chi_{\text{single}}^{(1b)} = 0$ and $\chi_{\text{single}}^{(2)} = 0$.

Substituting $r_{k,k+1}$, $r_{k+1,k}$, $t_{k,k+1}$, and $t_{k+1,k}$, we have

$$I_k = \hat{h}_{k+1,k}^{+} \left(\frac{\omega_k}{p_k^4} - \frac{\omega_{k+1}}{p_{k+1}^4} \right)$$

$$J_k = \hat{h}_{k+1,k}^{-} \left(\frac{\omega_k}{p_k^4} - \frac{\omega_{k+1}}{p_{k+1}^4} \right)$$

Hence

$$\begin{aligned} \chi_{\text{single}}^{(1b)} = & \sum_{k=0}^{n} \left(\frac{\omega_k}{p_k^4} - \frac{\omega_{k+1}}{p_{k+1}^4} \right) \times \\ & \left\{ \hat{h}_{k+1,k}^{+} \left(\left[\hat{C}_{n,k+1} \right] \hat{f}_k^2 \left[\hat{C}_{k-1,0} \right] + \left[\hat{D}_{n,k+1} \right] \left[\hat{E}_{k-1,0} \right] \right) \right. \\ & \left. + \hat{h}_{k+1,k}^{-} \left(\left[\hat{D}_{n,k+1} \right] \hat{f}_k^2 \left[\hat{C}_{k-1,0} \right] + \left[\hat{C}_{n,k+1} \right] \left[\hat{E}_{k-1,0} \right] \right) \right\} \\ = & \sum_{k=0}^{n} \left(\frac{\omega_k}{p_k^4} - \frac{\omega_{k+1}}{p_{k+1}^4} \right) \left[\hat{C}_{n0} \right] = 0 \end{aligned}$$

Now we look at $\chi_{\text{single}}^{(2)}$. Substituting $\hat{\Theta}_{nk}^{-}$, $\hat{\Lambda}_{k0}^{+}$ and using the definitions of $\left[\hat{X}_{k0}^{-} \right]$ and $\left[\hat{Y}_{kn}^{+} \right]$, we have

$$\chi_{\text{single}}^{(2)} = - \sum_{k=0}^{n} \left\{ \left[\hat{C}_{n,k+1} \right] \hat{f}_k^2 \left[\hat{C}_{k-1,0} \right] \left(\hat{S}_{k+1,k}^{-} + \hat{S}_{k,k+1}^{+} \right) \right.$$

$$- \left[\hat{D}_{n,k+1}\right] \hat{f}_k^2 \left[\hat{C}_{k-1,0}\right] \left(\hat{S}^-_{k+1,k} + \hat{S}^-_{k,k+1}\right)$$
$$+ \left[\hat{C}_{n,k+1}\right] \left[\hat{E}_{k-1,0}\right] \left(\hat{S}^+_{k+1,k} + \hat{S}^+_{k,k+1}\right)$$
$$- \left[\hat{D}_{n,k+1}\right] \left[\hat{E}_{k-1,0}\right] \left(\hat{S}^+_{k+1,k} + \hat{S}^-_{k,k+1}\right)\Big\}$$

Furthermore, it can be shown that

$$\hat{S}^\sigma_{k+1,k} + \hat{S}^\sigma_{k,k+1} = \sigma \hat{h}^-_{k+1,k} \left(\frac{1}{\epsilon_k^{(33)} p_k^2} - \frac{1}{\epsilon_{k+1}^{(33)} p_{k+1}^2} \right)$$

$$\hat{S}^\sigma_{k+1,k} + \hat{S}^{-\sigma}_{k,k+1} = -\sigma \hat{h}^+_{k+1,k} \left(\frac{1}{\epsilon_k^{(33)} p_k^2} - \frac{1}{\epsilon_{k+1}^{(33)} p_{k+1}^2} \right)$$

So

$$\chi^{(2)}_{\text{single}} = - \sum_{k=0}^{n} \left(\frac{1}{\epsilon_k^{(33)} p_k^2} - \frac{1}{\epsilon_{k+1}^{(33)} p_{k+1}^2} \right) \left[\hat{C}_{n0}\right] = 0$$

Collecting all terms together, we finally obtain

$$\chi_{\text{bdy}} = \frac{1}{\left[\hat{C}_{n0}\right]} \sum_{\sigma=\pm} \sum_{k=0}^{n} \sum_{j=k}^{n} z_{kj} \hat{\psi}^\sigma_{k+1,j} \left[\hat{X}^\sigma_{k0}\right] \left[\hat{Y}^\sigma_{jn}\right]$$

Bibliography

[1] J. Bruley. *Ph.D Thesis.* Cambridge University, 1987.

[2] N.W. Aschroft and N.D. Mermin. *Solid State Physics.* New York, 1976.

[3] H. Raether. *Springer Tracts in Modern Physics.* Springer-Verlag, Berlin, 1980.

[4] R.F. Egerton. *Electron Energy–loss Spectrocopy.* Plenum Press, New York, 1986.

[5] G.D. Mahan. *Many-Particle Physics.* Plenum Press, New York, 1981.

[6] R.H. Ritchie. *Physical Review*, 106:874–881, 1957.

[7] J.S. Stratton. *Electromagnetic Theory.* McGraw-Hill, New York, 1941.

[8] E Rudberg. *Proc. Roy. Soc.*, A 127:111, 1930.

[9] E Rudberg. *Physical Review*, 50:138, 1936.

[10] D. Bohm and D. Pines. *Physical Review*, 82:625, 1951.

[11] J Hubbard. *Proc. Phys. Soc.*, 68:411 and 976, 1955.

[12] G. Ruthemann. *Naturwissenschaften*, 29:648, 1941.

[13] S.J. Pennycook. *Ultramicroscopy*, 7:99, 1981.

[14] D. Pines and D. Bohm. *Physical Review*, 85:338–353, 1952.

[15] D. Pines. *Physical Review*, 92:626, 1953.

[16] P. Nozieres and D. Pines. *Physical Review*, 109:741, 1958.

[17] P. Nozieres and D. Pines. *Physical Review*, 109:762, 1958.

[18] P. Nozieres and D. Pines. *Physical Review*, 109:1009, 1958.

[19] R.A. Ferrell. *Physical Review*, 101:554, 1956.

[20] C.J. Powell and J.B. Swan. *Physical Review*, 118:640., 1960.

[21] E. Kroger. *Z. Phys.*, 216:115–135, 1968.

[22] E. Kroger. *Z. Phys.*, 235:403–421, 1970.

[23] J. Daniels, C.V. von Festenberg, H. Raether, and K. Zeppenfeld. *Springer Tracts in Modern Physics.* Springer-Verlag, Berlin, 1970.

[24] J. Yuan. In P.J. Goodhew and H.Y. Elder, editors, *EMAG-MICRO 89 Inst. Phys. Conf. Ser. No 98*, pages 45–48, 1989.

[25] H. Richter and J. Geiger. *Z. Phys. B*, 42:39–45, 1981.

[26] J.B. Chase and K.L. Kliewer. *Physical Review B*, 2:4389–4400, 1970.

[27] P.M. Echenique and J.B. Pendry. *J. Phys. C: Solid State Phys.*, 8:1936, 1975.

[28] P.M. Echenique. *The Philosophical Magazine*, B52:L9–L13, 1985.

[29] R.H. Milne and P.M. Echenique. *Solid State Commun.*, 55:909–910, 1985.

[30] A Howie and R.H. Milne. *J. Microsc.*, 136:279–285, 1984.

[31] A Howie and R.H. Milne. *Ultramicroscopy*, 18:427, 1985.

[32] P.E. Batson. In R. Geiss, editor, *Analytical Electron Microscopy*, 1981.

[33] P.E. Batson. *Ultramicroscopy*, 11:299–302, 1983.

[34] R. Garcia-Molina, A. Gras-Marti, A. Howie, and R.H. Ritchie. *J. Phys. C: Solid State Phys.*, 18:5335–5345, 1985.

[35] A. Parker. Part 2 project, University of Cambridge 1988.

[36] C.M. Walsh. Private Communication.

[37] R.H. Ritchie. *The Philosophical Magazine*, A44:931–942, 1981.

[38] P.E. Batson. *Ultramicroscopy*, 9:277, 1982.

[39] P.E. Batson. *Physical Review Letters*, 49:936, 1982.

[40] J.M. Cowley. *Surface Science*, 114:1587, 1982.

[41] A. Howie. *Ultramicroscopy*, 11:141, 1983.

[42] C. Colliex. *Ultramicroscopy*, 18:131, 1985.

[43] A.A. Fujimoto and K. Komaki. *J. Phys. Soc. Japan*, 25:1679, 1968.

[44] M. Schmeits. *J. Phys. C: Solid State Phys.*, 14:1203, 1981.

[45] H. Kohl. *Ultramicroscopy*, 11:53, 1983.

[46] M. Acheche. *These de Troisieme Cycle.* Orsay, 1985.

[47] M. Acheche, C. Colliex, and P. Trebbia. *Scann. Electron Microsc.*, 1986. SEM Inc., A.M.F. O'Hare, Illinois.

[48] M. Acheche, C. Colliex, H. Kohl, A. Noutier, and P. Trebbia. *Ultramicroscopy*, 20:99, 1986.

[49] P.E. Batson. *Solid State Commun.*, 34:477, 1980.

[50] P.E. Batson. *Surface Science*, 156:720, 1985.

[51] T.L. Ferrel and P.M. Echenique. *Physical Review Letters*, 55:1526, 1985.

[52] P.M. Echenique, A. Howie, and D.J. Wheatley. *The Philosophical Magazine*, B56:335–349, 1987.

[53] Z.L. Wang and J.M. Cowley. *Ultramicroscopy*, 21:77, 1987.

[54] M. Schmeits and L. Dambly. *Physical Review*, B44:12706, 1991.

[55] D. Ugarte, C. Colliex, and P. Trebbia. *Physical Review*, B45:4332, 1992.

[56] A. Murray, M. Isaacson, and I. Adesida. *Applied Physics Letters*, 45:589, 1984.

[57] S.D. Berger, I.G. Salisbury, R.H. Milne, D. Imeson, and C.J. Humphreys. *The Philosophical Magazine*, B55:341, 1987.

[58] M. Schmeits. *Solid State Commun.*, 67:172, 1988.

[59] C.A. Walsh. *The Philosophical Magazine*, A59:227, 1989.

[60] C.A. Walsh. *The Philosophical Magazine*, B63:1063, 1991.

[61] N. Zabala, A. Rivacoba, and P.M. Echenique. *Surface Science*, 209:465, 1989.

[62] M. Schmeits. *Physical Review*, B39:7567, 1989.

[63] Y.T. Chu, R.J. Warmack, R.H. Ritchie, R.J. Little, R.S. Becker, and T.L. Ferrell. *Particle Accelerators*, 16:13, 1984.

[64] D. DeZutter and D. De Vleeschauwer. *J. Appl. Phys.*, 59 (12):4146, 1986.

[65] L. Dobrzynski and A.A. Maradudin. *Physical Review*, B6:3810, 1972.

[66] L.D. Davis. *Physical Review*, B6:3810, 1976.

[67] R. Garcia-Molina, A. Gras-Marti, and R.H. Ritchie. *Physical Review B*, 31:121, 1985.

[68] L.D. Marks. *Solid State Commun.*, 43:727, 1982.

[69] J Hubbard. *Proc. Roy. Soc.*, A 243:336, 1957.

[70] K. Zeppenfeld. *Z. Phys.*, 211:391, 1968.

[71] B.M. Kincaid, A.E. Meixner, and P.M. Platzman. *Physical Review Letters*, 40:1296, 1978.

[72] R.D. Leapman, P.L. Fejes, and J. Silcox. *Physical Review B*, 28:2361, 1983.

[73] P.E. Batson and M.F. Chisholm. *Physical Review B*, 37:635, 1988.

[74] N. Nucker, H. Romberg, X.X. Xi, J. Fink, B. Gegenheimer, and Z.X. Zhao. *Physical Review B*, 39:6619, 1989.

[75] N.D. Browning, J. Yuan, and L.M. Brown. *Ultramicroscopy*, 38:291–298, 1991.

[76] N.D. Browning, J. Yuan, and L.M. Brown. *The Philosophical Magazine*, A67:261–271, 1993.

[77] M. Chen and J.P.R. Bolton. *Superlattices and Microstructures*, 12:531–534, 1992.

[78] R.H. Ritchie and H.B. Eldridge. *Physical Review*, 126:1935, 1962.

[79] L.D. Landau and E.M. Lifshitz. *Electrodynamics of Continuous Media.* Pergamon Press, New York, 1960.

[80] E.N. Economou. *Physical Review*, 182:539–554, 1969.

[81] S. Seely and A. D. Poularikas. *Electromagnetics.* Marcel Dekker, Inc., New York, 1979.

[82] R.A. Ferrell. *Physical Review*, 111:1214, 1958.

[83] E.D. Palik, editor. *Handbook of Optical Constants of Solids.* Academic, New York, 1985.

[84] H.R. Phillipp and E.A. Taft. *Physical Review*, 136:1455, 1964.

[85] P.J. Fallon. *Ph.D Thesis.* Cambridge University, 1992.

[86] P. Schattschneider. *Fundamentals of Inelastic Electron Scattering.* Springer-Verlag, Wien, 1986.

[87] F.R. McFeely, S.P. Kowalczyk, L. Ley, R.G. Cavell, R.A. Pollak, and D.A. Shirley. *Physical Review*, B9:5268–5278, 1974.

[88] E.D. Palik, editor. *Handbook of Optical Constants of Solids II.* Academic, Boston, 1991.

INDEX